Department of Physics and Astronomy

Porous Metal Scaffolds for Hydrogen Storage

Enrico Ianni

This thesis is presented for the Degree of
Doctor of Philosophy
of
Curtin University

December 2018

To the best of my knowledge and belief this thesis contains no material previously published by any other person except where due acknowledgement has been made. This thesis contains no material which has been accepted for the award of any other degree or diploma in any university.

Enrico Ianni

Statement of Contribution by Others

My input into this study and the associated papers included the execution of all the experimental work, data analysis, drawing up, as well as a dominant contribution to the intellectual input involved in the project. Other scientists made some contribution to the current work, as is almost always the case in the physical sciences. These contributions were significant enough to warrant co-authorship on the resulting journal articles. These are specified in the list of publications below.

- E. Ianni, M. V. Sofianos, D. A. Sheppard, M. R. Rowles, T. D. Humphries, S. Liu and C. E. Buckley, *Journal of Materials Science*, 2018, 53, 1076 – 1087.
- E. Ianni, M. V. Sofianos, M. R. Rowles, D. A. Sheppard, T. D. Humphries and C. E. Buckley, *International Journal of Hydrogen Energy*, 2018, 43, 17309 – 17317.

(Enrico Ianni, Candidate)

(Professor Craig E. Buckley, Supervisor)

Abstract

Due to increasing world-wide energy demands, limited fossil fuel resources and dangerous climate change caused by global greenhouse gas emissions, a renewable and sustainable energy economy is required. Green hydrogen, produced through electrolysis powered by renewable energy, has been highlighted as a promising alternative energy carrier due to its high energy-to-mass ratio of 120 MJ/kg. The goal of this thesis is to investigate and improve hydrogen storage systems for vehicle applications. Due to their thermodynamic, hydrogen specific weight, and volumetric properties, several complex metal hydrides, where the hydrogen is chemically bonded, are the most promising candidates. However, these metal hydrides suffer from poor hydrogen reversibility and slow hydrogen absorption/desorption kinetics. Nanoconfinement and the use of catalysts represent promising solutions to overcoming these limitations.

A simple and cost-effective method for the synthesis of porous Mg and Ti-enriched porous Al scaffolds has been optimised using only $NaMgH_3$ and $NaAlH_4$ + 2 mol% of $TiCl_3$, respectively. The starting materials were compacted into a pellet and sintered under dynamic vacuum to remove the Na and H_2. The sintering conditions, such as vacuum level, temperature and time were the key factors that influenced both the extraction of Na and H_2 from the pellet, and the overall porosity. The dynamics of porous formation and growth during the sintering process were investigated. $NaAlH_4$ was, successively, melt-infiltrated inside the porous Ti-enriched Al scaffold to investigate the combined effects of catalysis and nanoconfinement on its hydrogen desorption kinetics and thermodynamic

properties.

The following techniques were used to characterise the Mg and Al scaffolds and the $NaAlH_4$/Al system: X-Ray Diffraction (XRD), Small- and Wide-Angle X-ray Scattering (SAXS/WAXS), thermodynamic simulations (HSC software), Scanning Electron Microscopy (SEM), N_2 sorption (BET and BJH methods), Temperature Programmed Desorption (TPD) and TPD-Mass Spectrometry (TPD-MS).

Mg and Ti-enriched porous Al scaffolds possessing an open porous network were successfully produced with their structural integrity intact. The specific pore volume corresponding to the formation of mesopores of a Mg and a Ti-enriched Al scaffold were 0.034 and 0.027 cm^3/g, respectively. For this Al scaffold, the mesopores contributed a partial porosity of only 2.7%, whereas the remaining 41.9% of the scaffold's porosity was due to the presence of macropores and voids. The specific surface areas for these Mg and Ti-enriched Al scaffolds were determined to be 7.9(1) and 26(2) cm^2/g, respectively. The formation of mesopores depends on the crystal structure properties of metal hydrides used to produce the scaffolds, and their decomposition products. Large changes in the intensity of the crystalline phases during sintering correspond with the formation of more mesoporosity. During the first two steps of $NaAlH_4$ decomposition the mesoporosity was estimated to increase between 1.7 and 15×. The formed mesopores are observed to grow at a constant rate during the sintering process, leading to a final mesoporosity for an Al scaffold sintered for 12 hours, of $\simeq$ 5× higher than the initial $NaAlH_4$ pellet. The infiltrated $NaAlH_4$ homogeneously coats the walls of the Al scaffold with the smallest pores filled first. As the majority of pores are macro pores, kinetic improvements due to nanoconfinement effects are slightly evident; the infiltrated scaffolds at lower loadings release relatively more hydrogen than bulk Ti-catalysed $NaAlH_4$ in the temperature range of 148 – 220 °C, with the temperatures tending towards bulk $NaAlH_4$ with increased loadings.

A future work section is included in the final part of this thesis where several suggestions are listed based on the scientific knowledge gained from this research

for designing future hydrogen storage systems, and using metal hydrides infiltrated into porous metal scaffolds for vehicular applications.

Acknowledgements

I would like to acknowledge many people for their help in the completion of this thesis. First and foremost, my humblest gratitude goes to both my supervisors, Dr Matthew R. Rowles and Prof Craig E. Buckley. Prof Craig E. Buckley for giving me the opportunity to undertake this PhD project and Dr Matthew R. Rowles for his outstanding guidance and supervision throughout the second half of this long journey, you have taught me valuable lessons in research and academia. Thanks to Dr M. Veronica Sofianos and Dr Drew A. Sheppard for their professional guidance and supervision during the first half of my Ph.D.

I would like to acknowledge the organisations and facilities that supported my research. Curtin University and the Curtin International Postgraduate Research Scholarship (CIPRS) for financial support.

I would like to take this opportunity to thank the past and present members of the Hydrogen Storage Research Group for providing a friendly atmosphere and great support throughout the years. Special mentions go to Dr Terry D. Humphries, Dr Mark Paskevicius, Dr Kasper Moeller, Dr Dehua Dong, Dr Kevin Jarret, Dr Payam Javadian, Dr Tam Nguyen, Arnaud Griffond, Mariana Tortoza, Lucas Poupin, Greg Nolan, Ali Alamri and Sruthy Balakrishnan.

Finally, I would like to thank my family and friends for love and support throughout my studies and all my endeavours in life.

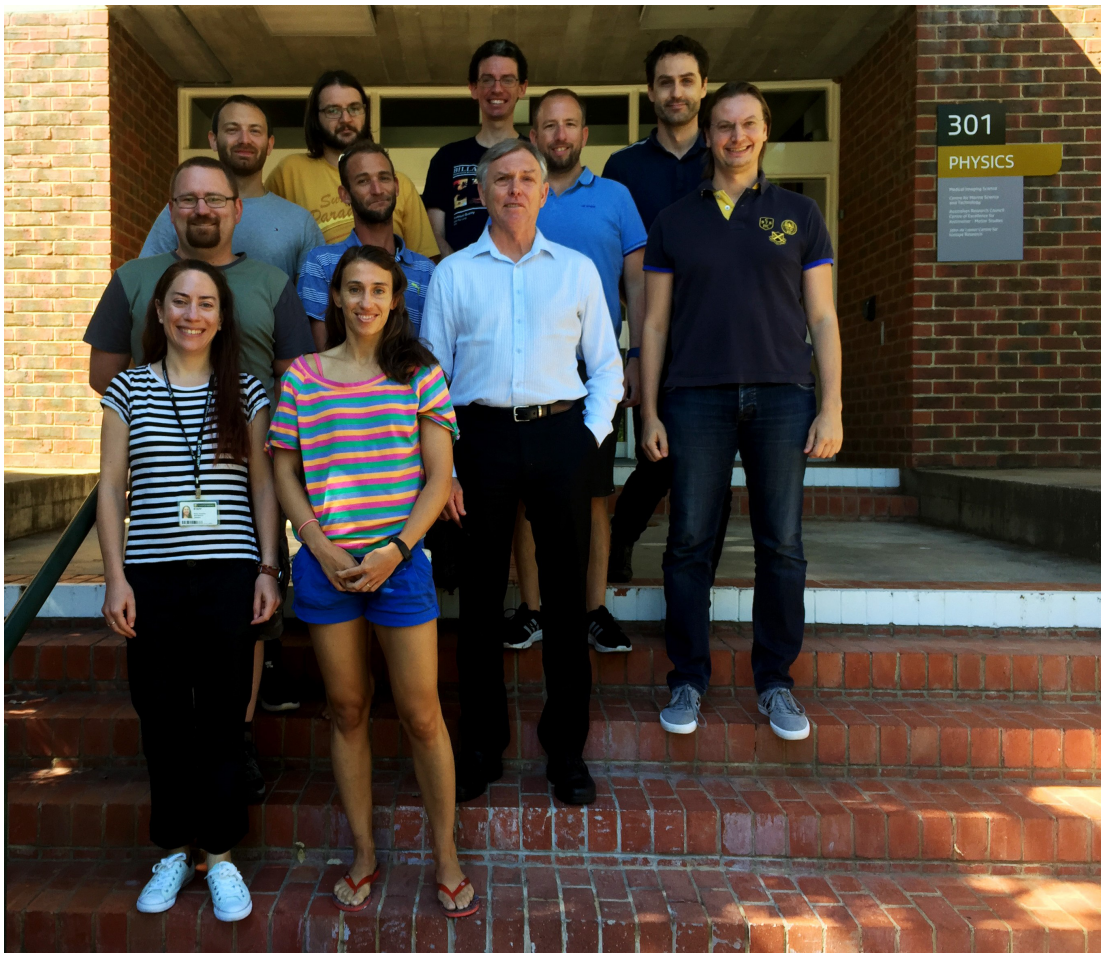

Hydrogen Storage Research Group: (top row, from the left to right) Arnaud Griffond, Dr Matthew R. Rowles, Dr Drew A. Sheppard, (second top row, from the left to right) Steffen Jensen, Lucas Poupin, Dr Terry D. Humphries, Enrico Ianni, (middle row, from the left to right) Dr Mark Paskevicius, Prof Craig E. Buckley, (bottom row, from the left to right) Dr M. Veronica Sofianos, Mariana Tortoza.

Contents

List of Figures

Chapter 1

Introduction

1.1 Significance

1.1.1 How do we supply the world's energy needs?

Most of the world's energy needs are currently supplied by non-renewable energy sources such as coal, crude oil, LPG, natural gas, and uranium[1,2]. There is widespread acceptance that current hydrocarbon fuels used as sources of energy will need to be substituted by low-carbon alternatives if global greenhouse gas emissions are to be reduced sufficiently to avoid dangerous climate change[3]. Long-term solutions in terms of viability, scalability, and sustainability of resources can only be achieved by renewable energy such as wind, solar, hydroelectric, wave, tidal, geothermal energies, ocean thermal gradients, and biomass. Table 1.1 shows the power outputs available from the main renewable energy sources compared to the total solar power incident on the surface of Earth. The table points out that they all supply less than 1% of available solar power. Among the renewable energies, solar is dominant in term of magnitude and longevity, considering that it also corresponds to more than 5000 times the all humankind's energy needs. All non-solar renewable energies, except for geothermal, are indeed solar converted energies due to indirect consequences from the presence of the sun. For instance,

Table 1.1: Power available from renewable sources[1].

Energy source	Max. power (TW)	% of tot. solar	Ref.
Total surface solar	85000	100	[4]
Desert solar	7650	9	[4]
Ocean thermal	100	0.12	[5]
Wind	72	0.08	[6]
Geothermal	44	0.05	[7]
River hydroelectric	7	0.008	[8]
Biomass	7	0.008	[8]
Open ocean wave	7	0.008	[9]
Tidal wave	4	0.003	[10]
Coastal wave	3	0.003	[11]

wind comes from the sun heating the ground, creating massive convection currents, biomass organisms have absorbed energy from the sun through the process of photosynthesis, and thermal gradients are due to solar radiation absorbed mainly on the ocean surfaces. Although, they still can be justified for niche power in cold countries and also providing some backup security for critical utilities in case of natural disasters.

1.1.2 Why hydrogen as a carrier of energy?

Hydrogen is one of the most abundant elements on Earth, but less than 1% is present as molecular hydrogen gas H_2. The overwhelming majority is chemically bond as H_2O in water and bond to liquid or gaseous hydrocarbons[12]. Hydrogen is non-toxic and it has been highlighted as a promising alternative energy carrier due to its high energy-to-mass ratio of 120 MJ/kg; over two times greater than that of other chemical fuels, see Table 1.2.

The hydrogen cycle is shown in Fig. 1.1 and listed below:

- Hydrogen is produced by the electrolysis of water or thermolysis (steam reforming) of hydrocarbons (see §1.1.3).
- It can be stored in high-pressure gas form, in very low-temperature liquid

form, or in chemically or physically bonded solid form (see §1.2). Depending on the application, it can be transported on board using tanks (in solid and high-pressure gas form) or in pipes (in high-pressure gas form only).

- The stored energy is released by the recombination of hydrogen with oxygen by combustion processes in a similar manner to petrol or natural gas or by hydrogen fuel cells (see §1.1.3).

Table 1.2: Physical and chemical properties of hydrogen, methane and petrol[12].

Properties	Hydrogen (H_2)	Methane (CH_4)	Petrol ($-CH_2-$)
Lower heating value (MJ/kg)	120	50	45
Self-ignition temperature (°C)	585	540	228 – 501
Flame temperature (°C)	2045	1875	2200
Ignition limits in air (Vol%)	4 – 75	5.3 – 15	1.0 – 7.6
Minimal ignition energy (mW s)	0.02	0.29	0.24
Flame propagation in air (m/s)	2.65	0.4	0.4
Diffusion coefficient in air (cm^2/s)	0.61	0.16	0.05
Toxicity	No	No	High

In order for it to be a renewable and sustainable carrier of energy, the hydrogen, and also the materials adopted in any step of the hydrogen cycle, have to be produced using non-carbon emitting methods (see §1.1.1). Due to the limited abundance of battery chemical constituents, such as lithium, and intermittent energy sources, such as solar or wind, a further benefit of the hydrogen energy cycle, in contrast with electricity, is that it allows the possibility of large-scale storage. For mobile applications, electric vehicles may appear more attractive due to a large existing infrastructure for distribution of electricity, but considering a near-futuristic scenario of driverless fuel cell powered sharing vehicles, only a limited number of hydrogen service stations would be required.

1.1.3 Electrolyser and fuel cell technology

Hydrogen is produced by separating it from other elements, for instance, such as carbon and oxygen, with which it forms methane (CH_4) and water (H_2O),

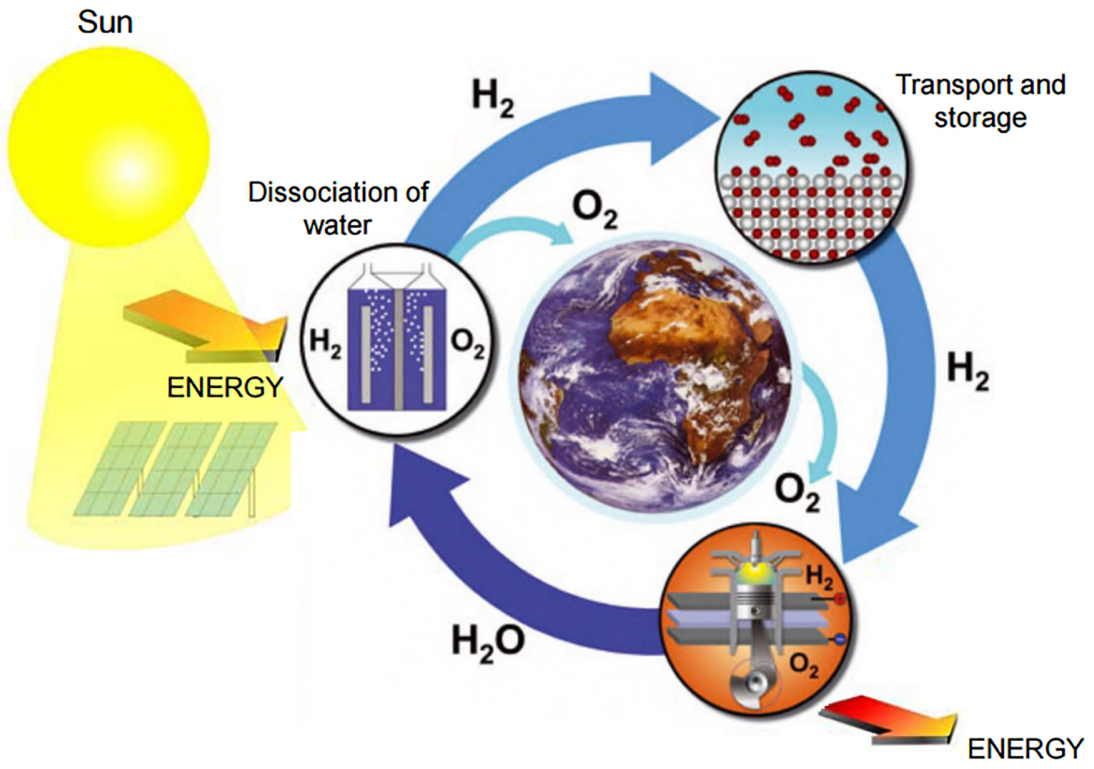

Figure 1.1: Hydrogen cycle[13].

respectively. The global hydrogen industry is well established and produces more than 50 million tonnes of hydrogen per year[14]. 95% of hydrogen production derives from wood or from fossil fuels, such as natural gas and oil, predominantly by a procedure called steam reforming[15]. The hydrogen production by electrolysis of water; using an electric current to split water (H_2O) into oxygen (O_2) and hydrogen (H_2), is only 4% of the worldwide production[16].

Hydrogen fuel cells represent a carbon-free method of heat and electricity generation compatible with many vehicle and domestic/industrial applications. Using pure hydrogen and air, fuel cells convert the chemical energy of the fuel directly into electricity with high efficiency, producing only water as a waste product, thus eliminating all local emissions. The efficiency measurements of hydrogen fuel cell powered cars (not limited by the Carnot efficiency) can reach 50 – 60%[12], which is a factor of 1.5 – 2× higher than the hydrogen-powered internal combustion engine (ICE) vehicles[13], but further technological innovation is needed

to improve the cost-competitiveness of fuel cells in the marketplace[17]. Fuel cells are usually classified according to the electrolyte and, depending on the nature of the electrolyte, the operating temperature ranges from 20 to 1000 °C. Low temperature (< 200 °C) fuel cells have superior dynamic operation and reliability with thermal cycling which make them suitable for vehicle applications. Low-temperature fuel cells consist of alkaline fuel cells (AFC), polymer electrolyte fuel cells (PEFC), direct methanol fuel cells (DMFC), phosphoric acid fuel cells (PAFC), and one of the most commonly used, due to their performance, proton exchange membrane (PEM) fuel cells[18–21]. PEM fuel cells require a high level of hydration, which limits the operating temperature to less than 100 °C at atmospheric pressure[20], see Fig. 1.6. In conclusion, an energy transition[22], towards a renewable and sustainable hydrogen economy would occur only if the hydrogen is produced through the electrolysis of water powered by renewable energy sources and used in fuel cells, where the only waste product is water which is not hazardous to public health or the environment[23,24].

1.2 Hydrogen storage for vehicle applications

One of the most difficult remaining technological issues for the conversion to a hydrogen economy from fossil fuels is the storage of hydrogen.

For vehicular applications, a hydrogen storage tank is required to store large amounts of hydrogen in a light and compact form, 1.8 kWh/kg (net useful energy/total system mass) and 1.3 kWh/L (net useful energy/total system volume) respectively according to 2025 target by the US Department of Energy (DOE)[25]. A modern, commercially available car optimized for mobility with a range of 400 km, burns about 24 kg of petrol in a combustion engine which occupies a volume of about 32 L. Considering the energy density of hydrogen and petrol (see Table 1.2) and the efficiencies of fuel cells and petrol internal combustion engines (see §1.1.3), in order to cover the same range, 4 kg of hydrogen, that in solid and liquid

form occupy about 57 L, are needed for an electric car powered by fuel cells[12]. Furthermore, a mobile hydrogen tank has to be safe, be able to be refuelled rapidly, have over 1500 charge/discharge cycles[25] and have a limited negative impact on the efficiency of the storage/power system (for example, minimal energy should be expended in order to release hydrogen from the storage media). Furthermore, and probably most challenging, is the net storage system cost that according to the 2025 target by the US Department of Energy (DOE)[25] has to be a maximum of 10 $/kWh.

1.2.1 Compressed gas and liquid storage

A number of methods can be used to achieve practical gravimetric and volumetric hydrogen density for the purpose of storage. For instance, the hydrogen can be cooled to cryogenic temperatures and stored as a liquid, compressed to high pressures and stored as a gas at near ambient temperature, or chemically bonded and stored in solid hydrides at near ambient temperature and pressure.

In order to produce liquid hydrogen, considering a 1 bar hydrogen back pressure, the hydrogen has to reach its boiling point of −252.8 °C or at least its critical temperature of −240.2 °C for a hydrogen back pressure higher than 30 bar. During the required liquefaction process, according to von Helmolt and Eberle[26], 30% of the stored chemical energy is consumed. Further disadvantages are the energy that needs to be consumed to maintain the cryogenic temperature and the cost of complex tank systems to meet safety requirements to prevent strong overpressure. Overall, the liquid hydrogen storage is particularly unsuitable for vehicle applications[27].

Compressed gas cylinders are the most advanced technology available, currently dominating the hydrogen storage market for vehicle applications. Although, because of several disadvantages listed below, high-pressure systems do not represent the best solution for future hydrogen storage systems for vehicle applications. Despite the small amount of hydrogen required by a fuel cell powered

car (see §1.2), the hydrogen storage vessel itself has a significant weight. This can be reduced through the use of low-density materials to construct the high-pressure tank[27]. The high-pressure tank (700 bar) mounted on the commercial Toyota Mirai car has a combined weight (not including valves), for an equivalent capacity of 4 kg of hydrogen, of 70 kg, corresponding to 5.7 weight total % (wt%) of H_2[28]. This high-pressure tank is made of hydrogen-inert aluminium and is strengthened using external carbon-fibre coatings. Its operative pressure of 700 bar leads to an internal volume occupancy of 98 L[28,29]. A further disadvantage occurs, as the fuel is available at a pressure dropping from 700 bar to zero overpressure, so additional pressure control is essential[12]. Although hydrogen gas is volatile and non-toxic, for high pressurised systems a failure in the containment vessel has the potential to cause violent release of gas and possibly an explosion[12,30]. Furthermore, 15% of the stored chemical energy is consumed for compressed hydrogen gas at 700 bar[27]. In conclusion, storing hydrogen as a liquid or compressed gas requires a large amount of energy, and is accompanied by many hazards associated with cryogenic temperatures and high pressures[31].

1.2.2 Chemically bonded hydrogen in solid materials

Solid materials used to store hydrogen are categorised by the mechanism through which they absorb/adsorb hydrogen[27]. Microporous materials adsorb molecular hydrogen through physisorption, where hydrogen molecules are attached to a surface via van der Waals forces. Microporous materials are characterised by having pore dimensions less than 2 nm in order to have an extraordinarily large internal surface areas and thus an increased hydrogen storage capacity. Unfortunately, microporous materials tend to have high storage capacities at temperatures near the boiling point of liquid nitrogen, which is not suitable for vehicular applications. This thesis is focused on metal hydrides, materials where the hydrogen gas reacts with metals to form a solid chemical compound which allows hydrogen to be released through thermal decomposition, generally referred to as chemisorption.

Some metal hydrides are suitable materials for hydrogen storage for vehicle applications due to their thermodynamic properties. The operative condition of 25 – 100 °C at 1 bar of H_2 for PEM fuel cells, introduced in §1.1.3, would be fulfilled by those hydrogen sorption reactions having their thermodynamic equilibrium temperatures at 1 bar of hydrogen in the range of $25 < T_{eq.}^{1\ bar\ H_2}$ (°C) < 100. The reason why the equilibrium temperatures cannot be too close to the lower and higher limits, as specified in the equilibrium temperature range above, is to meet the PEM operative condition across the entire peak of the hydrogen desorbed rate with temperature, indeed a thermodynamic equilibrium temperature is the temperature corresponding only to the maximum of the peak.

In principle, the standard Gibbs free energy requirement for a hydrogen sorption reaction has to be in a range that depends on the reaction itself. For metal hydrides, because the entropy change corresponds mostly to the change from molecular hydrogen gas to dissolved solid hydrogen, it is approximately equivalent to the standard entropy of hydrogen $\Delta S^{\Theta} = 130.7$ J/K mol of H_2, see Table 2.2[13]. Thus, considering $\Delta S_{reaction} \simeq 130.7$ J/K mol of H_2, for all metal hydrides systems, the standard Gibbs energies requirement for a hydrogen sorption reaction has to be in the range of $0 < \Delta G^{\Theta}$ (kJ/mol of H_2) < 9.8[20]. Dealing with near-ambient temperature and pressure, it is not only safer but also more efficient, than storing hydrogen as a gas or liquid, due to the limited energy ($\Delta Q = T\Delta S_{reaction}$) required to overcome potential energy changes in order to load and unload hydrogen in a solid-state storage system.

The energy density requirement for vehicle applications, in order to cover petrol ICE performance (from §1.2), for the specific case of metal hydrides corresponds to 16.7 wt% of hydrogen chemically bonded in the metal hydride (100 × 4 kg of H_2/24 kg of $-CH_2-$). Some complex metal hydrides present promising theoretical values of wt% of hydrogen, for instance $LiBH_4$ (18.5 wt%)[32,33], $NaAlH_4$ (7.4 wt%)[34] and Li_3AlH_6 (11.2 wt%)[35], but only those atoms of hydrogen that are desorbed/absorbed across reactions thermodynamically suitable for PEM operative

conditions can be used. Although the hydrogen atoms are initially bonded by thermodynamically suitable covalent/interstitial bonding, across multiple reactions some of them may end up being bonded by a stronger and thermodynamically unfavourable ionic bond. For instance, the effective wt% of hydrogen for the complex metal hydrides, cited above, drop to 13.8 wt% for $LiBH_4$, 5.6 wt% for $NaAlH_4$ (see the $NaAlH_4$ multi-step hydrogen desorption in equations 1.3 – 1.5 and their van't Hoff plots in Fig. 1.5) and 5.6 wt% for Li_3AlH_6 due to the formation of ionic compounds such as LiH and NaH. Indeed, the standard Gibbs free energy of sorption of NaH, $\Delta G^{\Theta} = 68$ kJ/mol H_2, is not in the range of Gibbs energies, $0 < \Delta G^{\Theta}$ (kJ/mol of H_2) < 9.8, suitable for PEM operative conditions[36]. Solid hydrogen storage systems can be sensitive to impurities, especially oxygen due to its elevated reduction power, and thus materials can reduce their reversible capacity across charge/discharge hydrogen cycles[27].

Some complex hydrides present promising volumetric energy densities. For example, Mg_2FeH_6 ($T_{eq.}^{1\ bar\ H_2} = 394$ °C[35]) has a volumetric density of 150 g of H_2/L, which is over double that of liquid hydrogen (70.8 g of H_2/L), leading to an equivalent tank volume of 26.7 L assuming a 100% dense metal hydride[12,30,37]. Unfortunately, for the known complex metal hydrides that present thermodynamic suitable properties for vehicle applications, the effective volumetric densities are inferior compared with petrol ICE technology. For instance, the complex metal hydrides cited above possess effective equivalent tank volumes of 43.5 L for $LiBH_4$ (13.8 wt%), 57.6 L for $NaAlH_4$ (5.6 wt%) and 70.0 L for Li_3AlH_6 (5.6 wt%), see Table 1.3.

It is clear from Table 1.3 that the effective energy density and volumetric energy density of metal hydrides developed so far for vehicle applications have some disadvantages compared with petrol ICE technology. Not by chance, current metal hydride tanks on the market are mainly installed on fuel cell powered forklifts.

The kinetic hydrogen sorption properties of a storage material determine the rate at which the hydrogen can be charged and discharged. If a material cannot take

Table 1.3: Energy and volumetric energy densities comparison between petrol and hydrogen stored in different forms.

Phase	Theoretical wt% of H_2	Effective wt% of H_2	Volume (L) occupied by 4 kg of H_2
Petrol (—CH_2—)		16.7 [a]	32 [b]
High-pressure gas tank (700 bar)	100	5.7	98
Mg_2FeH_6	5.4	0	26.7
$LiBH_4$	18.5	13.8	43.5
$NaAlH_4$	7.4	5.6	57.6
Li_3AlH_6	11.2	5.6	70.0

[a] Effective wt% of H_2 required for a metal hydride, in a fuel cell powered vehicle, for covering a petrol ICE vehicle performance.
[b] Volume (L) occupied by petrol in a ICE vehicle required for covering the performance of a fuel cell powered vehicle loaded with 4 kg of H_2.

up and release hydrogen in a practical timeframe, then it will be of limited use in a reversible on-board storage unit. Referring to the Arrhenius-based sorption rate models introduced in §2.7, the kinetic property that most affects the rate of a sorption is the macroscopic activation energy. A lower activation energy corresponds to faster kinetics and lower time required for loading/unloading hydrogen. The macroscopic (measurable) kinetic energy corresponds to the energy (per mol of H_2) required in order to overcome the highest potential barrier across different microscopic processes[38,39]. In order to emphasise the complexity of the mechanisms involved in hydrogen absorption, resulting in the macroscopic process being difficult to model using only two parameters (rate constant, ν_1, and activation energy, E_a — see §2.7.2.1), listed below are the microscopic processes involved in a hydrogen absorption.

i. Transport of the molecular hydrogen through the gas phase to the surface of metal grains.

ii. Physisorption of molecular hydrogen onto the surface.

iii. H_2 dissociation into atomic hydrogen.

iv. Atomic hydrogen migration by diffusion in the bulk of the material.

v. Nucleation of the hydride phase.

vi. Growth of the hydride phase.

A further stage (vii.) needs to be considered for nearly all complex hydride systems, including $NaAlH_4$. Despite the transport of hydrogen, the substantial mass transfer of metal atoms also has to occur, since the reactants (here Na_3AlH_6, NaH and Al, see eq. 1.3) are spatially separated over several hundred atomic layers[13,27]. These processes are referred to in the remainder of the chapter by their Roman numeral. Considering, for instance, the first step (see eq. 1.3) of $NaAlH_4$ hydrogen desorption, substituting its rate constant ($\nu_1 = 5.8 \times 10^{12}$ h^{-1})[†] and activation energy ($E_a = 118.1$ kJ/mol of H_2) provided by Sandrock *et al.*[40] into a rearranged and time-integrated eq. 2.54, the time that it would take to desorb hydrogen at 100 °C (>> $T_{eq.}^{1\ bar\ H_2}$) and 1 bar of hydrogen back pressure from a 99% initial hydrogen content to a 1% final content, was calculated to be about 3×10^4 hours. In §1.5, techniques adopted in order to improve the kinetics of desorption to meet the technology requirement of less than 3 hours (less than 5 minutes for absorption)[25] are discussed.

In conclusion, currently, none of the known hydrogen storage systems satisfy the requirements of the existing technology. The most promising hydrogen storage system that could meet these requirements is through the use of solid-state storage and, as a result, in this thesis, research will be presented aiming to improve the sorption kinetics of complex metal hydrides relying on catalytic and nanoconfinement effects, as introduced in §1.5.1 and §1.5.2 respectively.

[†]Considering the wt% of H_2 released in the first and second decomposition steps for a pure $NaAlH_4$, 3.7 and 1.85 respectively, the wt% of H_2 rate constant ($k = 1.98 \times 10^{13}$ wt% of H_2/h) and the total true H_2 capacity released across the first two-step (5.12 wt% of H_2) from Sandrock *et al.*[40], the H_2 rate constant was determined: $\nu_1 = 1.98 \times 10^{13} \times (1/5.12) \times [(3.7 + 1.85)/3.7]\ h^{-1} = 5.8 \times 10^{12}\ h^{-1}$.

1.3 Literature review of $NaMgH_3$

In this thesis, as described in detail in §3.1, $NaMgH_3$ is used as starting material to produce porous Mg scaffolds. Successively, the Mg scaffold can be used as a vessel to modify kinetic and thermodynamic properties of metal hydrides melt-infiltrated within, as discussed in details in §1.5.2.

$NaMgH_3$ (6.0 wt% H_2), characterised by an orthorhombic perovskite structure[41] (*Pnma*, Fig. 1.2), decomposes in a two-step hydrogen desorption, see equations 1.1 and 1.2[42,43].

$$NaMgH_3 \xrightarrow{①} NaH + Mg + H_2 \qquad (4\ \text{wt\% of } H_2\ ;\ T_{\text{eq.}}^{1\ \text{bar}\ H_2} = 382\ ^\circ\text{C}) \qquad (1.1)$$

$$NaH \xrightarrow{②} Na(\text{liquid}) + 1/2H_2 \qquad (2\ \text{wt\% of } H_2\ ;\ T_{\text{eq.}}^{1\ \text{bar}\ H_2} = 427\ ^\circ\text{C}) \qquad (1.2)$$

Fast hydrogen mobility in $NaMgH_3$ has been revealed by a Nuclear Magnetic Resonance (NMR) study and this mobility is related to its perovskite structure[45]. The superior hydrogen mobility makes $NaMgH_3$ a potential material for the next generation of electronic devices[46]. Also, the high thermal stability and relatively low cost of $NaMgH_3$ makes it a potential solar heat storage material[43].

The van't Hoff plots of equilibrium H_2 pressure as a function of temperature for $NaMgH_3$ and NaH sorptions are presented in Fig. 1.3. The phase diagram was calculated using eq. 2.45 and relying on the thermodynamic parameters reported in Table 2.2. It is in agreement with the thermodynamic model and measurements presented by Abdessameud *et al.*[47].

It is evident in Fig. 1.3, how the van't Hoff equilibrium plots, corresponding to the equilibrium temperatures as a function of hydrogen back pressure, of the first and second step of decomposition (black lines) are affected by a decrease in pressure. For instance, at 1 bar of hydrogen pressure, the equilibrium temperatures ($T_{\text{eq.}}^{1\ \text{bar}\ H_2}$) of the two steps of desorption are respectively 382 °C and 427 °C. While for a hydrogen back pressure of 1.5×10^{-2} mbar, corresponding to the dynamic vacuum pressure adopted for SAXS/WAXS experiments, the equilibrium temperatures are

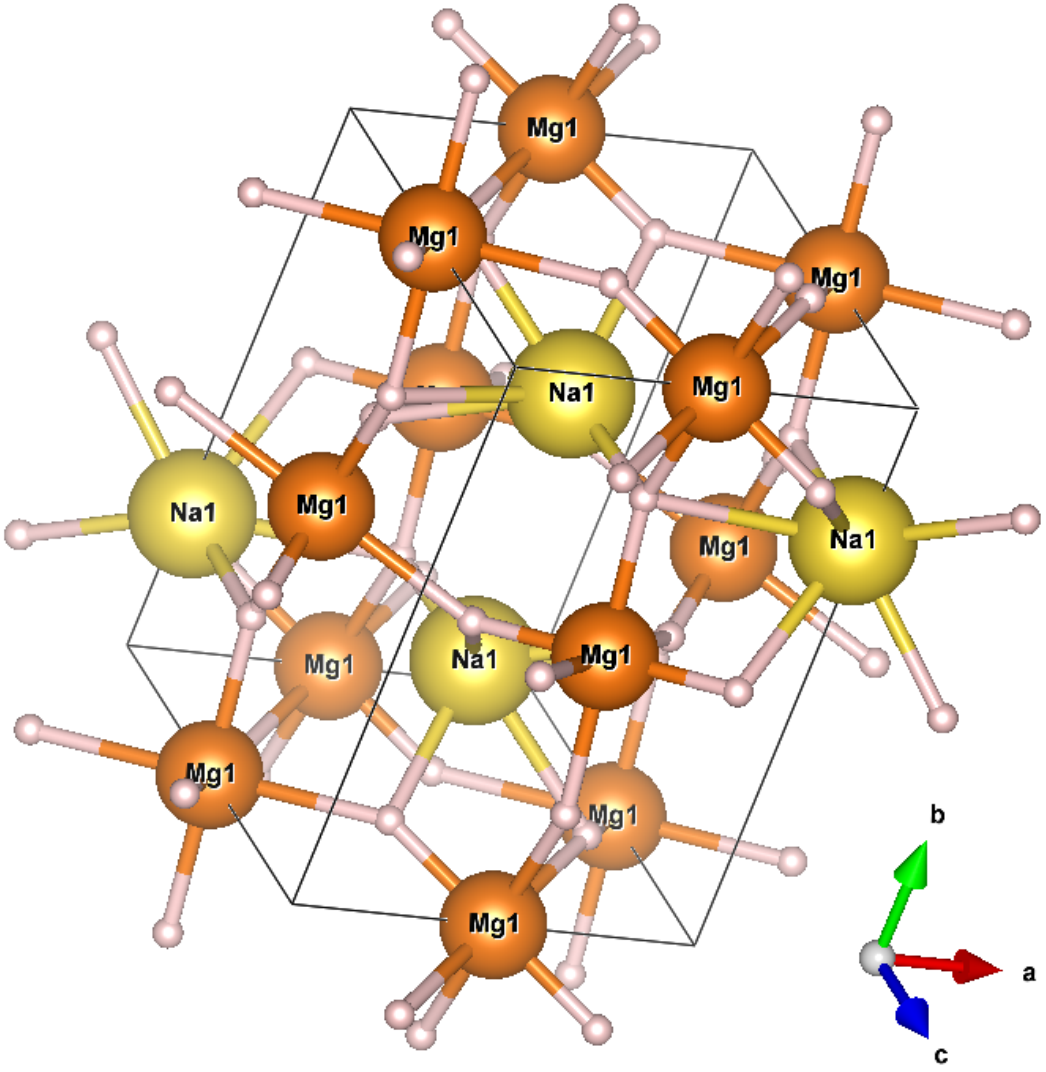

Figure 1.2: Atomic arrangement in of $NaMgH_3$ (COD ID 1525701) orthorhombic perovskite crystal structure (*Pnma*) in its unit cell. The $NaMgH_3$ crystal density, ρ_{NaMgH_3}, is 1.467(9) g/cm^3. The 3D visualization was obtained using Vesta software[44].

lower, 114 °C and 183 °C, respectively. It is worth noticing that although the product of NaH decomposition is predominantly the liquid phase of Na, a non-negligible amount of solid Na is also expected to be produced, see Figures 3.2 and 3.6. This is due to the relatively small differences in the Gibbs free energies between the two NaH decomposition thermodynamic pathways. At 1 bar of hydrogen pressure, the equilibrium temperatures for these two different pathways are 427 °C (black line)

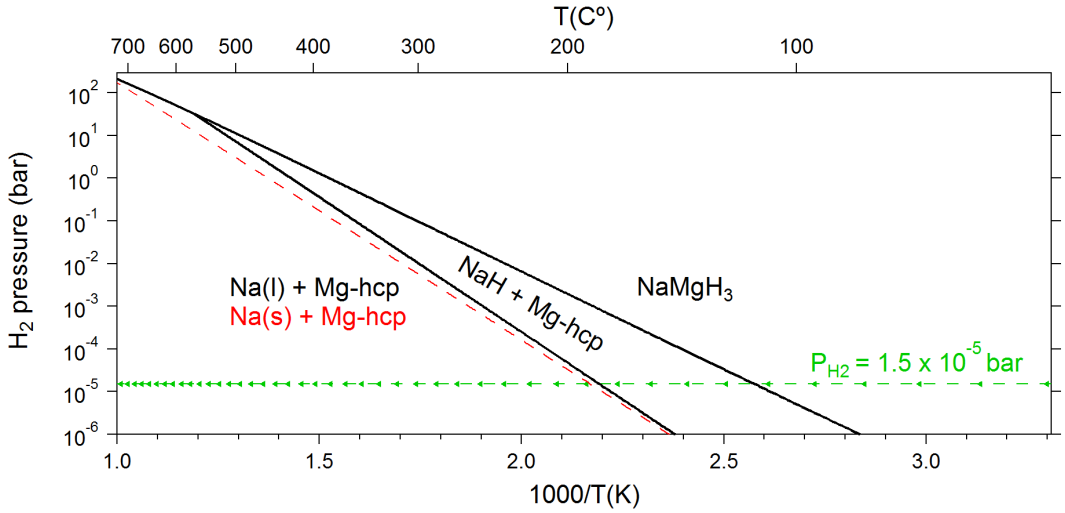

Figure 1.3: Van't Hoff plots of equilibrium H_2 pressure as a function of temperature for the $NaMgH_3$ and NaH sorption, calculated using eq. 2.45 and Table 2.2. The phase diagram of $NaMgH_3$ decomposition is represented by the black lines only of Van't Hoff plots. The phase transition between NaH and Na solid phase is in red dashed line. The horizontal dashed green line corresponds to the dynamic vacuum pressure of 1.5×10^{-2} mbar adopted for *in situ* SAXS/WAXS experiments (see §4.3).

and 458 °C (red dashed line), respectively.

$NaMgH_3$ complete desorption, across the two-step, was achieved by Ikeda *et al.* [48] in 8 minutes, using thermogravimetry and differential thermal analysis at 400 °C under 1 bar of helium.

1.4 Literature review of $NaAlH_4$

In this thesis, as described in detail in §3.2, $NaAlH_4$ is used as starting material to produce Ti-enriched porous Al scaffolds. Successively, the Al scaffold can be used as a vessel in order to modify kinetic and thermodynamic properties of metal hydrides melt-infiltrated within, as discussed in details in §1.5.2. $NaAlH_4$ melt-infiltrated within the as-prepared Al scaffold, as described in detail in §3.3, is also used as a test bench to investigate the H_2 desorption kinetic changes, as discussed in detail in §6.4.2.

$NaAlH_4$ (7.4 wt%), characterised by a tetragonal structure (*I 41/a :2*, Fig. 1.4), decomposes via a three-step hydrogen desorption, see equations 1.3 – 1.5.

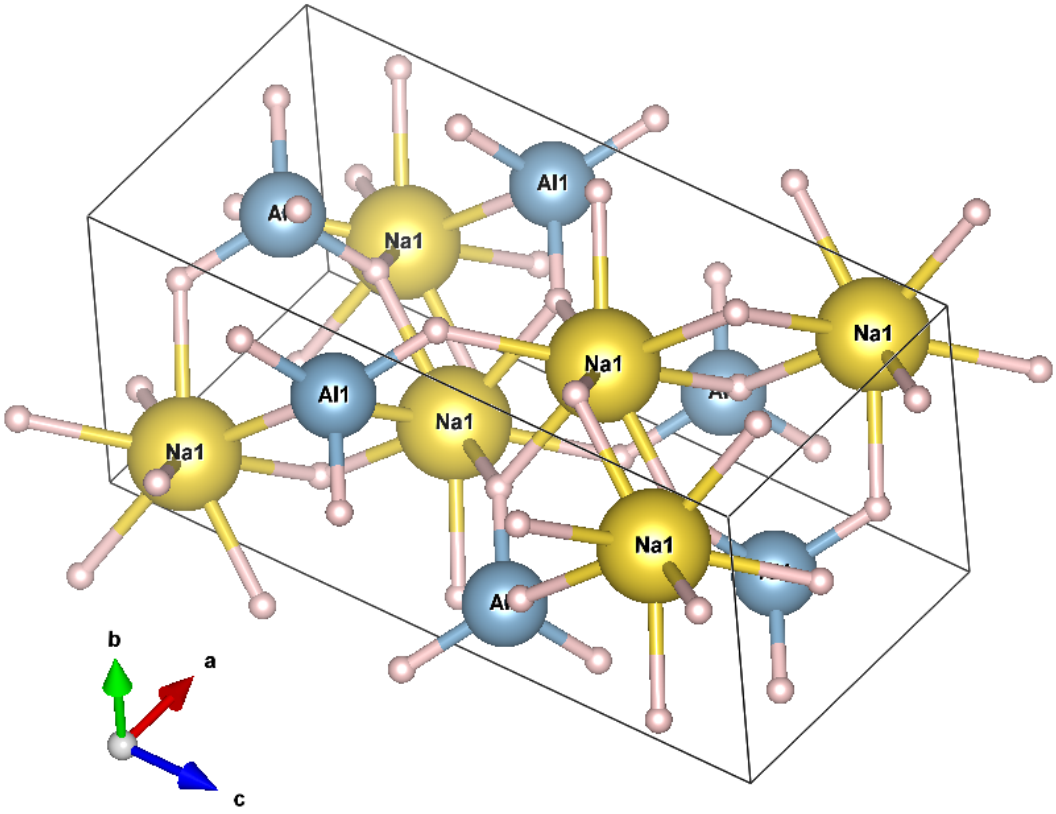

Figure 1.4: Atomic arrangement of $NaAlH_4$ (COD ID 1533929) tetragonal crystal structure (*I 41/a :2*) in its unit cell. The $NaAlH_4$ crystal density, ρ_{NaAlH_4}, is 1.456(9) g/cm^3. The 3D visualization was obtained using Vesta software[44].

$$NaAlH_4 \xrightarrow{①} 1/3Na_3AlH_6 + 2/3Al + H_2 \qquad (3.7 \text{ wt\% of } H_2 \text{ ; } T_{eq.}^{1 \text{ bar } H_2} = 30 \text{ °C}) \tag{1.3}$$

$$1/3Na_3AlH_6 \xrightarrow{②} NaH + 1/3Al + 1/2H_2 \quad (1.85 \text{ wt\% of } H_2 \text{ ; } T_{eq.}^{1 \text{ bar } H_2} = 109 \text{ °C}) \tag{1.4}$$

$$NaH \xrightarrow{③} Na(\text{liquid}) + 1/2H_2 \qquad (1.85 \text{ wt\% of } H_2 \text{ ; } T_{eq.}^{1 \text{ bar } H_2} = 427 \text{ °C}) \tag{1.5}$$

Other than hydrogen storage for vehicle applications, $NaAlH_4$ is also used as a reducing agent[49].

The van't Hoff plot of equilibrium H_2 pressure as a function of temperature for $NaAlH_4$ and Na_3AlH_6 sorption is presented in Fig. 1.5. The phase diagram was calculated using eq. 2.45 and relies on the thermodynamic parameters reported in Table 2.2. In Lee *et al.*[36] and Qiu *et al.*[50], it is shown that this thermodynamic model is in agreement with experimental measurements[51–53] and the partial disagreement ($T < 440$ K) with the measurements carried on by Bogdanović *et al.*[54] is discussed.

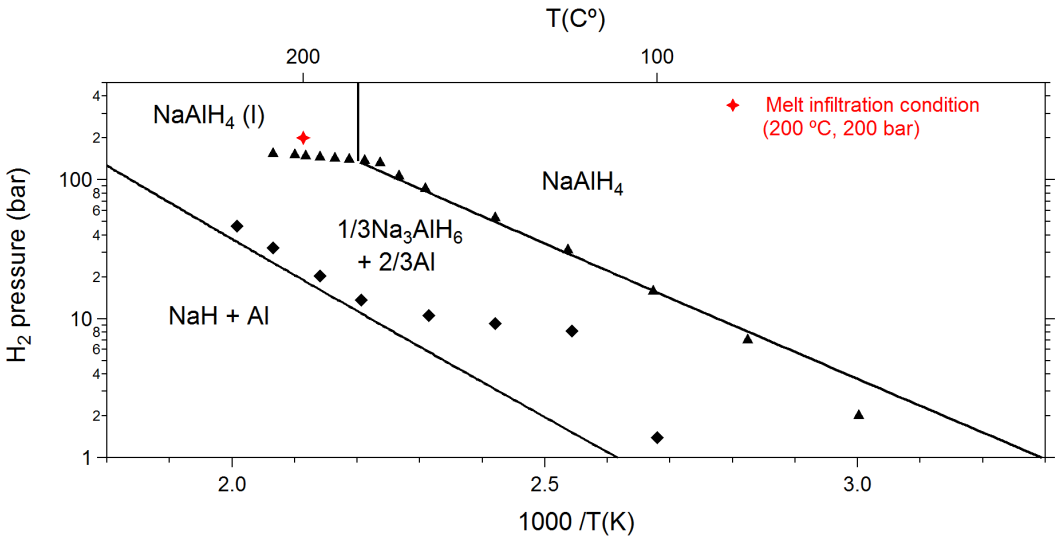

Figure 1.5: Van't Hoff plots of equilibrium H_2 pressure as a function of temperature for the $NaAlH_4$ and Na_3AlH_6 sorption. Calculated data (black line), using eq. 2.45 and Table 2.2, are compared with measured data (single black points) for $NaAlH_4$ samples with the addition of Ti, from Bogdanović *et al.*[54]. Melt-infiltrated conditions adopted in this thesis (single red point).

The equilibrium temperatures, in Fig. 1.5, drop due to a decrease in the hydrogen back pressure. For instance, at 1 bar of hydrogen pressure the equilibrium temperature ($T_{eq.}^{1\ bar\ H_2}$) of the first two-steps of desorption are 30 °C and 109 °C. For a hydrogen back pressure of 7×10^{-4} mbar, corresponding to the starting dynamic vacuum pressure adopted for Temperature Programmed Desorption-Mass Spectrometry (TPD-MS) experiments, the equilibrium temperatures are lower and

equal to −122 °C and −80 °C (see Fig. 1.6).

Dymova *et al.*[55,56] showed that the first two desorption steps of pure $NaAlH_4$, see equations 1.3 and 1.4, are reversible. However, due to the poor kinetics of the system, the reverse reaction requires impractically severe reaction conditions (200 – 400 °C, that is above the 183 °C melting point of $NaAlH_4$, and pressures of 100 – 400 bar).

1.5 H_2 sorption kinetic improvement

In order to reduce the time required for loading and unloading hydrogen in a metal hydride storage system and meet the technology requirements for vehicle applications[13,25], the kinetic limitations of the sorption reactions need to be overcome. A widely used technique is to mechanical grind[57] the sample, for instance by ball-milling it[58], in order to reduce the size and increase the specific surface area of the grains. On one hand, the kinetic limitation due to the atomic hydrogen diffusion in the bulk of the grains (iv.) can be overcome but, on the other hand, the sluggish reversibility due to the segregation of decomposition products (vii.) is not addressed. In the work presented in this thesis, in order to achieve reversibility under moderate conditions of thermodynamically favourable sorption reactions, two techniques have been adopted: the use of an additive (to produce a catalyst), see §1.5.1, and the nanoconfinement of metal hydrides within porous scaffolds, see §1.5.2.

1.5.1 Catalytic effect

The hydrogen desorption and absorption rate of metal hydrides can be increased by the use of additives[59]. A small mole percentage of these additives, used to produce catalysts, lower the hydrogen release activation energy and include nano-Ni/Fe[60–62], metal halides and oxides[63,64], transition metals[65] and metal alloys[66]. Several additives have been investigated for use with $NaAlH_4$ by different

researchers, including $TiCl_3$, $PrCl_3$, $CeCl_3$, titanium butoxide ($Ti(OBu)_4$), iron ethoxide ($Fe(OEt)_2$), and TiO_2, with Ti-based additives appearing to have the greatest effect[54,67–72], see Table 1.4.

Table 1.4: Chemical reaction between $NaAlH_4$ and additives studied in literature.

Reaction	Reference
$3NaAlH_4 + TiCl_3 \longrightarrow$ 'Ti' $+ 3Al + 3NaCl + 6H_2$	67,69
$3NaAlH_4 + PrCl_3 \longrightarrow$ 'Pr' $+ 3Al + 3NaCl + 6H_2$	54,68
$3NaAlH_4 + CeCl_3 \longrightarrow$ 'Ce' $+ 3Al + 3NaCl + 6H_2$	54,68
$NaAlH_4 + Ti(OBu)_4 \longrightarrow$ 'Ti' $+ NaAl(OBu)_4 + 2H_2$	54,69,70
$NaAlH_4 + xTi(OBu)_4 + yFe(OEt)_2 \longrightarrow$ 'Ti–Fe' alloy + ...	54
$NaAlH_4 + TiO_2@C \longrightarrow$ 'Ti'@C $+ NaAlO_2 + 2H_2$	71,72

Quotation marks denote a variety of species containing that element[54,67].

With the addition of 2 mol% of $TiCl_3$, the activation energies of the first two-step of $NaAlH_4$ decomposition, from 118.1 and 120.7 kJ/mol of H_2, decrease to 79.5 and 97.1 kJ/mol of H_2, respectively[40,73].

This time, we consider the first step of hydrogen desorption for $NaAlH_4$ (see eq. 1.3), ball-milled with 2 mol% of $TiCl_3$. Substituting the rate constant ($\nu_1 = 2.54 \times 10^{10}$ h^{-1}) and the activation energy ($E_a = 79.5$ kJ/mol of H_2) provided by Sandrock *et al.*[40] into a rearranged and time-integrated eq. 2.54, the time that it would take to desorb hydrogen at 100 °C ($>> T_{eq.}^{1\text{ bar }H_2}$) and 1 bar of hydrogen back pressure from a 99% initial hydrogen content to a 1% final content, was calculated to be about 24 hours. Such a simple estimation is comparable with measurements reported in[40,74,75]. Thus, the catalytic effect of titanium has reduced the desorption time from 3×10^4 hours (see §1.2.2) to 24 hours, but to be practical this needs to be reduced to 3 hours[25].

Over 15 years of effort have been invested by the community on endeavouring to understand the role of titanium as a catalyst on the behaviour of $NaAlH_4$, however, the situation is still not completely understood. As proposed by Leon *et al.*[76] and experimentally supported by Fu *et al.*[77] and Chaudhuri *et al.*[78], titanium may improve the kinetics of the surface reactions, which represent the highest potential

barrier across different microscopic desorption processes for uncatalysed $NaAlH_4$, see §1.2.2. Titanium present on aluminium surfaces dissociates hydrogen (iii.), which reacts with the aluminium surface and forms volatile AlH_x. It would also justify that only further minor improvements in the kinetics of reactions by an increase in the amount of $TiCl_3$ mol% are detected[40]. In Haiduc *et al.* work[69], it is shown that for $NaAlH_4$ ball-milled with $TiCl_3$ the Ti compounds formed during the sintering processes are irreversible and depend upon the temperatures reached. If low temperatures are used (up to 175 °C) an amorphous Al—Ti alloy forms, whereas using high temperatures (200 °C and higher) Ti is present as an Al_xTi intermetallic. It was proved that the most active catalyst species in the present system is the amorphous Al—Ti alloy, whereas a decreased catalytic activity is found for the Al_xTi intermetallic. The catalytic effect of Ti on the $NaAlH_4$ hydrogen desorption rate is reproduced in Fig. 1.6, where TPD-MS measurements (see §2.7.2), for uncatalysed[74,79] and catalysed[75] (ball-milled with + 2 mol% of $TiCl_3$) $NaAlH_4$ are compared. Fig. 1.6 also shows the hydrogen desorption rate pattern thermodynamically simulated at local equilibrium and constant H_2 back pressure, across different temperatures, of 7×10^{-4} mbar which corresponds to the starting dynamic vacuum pressure adopted for TPD-MS experiments, obtained.

In Fig. 1.6, the difference between T_{max} for the first two desorption peaks, of the catalysed system ($\Delta T_{max} = 179 - 132 = 47$ °C) is larger than the not catalysed system ($\Delta T_{max} = 276 - 260 = 16$ °C), which is in agreement with the relative changes in activation energies of the first two desorption peaks, from 118.1 to 79.5 and from 120.7 to 97.1 kJ/mol of H_2[40]. It is worth noting that for the specific case of the first two decomposition steps of $NaAlH_4$, relying on the $\Delta S^{\Theta} = 120.9$ $JK^{-1}mol^{-1}$ of H_2, obtained from thermodynamic quantities reported in Table 2.2, the standard Gibbs energies of reactions, in order to meet the PEM fuel cell operative condition (25 – 100 °C at 1 bar of H_2), have to be in the range: $0 < \Delta G^{\Theta}$ (kJ/mol of H_2) < 9.0. Although the standard Gibbs energy of the first decomposition step, $\Delta G^{\Theta} = 0.65$ kJ/mol of H_2 calculated using eq. 2.42 and thermodynamic quantities reported

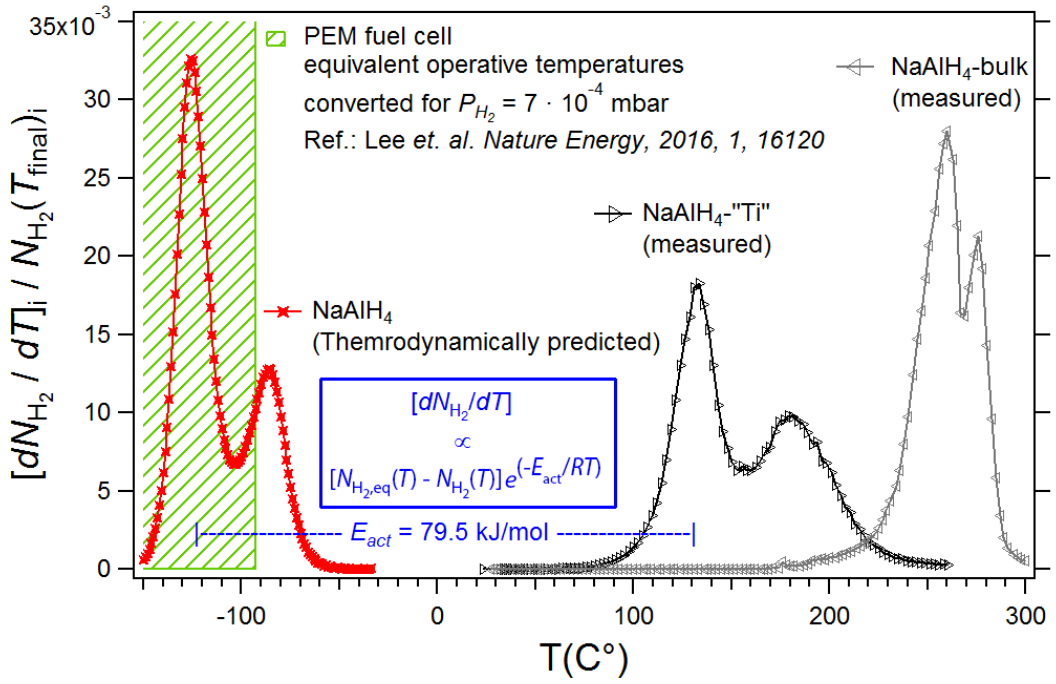

Figure 1.6: Hydrogen desorption rate from TPD-MS data, acquired by applying a constant heating rate of 2 °C/min, for uncatalyzed (grey line)[74,79] and catalyzed (black line)[75] (ball-milled with + 2 mol% of $TiCl_3$) $NaAlH_4$, compared to the hydrogen desorption rate simulated (red line) at local thermodynamic equilibrium and constant H_2 back pressure, across different temperatures, at 7×10^{-4} mbar corresponding to the starting dynamic vacuum pressure adopted for TPD-MS experiments. The green lined plan correspond to the equivalent operative temperatures for a PEM fuel cell (25 – 100 °C at 1 bar of H_2) for $P_{H_2} = 7 \times 10^{-4}$ mbar. The equation inside the blue box is eq. 2.54.

in Table 2.2, is within the range mentioned above, the second decomposition step, $\Delta G^{\ominus} = 10.3$ kJ/mol of H_2, is just over the higher limit, as shown in Fig. 1.6[‡]. In order to meet the PEM fuel cell technologic requirement for the second decomposition step of $NaAlH_4$, a thermodynamic destabilization is required, which could be achieved by nanoconfinement effects, see §1.5.2.

[‡]Considering a fuel cell used for vehicle applications having hydrogen back pressure operative conditions up to 10 bar, as reported by Schlapbach *et al.*[12], it would affect only the lower limit, $T = 25$°C, of the standard Gibbs energy ($\Delta G^{\ominus}$) that will decrease from 0 to −5.7 kJ/mol of H_2.

1.5.2 Nanoconfinement effects

Another approach that has been extensively applied in order to decrease/increase the appreciable hydrogen desorption temperatures (see Fig. 1.6), of metal hydrides is nanoconfinement within a porous scaffold[80,81]. The nanoconfined metal hydrides most often investigated are the light metal hydrides, as they offer the best potential for the highest gravimetric hydrogen capacity, and include $LiBH_4$ [32,33], LiH[82], $NaAlH_4$ [34], and MgH_2 [83,84], as well as mixtures of $LiBH_4$-$NaBH_4$ [85,86], and $LiBH_4$-Mg_2NiH_4 [87]. The porous scaffolds studied in the literature include many different forms of carbon[71,74,75,79,88–90], aluminium[31,86,91,92], magnesium[33], and metal-organic frameworks[34,93]. Nanoconfinement decreases the H_2 macroscopic (measurable) sorption kinetic energy through improvements on the several steps of microscopic processes, shown in §1.2.2:

- The metal hydride particles increase their active specific surface area[94].
- Surface diffusion (i., ii. and iii.) becomes the primary hydrogen diffusion mechanism[95,96].
- Avoiding the segregation of decomposition products (vii.) improves the reversibility[34,75,79,89,97].

Furthermore, the structure in which the metal hydride is nanoconfined also acts as a support to hold the metal hydride in place[81]. Baldé *et al.*[94] (see Fig. 1.7) showed an improvement in $NaAlH_4$ desorption reaction kinetics for particles under 1 μm through Kissinger analysis[98]. This analysis is based on the temperature shift of the desorption rate maxima for several heating rates using Temperature Programmed Desorption (TPD) under an Ar flow.

Thermodynamic destabilisation/stabilisation effects are also expected for binary and complex hydrides confined in particles smaller than 2 – 3 nm[99]. Reducing particle size increases the volume ratio between the hydrides on the surface and the hydrides present in the bulk volume. Thus, in the Gibbs free energy of sorption as a function of particle size, the surface component ($\Delta G^{\Theta}_{surface}$, see eq. 1.6)[100,101]

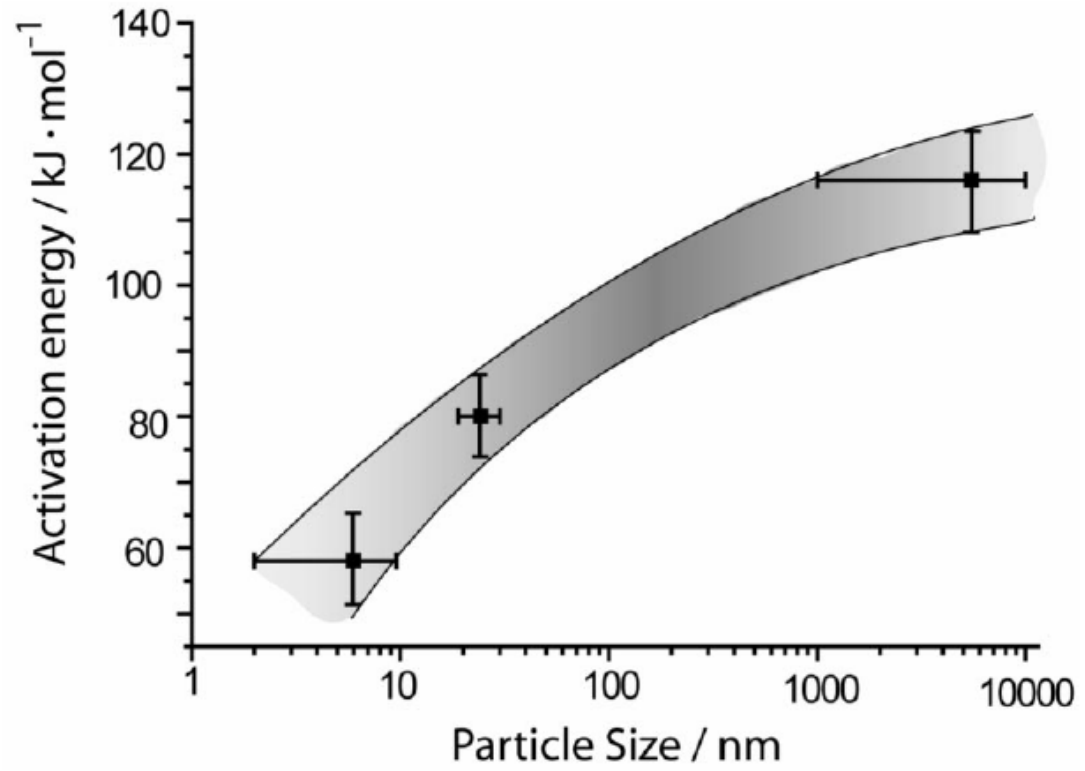

Figure 1.7: Relation between particle size and activation energy (kJ/mol of H_2) for hydrogen desorption from $NaAlH_4$/Carbon nanofibers. The spread in the particle size reflects the results from different characterisation techniques, and the error bars in activation energies were obtained from linear regression analysis[94].

that takes into consideration the interaction between the hydrides on the surface and the surrounding scaffold increases its contribution.

$$\Delta G^{\Theta}_{\text{surface}} = \frac{3V_{\text{M}}E_{\text{M}\longrightarrow \text{MH}_2}(\gamma, r)}{r} \tag{1.6}$$

where V_{M} is the molar volume, r the particle radius, γ the surface free energy or surface tension and $E_{\text{M}\longrightarrow \text{MH}_2}$ the surface energy term. For the specific case of $NaAlH_4$ nanoconfined within activated carbon fibre scaffolds having pore sizes of the order of 1 nm and below, Fichtner[99] showed that the first two-step of $NaAlH_4$ hydrogen desorption occurs in a single step, and suggested an increment in stability (due to the increased surface component of the standard Gibbs energy, $\Delta G^{\Theta}_{\text{surface}}$).

Table 1.5: Decomposition temperatures for $NaAlH_4$ infiltrated into porous scaffolds, as reported in the literature.

Scaffold characteristics			H_2 desorption			Reference
Porous scaffold	Size of pores nm	$NaAlH_4$ wt% melt-infiltrated	Method of analysis	Heating rate (°C/min)	T_{max}(°C)[a]	
CMK-1[b]	2 – 3	50	TPD-MS	2	192	88
CMK-1[b]	2 – 3	33	TPD-MS	2	180	88
CMK-1[b]	2 – 3	20	TPD-MS	2	186	88
RF-CA[c]	17	33.3	TPD-MS	5	176	75
RF-CA[c] (+3 wt% $TiCl_3$)	17	33.3	TPD-MS	5	125	75
RF-CA[c]	13 (max)	31.8 – 60.0	TPD-MS	1	146 – 150	74
RF-CA[c]	> 100 (max)	32	TPD-MS	1	162	74
RF-CA[c]	10	51.3	TPD-MS	1	180	79
RF-CA[c] (+8.7 wt% $TiCl_3$)	8	40.6	TPD-MS	1	91 – (120)	79
Carbon based (+2.9 wt% Sc_2O_3)	7	27.3	TPD-MS	1	143 – (146)	90
Carbon based (+9 wt% TiO_2)	< 1000	91.6[d]	TPD	2	99 – (128)	71
HSAG-500[e]	2 – 3	20	TPD-TCD	5	180 – (190)	89

[a] T_{max}(°C): Temperature corresponding to the first (second) maximum desorption rate.
[b] CMK-1: ordered mesoporous carbons synthesized from silica templates.
[c] RF-CA: resorcinol formaldehyde carbon aerogels.
[d] ball-milled.
[e] HSAG-500: high surface area graphites.

Such thermodynamic stabilization of the single step sorption would correspond to (omitting kinetic effects) an increase in the appreciable hydrogen desorption temperatures.

The decomposition temperatures for $NaAlH_4$ infiltrated into porous scaffolds measured using temperature-programmed desorption (TPD) based techniques are reported in Table 1.5. The greatest effect is seen using Ti-enriched resorcinol formaldehyde carbon aerogel RF-CA (+$TiCl_3$)[75,79] (see Fig. 1.8). The approach of

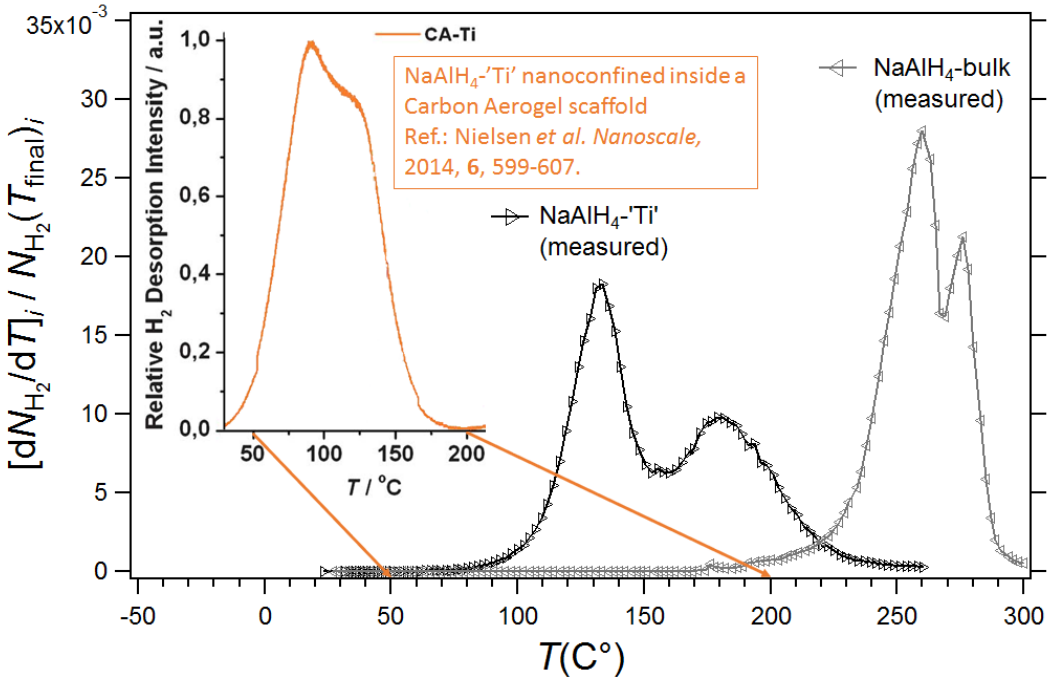

Figure 1.8: Hydrogen desorption rate from TPD-MS data, acquired by applying a constant heating rate of 2 °C/min, for uncatalyzed (grey line)[74,79] and catalyzed (black line)[75] (ball-milled with + 2 mol% of $TiCl_3$) $NaAlH_4$, and acquired by applying a constant heating rate of 1 °C/min, for nanoconfined $NaAlH_4$ (orange line)[79] within resorcinol formaldehyde carbon aerogel RF-CA (+$TiCl_3$)[79]. The lower heating rate for the nanoconfined $NaAlH_4$ justifies only a minor (3 – 5 °C) shift towards lower temperatures.

employing scaffolds and catalysts are reasonably effective, however, they face some drawbacks that negatively influence the performance of the system, such as:

- They add mass to the system, reducing the overall hydrogen density.
- They often contain oxygen, which can react with the infiltrated hydride

reducing the capacity and increasing the potential of becoming a fire hazard.

- Scaffolds, such as carbon aerogels, have poor thermal conductivity, which limits their use in practical applications. For instance, the heat produced during the exothermic absorption of hydrogen can result in self-heating that hinders further absorption[27].

Porous metal scaffolds are oxygen-free and are expected to have a higher thermal conductivity in comparison to the carbon-based scaffolds found in the literature to date[102]. The increase in thermal conductivity is of importance as it allows for better heat management during hydrogen absorption and desorption. The Al and Mg porous scaffolds recently employed by Sofianos *et al.* [33,92] show kinetic improvement in the decomposition of melt-infiltrated $LiBH_4$. For both porous scaffolds, TPD measurement acquired using a Sieverts/volumetric apparatus with a ramping rate of 5 °C/min showed appreciable hydrogen desorption from 100 °C, which is 250 °C lower than the bulk $LiBH_4$.

This research presents the properties of oxygen free porous Mg and Ti-enriched porous Al scaffolds and the combined catalytic and nanoconfinement effects of Ti-enriched porous Al scaffolds on the desorption kinetics of $NaAlH_4$.

Chapter 2

Sample Characterisation

In this thesis, X-Ray Diffraction (XRD), in §2.1, and Wide-Angle X-ray Scattering (WAXS), in §2.2, techniques are used to identify and quantify crystallized and amorphous compounds. XRD and WAXS are usually supported by spectroscopy techniques such as Nuclear Magnetic Resonance (NMR)[75] and X-ray Photoelectron Spectroscopy (XPS)[71] based on atomic bonding energies measurements.

Small-Angle X-ray Scattering (SAXS) and N_2 sorption techniques, in §2.2 and 2.6, are used to obtain mesoporosity distributions and specific surface areas. Alternative techniques are Small-Angle Neutron Scattering (SANS)[103] and Nonlocal Density Functional Theory (NLDFT)[104].

Thermodynamic simulations based on the CALPHAD method, in §2.3, are used to predict absorption/desorption phase diagrams and desorption pathways. Thermodynamic quantities of compounds and elements used in hydrogen storage are usually measured using thermal analysis techniques such as Pressure-Composition-Temperature (PCT)[105], Differential Scanning Calorimetry (DSC)[106] and Thermo-Gravimetric Analysis (TGA)[106].

The Scanning Electron Microscope (SEM) technique in §2.4 is used to observe the surface morphology of materials. An alternative technique is Transmission Electron Microscopy (TEM),[107] which is used to observe internal morphology, crystallization, and stress of materials relying on a higher resolution compared with

SEM observations.

Volume determination techniques, in §2.5, in combination with the XRD technique are also used to calculate total porosities.

Temperature Programmed Desorption (TPD) and TPD-Mass Spectrometry (TPD-MS) techniques in §2.7.1 and 2.7.2 are used to observe the combined effects of kinetics and thermodynamics, and the effect of only kinetics, respectively, on desorption processes.

2.1 X-ray diffraction

In this thesis, Wide-Angle X-ray Scattering (WAXS) will refer specifically to an incident X-ray beam transmitting through a specimen while X-Ray Diffraction (XRD) will refer to an incident X-ray beam reflecting from a specimen. Synchrotron light sources and lab-based X-ray generators have been used to conduct WAXS and XRD experiments, respectively. Please see a detailed discussion concerning the generation of X-rays in Appendix A.1, the X-ray interaction with matter in Appendix A.2, the coherence properties of X-rays in Appendix A.3, the photoelectric scattering in Appendix A.4 and the X-ray absorption by a media in Appendix A.5.

2.1.1 Powder diffraction

2.1.1.1 Role of crystal structure in X-ray scattering and diffraction

The defining property of an ideal crystalline material is the periodic space distribution of the composing atoms, as shown in Fig. 2.1. Exploiting the symmetric relative position of molecules in the crystal and the relative position of atoms within the molecules, the concept of lattice and unit cell are respectively introduced. Thus, the position of any atom in a crystal can simply be represented by the combination of the lattice vector ($\boldsymbol{R}_n$) corresponding to the atom unit cell and the position vector of the atom with respect to the unit cell ($\boldsymbol{r}_j$), see Fig. 2.1(b). A further investigation of such symmetries is beyond the scope of this thesis and can be found

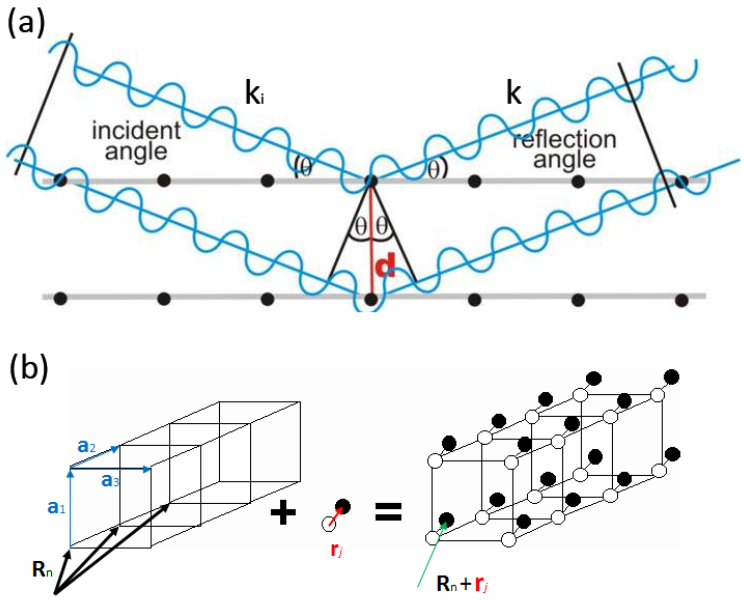

Figure 2.1: (a) schematic geometry of diffraction from a crystal that produce a time-modulated interference. (b) Position of a generic atom in a crystal composed by a lattice vector ($\boldsymbol{R}_n$) and by the atom position vector ($\boldsymbol{r}_j$) with respect to the lattice site[108].

in a crystallography textbook[109].

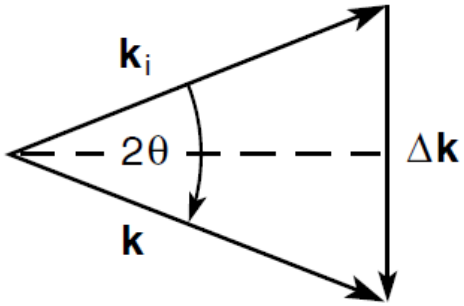

Figure 2.2: A vector scattering diagram for incident wave vector $\boldsymbol{k}_i$ and scattered wave vector $\boldsymbol{k}$. If both waves are at the same frequency (stationary scatterer), the vector diagram is isosceles[110].

Approximating X-ray photoelectric scattering as elastic (refractive index $n(\omega) \simeq 1$), from Fig. 2.2, it is found that $|\boldsymbol{q}| = |\Delta\boldsymbol{k}| = 2k_i \sin(\theta) = 2(2\pi/\lambda)\sin(\theta)$, where $\boldsymbol{q}$ is the momentum transferred vector. The condition for time-modulated (constructive) interference of the scattered X-ray, from Fig. 2.1(a), is $|\boldsymbol{q}| = 2\pi m/d$.

It is commonly referred to Bragg's law: $m\lambda = 2d\sin(\theta)$, where m is an integer and d (d-spacing) is the distance between lattice planes responsible for the particular time-modulated interference.

The spatial dispersive term in the differential cross section, see Appendix A.4, for a crystal is $|F^{\text{crystal}}(q)|^2$. Considering the spatial symmetries of the crystal, the crystal scattering factor can be expressed as:

$$F^{\text{crystal}}(\boldsymbol{q}) = \sum_{j}^{\text{unit cell}} F_j^{\text{atom}}(\boldsymbol{q}) \exp\left(\mathrm{i}\boldsymbol{q}\cdot\boldsymbol{r}_j\right) \sum_n \exp(\mathrm{i}\boldsymbol{q}\cdot\boldsymbol{R}_n) = F^{\text{unit cell}}(\boldsymbol{q}) \sum_n \exp(\mathrm{i}\boldsymbol{q}\cdot\boldsymbol{R}_n) \tag{2.1}$$

where the first term is the unit cell structure factor and the second term is a sum over lattice sites. The elementary condition for time-modulated (constructive) interference, imposed by the elementary Bragg's law, is replaced by the generalized conditions $\boldsymbol{q}\cdot\boldsymbol{R}_n = 2\pi m$ which are fulfilled only when the momentum transferred vector $\boldsymbol{q}$ coincides with a reciprocal lattice vector[108,109] $\boldsymbol{G}_{\text{h,k,l}}$, see eq. 2.2 and 2.3.

$$\begin{gathered} \boldsymbol{R}_n = n_1\boldsymbol{a}_1 + n_2\boldsymbol{a}_2 + n_3\boldsymbol{a}_3 \qquad ; \qquad \boldsymbol{G}_{h,k,l} = h\boldsymbol{a}_1^* + k\boldsymbol{a}_2^* + l\boldsymbol{a}_3^* \\ \boldsymbol{a}_1^* = 2\pi\frac{\boldsymbol{a}_2\times\boldsymbol{a}_3}{\boldsymbol{a}_1\cdot(\boldsymbol{a}_2\times\boldsymbol{a}_3)} \;;\; \boldsymbol{a}_2^* = 2\pi\frac{\boldsymbol{a}_3\times\boldsymbol{a}_1}{\boldsymbol{a}_2\cdot(\boldsymbol{a}_3\times\boldsymbol{a}_1)} \;;\; \boldsymbol{a}_3^* = 2\pi\frac{\boldsymbol{a}_1\times\boldsymbol{a}_2}{\boldsymbol{a}_3\cdot(\boldsymbol{a}_1\times\boldsymbol{a}_2)} \end{gathered} \tag{2.2}$$

where n_1, n_2, n_3, h, k, and l are integers.

$$F^{\text{crystal}}(\boldsymbol{G}_{h,k,l}) = F^{\text{unit cell}}(\boldsymbol{G}_{h,k,l}) \sum_n \exp(\mathrm{i}2\pi(hn_1 + kn_2 + ln_3)) = F^{\text{unit cell}}(\boldsymbol{G}_{h,k,l}) \tag{2.3}$$

2.1.1.2 The principles of the technique

The powder method derives its name from the fact that the sample is typically in the form of a microcrystalline powder. 'Powder' means that all crystal orientations are equally likely, not that it is a literal powder. The technique consists in resolving the recorded time-averaged intensity of a suitably monochromatized X-ray, diffracted upon interaction with a specimen scanned across the diffracted angles (θ). The

space group symmetries associated with the lattice parameters ($G_{h,k,l}$) produce time-modulated constructive interferences at associated diffracted angles ($\theta_{h,k,l}$)[†]. The intensity pattern associated, $I(\theta_{h,k,l})$, recorded from the diffraction events at a distance longer than the longitudinal coherence length (ξ_l, see Appendix A.3) associated, results in time-averaged constructive interferences (no tracks of phase information). Due to the assumption that all crystal orientations are equally likely (3D averaging, the three dimensions of diffraction data collapse onto the one dimension of a powder pattern), some space groups give identical powder diffraction patterns. For example, the cubic reflection $(h,k,l) = (550)$, (710) and (543) exactly overlap[111‡]. The intensity of a diffraction line is thus, from eq. A.12, proportional to $m_{h,k,l}|F_{\text{unit cell}}(\boldsymbol{G}_{h,k,l})|^2$, where m is the multiplicity due to (h,k,l) planes of symmetry reproducing the same d-spacing. The intensity pattern, $I(\theta)$, generally consisting of a number of counts recorded by a scintillation-based detector, is the result of a combination between diffraction lines and several types of aberration due to the X-ray and samples features, instrument geometry and sample placement and holder, that have to be considered in order to obtain qualitative and quantitative phase information. Some of the aberrations affecting the pattern are[112]:

- Multiple X-ray wavelengths.
- Finite X-ray source width.
- Flat sample error.
- Sample transparency/absorption ($A(\theta) = (1/V_{\text{ss}})\int \mathrm{e}^{-\mu_{\text{mixture}}\tau}\mathrm{d}V_{\text{ss}}$). For Bragg-Brentano geometry absorption correction is θ independent ($I_{\text{measured}} \propto A_{\text{BB}} \propto 1/2\mu_{\text{mixture}}$) when constant illumination length is not applied. In transition mode (SAXS/WAXS), $A_{\text{transmission}}(0) = \mathrm{e}^{-\mu_{\text{mixture}}x}$.

[†]The diffracted angles ($\theta_{h,k,l}$) is related to the reciprocal lattice vector $2\pi/d_{h,k,l} = |\boldsymbol{G}_{h,k,l}| = 4\pi\sin(\theta_{h,k,l})/\lambda$.

[‡]Inversion centres: P1 and P-1 give identical reflections. Different reciprocal lattice vectors ($\boldsymbol{G}_{h,k,l} \neq \boldsymbol{G}_{h',k',l'}$) collide on the same diffraction peak when $|\boldsymbol{G}_{h,k,l}| = |\boldsymbol{G}_{h',k',l'}|$.

- Axial divergence[113,114].
- Lorentz-Polarisation (see Appendix B).
- Sample displacement (see §2.1.1.4 for Bragg-Brentano geometry and §2.2.1 for Debye-Scherrer geometry).
- Zero error.
- Equatorial divergence (not considered when constant illumination length applied, see §2.1.1.3).
- Diffraction line broadening due to structure factor correction for finite crystallite size (see §2.1.3.2).
- Temperature factor[113] (see Appendix B).

2.1.1.3 XRD apparatus and experimental setup

XRD measurements were performed using a Bruker D8 advance. The instrument is a diffractometer that uses Bragg-Brentano geometry, see Fig. 2.3, which exploits the para-focussing arrangement of the X-ray divergent beam. A Bragg-Brentano diffractometer is essentially a device that allows a range of θ values to be scanned. Rotating the X-ray source and detector at the same angular speed, the same angular distance from the axis perpendicular to plane where the sample surface lays is maintained.

A CuK_α tube (λ = 0.1542 nm, 8.05 keV, $\Delta V_{\text{anode-cathode}} = -40$ kV, Current = 40 mA) produce an unpolarised radiation that passes through parallel Soller slits (0.6 mm fixed slits at 2.5°) in order to improve the spatial transverse coherence length (collimation) due to the finite size of the X-ray source. Due to the reduced amount of specimen available for measurements, motorized divergence slits are used to keep the illumination length at the specimen constant at 6 mm, ensuring that all data were collected within the physical dimensions of the specimens (8 mm). A 0.2 mm nickel foil filter, used to cut-out K_β radiation, was present at the

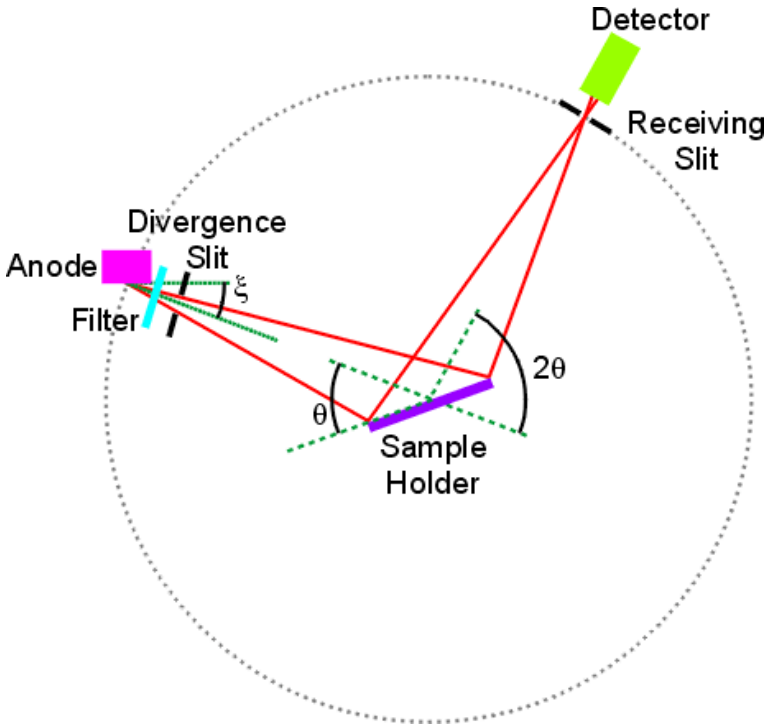

Figure 2.3: Schematic representation of a Bragg-Brentano diffractometer[115].

'compound silicon strip' detector 192 channel Lynxeye XE-T (it covers 3° at 250 mm distance from the specimen). Further scan parameters are: $5° < 2\theta < 120°$, $\Delta 2\theta = 0.019463°$, # of steps 5911, time/step = 1.2 s, total scan time 2 hours, anti-scattering slit = 0.5°. During the measurements, the specimen was rotating around the axis perpendicular to the plane where the specimen surface lays at a rotation speed of 0.5 rotation per second, in order to improve particle statistics.

2.1.1.4 XRD sample preparation and holder

Before conducting XRD measurements, the specimens were manually ground in order to increase the homogeneity of the multiphase material and reduce particle size, in order to ensure correct relative intensities of the diffraction lines. The ground specimens were placed on a sample holder and levelled in order to present a flat surface and most importantly be positioned at the centre of the goniometer. The biggest source of systematic error in line diffraction position is caused by vertical

displacement (s), see Fig 2.4(a). The changes in 2θ position are:

$$\Delta 2\theta = -\frac{2s\cos\theta}{R} \tag{2.4}$$

From eq. 2.4, it is evident that $\Delta 2\theta$ is more pronounced at smaller angles.

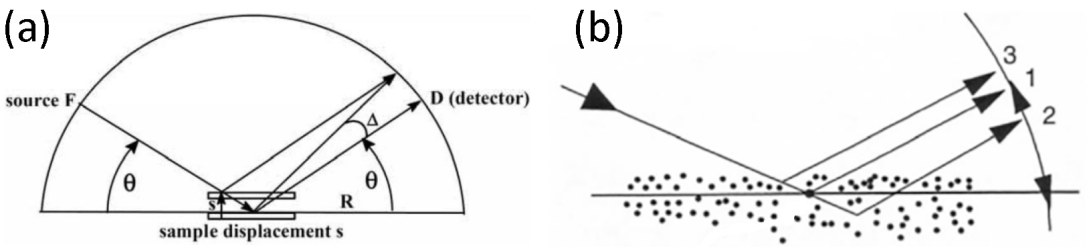

Figure 2.4: Schematic representation of a Bragg-Brentano diffractometer where (a) vertical sample displacement (s) [116] and (b) sample transparency cause changes in 2θ positions [117].

Low absorbing samples, where the average diffraction surface is below the physical sample surface, similarly to the vertical sample displacement, see Fig. 2.4(b), also produce displacement effects. In this case, the changes in 2θ position are given by:

$$\Delta 2\theta = \frac{\sin 2\theta}{2\mu R} \tag{2.5}$$

μ is the linear absorption coefficient (Appendix A.5). The diffraction information acquired mainly comes from the surface of the sample exposed to the X-rays. In order to put a limit on the thickness of the surface exposed, the concept of infinite-thickness (d_∞) is introduced. Such infinite-thickness is the vertical penetration depth of the 99% of intensity for an X-ray incident at a specific angle (θ), ($I = 0.01 I_0$), see eq. 2.6.

$$d_\infty = \frac{\ln(100)\sin\theta}{2\mu} \tag{2.6}$$

To prevent oxygen/moisture contamination of the specimens during data collection, an airtight polymethylmethacrylate (PMMA) dome was placed on top of the off-cut Si low-background sample holder. The dome resulted in a broad

hump at 20° 2θ as shown in Fig. 2.5.

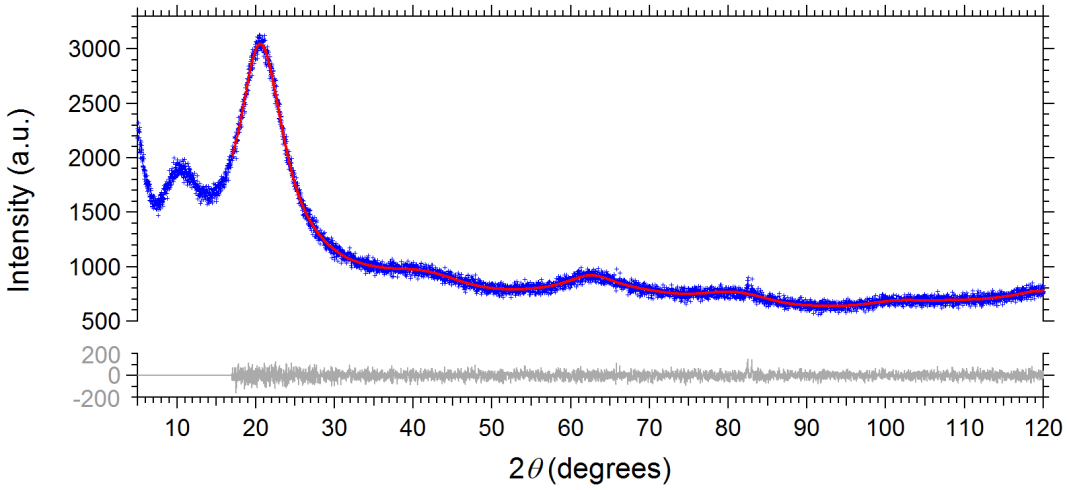

Figure 2.5: Rietveld refinement of the diffraction pattern for empty (blank) airtight polymethylmethacrylate (PMMA) dome placed on top of the off-cut Si low-background specimen holder. The blue plus symbols and the red overlapping line denote the observed and calculated intensities, respectively. $\lambda = 1.5406$ Å.

2.1.2 Qualitative phase characterisation by X-ray diffraction

The goal is to determine which phases are present in an unknown mixture.

2.1.2.1 Qualitative analysis of polycrystalline material

The first step in phase analysis is to determine what major crystalline phases (*e.g.* compounds) are present in a sample. Each phase produces a set of characteristic diffraction lines ($\theta_{h,k,l}$) in the scattering pattern. Because localised electromagnetic fields linearly overlap each other, the pattern of multiphase materials is formed by a superposition of a characteristic set of diffraction lines from each phase. Identifying which lines belong to which phase may result in complications. A set of diffraction peaks for a specific phase contains a good deal of information of which three parameters are of special interest:

- Position of the diffraction maxima ($2\pi/d_{h,k,l} = |\boldsymbol{G}_{h,k,l}| = 4\pi \sin\big(\theta_{h,k,l}\big)/\lambda$).

- Peak intensities (area over the background).

- Peak intensity distribution as a function of diffraction angle (peak broadening).

2.1.2.2 Search procedures

Identification of phases by powder diffraction is achieved by comparison with standard patterns. The observed peaks and relative intensities from a sample are compared with peaks and relative intensities from a large set of 'standard' data (7 – 80 2θ range), through a so-called search/matching process. There are two main databases that can be used for this purpose:

- The International Center for Diffraction Data (ICDD) — Powder Diffraction File database (ICDD-PDF)[118].

- Crystallography Open Database (COD)[119–121].

ICDD is a non-profit scientific organisation dedicated to collecting, editing, publishing, and distributing powder diffraction data for the identification of crystalline materials. The membership of the ICDD consists of worldwide representation from academia, government, and industry. All data added to the database is rigorously assessed. COD is an open-access collection, but limited quality control, of crystal structures of organic, inorganic, metal-organic compounds and minerals, excluding biopolymers. To access these massive (and continually growing) databases (ICDD-PDF4+ (2011) or COD), the computer software package EVA (DIFFRAC EVA 3.0, from Bruker-AXS, Germany) is used. EVA has both automated and manual search-match and in order to reduce the number of matches, it is commonly applied a filter to the expected elements forming the phases.

2.1.3 Quantitative phase characterisation by X-ray diffraction

Each individual diffraction event results in a single diffraction spot. Quantification of phases from an X-ray diffraction pattern is achieved by fitting the intensities of each set of lines associated with each crystalline structure.

2.1.3.1 Rietveld refinement method

In this thesis, phase quantification analyses are performed using the Rietveld refinement method, which is a structure refinement method. The time-averaged intensity scattered from a sample and measured by a detector (# of photons/s) as a function of the momentum transferred and X-ray wavelength is given by:

$$\begin{aligned} I_{\text{measured, ss}}(q,\lambda) =& \frac{N_{\text{ss}}(q,\lambda)}{t_{\text{ss}}} = \\ =& I_0(q,\lambda)\Delta\Omega\eta(\lambda)L(q)P(q)A_{\text{BB}}(\lambda)V_{\text{ss}}\left(\frac{\partial\Sigma_{\text{PE}}}{\partial\Omega}(q,\lambda)\right)_{\text{ss}} + BG_{\text{ss}} \end{aligned} \tag{2.7}$$

I_0 is the incident flux of photons (# of photons/cm^2 s), $\Delta\Omega$ is the solid angle element defined by the size of the detector pixel, η is the detector efficiency, L, P and A are respectively the Lorentz, Polarization, and Absorption (Bragg-Brentano geometry) factors (see Appendix B)[113]. V_{ss} is the solid volume of the sample. The background (BG_{ss}) is mainly due to no photoelectric interactions. Finally, $(\partial\Sigma_{\text{PE}}/\partial\Omega)_{\text{ss}}$ (eq. 2.8) is the photoelectric differential cross section of the solid sample, or per unit of solid volume, from the contribution of each crystalline phase (in units of inverse length).

$$\frac{\mathrm{d}\Sigma_{\text{PE}}}{\mathrm{d}\Omega}(q) \simeq \sum_{\alpha}\frac{1}{V_{\alpha,\text{ss}}}\frac{\mathrm{d}\sigma_{\text{PE},\alpha}}{\mathrm{d}\Omega}(q) \tag{2.8}$$

where $\mathrm{d}\sigma_{\text{PE},\alpha}/\mathrm{d}\Omega$ is the crystal phase α differential cross section. Eq. 2.8 is based on the assumption that the diffraction patterns of different phases (components) overlap without interference[122,123]. The variation of the photoelectric differential

cross section with wavelength is reported in Appendix D.

$$\frac{V_{\alpha,\,\mathrm{ss}}}{V_{\mathrm{ss}}} = \frac{\rho_{\mathrm{mix}}\omega_\alpha}{\rho_\alpha} \qquad ; \qquad \rho_\alpha = 1.66054\frac{Z_{\mathrm{uc}\alpha}M_{\mathrm{uc}\alpha}}{V_{\mathrm{uc}\alpha}} \tag{2.9}$$

In eq. 2.9 two elementary relations are introduced, where $V_{\alpha,\,\mathrm{ss}}$ is the solid volume of the sample occupied by a generic phase α and ω_α is the weight fraction (normalized to 1) of such phase. The parameters $Z_{\mathrm{uc}\alpha}$, $M_{\mathrm{uc}\alpha}$, $V_{\mathrm{uc}\alpha}$ are respectively the number of atoms, the average mass of atoms and the volume of the unit cell for a generic phase α. Eq. 2.9 is used in eq. 2.10. Considering a diffraction peak (h,k,l) of a specific phase (α), $I_{\mathrm{measured}}(\theta_{(h,k,l)\alpha})$ is now the measured relative integrated intensity (# of counts/s), corresponding to the area under the curve of the measured intensity around the diffraction peak $(\Delta\theta_{(h,k,l)\alpha})$. Eq. 2.7, where $\Delta\Omega$ now is referring to the solid angle element corresponding to $\Delta\theta_{(h,k,l)\alpha}$, is reduced to [122,124]:

$$\begin{aligned} I_{(h,k,l)\alpha}(\theta_{(h,k,l)\alpha}) - BG_{\mathrm{ss}} &\propto K''(\theta_{(h,k,l)\alpha})\frac{1}{V_{\mathrm{uc}\alpha}}\frac{V_{\alpha,\,\mathrm{ss}}}{V_{\mathrm{uc}\alpha}}\frac{\mathrm{d}\sigma_{\mathrm{PE,\,uc}\alpha}}{\mathrm{d}\Omega}(G_{(h,k,l)\alpha}) \propto \\ &\propto K'(\theta_{(h,k,l)\alpha})\frac{1}{V_{\mathrm{uc}\alpha}^2}\frac{V_{\mathrm{ss}}\rho_{\mathrm{mix}}\omega_\alpha}{\rho_\alpha} m_{(h,k,l)\alpha}|F^{\text{unit cell}}(\boldsymbol{G}_{(h,k,l)\alpha})|^2 \propto \\ &\propto K(\theta_{(h,k,l)\alpha})\underbrace{\left(\frac{\omega_\alpha}{Z_{\mathrm{uc}\alpha}M_{\mathrm{uc}\alpha}V_{\mathrm{uc}\alpha}}\right)}_{s_\alpha} m_{(h,k,l)\alpha}|F^{\text{unit cell}}(\boldsymbol{G}_{(h,k,l)\alpha})|^2 \end{aligned} \tag{2.10}$$

where $K(\theta_{(h,k,l)\alpha})$ is an experimental constant for a particular instrumental setup. The effect of atomic thermal vibration is included in the unit cell form factor by the introduction of an isotropic temperature factor B^{atom}, as given by:

$$F^{\text{unit cell}}(\boldsymbol{G}_{(h,k,l)\alpha}) = \sum_{j}^{\text{unit cell}} F_{0,j}^{\text{atom}}(|\boldsymbol{G}_{(h,k,l)\alpha}|)\mathrm{e}^{-B_j(|\boldsymbol{G}_{(h,k,l)\alpha}|/4\pi)^2}\mathrm{e}^{\mathrm{i}\boldsymbol{G}_{(h,k,l)\alpha}\cdot\boldsymbol{r}_j} \tag{2.11}$$

s_α, in eq. 2.10, is called the scale factor of phase α, and it is linked only to the weight fraction, unit cell mass, and unit cell volume of phase α. The calculated profile yields scale factors, s_α, for each phase to fit the intensity of the observed

pattern. If all phases are identified and crystalline, the sum of the weight fractions is unity and the absolute weight fractions are obtained. These scale factors are related to the respective relative weight fractions by eq. 2.12[122].

$$\omega_\alpha = \frac{s_\alpha (ZMV)_{\mathrm{uc}\alpha}}{\sum_j s_j (ZMV)_{\mathrm{uc}j}} \tag{2.12}$$

Such a profile integrated method, restricted to individual peaks, or even to groups of peaks, reduce the complexity of constraints between the parameters (see eq. 2.12) in the least-squares (see §2.1.3.4) refinement procedure[124], but it leads to the loss of all the information contained in the often detailed profile of these composite peaks. This limitation is overcome by considering the 'whole-pattern' fitting procedure using a step-scan diffraction pattern where the restriction on peak intensities can be extended to incorporate the entire diffraction pattern.

2.1.3.2 Crystallite average size determination

Diffractometers contribute with characteristic broadening and shape to the diffraction peak based on their optics and geometry. Each separate combination of divergence slit apertures, Soller slits, beta filter or monochromators, and detectors will have their own characteristic instrument profile. Sample attributes also contribute to the diffraction peak shape and width:

- Mass absorption coefficient (sample transparency).
- Sample thickness.
- Crystallite size.
- Microstrain.
- Defect concentration.

The diffraction peak broadening due to finite crystallite size, not to be confused with the grain size of a phase, is the effect of a net partial constructive interference

of X-rays incident at an angle ($\theta \simeq \theta_{h,k,l} + \Delta\theta_{h,k,l}$) not corresponding to the ideal diffraction angle ($\theta_{h,k,l}$) derived from Bragg's law[§]. The X-rays resulting from the scattering of these X-rays incident at non- ideal diffraction angles, present a further phase difference other than the phase difference due to the relative position of the electron scatterers in the crystallite ($\boldsymbol{k}\cdot\boldsymbol{r}$, see eq. A.15). Such further phase differences increase with the distance of the relative position of the electron scatterers in the crystallite[113]. For smaller crystallites, the time-modulated intensity of a scattered X-ray is less compensated with a complementary counter phase scattered X-ray. The inversely proportional relation between the peak broadening $\Delta\theta_{h,k,l}$ and crystallite size L_{cry} is given by the Scherrer equation:

$$\Delta\theta_{hkl} = \frac{k\lambda}{L_{\text{cry}} \cos\theta_{hkl}} \tag{2.13}$$

where k is a shape factor.

2.1.3.3 Quantification of amorphous contents

In order to quantify the non-crystalline (amorphous or liquid) and undefined phases, for some of XRD measurements presented in this thesis an internal standard of known quantity, commonly between 33 and 50 wt%, and crystallinity was added to and mixed with the specimens. The internal standard adopted was corundum (α-Al_2O_3, PDF 46-1212, Inframat Advanced, 99.99%, crystallinity 100%, average particle size 3 – 4 μm) for the following reasons:

- It is stable.
- When mixed with the specimens measured in this thesis, it does not react.
- Its diffraction peaks have a minimum overlapping with the diffraction peaks of the specimens measured in this thesis.

[§]It is a relative concept. In XRD measurements, the crystallites are actually off diffraction angle and the corresponding scattered X-rays produce a net partial constructive interference.

- It has a linear absorption coefficient (Appendix A.5) similar to one of the specimens measured in this thesis.

The crystallinity of corundum was previously measured by mixing it with a calibrated standard provided by the National Institute of Standards and Technology (NIST) under the same conditions of the XRD measurements presented in this thesis. The weight fractions of the identified phases in the specimen can be rescaled considering the known wt% of corundum (multiplied by its coefficient of crystallinity) added as a fixed value. The absolute weight fractions are given by:

$$\omega_{\alpha,\text{absolute}} = \omega_{\alpha} \frac{\omega_{\text{standard,absolute}}}{\omega_{\text{standard}}} \left(\frac{1}{1 - \omega_{\text{standard,absolute}}} \right) \tag{2.14}$$

where $\omega_{\alpha,\text{absolute}}$ is the recalculated actual weight fraction of phase α, ω_{α} and ω_{standard} are the refined weight fractions of phase α and the internal standard respectively, and $\omega_{\text{standard,absolute}}$ is the actual added weight of the internal standard. The weight fraction $\omega_{\text{amorphous}}$ pertaining to X-ray amorphous or undefined phases is then calculated as $\omega_{\text{amorphous}} = 1 - \sum_{\alpha} \omega_{\alpha,\text{absolute}}$, see Appendix C.1.

2.1.3.4 TOPAS software

TOPAS software was adopted to perform Rietveld refinement for diffraction pattern analysis. It is a nonlinear least-squares optimisation program written in the *C++* programming language. During the progress of refinement, its algorithm minimises the 'goodness of fit', χ, between the measured and calculated pattern varying (refining) selected parameters[125]. χ is defined as the ratio of weighted profile R_{wp} and statistically expected R_{exp}. R_{wp} and R_{exp} are defined as[126]:

$$R_{\text{wp}} = \sqrt{\frac{\sum_{i=1}^{N} \left(\frac{y_{\text{o},i} - y_{\text{c},i}}{\sigma_{y_{\text{o},i}}} \right)^2}{\sum_{i=1}^{N} \left(\frac{y_{\text{o},i}}{\sigma_{y_{\text{o},i}}} \right)^2}} \quad ; \quad R_{\text{exp}} = \sqrt{\frac{N - P}{\sum_{i=1}^{N} \left(\frac{y_{\text{o},i}}{\sigma_{y_{\text{o},i}}} \right)^2}} \tag{2.15}$$

where y is observed/calculated intensity, N is the number of observations (data points) and P is the number of parameters refined. For every refined diffraction pattern presented in this thesis, the goodness of fit was acceptable. It is evident considering a refinement output file for a generic specimen. In Appendix C.1 the refinement output file of sample 7-$NaAlH_4$, introduced in Chapter 5 is reported. The reported ratio of R_{wp} ($\simeq 4.12$) and R_{exp} ($\simeq 2.85$) is $\chi \simeq 1.45$. TOPAS database contains the atomic form factors ($F^{atom}(q)$) for all neutral atoms and for the most common ionized ones. The instrumental and scan setup parameters adopted for XRD measurements (see §2.1.1.3) and WAXS (see §2.2.1) were provided to the software. The complex background shape of the diffraction pattern for both techniques (XRD and WAXS) was modelled by collecting a diffraction pattern of a blank sample, an empty sample holder with the PMMA dome in place and an empty capillary for XRD (see Fig. 2.5) and WAXS measurements respectively, at the same conditions. The resultant pattern was refined with a flat background and a Pawley fit with a tetragonal lattice (P4) with $a = 0.5$ Å and $c = 40$ Å. For every specimen's diffraction pattern, the background pattern was modelled keeping fixed both the peak widths and relative intensities that were previously refined for the pattern of a blank sample. While an overall scale factor and a 3rd order Chebyshev polynomial background were refined. In Appendix C.1 is reported the *.bgk* matrix that module the background used to refine XRD diffraction patterns.

For each measured intensity pattern, the user provided for each phase the following structure information: lattice space group, nominal unit cell vector lengths, $|\boldsymbol{a}_1|, |\boldsymbol{a}_2|, |\boldsymbol{a}_3|$ (see eq. 2.2), relative coordinates of atoms in the unit cell, type of atoms and the atom's ionization. Also provided for each atom is the isotropic vibrational factor B^{atom} (see Appendix B). TOPAS was run in launch mode (see Appendix C.1) and normally the refinement variables were the unit cell vector lengths, the scale factor (s_α) and crystallite size L_{cry} for each phase, while the unit cell relative coordinates of the atoms were fixed. Also, specimen displacement parameters were refined. For laboratory XRD measurements, only

the vertical displacement, see eq. 2.4, was refined, while for WAXS measurements, a displacement parallel to the incident beam was also refined, see Fig. 2.7.

2.2 Small- and wide-angle X-ray scattering

2.2.1 Apparatus and experimental setup

Small- and Wide-Angle X-ray Scattering (SAXS/WAXS) measurements were performed at Australian Synchrotron adopting a Debye-Scherrer geometry as shown in Fig. 2.6.

The scattered beam is detected on a two-dimensional, position sensitive detector (PSD). For isotropic samples, the scattering can be azimuthally averaged to produce a plot of scattered intensity (counts/s) versus momentum transfer (q). The SAXS beamline uses two Pilatus detectors for SAXS (1 M, 170 mm × 170 mm) and WAXS (200 K, 33 mm x 170 mm) data collection. Time-resolved data collection is also well supported as the Pilatus detectors are capable of collection at 10 Hz (1 M) and 30 Hz (200 K). See full specification in Table 2.1.

A beam stop was placed in front of the SAXS detector, approximately at $q = 0$, in order to avoid damaging the detector due to overexposure. The sample transmission, τ_s, was calculated by taking the ratio between the beam stop counts, I_{BS}, and the upstream counts, I_0. For the transmission measurement of specimens, it was also taken into account the normalisation due to the presence of air, conducting measurements on an empty capillary ($\tau_{cap} = I_{BS}(\text{counts/s})/I_0(\text{counts/s}) = 51787/58095$). The SAXS/WAXS measurements presented in this thesis (except Fig. 6.3) were obtained using X-ray energy centred at 12 keV ($\lambda = 1.0332$ Å), SAXS camera length of 1604.13 mm while the WAXS camera length was 448.00 mm. The measurements presented in Fig. 6.3 were obtained using X-ray energy centred at 11 keV ($\lambda = 1.1271$ Å), SAXS camera length of 1029.5 mm while the WAXS camera length was 448.00 mm. For each measurement the exposure time was 1 second, and for *in situ* measurements, the time between consecutive measurements was 30

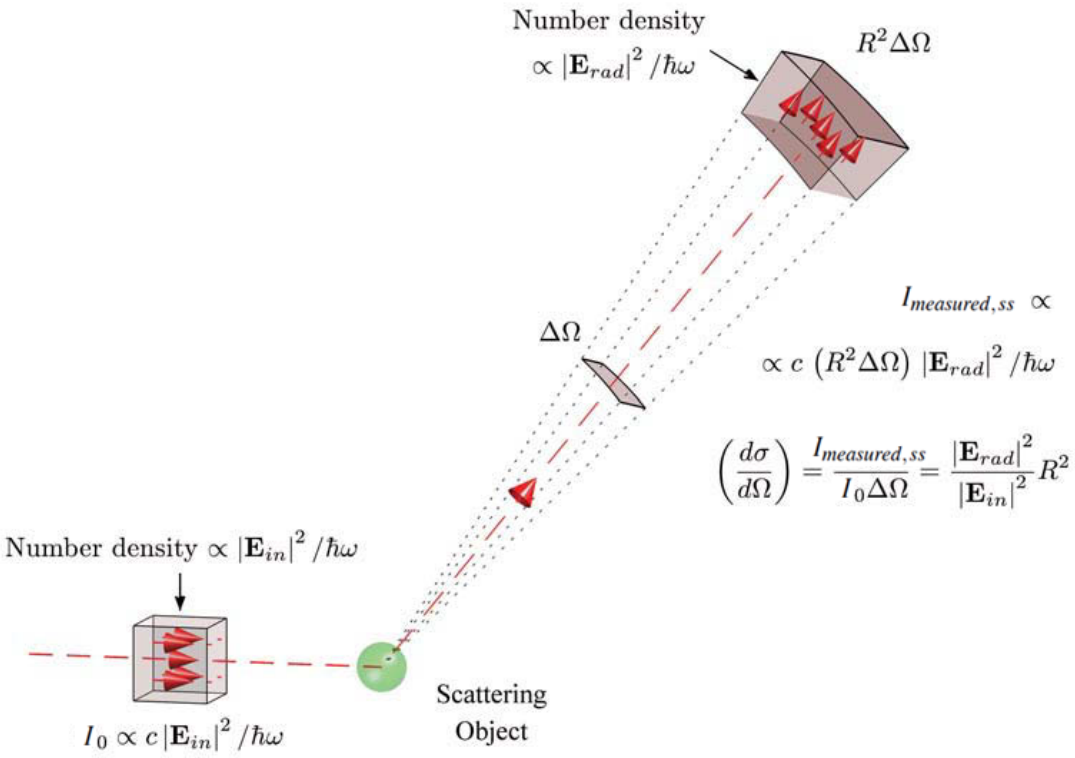

Figure 2.6: Schematic layout of a generic scattering experiment used to determine the differential cross section ($d\sigma/d\Omega$): see eq. 2.7 or 2.16. The incident beam flux I_0 is the number of particles per second per unit area. For an electromagnetic wave this is proportional to $|\boldsymbol{E}_{\text{in}}|^2$ times the velocity of light, c. The incident beam interacts with the target object to produce the scattered beam. A detector records the scattered intensity, $I_{\text{measured, ss}}$, defined as the number of counts recorded per second, which is proportional to $|\boldsymbol{E}_{\text{rad}}|^2$ times the area of the detector and the velocity of light. The detector is located a distance R from the target object, and subtends a solid angle of $\Delta\Omega$[108].

seconds.

2.2.2 Sample holder and temperature calibration

The specimens were placed into a 1 mm outer diameter borosilicate glass capillary. The X-ray pathway was entirely kept under vacuum except in the proximity of the specimen where it passed through the air for $\simeq$ 4 cm. For *in situ* measurements, a dynamic vacuum was applied to the capillary ($P = 1.5 \times 10^{-2}$ mbar), while for

Table 2.1: SAXS/WAXS detectors specifications[127].

Detector	Specifications
Dectris - Pilatus (1 M)	• Photon counting detector • Multi-modules (10 modules in 2 × 5 array with 7 × 17 pixel gap between each) • Size: 169 × 179 mm; 981 × 1043 pixels (8.4% = intermodule gap) • Mounted on X-Y stages to automatically produce gap-free images from 3 raw frames • Pixel size: 172 × 172 μm • Dynamic range: 6 orders of magnitude • Frame rate: 10 Hz
Dectris - Pilatus (200 K)	• Photon counting detector • Multi-module (2 modules in 2 × 1 array with 7 pixel gap) • Size: 169 × 33 mm; 981 × 195 pixels (0.7% = intermodule gap) • Pixel size: 172 × 172 μm • Dynamic range: 6 orders of magnitude • Frame rate: 30 Hz

ex situ measurements, the capillary was sealed under an argon atmosphere ($P = 3$ mbar). In situ measurements were performed applying a heating rate of 5 °C/min. The heat blower temperature was calibrated by conducting WAXS measurements on an Ag/NaCl up to 500 °C (5 °C/min). Thus, it was possible to associate an effective specimen temperature with a heat blower temperature.

2.2.3 Absolute intensity data conversion

In order to carry out quantitative analysis on intrinsic specimen features, the measured intensity (counts) distribution (as a function of q) acquired during an exposure time of 1 second, needed to be converted into the corresponding photoelectric differential cross section of the specimen, generally called absolute intensity. Such absolute intensity is independent of the intensity of the source (I_0), by the settings/instrumental parameters (camera length, for instance) or extrinsic

features of the specimen (specimen solid thickness, for instance). Rewriting eq. 2.7 for Debye-Scherrer geometry, the measured intensity (counts/s) is given by:

$$I_{\text{measured, ss}}(q,\lambda) = \frac{N_{\text{ss}}(q,\lambda)}{t_{\text{ss}}} = I_0(q,\lambda)\Delta\Omega\eta(\lambda)P(q)A_{\text{DS}}(\lambda)Ad_{\text{ss}}\left(\frac{\partial\Sigma_{\text{PE}}}{\partial\Omega}(q,\lambda)\right)_{\text{ss}} + BG_{\text{ss}} \tag{2.16}$$

The solid specimen volume (V_{ss}) is replaced by $A \times d_{\text{ss}}$, where A is the area illuminated by the beam and d_{ss} is the solid thickness of the specimen. Due to the small-angle approximation ($\sin(\theta) = q\lambda/4\pi << 1$), the X-ray pathway, $\tau(q)$, through the medium was assumed constant. Thus, the absorption correction factor, A_{DS}, was approximated as[128]:

$$A_{\text{Debye-Scherrer}}(q,\lambda) = \frac{1}{V_{\text{ss}}}\int e^{-\tau(q)\mu(\lambda)}dV_{\text{ss}} \simeq \frac{1}{V_{\text{ss}}}\int e^{-\tau(0)\mu(\lambda)}dV_{ss} = A_{\text{DS}}(\lambda) \tag{2.17}$$

A_{DS} is also referred to as the transmission of the specimen, τ_s, (see §2.2.1) and $\tau(0)$ is also referred to as d_{ss}. In order to convert the measured intensities to absolute intensities a standard of known absolute intensity is used[¶].

The concept of calibration factor is introduced, in eq. 2.18, considering the relation between the measured intensities of a specimen (from eq. 2.16) and the standard.

$$\begin{aligned} I_{\text{Abs}}(\text{cm}^{-1}) &= \left(\frac{\partial\Sigma_{\text{PE}}}{\partial\Omega}(q,\lambda)\right)_{\text{ss}} = \\ &= \underbrace{\left(\frac{\partial\Sigma_{\text{PE}}}{\partial\Omega}(q,\lambda)\right)_{\text{st}} \frac{A_{\text{DS, st}}(\lambda)d_{\text{st}}}{[I_{\text{measured, st}}(q) - BG_{\text{st}}]}}_{\text{calibration factor}} \frac{[I_{\text{measured, ss}}(q) - BG_{\text{ss}}]}{A_{\text{DS}}(\lambda)d_{\text{ss}}} \end{aligned} \tag{2.18}$$

The standard adopted was a 1 mm thick glassy carbon SRM 3600[129], which was measured using the same settings/instrumental condition used for the specimens. A blank sample measurement was also conducted in order to consider the background scattering effect due to the presence of air (BG_{st}). Relying also on the measured absorption correction factors (transmissions) of the standard and of the air, the

[¶]It is important to note that the absolute intensity depends upon the choice of the system. In eq. 2.18, the system chosen contains only the solid part of the specimen (d_{ss}).

calibration factor ($CF = 0.000377963\ s^{-1}mm^{-1}$), see eq. 2.18, was calculated using scatterBrain software following the procedure reported in[130,131]. The BG_{ss} of the specimens was obtained by measuring an empty capillary. Before subtracting the empty capillary pattern from the measured specimen patterns, the empty capillary pattern was normalized taking into consideration its relative transmission factor compared to the specimens relative transmission factor[132]. The thickness of the BG_{ss} was considered identical to the specimen as stated in[133]. In general, the BG_{ss} pattern counts were three orders of magnitude smaller compared to the specimens pattern counts for the SAXS patterns ($q < 0.2\ Å^{-1}$) used in the analysis.

2.2.4 Artefact data and sample displacement

SAXS data presented artefacts due to the presence of the beam stop, and this corrupted data has been removed (see Appendix E). In general, the first few points (between one and three) in the intensity pattern corresponding to the lowest q values (lowest scattered angles) were corrupted because part of the photons scattered by a specimen interacted (were scattered) with (by) the beam stop, before reaching the detector. Those photons, scattered again by the beam stop, produced (second-order scattering) single point artefact at high q, see Fig. 5.4. Such artefact could not be removed by background subtraction (empty capillary pattern) because the specimen itself was the cause of the first scattering event.

The camera lengths were measured by placing a reference standard in a set position. Matching the θ values with the q values corresponding to the diffraction peaks characteristic of the reference standard, the camera lengths were obtained. Unfortunately, the specimens measured were generally placed a few mm away from this set position affecting the true q positions of a measured pattern. The effective diffraction angles are $2\theta - \alpha$ for a parallel to the incident beam displacement (u_1) and $2\theta - \beta$ for a perpendicular to the incident beam displacement (u_2), see Fig.

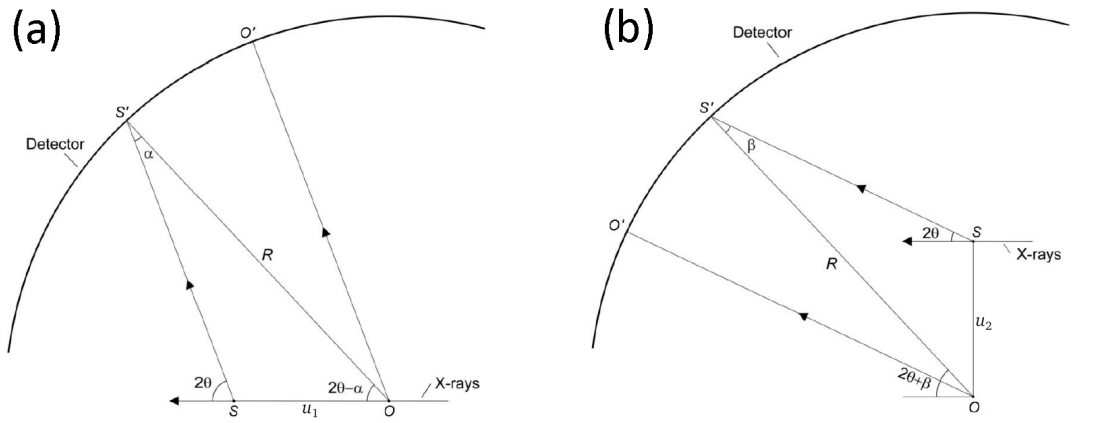

Figure 2.7: Peak shift due to sample displacement in Debye-Scherrer geometry. The sample, S, can be displaced from the origin, O, in a direction either (a) parallel or (b) perpendicular to the incident beam, resulting in the diffraction peak shifting from O' to S' [134]. The detector radius is given by R.

2.7. The relations between position and θ displacements are given by[134]:

$$\sin\alpha = \frac{u_1}{R}\sin 2\theta \qquad ; \qquad \sin\beta = \frac{u_2}{R}\cos 2\theta \tag{2.19}$$

For *in situ* WAXS Rietveld refinement phase quantification analysis, the displacement components were refined (calculated), see Appendix C.2.

Across several *in situ* measurements, presented in Fig. 5.9, the refined parallel displacement toward the detector was 2.3 mm. The perpendicular displacement, attributed to a vertical WAXS detector displacement toward the specimen, was 6.1 mm.

2.2.5 SAXS data analysis

The SAXS pattern features of all specimens in this thesis are generally dominated by the effect of pores/particles structures because the probe size d of the related SAXS q-range, $2\pi/d$, is comparable with the dimension of such structures. The interference effects between smaller structures, for instance crystals diffraction ($e^{i\boldsymbol{q}\cdot 2\pi/\boldsymbol{G}_{(h,k,l)\alpha}}$, see §2.1.1.1) or interference effects caused by atomic electrons

dispersion ($e^{iq\cdot 2\Delta r}$, see Appendix A.2) can be neglected because $q << |\boldsymbol{G}_{(h,k,l)\alpha}| << \pi/|\Delta \boldsymbol{r}_s|$. A system, in general, is composed by an arbitrary number of overlapping structural features, but when such structural features present different sizes they can be modelled separately (see structure levels in §2.2.5.2) if each individual structural feature is dominant over a sufficient q-range. The goal of the SAXS data analysis presented in this thesis is to obtain information about distribution and specific surface area of (single grain/piece) pores in the Al and Mg scaffolds. Our systems contain two different homogenous phases, a solid phase and a gas (pore) phase. The electron density of gas is negligible ($n_{\text{e, solid}} >> n_{\text{e, gas}}$) compared with the electron density of solid. The homogeneity approximation is valid for structures, investigated by a probe size $2r \simeq d = 2\pi/q$, having larger dimensions compared with the crystallite dimensions that compose the specimen mixture. The structures that need to be considered to fulfill the goal contain at least 2 (levels); a pore structure dominant at low q of the SAXS pattern, and an internally (nearly) closed-packed particle structure dominant at high q (see Fig. 2.8). For both structures, in their corresponding dominant q-range, it is convenient to take advantage of their symmetries and thus, express the scattering factor, F^{ss}, of the solid specimen, see eq. 2.20, by the scattering factors of pores or closed-packed particles respectively and their positions ($\boldsymbol{r}_j$).

$$F^{\text{ss}}(\boldsymbol{q}) = \sum_j F_j^{\text{pp}}(\boldsymbol{q}) \exp\left(i\boldsymbol{q}\cdot\boldsymbol{r}_j\right) \tag{2.20}$$

In order to obtain intrinsic information about these structures from the absolute intensity converted patterns, the square modulus of the solid specimen, for identical pores or particles (denominated pp) randomly orientated, is calculated from eq. 2.21.

$$|F^{\text{ss}}(\boldsymbol{q})|^2 = \sum_j \sum_k F_j^{\text{pp}}(\boldsymbol{q}) F_k^{\text{pp}}(\boldsymbol{q}) \frac{\sin(qr_{jk})}{qr_{jk}} = N_{\text{pp}} |F^{\text{pp}}(\boldsymbol{q})|^2 S^{\text{pp}}(q) \tag{2.21}$$

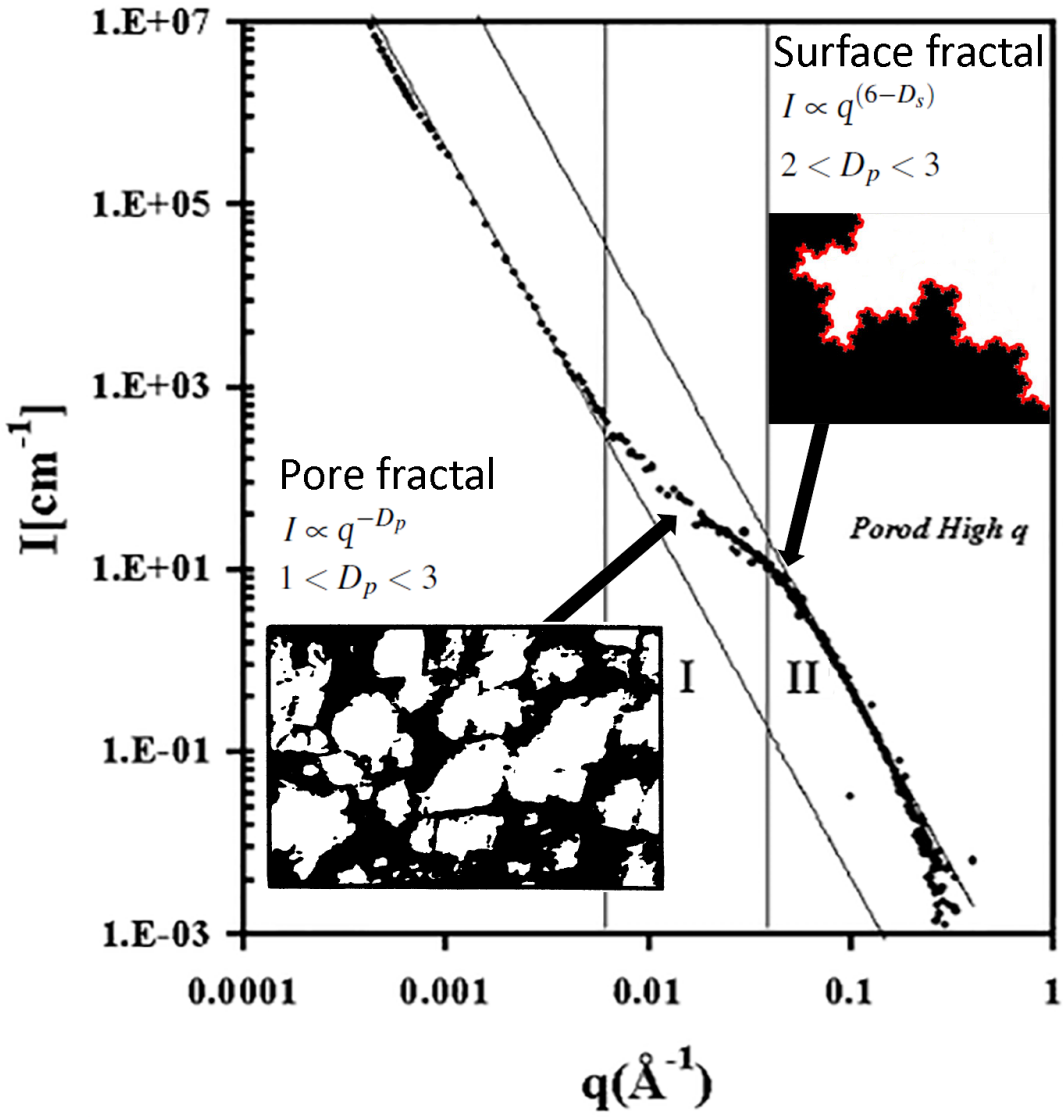

Figure 2.8: Typical apparent intensity of a two structure porous system (solid and gas phases). The two regions are identified: (I) Pore structure and (II) internally (nearly) closed-packed particle structure[135–137].

In eq. 2.21 $S^{pp}(q)$ is the structure factor and N_{pp} is the number of pores or particles in the specimen. The structure factor takes into consideration the interference between pores or particles due to their relative position (see Fig. 2.9(b)). Considering the simplest case where each pore or particle in the specimen has the same average relationship with its neighbours, the structure factor is given

by[138]:

$$S^{pp}(q) = 1 + \frac{1}{N_{pp}} \sum_{j \neq k} \sum_{k} \frac{\sin(qr_{jk})}{qr_{jk}} \simeq 1 + N_{pp} \sum_{k} \frac{\sin(qr_k)}{qr_k} \tag{2.22}$$

In fact, the assumption of a similar relationship of pores or particles with its neighbours has to be refined. For this purpose, the radial distribution function $g(r)$[‖] can be introduced, which gives the probability of locating a pore or particle at some distance r from an arbitrary origin. Taking into consideration $g(r)$, eq. 2.22 can be written as:

$$S^{pp}(q) = 1 + \frac{N_{pp}}{V_{pp}} \int_0^\infty 4\pi r^2 g(r) \frac{\sin(qr)}{qr} \mathrm{d}r \tag{2.23}$$

Finally, considering the definition of differential cross section of a specimen and combining it with eq. 2.21, the following relation is obtained[139]:

$$\begin{aligned} I_{Abs}(\mathrm{cm}^{-1}) &= \left(\frac{\partial \Sigma_{PE}}{\partial \Omega}(q, \lambda) \right)_{ss} = \frac{1}{V_{ss}} r_e^2 |F^{ss}(\boldsymbol{q})|^2 = \\ &= \frac{N_{pp}}{V_{ss}} r_e^2 |F^{pp}(\boldsymbol{q})|^2 S^{pp}(q) = \\ &= \underbrace{\frac{N_{pp} V_{pp}}{V_{ss}}}_{\varphi_{pp} = 1} V_{pp} (\underbrace{r_e \Delta n_e}_{\Delta\rho_{SLD}})^2 P^{pp}(q) S^{pp}(q) \end{aligned} \tag{2.24}$$

$V_{pp} (= V_{particle}$ or $= V_{pore} \times (1 - \varphi_{total})/\varphi_{total})$ denotes the volume of a particle or the volume of a pore multiplied by $(1 - \varphi_{total})/\varphi_{total}$, where φ_{total} is the total porosity, because the measured intensities were converted to solid specimen ($V_{ss} = V_{\text{solid+gas specimen}} \times (1 - \varphi_{total})$, see eq. 2.16) absolute intensities and no to gas specimen ($V_{gas} = V_{\text{solid+gas specimen}} \times \varphi_{total}$) absolute intensities. φ_{pp} is the total volume fraction of the pores or particles in the matrix[139]. For the system we chose, during the conversion from measured to absolute intensity in which only the solid phase is included, $\varphi_{pp} = 1$. The term $\Delta\rho_{SLD}$ is the scattering length density difference between the two phases. It is worth noting that the photoelectric scattering features

[‖]Note that we still retain spherical symmetry by choosing $g(r)$ to depend only on the radial coordinate r.

are formed due to an electron density discontinuity and in our system this occurs on the surface of the two phases. Because the scatterers (electrons) are spatially dispersed, the refractive index is dependent on the momentum transferred, $n(\omega, q)$, in a different way from what we saw in eq. A.7. Due to the electron density differences between the solid and gas phases ($n_{\text{e, solid}} >> n_{\text{e, gas}}$)[††], scattering length density difference is approximated as $\Delta\rho_{\text{SLD}} = \rho_{\text{SLD-solid}} - \rho_{\text{SLD-gas}} \simeq \rho_{\text{SLD-solid}}$. Using the real part of the scattering factors of each element ($f_{1,i}$), provided in Table A.1, and the elements molar concentration (%), c_i, of each element calculated from the respective phase composition obtained by applying the Rietveld refinement method on the WAXS and XRD patterns respectively for *in situ* and *ex situ* measurements, the solid scattering length density is given by:

$$\rho_{\text{SLD}} = r_{\text{e}} n_{\text{e}} = r_{\text{e}} \rho_{\text{mixture}} N_{\text{Avogadro}} \frac{\sum_i c_i f_{1,i}}{\sum_i c_i M_i} \tag{2.25}$$

In the last step of eq. 2.24, the homogeneity property of the pores or particles (uniform average electron density approximation) has been used, thus the isotropic form factor intensity, $P^{\text{pp}}(q)$, is introduced. Its definition is given by eq. 2.26, where the isotropic form factor intensity for spherical symmetry is also reported.

$$P^{\text{pp}}(q) = \frac{1}{V_{\text{pp}}^2} \left| \int_{V_{\text{pp}}} \mathrm{e}^{\mathrm{i}\boldsymbol{q}\cdot\boldsymbol{r}} \mathrm{d}^3\boldsymbol{r} \right|^2 \quad ; \quad P^{\text{pp}}_{\text{sphere}}(q) = \left[3 \frac{\sin(qR) - qR\cos(qR)}{(qR)^3} \right]^2 \tag{2.26}$$

Form factor intensity, P^{pp}, depends on the inter-pore or inter-particle shape through the integral over its volume. The meaning of the form factor intensity is also illustrated in Fig. 2.9(a) while in Fig. 2.10 the form factor intensity for two different size monodisperse spheres are plotted, showing the typical fringes that have a series of minimums at $\tan(qR) = qR$.

[††]For the *in situ* SAXS measurement the ratio between mass density and molar mass of the solid Al scaffold is 0.069 cm^{-3} and for that of the argon gas at 3 mbar it is 1.27×10^{-7} cm^{-3}.

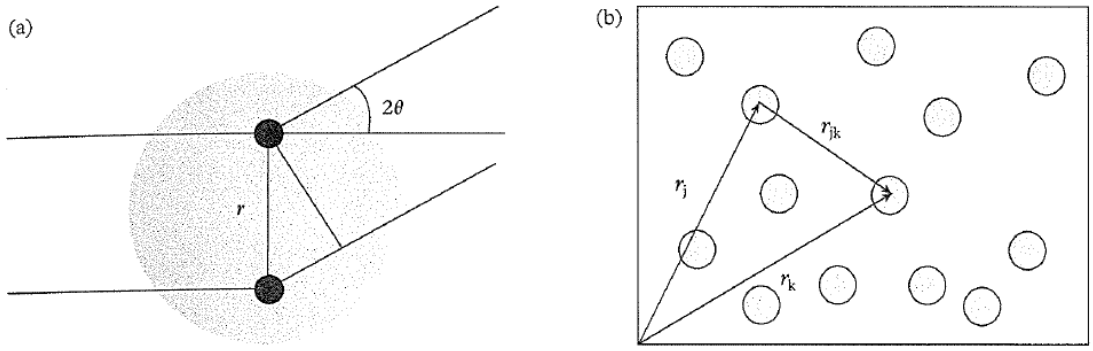

Figure 2.9: Illustration for a system of spherical pores or particles of (a) the form facture intensity $P^{pp}(q)$ describing the inter-pore or inter-particle shape, and (b) the structure factor $S^{pp}(q)$ which is a function of the local order and the interaction potential[138].

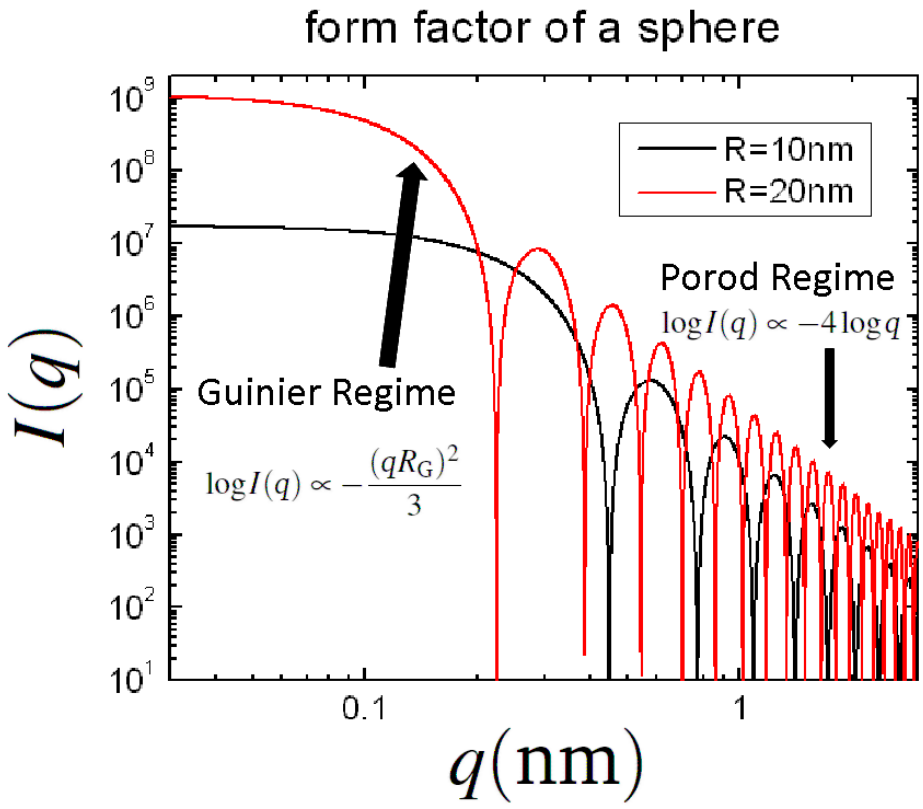

Figure 2.10: Form factor intensity[140] for two spheres of radius 10 nm (black line) and 20 nm (red line) plotted as a function of the momentum transferred q.

2.2.5.1 Fractal scattering theory

In order to obtain information about the size and shape of pores and also about the degree of roughness of their surfaces, the low ($qR << \pi$) and high ($qR >> \pi$) q limit approximation, respectively, of the form factor intensity, $P^{\text{pore}}(q)$, has to be considered. The shape of the pores is modelled choosing the corresponding form factor intensity as a function of q, see eq. 2.26. For spherical pores the low q limit, $qR << \pi$, where R is the radius of the pore, of the form factor intensity, derived from eq. 2.26, is referred to as the Guinier regime and it is given by[138]:

$$\begin{aligned} P^{\text{pore}}_{\text{sphere}}(q) &\simeq 1 - \frac{(qR)^2}{5} + \ldots \\ &\simeq 1 - \frac{(qR_{\text{G}})^2}{3} + \ldots \\ &\simeq \mathrm{e}^{-\frac{(qR_{\text{G}})^2}{3}} \end{aligned} \tag{2.27}$$

Working in the Guinier regime, it is useful to introduce the radius of gyration R_{G} of the pore, defined in eq. 2.28. The radius of gyration is the spatial average of the electron density distribution (in our case uniform) by the squared transverse distance from the axis passing through the electron density distribution centre (in our case coincident with its geometrical centre) along the direction of the propagating X-rays.

$$R_{\text{G}}^2 = \frac{1}{V_{\text{pore}}} \int_{V_{\text{pore}}} r^2 \mathrm{d}\boldsymbol{r} \tag{2.28}$$

The solution of eq. 2.28 for a sphere is $R_{\text{G}} = R \times (3/5)^{1/2}$. The last step of eq. 2.27 is obtained from an alternative derivation, and it is justified considering the expansion $\mathrm{e}^{-x} \simeq 1 - x$.

In order to obtaining analytical relations between the measured scattering pattern and the properties of pores such that the degree of roughness of a surface and its specific surface area, the high ($qR >> \pi$) q limit of the pore form factor intensity, $P^{\text{pore}}(q)$, can be used only when the form factor intensity is known. For identical pores of spherical shape, the high q limit, $qR >> \pi$, where R is the radius of the

pore, of the form factor intensity, is referred to as the Porod regime and is derived from eq. 2.26, resulting in $P^{\text{pore}}(q) \simeq (9/2) \times (qR)^{-4}$. The Guinier and Porod regimes are also shown in Fig. 2.10. The high q limit ($q >> \pi/R$) of the q-range of the scattering pattern dominated by the pore structure (q-range referred to as I in Fig. 2.8) coincides with the low q limit ($q << \pi/r_{\text{mh}}$, r_{mh} is the minimum probe size ($r = \pi/q$) where the homogeneous condition is met[‡‡]) of the q-range dominated by the homogenous closed-pack particle structure (q-range referred to as II in Fig 2.8). Such closed-pack particles are not defined by the common concept of boundaries such as phases or electron density changes, but are exclusively related to the probe size, $d = 2r$, of the related SAXS q-range ($q = 2\pi/d$). In the q-range boundary between the two structures, the two models, from eq. 2.24, are given by:

$$\begin{aligned} I_{\text{Abs}}(\text{cm}^{-1}) = \left(\frac{\partial \Sigma_{\text{PE}}}{\partial \Omega}(q,\lambda)\right)_{\text{ss}} &= V_{\text{pore}} \frac{1-\varphi_{\text{total}}}{\varphi_{\text{total}}} (\Delta\rho_{\text{SLD}})^2 P^{\text{pore}}(q) \\ &= V_{\text{particle}} (\Delta\rho_{\text{SLD}})^2 S^{\text{particle}}(q) \end{aligned} \tag{2.29}$$

Because in general the pores are polydisperse, and present different and irregular shapes although randomly orientated, in order to obtain surface information, it is convenient to model the scattering pattern, eq. 2.29, in this boundary q-range in terms of volume, V_{particle}, and structure factor, $S^{\text{particle}}(q)$, of the homogenous closed-pack particles. The degree of roughness of a surface is defined by the variable $D_s (2 < D_s < 3)$, introduced in eq. 2.30[141–143]. It is defined applying the limit $\pi/R << q << \pi/r_{\text{mh}}$ on the particles radial distribution function, $g(r)$, previously introduced in eq. 2.23.

$$\lim_{\substack{r/r_{\text{mh}} \to \infty \\ r/R \to 0}} g(r) = 1 - \frac{V_b(r)}{V_{ss}} = 1 - \frac{N_0 r^{3-D_s}}{V_{ss}} \tag{2.30}$$

In a system including only the solid material sides, the probability to find a solid closed-pack particles, of size $2r$, in the bulk part of the system is 100%, $g(r) =$

[‡‡]Minimum condition where the electron density distribution discontinuity between real particles belonging to different phases are neglected.

1, while on the surfaces, due to the resolution, r, imposed by the probe size, the probability is lower, $g(r) < 1$. Reducing the resolution, $r << R$, it is possible to distinguish between the volume V_b[†], occupied by closed-pack particles lying on the surface of the pores, and the rest of the bulk volume of the system. Information about the specific surface area can be obtained by considering eq. 2.30, where the relation, $dV_b(r) = S(r)dr$, between V_b and the total surface area $S(r)$ is a function of the resolution, r, adopted[144]. It is, thus, evident that N_0 is a constant characteristic of the fractal boundaries. Applying the limits, mentioned above, to the particles structure factor, $S^{particle}(q)$, see eq. 2.31[139], and replacing it in the eq. 2.29, eq. 2.32 is obtained[142].

$$\lim_{\substack{r/r_{mh}\to\infty \\ r/R\to 0}} S^{particle}(q) = 1 + \frac{N_{particle}}{V_{ss}} \lim_{\substack{r/r_{mh}\to\infty \\ r/R\to 0}} \int_0^\infty 4\pi r^2 g(r) \frac{\sin(qr)}{qr} dr \tag{2.31}$$

$$\begin{aligned} \lim_{\substack{r/r_{mh}\to\infty \\ r/R\to 0}} I_{Abs}(cm^{-1}) =& (\Delta\rho_{SLD})^2 \lim_{\substack{r/r_{mh}\to\infty \\ r/R\to 0}} \left(V_{particle}(r) + \int_0^\infty 4\pi r^2 g(r) \frac{\sin(qr)}{qr} dr \right) \simeq \\ \simeq& \pi(\Delta\rho_{SLD})^2 \frac{S(r)}{m} \frac{m}{V_{ss}} F(D_s) q^{D_s-6} r^{D_s-2} \end{aligned} \tag{2.32}$$

Rearranging the terms in eq. 2.32, in order to explicitly include the specific surface area, $\sigma(r)$, the following relation is obtained:

$$\sigma(r) = \frac{S(r)}{m} = \frac{\lim\limits_{\substack{qr_{mh}/\pi\to 0 \\ qR/\pi\to\infty}} I_{Abs}(cm^{-1}) q^{6-D_s}}{\pi(\Delta\rho_{SLD})^2 F(D_s) \rho_{mixture}} r^{2-D_s} \tag{2.33}$$

The SAXS pattern of a porous scaffold, where the scaffold material is a single homogeneous solid phase, would present a $I_{Abs}(q) \propto q^{D_s-6}$ trend over a q-range that satisfies the relation: $\pi/R << q << \pi/r_{mh}$, if such an inequality exists; see Fig. 2.10. For resolutions, probe size r, associated with this boundary q-range, the surfaces would present a self-similar trend characterised by a D_s degree of

[†] $V_b(r)$ is the volume of material within distance r of the interface, *i.e.* the material inside 'Minkowski' spheres of radius r centered at every point on the surface.

roughness. In eq. 2.33, $F(D_s) = \Gamma(5 - D_s)\sin[(3 - D_s)\pi/2]/(3 - D_s)$, where Γ is the gamma function, and it is worth noting that the specific surface area is a function of the resolution r. A smooth surface corresponds to $D_s = 2$, which is a particular case where the surface appears flat, where $N_0 = S$ in eq. 2.30. It is also the case for spherical pores, $I_{\text{Abs}} \propto P^{\text{pore}}(q) \simeq (9/2) \times (qR)^{-4} \propto q^{-4}$ from above, where the curvature effect is neglected due to the $r << R$ approximation.

2.2.5.2 Unified model

For a system composed of n structures (levels) of different sizes where each individual structural feature is dominant over a sufficient q-range, it would be possible to model the pattern, using the Unified fit[145,146]. From the Unified fit analysis, several pieces of useful information can be obtained, such as the size of the main objects, in terms of volume occupied, for each structure (level i) and the corresponding volume-averaged fractal degree of mass, pore, or surface formed by the aggregation of the smaller structure objects (level $i + 1$)[143,147]. The Unified scattering function is given by:

$$I_{\text{measured}}(q,\lambda) = BG_{ss} + \sum_{1}^{n} \underbrace{G_i e^{-\frac{(qR_{G_i})^2}{3}}}_{\text{Guinier term}} + \underbrace{B_i \left\{ \frac{\left[erf\left(\frac{qR_{G_i}}{6^{1/2}} \right) \right]^3}{q} \right\}^{P_i}}_{\text{Porod term}} \tag{2.34}$$

The form factor intensity (see 2.26) of each structure level i is replaced by a Guinier and Porod term, previously introduced in §2.2.5. In general, because scattering objects of the structure level i are polydisperse[148], randomly averaged about their orientation and their position relative to the scattering reference frame ($g(r)$, used in eq. 2.23, has an arbitrary origin), the fringe features (see Fig. 2.10) are averaged out. Thus, in the q-range where the scattering pattern is dominated by the structure level i, the Guinier and Porod regimes approximation are obeyed only for the low and high q-range limits respectively. The averaged fringes feature in the middle q-range is considered in the model, by the introduction in the Porod term

of the error function (*erf*(), see eq. 2.35), obtained using a log-normal distribution (Gaussian log-size distribution) of the scattering objects[145].

$$erf(Y) = \frac{2}{\pi^{1/2}} \int_0^Y e^{-w^2} \mathrm{d}w \tag{2.35}$$

The Unified fit and its Gaussian log-size distribution (read below) were implemented[149] by the Irena 2.62 SAS tool package, a macro that runs on Igor Pro 7 software. For each level i, only two variables are refined only across the q-range where the structure i is dominant; the radius of gyration, $R_{G,i}$, which provides information about the size of the main objects of the structure knowing the shape of the objects, and the scattering power-law, P_i, which provides structural information. The prefactors G_i and B_i instead, that in this thesis are not going to be related to any physical properties of the specimen, are refined across the q-range of all structures. The q independent BG_{SS} variable was also refined at the highest q-range of the final level where the pattern intensity tends to be q independent.
When plotted in $\ln I$ *vs.* $\ln q$ scale, the scattering pattern, in the Porod regime, result in a line having a slope equal to the negative value of the scattering power-law, $-P_i$. In the particular case of a structure presenting a smooth surface, $P_i = 4$, its form factor intensity can be approximated as spherical (see P_{sphere} in eq. 2.26). Thus, it is possible, using Maximum Entropy and Total Non-negative Least Square (TNNLS), to determine the Gaussian log-size distribution function of the scattering objects considered in the unified model[148].

2.2.5.3 Calculation of porosity using the method of the invariant

In general, the total porosity, φ_{total}, of a homogeneous two-phase system can be calculated from its scattering pattern, if dominated exclusively by porous features across the entire q-range, considering the invariant[123], Q, of the system given by

eq. 2.36[136,150‡].

$$Q = \int_0^\infty I_{\text{Abs}} q^2 \mathrm{d}q = 2\pi^2 \varphi_{\text{total}} \Delta\rho^2 \tag{2.36}$$

In this thesis, the cumulative porosity (φ_{partial}) as a function of q, in the q-range 0.0111 - 0.1844 Å^{-1}, from the *in situ* SAXS measurements of an Al scaffold, presented in Fig. 5.7, is calculated according to eq. 2.37, which has been derived from eq. 2.36.

$$\varphi_{\text{partial}}(q) = \frac{\int_{0.0111}^{q} I_{\text{Abs}} q^2 \mathrm{d}q}{2\pi^2 \Delta\rho^2} \tag{2.37}$$

The relation between $d = 2\pi/q$ and the size of the pores, $2R$, is constant only when the poreshape is self-similar. In this case, applying an approximation where $d = 2R$ would mean that the pores contribute only locally at a single $q = \pi/R$ point in the scattering pattern.

2.2.5.4 Calculation of porosity distribution using McSAS analysis

The pore structures presented in the scaffolds studied in this thesis have a wide polydisperse size distribution, which is not a peak (log-normal for instance). Thus, the size distribution calculated from the Unified fit analysis, introduced in §2.2.5.2, is not adequate. It can be used though to highlight the size of the dominant pores in term of porosity, restricted to the q-range used for this enalaysis. On the other hand, determining the cumulative porosity distribution using eq. 2.37, which considers a wide polydisperse pore size distribution, is limited to a local contribution of $2R_i$ size pores (single $q = \pi/R_i$ point approximation) to the scattering pattern. In order to overcome these limitations, a model is adopted that describes the absolute intensity pattern in terms of multiple i levels of $2R_i$ size spheroidal pore form factor intensities. These levels are no longer dominant over a sufficient q-range that allows one to distinguish a Guinier and a Porod regime for every level, but are overlapping in the q-range considered. Generalizing eq. 2.29 for multiple levels of spherical

‡The choice of absolute intensity is consistent with the choice made in §2.2.3, where the system consists only in the solid part of the spacemen. $I_{\text{Abs, ss}} = I_{\text{Abs(solid+gas)}}/(1-\varphi_{\text{total}})$.

pores, the absolute intensity pattern is modelled by:

$$I_{\mathrm{Abs}}(\mathrm{cm}^{-1}) = (\Delta\rho_{\mathrm{SLD}})^2 \frac{1-\varphi_{\mathrm{total}}}{\varphi_{\mathrm{total}}} \sum_{i}^{Bins\#} \left(\frac{4\pi R_i^3}{3}\right) \frac{\varphi_i}{\varphi_{\mathrm{total}}} \left[3\frac{\sin(qR_i) - qR_i\cos(qR_i)}{(qR_i)^3}\right]^2 \tag{2.38}$$

Each level has a partial porosity, $\varphi_i = V_{R_i,\,\mathrm{pores}}/V_{\mathrm{solid+pores}}$, that contributes to the volume-weighted of the pore size distribution. For spheroidal pore shapes, R_i is replaced with $R_{\theta,i}$ which is the distance from the origin of the pore to the surface of the ellipsoid for a line titled at an angle θ with respect to the X-ray propagation axis. In order to extrapolate the contribution of the partial porosity, φ_i, from the absolute intensity pattern a Monte Carlo regression package (McSAS, version 1.0.1), implemented to analyse small-angle scattering (SAS) based on eq. 2.38, was adopted[151,152]. In order to give a general idea about analysis results obtained by Mc fit, Fig. 2.11 describes the refined contributions of the relative partial porosity, φ_i, for *in situ* SAXS measurements of an Al scaffold. Such results will be discussed in more detail in Chapter 5 (Fig. 5.3 and 5.17). The parameters input into the software were the form factor shape (spherical), scattering length density, the number of different pore sizes (that is, the number of bins = 40) and the radius range (0.789809 – 28.3411 nm) distributed in a logarithmic scale among bins. The bin widths in Fig. 2.11 appear uniform because the x-axis (radius) scale is logarithmic. The refinement of parameters were repeated 10 times for each specimen from which uncertainties were determined. The refined parameters were stored only when and if the χ value (eq. 2.15, convergence criterion) dropped to 1 before reaching 500 cycles (number of repetition). From eq. 2.38, the [Rel.] volume fraction in Fig. 2.11, corresponds to $(\varphi_{\mathrm{total}} - 1)\varphi_i/\varphi_{\mathrm{total}}^2$.

2.2.5.5 *In situ* SAXS/WAXS analysis

In situ SAXS/WAXS absolute intensity patterns and relative partial porosity, φ_i, distributions, obtained from McSAS analysis, were plotted in 3D surface graphs (see Fig. 2.12 and 2.13). In Chapters 4 and 5, the 3D surface graphs are presented

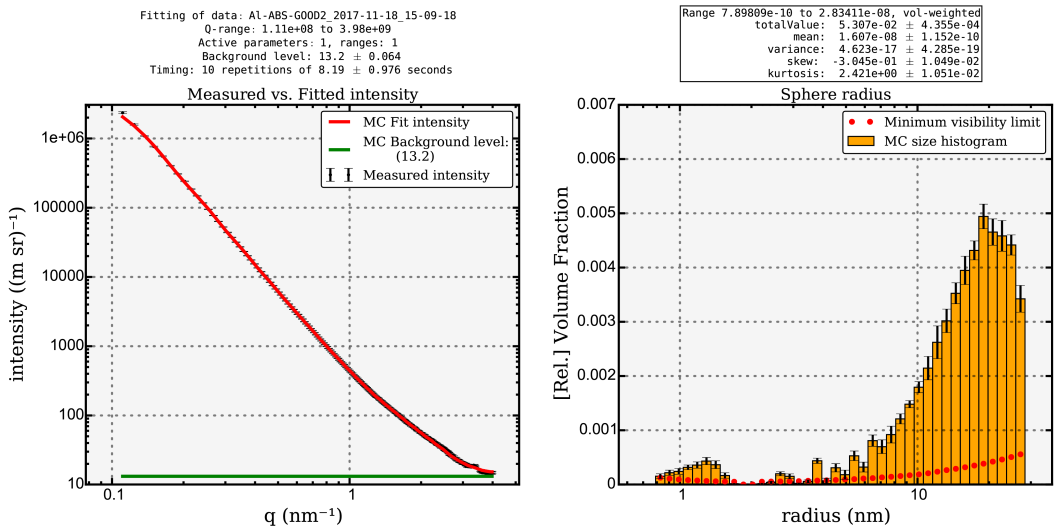

Figure 2.11: *In situ* SAXS measurements and McSAS analysed data of an Al scaffold.

from a point of view along the direction of the vertical axis, resulting in a 2D graph where the vertical values are represented by colours[§].

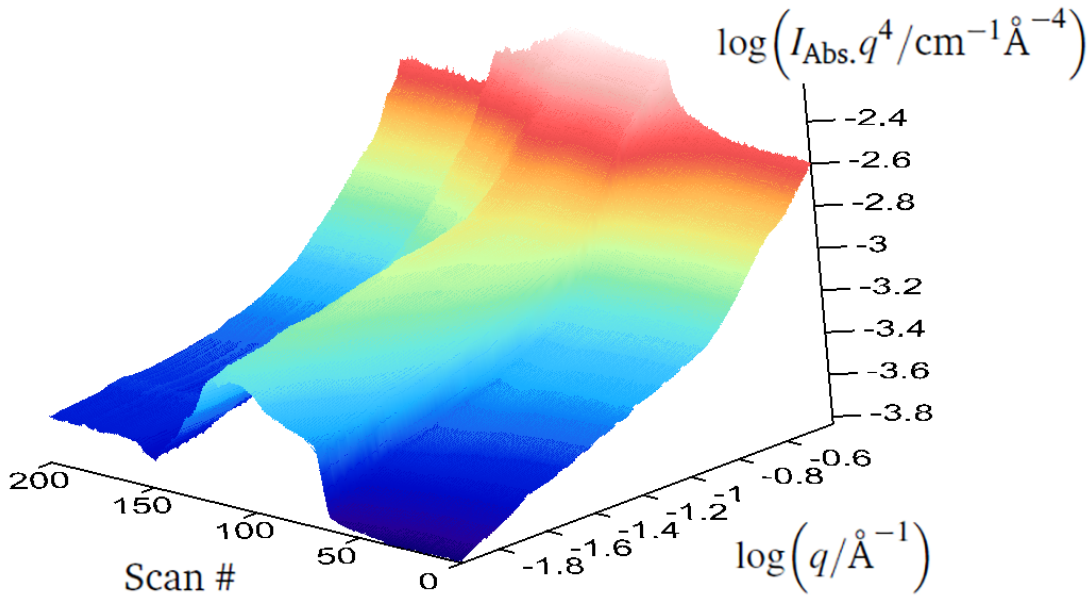

Figure 2.12: 3D surface graph of *in situ* (5 °C/min heating ramp, 2 scans/min) absolute intensity SAXS patterns expressed as $I_{\mathrm{Abs}}q^4$ for $NaAlH_4$ decomposition.

[§]Shades of colour were normalized for each set of patterns ranging from the maximum to minimum vertical values.

In order to convert each *in situ* small-angle scattering pattern to absolute intensities, the solid thickness (d_{ss}, scan #) of the specimen for each scan number, is required (see eq. 2.18). In order to calculate the solid thickness, the linear absorption coefficient ($\mu_{\text{scan \#}}$) for each scan number is required (see eq. 2.17, also rearranged in eq. 5.1). The linear absorption coefficient was calculated (see eq. A.14) from an *in situ* Rietveld refinement quantitative phase analysis carried out on the associated wide-angle scattering patterns. The quantitative phase analysis results are reported in detail in Chapter 5. Absolute intensity conversion was carried out in two steps: (*i*) scatterBrain was used to convert the SAXS/WAXS images to 1D patterns which were then partially converted to absolute intensities using eq. 2.18, considering the calibration factor ($CF = 0.000377963$ $s^{-1}mm^{-1}$, see §2.2.3), the transmission ($\tau_{\text{s, scan \#}} = A_{\text{DS, scan \#}}$) and assuming $d_{\text{ss, scan \#}} = d_{\text{st}}$, and (*ii*) MATLAB code (see Appendix E) was written to subtract the background (BG_{SS}), complete the conversion to absolute intensity considering the specimen solid thickness for each scan number ($d_{\text{st}}/d_{\text{ss, scan \#}}$, where for the standard glassy carbon d_{st} is 0.1055 cm), remove data points corrupted by second-order scattering effects, and change the unit of q (from $Å^{-1}$ to nm^{-1}) and I_{Abs} (from cm^{-1} to m^{-1}). See Fig 2.12 for a 3D representation of the SAXS patterns for $NaAlH_4$ decomposition.

The 3D surface graphs for *in situ* ($NaAlH_4$ and $NaMgH_3$ decompositions) relative partial porosity, φ_i, distributions were obtained by a McSAS analysis. In these analyses, due to software limitations for multi-pattern analysis, every scan was required to have the same scattering length density. For example, for the $NaAlH_4$ decompositions (Fig. 2.13), the scattering length density of the final product, the Al scaffold, was used. Fig. 2.13 is presented to give an overview concerning the 3D surface result, highlighting that the vertical axis depends on φ_i, and the actual scattering length density, $\Delta\rho_{\text{SLD, scan \#}}$. When carrying out individual pattern analysis with McSAS, it was possible to provide the correct scattering length density for each individual pattern. Such results are reported in Fig. 5.14 and 5.17. However, the normalization of the partial porosity, φ_i, still remain an issue due to

the unknown total porosity, φ_{total}, which is variable across different scan numbers (Fig. 2.13). This is discussed further in Chapter 5.

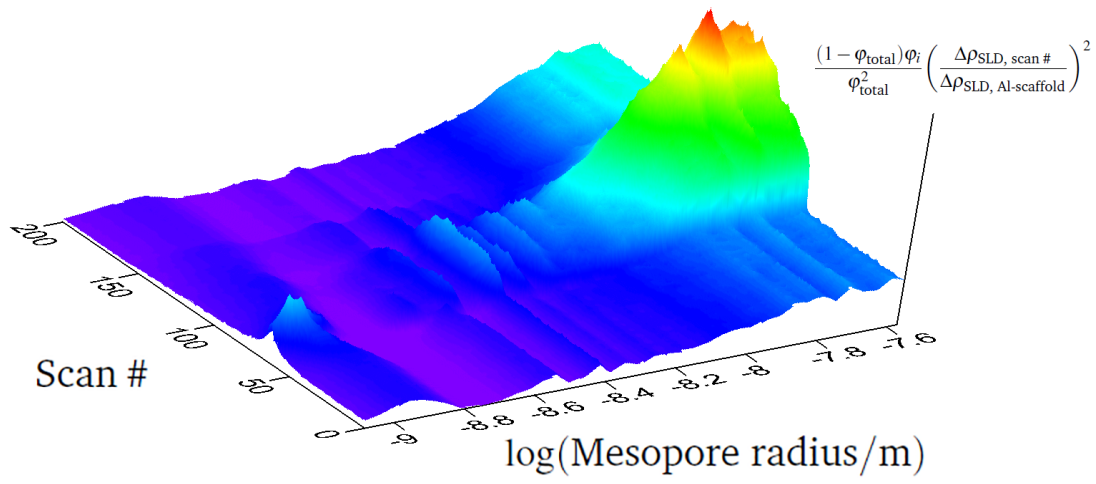

Figure 2.13: 3D surface graph of *in situ* (5 °C/min heating ramp, 2 scans/min) mesoporosity distribution obtained by McSAS analysis of absolute intensity SAXS patterns of $NaAlH_4$ decomposition.

2.3 Thermodynamic simulations

Thermodynamic calculations were performed using the software package HSC Chemistry 6.12 (Outotech Research). The software calculated the amount of products at equilibrium under isothermal and isobaric conditions, given the mole fractions and phases of the starting substances, by considering the reaction

$$\alpha A + \beta B + ... \longrightarrow \nu U + \omega W + ... \tag{2.39}$$

for each possible compound at each temperature step.

Repeating the process for the same pressure but at different temperatures (corresponding to different volumes of the closed system), provided starting phases, the quantitative phase pathway was simulated without taking into account any kinetic effects (Fig. 3.2 and 3.6). The thermodynamic quantities and heat capacity

coefficients (eq. 2.40) provided as input are listed in Table 2.2. In the CALPHAD method[153] the parameterized heat capacity of a compound is modelled by:

$$C_p(T) = A + B \times 10^{-3} \times T + C \times 10^5 \times T^{-2} + D \times 10^{-6} \times T^2 \tag{2.40}$$

where A, B, C and D are heat capacity coefficients. The heat capacity enables the entropy and enthalpy to be calculated respectively as

$$\Delta S = \int \frac{C_p(T)}{T} dT \quad ; \quad \Delta H = \int C_p(T) dT \tag{2.41}$$

The Gibbs free energy is then calculated as

$$\Delta G(P,T) = \Delta H(P,T) - T\Delta S(P,T) \tag{2.42}$$

$$\Delta G^{\ominus}_{\text{reaction}}(P,T) = -RT \ln\left(K_{\text{eq}}\right) \tag{2.43}$$

The equilibrium constant, K_{eq}, is given by

$$K_{\text{eq}} = \frac{[U]^{\nu}[W]^{\omega}\ldots}{[A]^{\alpha}[B]^{\beta}\ldots} \tag{2.44}$$

where the square brackets represent the concentration or partial pressure of the particular compound.

Using the van't Hoff equation of equilibrium H_2 pressure as a function of temperature (eq. 2.45), the phase diagrams of $NaAlH_4$ and $NaMgH_3$ sorption, over different steps of decomposition were obtained (Fig. 1.3 and 1.5).

$$\ln\left(\frac{P_{H_2}}{1\text{ bar}}\right) = -\frac{\Delta H^{\ominus}_{\text{reaction}}(P,T)}{RT} + \frac{\Delta S^{\ominus}_{\text{reaction}}(P,T)}{R} \tag{2.45}$$

HSC software uses the relations expressed in equations 2.40 – 2.45 to calculate the activity and mole (%) of each substance.

At low pressure and high temperature compared to standard conditions, a gas behaves similarly to an ideal gas. In such conditions, the isobaric heat capacity

Table 2.2: Thermodynamic quantities and heat capacity coefficients (A, B, C and D) of compounds and elements involved in $NaAlH_4$ and $NaMgH_3$ decompositions.

Phase	$\Delta H^{\ominus}$ (kJ/mol)	$\Delta S^{\ominus}$ (J/mol K)	A (J/mol K)	B (kJ/mol K^2)	C (10^{-5} J K/mol)	D (MJ/mol K^3)	T(K) range at 1 bar	Ref.
$NaAlH_4$ solid	−116.3	83.0	84.1	30.8	−8.1	12	298.15 – 700	36
Na_3AlH_6 solid	−238.8	163.0	138.3	101.5	−17.9	12	298.15 – 700	36
NaH solid	−56.4	40	31.4	35.3	−4.9	0.0075	298.15 – 700	36
Al solid (FCC)	0	28.3	24.4	3.8	−1.5	5.3	298.15 – 700	36
H_2 gas	0	130.7	31.6	−5.5	−1.1	4.5	298.15 – 1000	36
Na solid (BCC)	0	51.3	51.0	−144.6	−2.6	261.8	200 – 371	36
	−0.2	50.7	38.1	−19.5	−0.7	10.2	371 – 2300	36
Na gas	107.5	153.7	21.0	−0.4	−0.13	0.14	298.15 – 2700	155–157
Na liquid	2.6	58.2	51.0	−144.6	−2.6	261.8	200 – 371	36
	2.4	57.7	38.1	−19.5	−0.7	10.2	371 – 2300	36
$NaMgH_3$ solid	−142.44	75.745	33.6	122.54	0	0	298.15 – 2000	47
MgH_2 solid	−77.3	26.39	2.87	110.6	0.686	0	298.15 – 2000	47
NaH solid	−56.98	39.65	48.69	0.52	−12.65	−0.108	298.15 – 2000	47
Mg solid (HCP)	0	32.7	26.185	−0.9716	−1.58	8.63	298.15 – 2000	158

coefficients can be approximated as constant, independent of temperature, see eq. 2.46[¶ 154].

$$\left[\frac{\mathrm{d}C_p}{\mathrm{d}P}\right]_T = \left[\frac{\mathrm{d}\left(\frac{T\mathrm{d}S}{\mathrm{d}T}\right)_P}{\mathrm{d}P}\right]_T = \left[\frac{\mathrm{d}\left(\frac{\mathrm{d}G^2}{\mathrm{d}^2T}\right)_P}{\mathrm{d}P}\right]_T = \left[\frac{\mathrm{d}\left(\frac{\mathrm{d}G}{\mathrm{d}P}\right)_T^2}{\mathrm{d}^2T}\right]_P = \left[\frac{\mathrm{d}V^2}{\mathrm{d}^2T}\right]_P = 0 \qquad (2.46)$$

2.4 Scanning electron microscopy

2.4.1 SEM principles

Scanning Electron Microscopy (SEM) uses an energetically well-defined and highly focused electron beam for observing surface morphology of a material. Magnetic lenses are used to form the beam and a set of scan coils are used to raster the beam over the surface of the sample (see Fig. 2.14(b)). The signals from each point of the sample (see Fig. 2.14(a)) are used to produce an image. Secondary

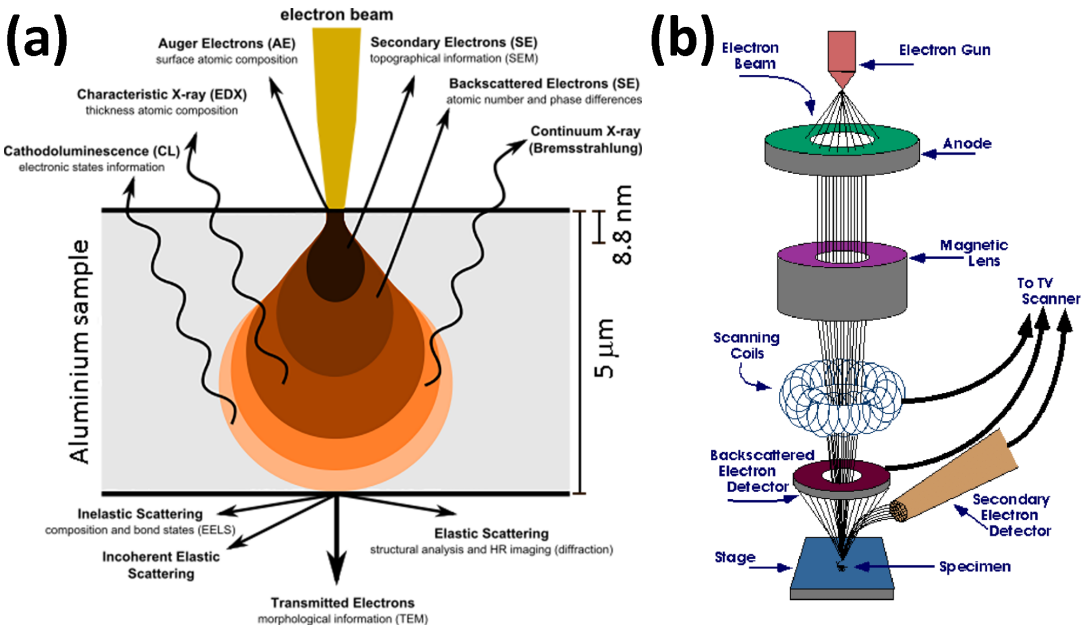

Figure 2.14: (a) Schematic representation of signals emitted from different sections of an Al sample volume interacting with the primary electron beam of 5 keV[159]. (b) Simplified layout of a SEM[160].

[¶]The notifications $)_T$, $]_T$ and $)_P$, $]_P$ mean that the derivatives ($\mathrm{d}^x/\mathrm{d}^xP$ and $\mathrm{d}^x/\mathrm{d}^xT$) are applied at constant temperature and pressure, respectively.

electrons are electrons generated as ionization products and they are emitted from atoms very close to the specimen surface. They are called 'secondary' because they are generated by electrons of the primary beam. For instance, a primary electron beam of 5 keV interacting with an aluminium specimen, will have an inelastic mean free path of 8.8 nm. Consequently, SEM can produce high-resolution images of a sample surface, revealing details on the order of the mean free path[161]. A simplified layout of an SEM is shown in Fig. 2.14(b). The electrons are initially produced via a thermionic or field emission from an electron gun focused down to a spot on the specimen by a system of ion optics (*i.e.* electromagnetic coils). The distance from the final pole piece of the lens to the exposed surface of the sample when the image is in focus is referred to as the working distance. Emitted electrons are collected by a secondary electron detector. Successively, an image of the sample surface is reconstructed by measuring secondary electron intensity as a function of the primary beam position[160].

2.4.2 Apparatus and experimental setup

Scanning Electron Microscopy (SEM) was performed using a Zeiss Neon 40EsB. This study largely used secondary electrons to obtain high-resolution images. The images were taken at 5 kV at various magnifications corresponding to a field of view in the range of 4 to 40 μm. Working distances employed were between 4 and 11 mm and the beam aperture size was 30 μm.

2.4.3 Sample preparation and holder

Specimens were broken, and the exposed fracture surfaces were imaged. The specimens were placed onto carbon tape mounted on an aluminium stub and transferred into the SEM chamber in a custom-made shuttle, minimising exposure to air.

2.5 Volume determination techniques

It was important to calculate the Al and $NaAlH_4$ total scaffold densities in order to find out their respective total porosities, see eq. 2.47. Although the scaffold masses were measured directly using a scale, measuring the volume of the Al scaffold was more complicated due to its irregular and small size (Fig. 3.4(b)). The total porosity was calculated from the measured total density and theoretical crystalline density of the scaffolds obtained by using the wt% (w_α) and crystal density (ρ_α) of each phase, reported in Fig. 3.5 and Table 3.3.

$$\varphi_{\text{total}}(\%) = 100\frac{V_{\text{total pore}}}{V_{\text{total}}} = 100\left(1 - \frac{\rho_{\text{total}}}{\rho_{\text{crystal}}}\right) \quad ; \quad \rho_{\text{crystal}} = \sum_{\alpha}^{\#\text{ of phases}} w_\alpha \rho_\alpha \tag{2.47}$$

2.5.1 Volume measurement using a caliper

The volumes of the entire pellets (Fig. 3.4(a) and (b)) before and after sintering were calculated by measuring the pellet dimensions using a caliper. The top and the bottom of the pellet were smoothed before measuring in order to create a more regular shape. Despite the pellet being smoothed the uncertainty of these volume measurements was dominated by the irregular shape of the pellet and not by the uncertainty of the caliper itself (± 0.1 mm). Thus, the uncertainty was not determined because it could only rely on a subjective estimation based on the appearance of the irregular shape of the smoothed pellet.

2.5.2 Volume measurement using 3D object reconstruction

In order to improve the accuracy of the volume measurements, a 3D object reconstruction was attempted. The volume measurements using the 3D object reconstruction technique consisted of assembling/reconstructing pictures taken from different angles of an object into a 3D image[162]. The pictures were taken inside the glovebox at ≃ 4 cm from the sample using a 12 MP (4:3) smartphone camera

mounting a macro lens. The sample was placed vertically on a millimeter paper used as a reference (Fig. 3.4(b)). The volume calculation of the entire pressed pellet was obtained by using Autodesk ReCap 360 in combination with AutoCAD Architecture 2016[163,164]. Unfortunately, most of the pictures were not properly focused and relying only on a limited number of high-quality pictures, it was only possible a partial reconstruction of the 3D mesh, see Fig. 3.4(c). The technique was proven to be reliable by successfully measuring a rectangular parallelepiped shape of known dimension ($V_{\text{caliper}} = 1540 \pm 50$ mm^3) with an uncertainty of $\approx 3\%$ ($V_{\text{3D}} = 1590$ mm^3).

2.6 N_2 sorption technique

The nitrogen adsorption/desorption technique was used to measure the specific surface area and the pore size distribution of magnesium and aluminium scaffolds using the Brunauer-Emmett-Teller (BET)[165–167] and Barrett-Joyner-Halenda (BJH)[168] analysis methods, respectively.

2.6.1 Apparatus setup and procedure

The measurements were performed at −195.79 °C using a Micromeritics ASAP 3020 apparatus (Micromeritics, Norcross, GA, USA). In order to obtain specific properties, specimen masses were measured. The sample tube was degassed for 12 hours before conducting the measurements. Prior to degassing, the sample was exposed for approximately one second to air and thus to oxygen. Isothermal adsorption/desorption cycles were performed over 79 and 19 steps for Al and Mg porous scaffold, respectively. At each step, the same known amount of nitrogen gas was respectively introduced or removed into or from the system. The pressure at the end of each step was measured once the nitrogen gas and liquid nitrogen, in the sample, reached a dynamic equilibrium. The specific adsorbed volume (V_s), converted to standard temperature and pressure (STP) conditions,

was calculated considering a close-packed hexagonal arrangement of the liquid nitrogen at −195.79 °C having a density of 0.807 g/cm^3. The first stage in the interpretation of a physisorption isotherm is to identify the isotherm reversibility type and hence the nature of the adsorption process(es): monolayer-multilayer adsorption, capillary condensation or micropore filling. In Fig 2.15 (a) the types of isotherms and (b) the hysteresis loops that they may present are plotted. The pressure on the x-axis is relative to the saturation pressure (P_0).

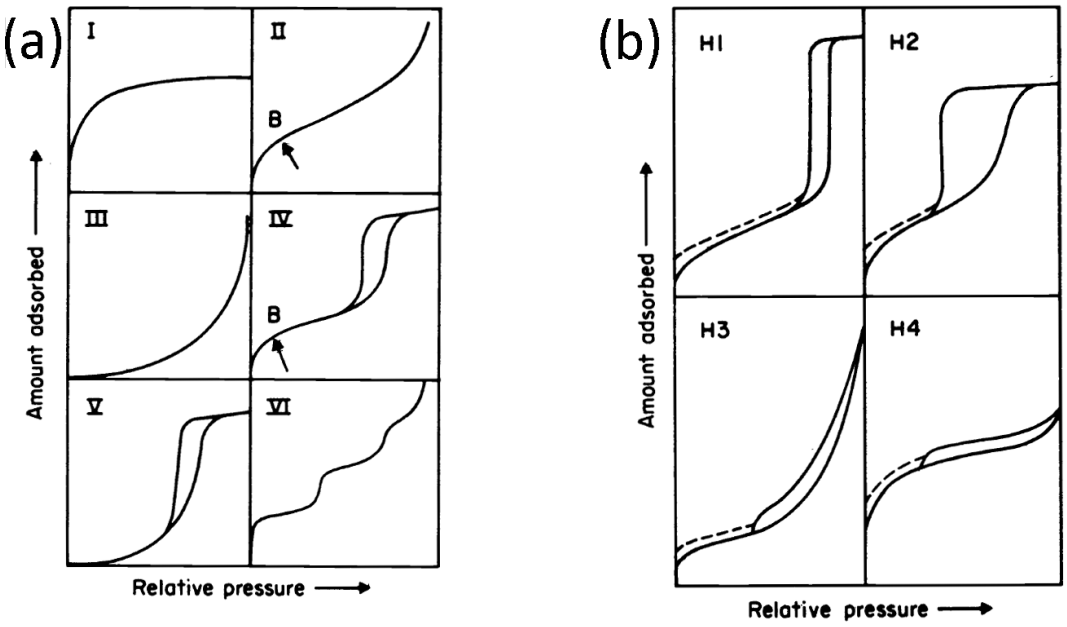

Figure 2.15: The types of physisorption isotherms are: I adsorption in micropores, II unrestricted monolayer-multilayer adsorption, III weak adsorptive-adsorbent interactions, IV monolayer-multilayer adsorption and capillary condensation, V weak interactions and capillary condensation, VI stepwise multilayer adsorption on a nonporous non-uniform surface (b) the type of hysteresis loops are: H1 well defined cylindrical pore channels, H2 disordered pores (pore blocking, percolation phenomena), H3 non-rigid aggregates of plate-like particles (slit-shaped pores) and H4 narrow slit pores including pores in the micropore region[167].

Type I isotherms are dominated by the effect of adsorption in micropores that is limited to a few molecular layers (*e.g.* activated carbons, molecular sieve zeolites, and certain porous oxides). The Type II isotherm is the normal form of isotherm obtained with a non-porous or macroporous adsorbent representing

unrestricted monolayer-multilayer adsorption. Point B, the beginning of the almost linear middle section of the isotherm, is often taken to indicate the stage at which monolayer coverage is complete and multilayer adsorption is about to begin. In Type III isotherms, adsorptive-adsorbent interactions play an important role (*e.g.* nitrogen on polyethylene). Characteristic features of the Type IV isotherm are its hysteresis loop, which is associated with capillary condensation taking place in mesopores (pores in the 2 – 50 nm size), and the limiting uptake over a range of high P/P_0. The initial part of the Type IV isotherm is attributed to monolayer-multilayer adsorption since it follows the same path as the corresponding part of a Type II isotherm obtained with the given adsorptive on the same surface area of the adsorbent in a non-porous form. Type IV isotherms are given by many mesoporous industrial adsorbents. The Type V isotherm is related to the Type III isotherm in that the adsorbent-adsorbate interaction is weak, but the hysteresis loop feature is associated with capillary condensation. The Type VI isotherm represents stepwise multilayer adsorption on a non-porous non-uniform surface (*e.g.* Ar or Kr on graphitized carbon blacks at liquid nitrogen temperature)[167].

Hysteresis loops (see Fig. 2.15(b)) appearing in the multilayer range of physisorption isotherms is usually associated with capillary condensation in mesopore structures. The wider the pore size distribution the less sharp is the pore condensation step. The Type H1 loop is associated with well-defined cylindrical pore channels, type H2 with disordered pores (pore blocking, percolation phenomena), type H3 with non-rigid aggregates of plate-like particles (slit-shaped pores), while type H4 with narrow slit pores including pores in the micropore region[167].

2.6.2 BJH method of analysis

The pore size distribution and cumulative pore volume in the mesopore size range were calculated using the Barrett-Joyner-Halenda (BJH)[168] method from

the desorption branch of the isotherm reflecting the equilibrium phase transition. The BJH method relates the specific volume ($\Delta V_{s,\,n}$) previously occupied by the

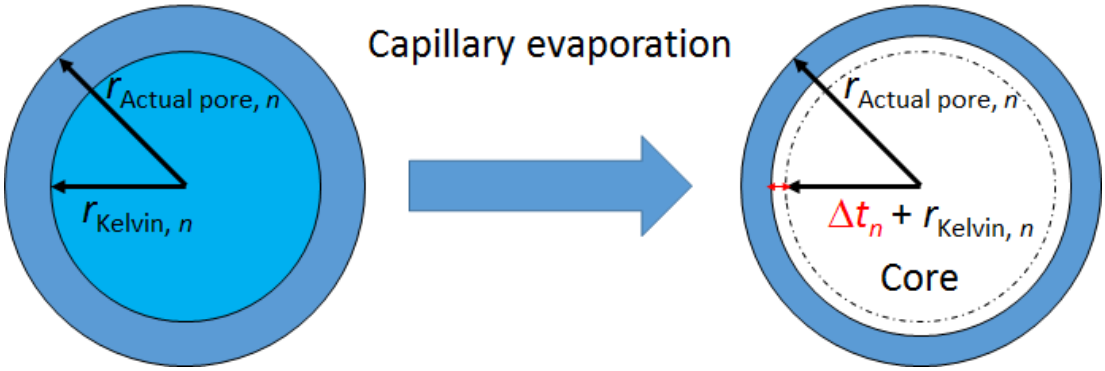

Figure 2.16: Nitrogen contained within a pore. Light blue represents nitrogen removed during capillary evaporation. Dark blue represents the remaining nitrogen adsorbed on the pore surfaces. The contribution to the specific volume ($\Delta V_{s,\,n}$), in a step from the $(n-1)^{\text{th}}$ to n^{th} points in the N_2 desorption isotherm, is due to two components: the specific volume of nitrogen (*i*) removed by capillary evaporation from the cores ($r_{\text{Kelvin, }n}$), and (*ii*) desorbed from the surfaces (Δt_n) of the average size pores ($r_{\text{actual pore, }n}$) which underwent capillary evaporation, during either this step, or previously.

measured quantity of gas desorbed during the step from the $(n-1)^{\text{th}}$ to n^{th} points in the N_2 desorption isotherm ($\Delta P_n/P_0$), to the specific volume occupied by the pores of average size, $r_{\text{actual pore, }n}$, which undergo capillary evaporation during this step. This allows a pore size distribution to be calculated.

The quantity of gas desorbed during the n^{th} step is composed of a quantity equivalent to the liquid cores from capillary evaporation during the n^{th} step ($r_{\text{Kelvin, }n}$), and a quantity desorbed from the pore surfaces of those cores which were evaporated either during the n^{th} step (Δt_n), or at some previous step ($\Delta t_m, \forall m < n$)[169] — see Fig 2.16. The relation between relative pressure (P/P_0) and core radius (r_{Kelvin}) is given by the Kelvin equation[168,170]:

$$\ln \frac{P}{P_0} = \frac{-2\gamma V_{\text{liq}}}{r_{\text{Kelvin}} RT} \tag{2.48}$$

where R (8.314 kg m^2/s^2 K mol) is the gas constant, γ (8.88 $\times$ 10^{-3} kg/s^2) is the surface tension of liquid nitrogen, V_{liq} (34.6 $\times$ 10^{-6} m^3/mol) is the liquid molar volume of N_2 and T (−195.79 °C) is the N_2 boiling point. The dynamic thickness (t) of the remaining adsorbed layer at this relative pressure is calculated from the Halsey thickness equation (see eq. 2.49) for cylindrical (slit) shape pores[‖]. Finally, the actual average radius of the pores, which undergo capillary evaporation, as a function of relative pressure is, thus, obtained:

$$r_{\text{actual pore}}(\text{Å}) = r_{\text{Kelvin}} + t = \overbrace{\frac{-9.56}{\ln\frac{P}{P_0}}}^{\text{Kelvin equation}} + \overbrace{3.54\left(\frac{-5}{\ln\frac{P}{P_0}}\right)^{\frac{1}{3}}}^{\text{Halsey equation}} \tag{2.49}$$

2.6.3 BET method of analysis

The following Langmuir model of gas adsorption extended to a multi-layer was adopted to measure the specific surface area of the samples[165–167]. It is an empirical model that represents the general shape of the actual isotherm, $V_s(P/P_0)$, and its linear form is:

$$\frac{1}{V_s\left(\frac{P_0}{P}-1\right)} = \underbrace{\frac{1}{V_m C}}_{\textit{intercept}} + \underbrace{\frac{C-1}{V_m C}}_{\textit{slope}}\frac{P}{P_0} \tag{2.50}$$

where V_m is the monolayer specific volume at STP, occupied if the entire adsorbent surface is covered and V_s is the actual multilayer specific volume adsorbed. P/P_0 is the relative pressure. C is the constant adsorption coefficient which represents the gas-sample surface physisorption interaction. The adsorption coefficient is related exponentially to the enthalpy (heat) of adsorption of the first adsorbed layer (V_m)[171]. However, it is generally recognised that, although the value of C may be used to characterise the shape of the isotherm in the BET range, it does not provide a quantitative measure of enthalpy of adsorption[167,171]. V_m was obtained by fitting eq. 2.50 versus P/P_0 ($V_m = 1/[slope + intercept]$) at relative pressures

[‖]The assumption of cylindrical pore shape is justified by the results from the SEM images in Figures 4.1 and 5.1.

between 0.10(5) and 0.3(1)[††] relying on the plot of the isotherm V_s as a function of P/P_0 for magnesium and aluminium scaffolds (See Fig. 4.2 and 5.2 respectively). Finally, the total surface area S_t is given by:

$$S_t = \frac{V_m N_{av} A_m}{V_l} \tag{2.51}$$

where N_{av} (6.022×10^{23} mol^{-1}) is Avogadro's constant and V_l (22414 mL) is the volume of a mole of an ideal gas under STP conditions. A_m ($0.162 \pm 20\%$ nm^2)[172] is the cross section of spherical N_2 adsorbed, forming a close-packed hexagonal arrangement at -195.79 °C. Because C values obtained are between 60 and 70, the monolayer-multilayer formation is operative and is not accompanied by micropore filling, which is usually associated with an increase in the value of C (> 200)[167]. The BET method is unlikely to yield a value of the actual surface area if the isotherm is either Type I or Type III; but Type II and Type IV isotherms are, in general, amenable to the BET analysis, provided that the value of C is neither too low nor too high, and that the BET plot is linear in the region of the isotherm containing Point B (see Fig. 2.15). The uncertainty for the specific surface areas, calculated exclusively from the uncertainty of the fitted parameters, is $\pm$ 0.1 m^2/g. Such uncertainty is based on the assumption that the monolayer is a close-packed structure, having a cross section (A_m) of spherical N_2 adsorbed of 0.162 nm^2 at -195.79 °C. With a wide range of adsorbents, it appears that the use of this value leads to BET specific surface areas which are within 20% of the true specific surface areas. The existence of a strictly constant value of A_m (N_2) is unlikely, however, and a growing amount of evidence suggests that it may vary by up to approximately 20% from one surface to another[167,173].

[††]Which corresponds to a monolayer coverage (V_s/V_m) in the range of 0.50 and 1.50.

2.7 Sievert's apparatus techniques

A Sievert's apparatus consists of multiple compartments of well-known volumes that are connected by valves[174].

Sievert's apparatus techniques such as Temperature Programmed Desorption (TPD) and TPD-Mass Spectrometry (TPD-MS) were employed to detect the wt% desorbed and wt% desorption rate of H_2, respectively, as a function of temperature, for a constant heating rate. While closed system TPD measurements are affected by kinetic and thermodynamic combined effects, under dynamic vacuum TPD-MS measurements are only affected by kinetic effects.

2.7.1 Temperature Programmed Desorption (TPD)

2.7.1.1 The principles of the technique

Wang-Suda[175] first and Luo-Gross[73] have provided simple empirical models to describe the H_2 desorption rate during $NaAlH_4$ decomposition based on an Arrhenius analysis using Sievert's experimental apparatus. It was assumed that each step of the decomposition of $NaAlH_4$ is independent, meaning that for each decomposition step only a single reactant phase contributes to the desorption rate. In principle, such an approximation is applicable only when each step of decomposition results in a visibly separated peak in the hydrogen desorption rate pattern (see Fig. 1.6)[40]. For a single-step chemical reaction, the modelled H_2 net desorbed rate, $\mathrm{d}N_{H_2}/\mathrm{d}t$, adopted by Luo-Gross[73] is given by:

$$\frac{\mathrm{d}N_{H_2}}{\mathrm{d}t}(T) = (N_{H_2,\mathrm{plateau}} - N_{H_2}(T)) \ln\left(\frac{P(T)}{P_{\mathrm{plateau}}}\right) \nu \mathrm{e}^{-\frac{\Delta E_{\mathrm{des}}}{RT}} \tag{2.52}$$

The terms $N_{H_2,\mathrm{plateau}}$ and P_{plateau} are respectively the total amount and pressure of H_2 released across a single reaction step and correspond to the amount and pressure at thermodynamic equilibrium[21]. These terms take into consideration thermodynamics effects and are approximated to be independent of temperature.

In eq. 2.52, the kinetic effect is considered introducing the concept of rate constant, ν, and activation energy of desorption, ΔE_{des}, that were approximated to be independent of temperature and number of H_2 molecules desorbed, N_{H_2}.

2.7.1.2 Apparatus and experimental setup

Temperature programmed desorption (TPD) measurements were undertaken on a computer controlled Sievert's/volumetric apparatus[176]. The sample temperature and pressure were recorded every 30 seconds using a K-type thermocouple with a precision of 0.1 °C at 300 °C and a digital pressure transducer (Rosemount 3051S) with a precision/accuracy of 14 mbar. Hydrogen desorption data were obtained in the temperature range of room temperature to 300 °C with a ramp rate of 2 °C/min. The temperature was, then, kept constant at 300 °C for 10 hours. During the desorption, each sample produces a different final back pressure due to the different total amount of H_2 initially present in the sample.

2.7.1.3 Volume calibration

The total closed volume system of a custom-made Sieverts apparatus at Curtin University, referred to as 'the rig', comprises a removable reactor plugged into a stationary part. The stationary part of the rig, referred to as 'the reference', was contained wholly inside a case covered by panels, referred to as 'the box'. The apparatus was divided into three connected volume components characterised by different temperatures:

- The reference volume ($V_{ref} = 16.4$ cm^3) and the connected part volume of the reactor ($V_{conn} = 1.58$ cm^3) inside the box where the temperature was monitored ($T_{box} \simeq 28$°C).
- The reactor side volume outside the box and outside the furnace ($V_s - V_{na} = 7.98$ cm^3 $- 2.58$ cm^3) where the ambient temperature was monitored ($T_{ambient} \simeq 22$°C).

- The non-ambient reactor side volume not occupied by the volume of sample ($V_{na} - V_{sample}$)[‡‡] inside the furnace where the temperature was monitored ($T_{furnace/sample}$).

The reference volume (V_{ref}) and connected part volume of the reactor (V_{conn}) inside the box were calibrated using a previously prescribed methodology[177]. In order to calibrate the volume of the reactor outside the box (V_s), the following procedure was followed:

- The valve inside the box that connected the reference and the reactor was closed.
- An amount of (< 1 bar pressure) hydrogen gas was let into the reference volume from the laboratory hydrogen system.
- The reference volume was isolated by closing the valve connecting it to the laboratory hydrogen system.
- From the known volume of the reference (V_{ref}) and the measured pressure in the reference, it was possible, using the ideal gas law, to calculate the moles of hydrogen in the reference volume.
- The valve inside the box connecting the reference and the reactor was opened.
- Measuring the new pressure, knowing the volumes of the reference (V_{ref}), of the reactor inside the box (V_{conn}), the temperature inside the box ($T_{box} \simeq 28$°C) and the ambient temperature ($T_{ambient} \simeq 22$°C), it was algebraically possible to calculate the reactor side volume (V_s).

Successively, part of the reactor (V_{na}) was inserted up to a specific depth into a furnace in order to calibrate such non-ambient reactor side volume (V_{na}) for

[‡‡]The volume of the sample (V_{sample}) was calculated from the mass of the sample and the density of the sample obtained from phases quantification analysis. However, for every TPD measurements the volume of the sample was found to be negligible compared with the non-ambient reactor side volume (V_{na}).

a furnace temperature of 550 °C. Every TPD measurement was performed by inserting the reactor up to the same depth inside the furnace. The procedure above was repeated except for the last step that was replaced by the following step:

- Measuring the new pressure, knowing the volumes of the reference (V_{ref}), of the reactor inside the box (V_{conn}), of the reactor side volume (V_s), the temperature inside the box ($T_{box} \simeq 28$°C), the ambient temperature ($T_{ambient} \simeq 22$°C) and the non-ambient temperature ($T_{furnace/sample} \simeq 550$°C), it was algebraically possible to calculate the non-ambient reactor side volume (V_{na}).

2.7.1.4 Quantification of H_2 content in the sample

Knowing the previously calibrated volumes and the temperatures for each component of the system, it was possible to calculate the moles of H_2 desorbed from the sample from the measured H_2 pressures. The number of H_2 moles of the system was calculated summing the number of H_2 moles from each of the three volume components of the rig at different temperatures. Because the final pressure for every sample was under 2 bar (at 300 °C), the number of moles of H_2 of the system were calculated using the following ideal gas law:

$$n_{H_2} = \frac{P_{H_2}}{R}\left(\frac{V_{ref} + V_{conn}}{T_{box}} + \frac{V_s - V_{na}}{T_{ambient}} + \frac{V_{na} - V_{sample}}{T_{furnace/sample}}\right) \tag{2.53}$$

It was possible to convert the number of moles of H_2 to wt% of H_2 because every sample was weighed prior to TPD measurements. Two $NaAlH_4$ powder samples were run as standards (+ 2 mol% $TiCl_3$ ball-milled and as provided by the manufacture).

The initial $NaAlH_4$ content for both standards was calculated using two independent methods. The first method is based on the information acquired from the final/asymptotic TPD values of the H_2 measured pressure considered desorbed across the first two steps of decomposition and the initial sample weight.

The second method is based on the theoretical value for the wt% of $NaAlH_4$ of the starting material as provided by the manufacturer considering also the 97.9% $NaAlH_4$ hydrogen evolution, see Appendix F. For the + 2 mol% $TiCl_3$ ball-milled standard, the quantity of $TiCl_3$ added was also considered. The two independent estimations for $NaAlH_4$ content were in agreement for both standards (under 0.1 wt% uncertainty), proving that the $NaAlH_4$ content for non-standard samples can be calculated relying on the method based on TPD measurements.

2.7.2 TPD-Mass Spectrometry (TPD-MS)

2.7.2.1 The principals of the technique

For systems under low H_2 pressure conditions compared with their equilibrium pressure ($P(T) << P_{eq}(T)$), the kinetic terms in eq. 2.52 are dominant with respect to the thermodynamic terms that are responsible for H_2 reabsorption. Thus, eq. 2.52 is further simplified to model TPD-MS measurements and it is given by:

$$\frac{dN_{H_2}}{dt}(T) = (N_{H_2,eq} - N_{H_2}(T))\,\nu_1 e^{-\frac{\Delta E_{des}}{RT}} \tag{2.54}$$

where ν_1 is the rate constant. It is worth noting that $N_{H_2,eq}$ is approximated as being independent of temperature for the TPD-MS measurements reported in this thesis. This approximation is justified by the results from the literature[74,75,79] presented in Fig. 1.6, where the hydrogen equilibrium ($dN_{H_2,\,eq}/dT$) and measured (dN_{H_2}/dT) desorption rate patterns do not overlap each other.

2.7.2.2 Apparatus and experimental setup

Measurements proportional to the change in hydrogen pressure (dP_{H_2}/dt), were performed by Temperature Programmed Desorption-Mass Spectrometry (TPD-MS) using a Stanford Research Systems (SRS) Residual Gas Analyser (RGA 300), consisted of a quadrupole mass spectrometer and an electronic control unit. The RGA analyses residual gases (regularly obtained from the system) by ionizing some

of the gas molecules (positive ions), separating the resulting ions according to their respective masses and measuring the ion currents at each mass. The system was connected to a turbo molecular pump and relies on a constant pumping speed designed to be higher than the desorption rates of the samples in order to avoid gas phase reabsorption. Thus, the thermodynamic effects are neglected and the monitored desorption rate ($\mathrm{d}N/\mathrm{d}t$) was assumed proportional to the pressure variation ($\mathrm{d}P/\mathrm{d}t$)[178]. The samples were initially evacuated at room temperature to a pressure of approximately 7×10^{-4} mbar for 8 hours and remained under dynamic vacuum for the duration of the experiment. The samples were heated from room temperature to 300 °C at 2 °C/min. The amount of hydrogen released was recorded every 68 s.

2.7.2.3 Habenschaden-Küppers analysis

In order to determine the activation energy for desorption from a single TPD-MS pattern, Habenschaden-Küppers (leading edge) analysis can be applied[179,180]. The method analyses the data points in a relatively short temperature interval at low temperature (leading edge) compared with the temperature corresponding to the first decomposition rate maximum ($T << T_{\mathrm{max}}$). In such a relatively short temperature interval, the desorption rate as a function of temperature is dominated by the contribution of the exponential term ($\exp[\Delta E_{\mathrm{des}}/RT]$). Thus, in the leading edge interval, the number of H_2 molecules desorbed during a single step reaction, $N_{H_2}(T)$, in eq. 2.54 can be neglected ($N_{H_2,\mathrm{eq}} - N_{H_2}(T) \simeq N_{H_2,\mathrm{eq}}$). Plotting the H_2 desorption rate in logarithmic scale versus $1/T$, it was possible, by fitting the data points in the leading edge interval with the model expressed in eq. 2.55[†], to obtain the value for the angular coefficient, $-\Delta E_{\mathrm{des}}/R$.

$$\ln\left(\frac{\mathrm{d}N_{H_2}}{\mathrm{d}t}(T)\right) = -\frac{\Delta E_{\mathrm{des}}}{RT} + \ln N_{H_2,\mathrm{eq}} + \ln \nu_1 \tag{2.55}$$

[†] $\mathrm{d}N_{H_2}/\mathrm{d}t$ and ν_1 have to be considered dimensionless because both multiplied by the same generic temporal unit of measure before applying the ln.

The disadvantage of the method is that the desorption rate at the leading edge temperature interval is characterised by a low accuracy due to the scarce number of desorption event recorded per second[179].

Chapter 3

Sample Preparation and Phase Quantification

The materials and their precursors were handled and stored inside an argon (Ar)-filled glove box due to their high sensitivity to oxygen (O_2) and moisture (H_2O). The O_2 and H_2O levels were kept at less than 1 ppm to avoid sample oxidation and contamination[31,91].

3.1 Porous Mg scaffold

The starting materials, NaH (Sigma Aldrich, 95%) and MgH_2 (Alfa Aesar, 98%), molar ratio 1:1, were ball-milled under an argon atmosphere at room temperature, inside an Across International Planetary Ball Mill (PQ-N04) employing stainless steel vials. An equal number of 10 mm and 6 mm diameter stainless steel balls were used in a ball-to-powder mass ratio of 30:1. The ball mill rotational speed was 350 rpm, and the rotation direction was alternated across 12 intervals. At each interval, the powders were milled for 15 minutes with a 5 minute interval in between intervals, for a total effective milling time of 3 hours over an elapsed time of 4 hours. These settings were applied to minimise the temperature increase inside the vials and avoid thermal decomposition of the materials[31,33]. The final

product was then annealed overnight at 300 °C under 50 bar of H_2 which, according to Fig. 1.3, are thermodynamically favourable conditions to form $NaMgH_3$. The diffraction pattern of the as-prepared $NaMgH_3$ powder is presented in Fig. 3.1. It can be seen that $NaMgH_3$ was formed, while diffraction peaks corresponding to the starting material, NaH, are minor. The remaining NaH after annealing is 1.9(8) wt% according to Rietveld refinement analysis. Several pellets were produced by

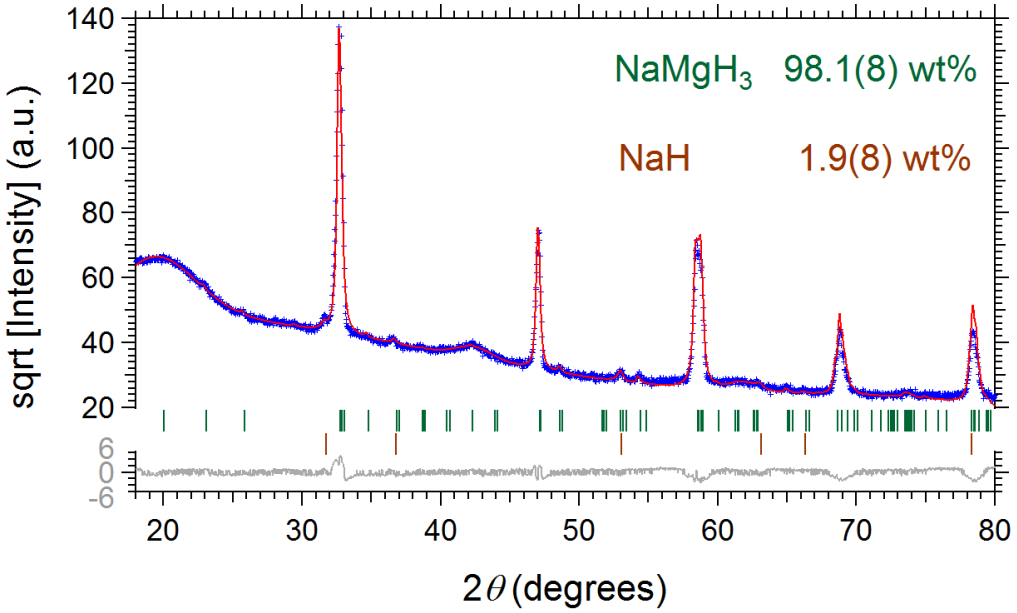

Figure 3.1: Rietveld refinement plot of the as-prepared $NaMgH_3$ powder. The blue plus symbols and the red line denote the observed and calculated intensities, respectively. Short vertical lines indicate the position of the Bragg reflections of the following compounds from top to bottom: $NaMgH_3$ (PDF 01-080-6771) and NaH (PDF 04-003-6873). X-ray wavelength $\lambda = 1.5406$ Å. Quantitative analysis with the uncertainty corresponding to one standard deviation as derived from Rietveld refinement[31,91].

compacting 0.1 g of as-prepared $NaMgH_3$ into an 8 mm stainless steel die. The pellets were compacted using a hydraulic press that applied an initial pressure of 442 MPa to the die for 10 minutes. The pellets were then extracted from the die and sintered inside a stainless steel reactor under a dynamic vacuum ($\simeq$ 0.03 mbar) at 450 °C using a Labec VTF 80/12 tube furnace. The reaction vessel was heated at 5 °C/min, left isothermal for 6 hours, and then was left to cool to room temperature.

During the sintering process, the desorbed H_2 gas was removed by the applied vacuum and the evaporated Na was captured by a trap placed inside the reactor. The applied sintering conditions are thermodynamically favourable (see Fig. 1.3) for the complete desorption of $NaMgH_3$ across the two-step reaction (see equations 1.1 and 1.2).

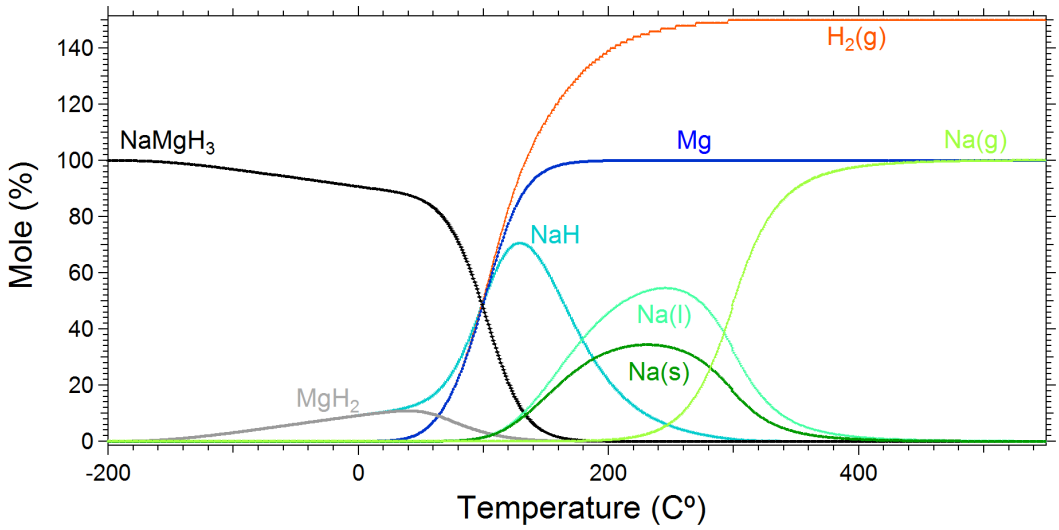

Figure 3.2: $NaMgH_3$ quantitative decomposition pathway simulation at local thermodynamic equilibrium and constant H_2 back pressure across the pathway. The simulation, performed by HSC software, used $NaMgH_3$ starting phase (100 mole %), thermodynamic phase parameters reported in Table 2.2 and $P = 1.5 \times 10^{-2}$ mbar. The constant pressure used corresponds to the dynamic vacuum pressure adopted for SAXS/WAXS experiments. On the *y*-axis, the mol% values are intended as relative mol% compared to the total initial $NaMgH_3$ moles.

Fig. 3.2 shows the simulation of the $NaMgH_3$ decomposition pathway at local thermodynamic equilibrium for a pressure (1.5×10^{-2} mbar) corresponding to the starting dynamic vacuum pressure adopted for SAXS/WAXS experiments[†]. The NaH liquid phase was not taken into consideration for the thermodynamic path way simulated in Fig. 3.2 and 3.6.

An indicative diffraction pattern of an as-prepared sample after the sintering

[†]The NaH liquid phase was not taken in consideration in the thermodynamic path way simulated in Fig. 3.2 and 3.6, but according to Abdessameud *et al.*[47] it would be expected to be comparable with the NaH solid phase.

process (referred to as the Mg scaffold) is presented in Fig. 3.3. The pattern is dominated by the presence of Mg (PDF 35-0821) phase diffraction peaks while no trace of remaining Na containing phases are visible. The broad peaks that correspond to MgO (PDF 45-0946) are most likely due to bulk impurities from the starting material[33,181] and not due to surface oxidation occurring during the sintering process or during XRD measurements. Unfortunately, for a system composed of a metal hydride infiltrated within this Mg scaffold, the oxidation reaction between the oxygen from the scaffold and the infiltrated metal hydride would cause a loss of hydrogen capacity upon absorption/desorption cycling. The

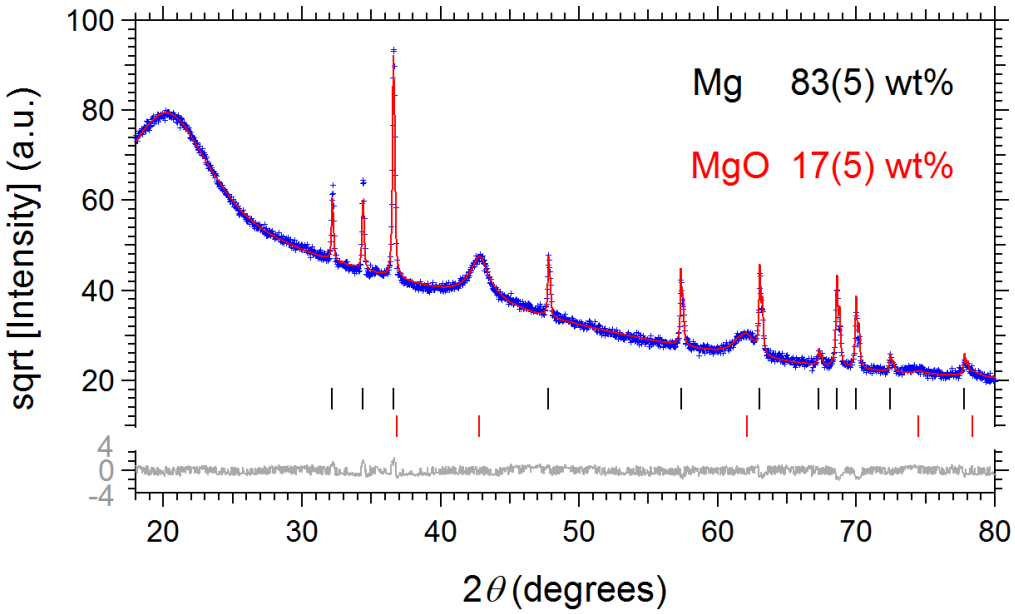

Figure 3.3: Rietveld refinement plot of the as-prepared Mg scaffold. The blue plus symbols and the red line denote the observed and calculated intensities, respectively. Short vertical lines indicate the position of the Bragg reflections of the following compounds from top to bottom: Mg (PDF 35-0821), and MgO (PDF 45-0946). X-ray wavelength $\lambda = 1.5406$ Å. Quantitative analysis with the uncertainty corresponding to one standard deviation as derived from Rietveld refinement[31,91].

sintering conditions (temperature at 450 °C), sintering time (3 hours) and initial mass of the sample (0.1 g) were chosen after being characterised using phase identification from XRD measurements. The characterisation was carried out

across every combination of three temperatures (400, 450 and 500 °C) and five sintering times (0.5, 1.5, 3 and 6 hours), with the chosen conditions resulting in the maximum sodium removal from the Mg scaffold at the lowest sintering temperature and the minimum sintering time.

3.2 Ti-enriched porous Al scaffold

The starting materials for the synthesis of the porous Al scaffold were $NaAlH_4$ (Sigma Aldrich, 97.9% hydrogen evolution[‡]) and $TiCl_3$ (Sigma Aldrich, purity $\geq$ 99.999%). Metal traces, mainly lead and aluminium, in the $NaAlH_4$ (Sigma Aldrich) were quantified from the Inductively Coupled Plasma (ICP) trace analysis reported in the certificate of analysis of $NaAlH_4$, as provided by the manufacturer, given in Appendix F. Assuming that a quarter[§] of the aluminium traces, as suggested by Felderhoff *et al.* [107], came from a partial first step (see eq. 1.3) decomposition of $NaAlH_4$, the concentration of Na_3AlH_6 was accordingly calculated, with the remainder attributed to $NaAlH_4$. The measured 97.9% hydrogen evolution, as provided by the manufacturer (see Appendix F), and the hydrogen evolution calculated relying on the estimated concentrations (Table 3.1 renormalized excluding $TiCl_3$) are in agreement, justifying the assumption behind the estimation of Na_3AlH_6. Afterward, the mol% of $NaAlH_4$ (Sigma Aldrich) was normalized taking into consideration the addition of + 2 mol% of $TiCl_3$. Finally, it was possible to quantify the phases of the starting materials in terms of mass contribution (wt%), which were calculated using the nominal molar mass of each phase. The results are shown in Table 3.1.

The starting materials, $NaAlH_4$ + 2 mol% $TiCl_3$, were ball milled using an Across International Planetary Ball Mill (PQ-N04) under an argon atmosphere at room temperature. An equal number of 10 mm and 6 mm diameter stainless steel balls

[‡]It is a measure of how much H_2 the $NaAlH_4$ (Sigma Aldrich) desorbed compared to the theoretical value. The 97.9% value of hydrogen evolution was also confirmed by TPD measurements.

[§][wt% of Al]/[wt% of Na_3AlH_6] = 4.

Table 3.1: $NaAlH_4$ + 2 mol% $TiCl_3$ pre-milled phase quantification.

Phase	mole %	wt%
$NaAlH_4$	95(1)	92.4(9)
Na_3AlH_6	0.17(1)	0.31(1)
Al	2.61(5)	1.27(1)
Trace metals	0.26(1)	0.65(1)
$TiCl_3$	1.95(2)[a]	5.4(1)

[a] + 2 mol% of $TiCl_3$ was added assuming that $NaAlH_4$ (Sigma Aldrich) was 100% pure.

were used in a ball-to-powder mass ratio of 30:1. The ball mill rotational speed was 350 rpm, and the rotation direction was alternated across 12 intervals. At each interval, the powders were milled for 15 minutes with 5 minute intervals in between intervals, for a total effective milling time of 3 hours over an elapsed period of 4 hours. These settings were applied to minimise the temperature increase inside the vials and avoid thermal decomposition of the materials. Supported by Rietveld refinement analysis (see Fig. 3.5), it was assumed that the entire amount of $TiCl_3$ reacts during ball-milling. Table 3.2 reports the phase quantification of the ball-milled starting materials based on the pre-milled phases reported in Table 3.1 and on the reaction presented in eq. 3.1, where the molar ratio between $TiCl_3$ and $NaAlH_4$, $x = 0.0205$, is obtained from Table 3.1.

Table 3.2: $NaAlH_4$ + 2 mol% $TiCl_3$ ball-milled phase quantification.

Phase	mole %	wt%
$NaAlH_4$	84.3(9)	87.1(9)
Na_3AlH_6	0.16(1)	0.32(1)
Al	8.0(1)	4.1(1)
NaCl	5.5(1)	6.2(1)
Ti	1.84(2)	1.68(2)
Trace metals	0.25(1)	0.66(1)

$$NaAlH_4 + xTiCl_3 \rightarrow (1-3x)NaAlH_4 + xTi + 3xNaCl + 3xAl + 6xH_2 \qquad (3.1)$$

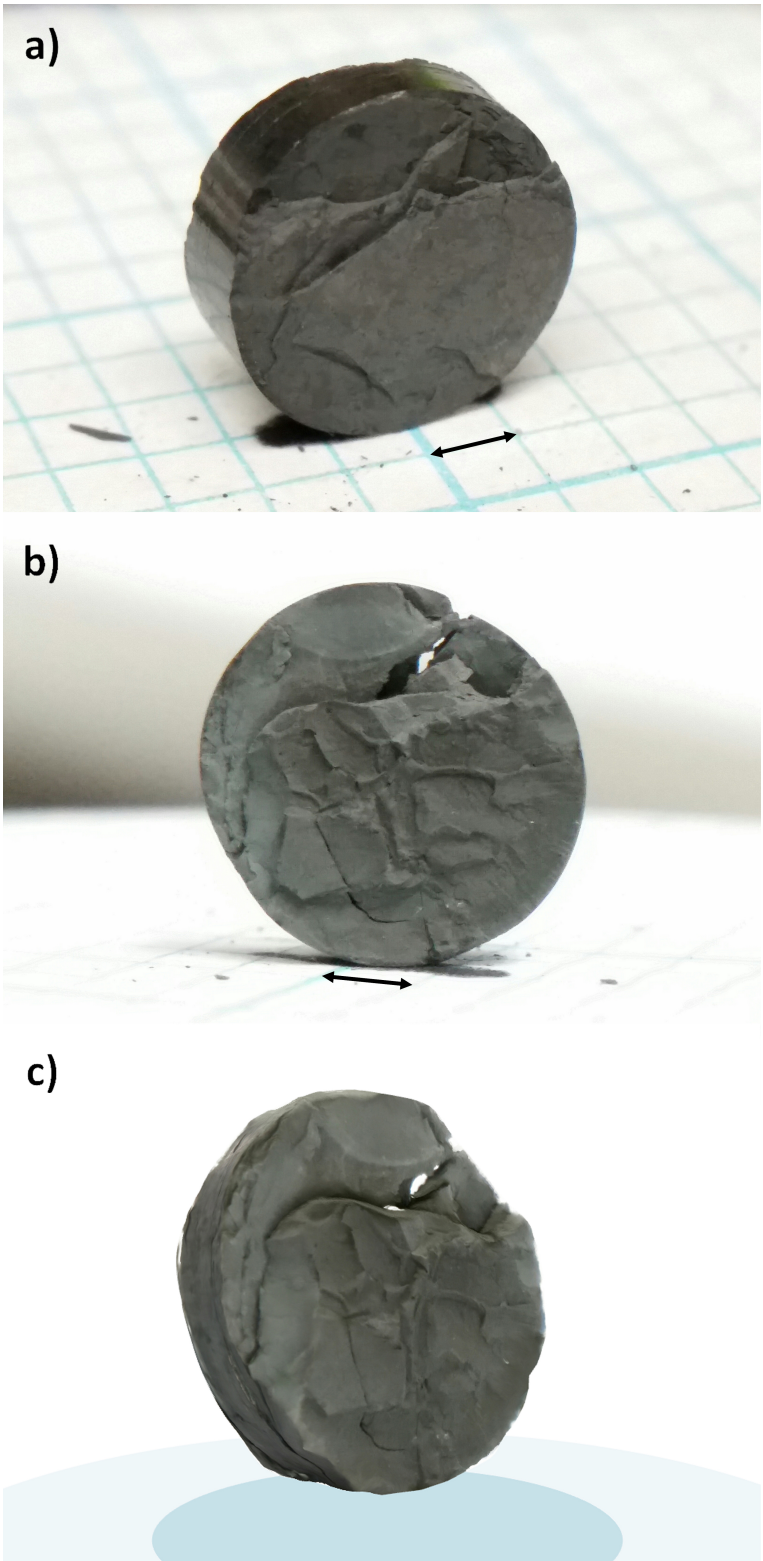

Figure 3.4: a) Picture of $NaAlH_4$ and b) Al scaffold respectively (⟷ 2 mm). c) 3D image of Al scaffold.

Several pellets were produced, each one by compacting 0.2 g of ball-milled starting materials in an 8 mm diameter stainless steel die (see Fig. 3.4(a)). The pellets were compacted using a hydraulic press that applied an initial pressure of 442 MPa to the die for 30 minutes. Rietveld refinement analysis was performed on *in situ* (see Fig. 5.10) and *ex situ* (see Fig. 3.5) diffraction patterns of the as-prepared $NaAlH_4/TiCl_3$ pellet. Ti-containing phases (*e.g.*, Ti, titanium hydrides, and various alloys with aluminium) were not detected, as the phases were either amorphous, as reported by Haiduc *et al.* [69] for synthesis temperatures lower than 175 °C, or because their characteristic diffraction peaks overlapped exactly with those belonging to Al. The enhanced relative quantity, determined from Rietveld refinement analysis, of Na_3AlH_6, Al, and NaCl present in the $NaAlH_4/TiCl_3$ pellet (see Fig. 3.5) compared to the quantity present in the ball-milled starting materials (see Table 3.2) suggests a partial first step decomposition of $NaAlH_4$ (see Fig. 3.6 and eq. 1.3); *i.e.* when the powder was compressed into a pellet, the pressure applied produced enough energy to partially trigger the first step of the decomposition pathway of $NaAlH_4$ [19,67,69,71]. The relative amount of $NaAlH_4$ decomposing during the compression of $NaAlH_4/TiCl_3$ ball-milled powder varied from sample to sample. The pellets were then extracted from the die and sintered inside a stainless steel reactor under dynamic vacuum ($\simeq$ 0.03 mbar) at 450 °C using a Labec VTF 80/12 tube furnace. The reaction vessel was heated at 5 °C/min, left isothermal for 12 hours, and then was left to cool to room temperature. During the sintering process the desorbed H_2 gas was evacuated and the evaporated Na was captured by a trap placed inside the reactor. The sintering conditions applied are thermodynamically favourable (see Fig. 1.5), to completely desorb $NaAlH_4$ across the three-step reaction (see equations 1.3 – 1.5). Fig. 3.6 shows the simulation of the $NaAlH_4$ decomposition pathway at local thermodynamic equilibrium for a pressure (7×10^{-4} mbar) corresponding to the starting dynamic vacuum pressure adopted for TPD-MS experiments.

An indicative Rietveld refinement of an as-prepared sample after the sintering

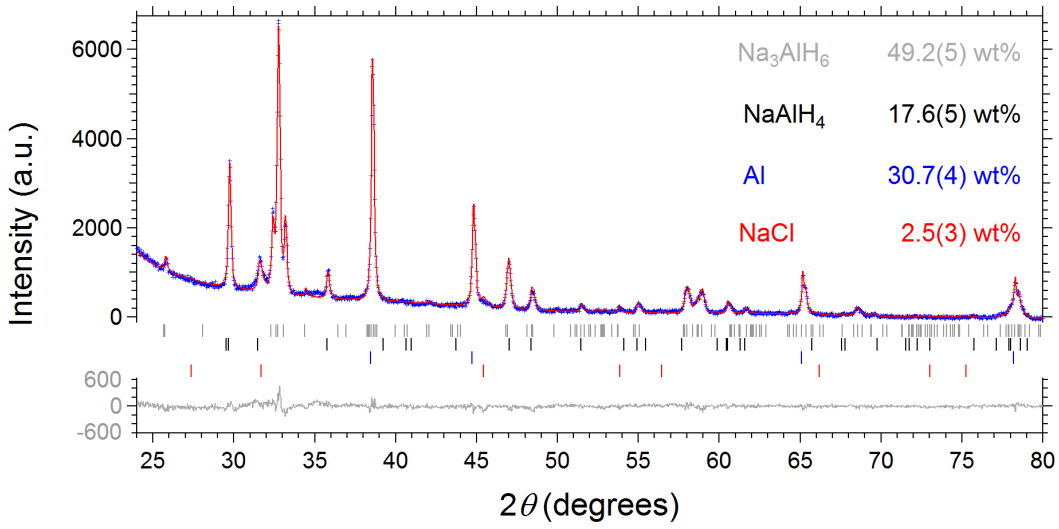

Figure 3.5: Rietveld refinement plot of the as-prepared $NaAlH_4/TiCl_3$ pellet. The blue plus symbols and the red line denote the observed and calculated intensities, respectively. Short vertical lines indicate the position of the Bragg reflections of the following compounds from top to bottom: Na_3AlH_6 (COD ID 1533931), $NaAlH_4$ (COD ID 1533929), Al (PDF 04-0787) and NaCl (PDF 05-0628). X-ray wavelength $\lambda = 1.5406$ Å. Quantitative analysis with the uncertainty corresponding to one standard deviation as derived from Rietveld refinement[31,91].

process, (referred to as the Al scaffold) used for N_2 sorption measurements, is presented in Fig. 3.7. Corundum was added as an internal standard. It can be seen that the diffraction peaks corresponding to $NaAlH_4$ and Na_3AlH_6 have completely disappeared, while peaks for Al, as result of thermal decomposition, increased in intensity. $TiCl_3$ has reacted with Al and formed Al_3Ti and $Al_{1-x}Ti_x$ phases. The difference between the experimental and calculated intensities that correspond to the diffraction peaks of Al is due to the presence of the formation of $Al_{1-x}Ti_x$ phases in the sample[182–186]. Moreover, the shoulder that is observed on the right side of the Al Bragg peak located at $2\theta = 38.46°$ ($hkl = 111$) is most likely due to the formation of the $Al_{0.85}Ti_{0.15}$ phase[139]. Considering the elevated temperature (> 200 °C) and extended time (12 h) of the sintering process, the results are in agreement with XRD measurements reported by Haiduc *et al.*[69]. $Al_{1-x}Ti_x$ phases were unable to be quantified by the Rietveld refinement method mainly because their characteristic

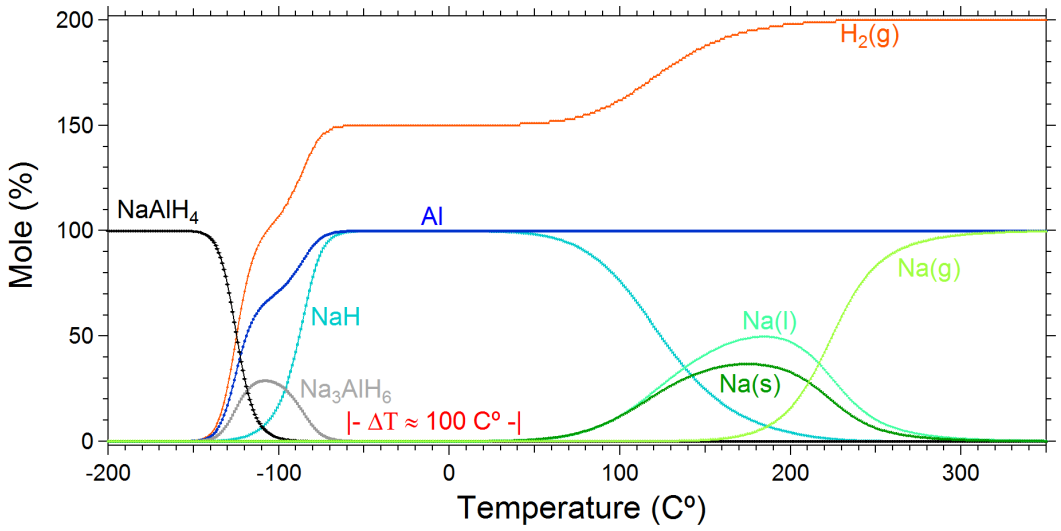

Figure 3.6: $NaAlH_4$ quantitative decomposition pathway simulation at local thermodynamic equilibrium and constant H_2 back pressure across the pathway. The simulation, performed by HSC software, used $NaAlH_4$ starting phase (100 mole %), thermodynamic phase parameters reported in Table 2.2 and $P = 7 \times 10^{-4}$ mbar. The constant pressure used corresponds to the starting dynamic vacuum pressure adopted for TPD-MS experiments. On the y-axis, the mol% values are intended as relative mol% compared to the total initial $NaAlH_4$ moles.

diffraction peaks overlap with those belonging to Al. A minor limitation for the quantification of Ti-containing phases using the Rietveld refinement method is also caused by the use of an approximated Ti atomic scattering factor implemented in TOPAS (see Appendix G).

The quantitative Rietveld refinement results for three typical Al scaffolds, see Fig. 3.4(b), are presented in Table 3.3.

The samples were weighed before and after the sintering process. The samples show a different relative mass loss[¶], between 37.8(8) and 42.4(9)%, that may be associated to an incomplete desorption of Na, although Na diffraction peaks are not detected on XRD of Al scaffolds (see Fig. 3.7). Samples that show a reduced relative mass loss also showed enhanced amorphous content (see Table 3.3), suggesting that any Na left over is not detected because it is amorphous.

[¶]Due to sample handling, the scaled mass of the sintered samples could be underestimated.

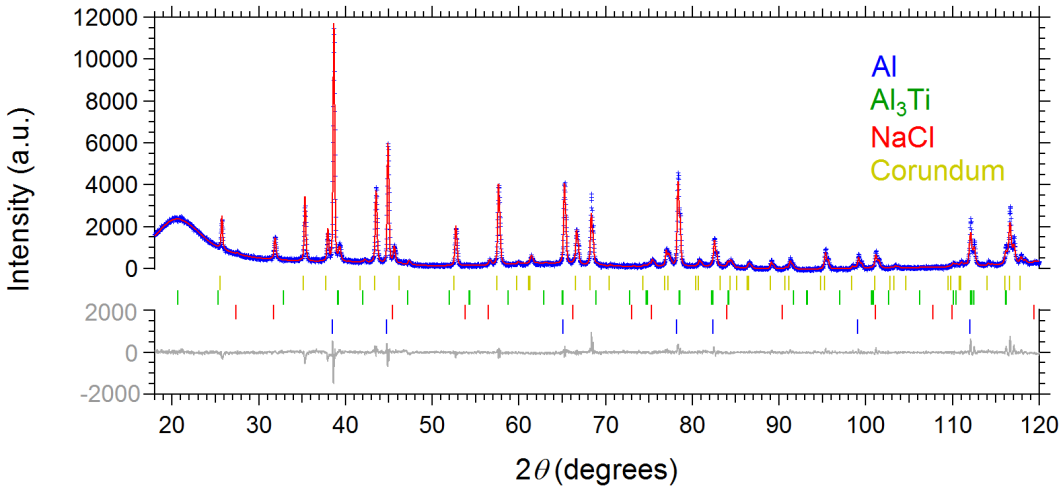

Figure 3.7: Rietveld refinement plot of the as-prepared Al scaffold used for N_2 sorption measurements, (see quantitative analysis results in Table 3.3). The blue plus symbols and the red line denote the observed and calculated intensities, respectively. Short vertical lines indicate the position of the Bragg reflections of the following compounds from top to bottom: Al (PDF 04-0787), $AlTi_3$ (PDF 37-1449), NaCl (PDF 05-0628) and corundum (PDF 46-1212). X-ray wavelength $\lambda = 1.5406$ Å[31,91].

Table 3.3: Quantitative phase analysis and relative (%) mass loss during the sintering process of three porous Al scaffolds[31,124]. The uncertainties for the quantitative phase analysis.

Phase	wt% [a]	wt% [b]	wt% [c]
Al	75.4(5)	81.2(9)	79.7(5)
$TiAl_3$	5.5(3)	6.0(6)	5.8(3)
NaCl	10.2(2)	11.0(5)	10.8(2)
Amorphous	8.9(7)	1.8(4)	3.7(3)
Mass loss	≤37.8%	≤42.4%	≤41.2%

[a] Used for N_2 sorption measurements. After melt-infiltration, this specific sample is denoted '7-$NaAlH_4$'.
[b] After melt-infiltration, this specific sample is denoted '20-$NaAlH_4$'.
[c] Used for in-situ SAXS/WAXS measurements.

Although every sample was produced under the same conditions and from the same batch of $NaAlH_4/TiCl_3$ ball-milled powder, the final phase composition of different Al scaffolds showed some appreciable differences.

Determining the optimum sintering conditions required balancing sodium removal from the Al scaffold and limiting pore size growth; *i.e.* increasing the temperature and sintering time reduces the Na left in the Al scaffold, but it may also affect the total porosity and the pore size distribution, increasing the volume contribution due to macro-pores. The dynamic vacuum pressure that a sample experiences would increase the sintering time needed to remove most of the Na only if the Na gas removal rate (effective pumping rate) is lower than the Na desorption rate. It has been shown[187] that the vacuum experienced by a sample is primarily dependent on the diameter of the tubes used in the construction of the experimental apparatus, with diameters below 12.7 mm experiencing the same vacuum for roughing and turbo-molecular pumps, and thus, increasing the maximum vacuum would require increasing the tube diameter. As the samples fit the 8 mm diameter tube, the solution adopted to ensure that the applied vacuum did not limit the reaction was to limit the initial mass of the sample. The sintering conditions, temperature (450 °C), sintering time (12 hours), and initial mass of the sample (0.2 g), were chosen after being characterised using phase identification from XRD measurements and relative mass loss measurements. The characterisation was carried out across every combination of three temperatures (400, 450, and 500 °C) and five sintering times (0.5, 1.5, 3, 6, and 12 hours). For the ideal sintering temperature and time (450 °C and 12 hours) the initial mass of the $NaAlH_4$ pellet was chosen after testing with 0.1 and 0.2 g.

3.3 $NaAlH_4$ melt-infiltrated into Ti-enriched porous Al scaffold

Successively, enough $NaAlH_4$ for the required loadings, between 7 and 34 wt%, was melt-infiltrated into an as-prepared Al scaffold (see Table 6.1)[31]. The melt-infiltrated $NaAlH_4$ (Sigma Aldrich) was the same (see §3.2) used as the starting material used to produce the Al scaffolds. The melt-infiltration process

consisted of carefully seating the Al scaffold on an aluminium foil bed to contain the molten $NaAlH_4$ during infiltration. Successively, the $NaAlH_4$ powder was placed on top of the Al scaffold. The sample was then positioned in a stainless steel reactor with 200 bar of H_2 pressure at room temperature, heated at 5 °C/min to 200 °C, and finally allowed to slowly cool to room temperature. These were found to be the minimum conditions to have repeatable successful infiltration (see Fig. 1.5). The nomenclature of the samples is based upon the loading of the $NaAlH_4$ in the Al scaffold determined by quantitative phase analysis of X-ray diffraction data. For example 7-$NaAlH_4$ designates a melt-infiltrated scaffold containing 7 wt% of $NaAlH_4$. Quantitative phase analysis was carried out for the crushed specimens, with corundum (Al_2O_3) as an internal standard to allow the quantification of amorphous phases in 7-$NaAlH_4$ and 20-$NaAlH_4$. For crushed 13-$NaAlH_4$ and 30-$NaAlH_4$, the amorphous phases were quantified from the known quantity of amorphous phases present in the Al scaffold used for each infiltration (see Table 3.3). The quantity of $NaAlH_4$ observed is in agreement with the amount of $NaAlH_4$ added in the infiltration process. The Rietveld refinements are presented in Fig. 3.8 – 3.11, while Table 3.4 summaries the quantitative phase analysis. NaCl is present due to the reaction between $TiCl_3$ and $NaAlH_4$ during ball-milling[18]. Al_3Ti and Al are present from both ball-milling and the sintering processes[71].

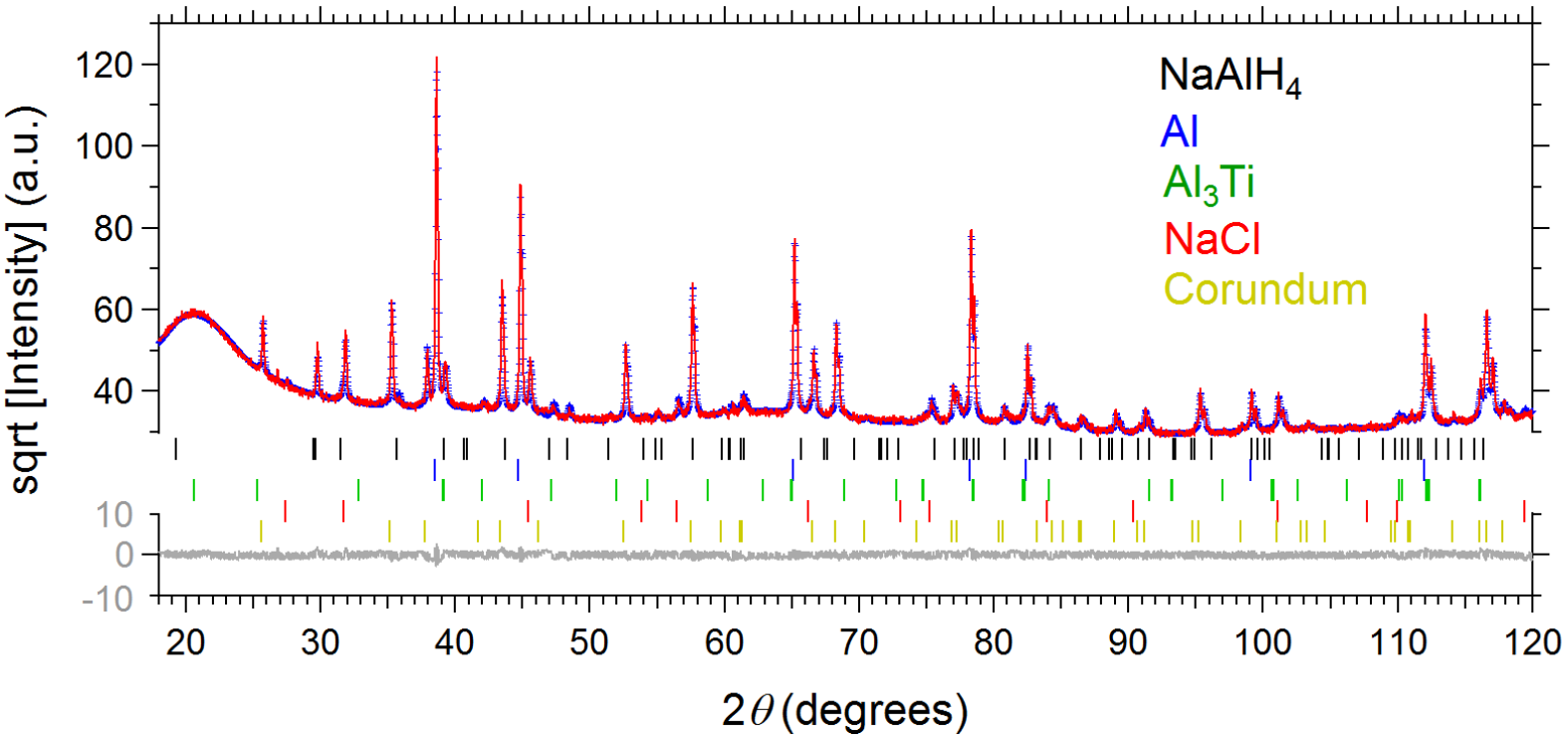

Figure 3.8: Rietveld refinement of the diffraction pattern for crushed 7-$NaAlH_4$. The blue plus symbols and the red line denote the observed and calculated intensities, respectively. Short vertical lines indicate the position of the Bragg reflections of the following compounds from top to bottom: $NaAlH_4$ (COD ID 1533929), Al (PDF 04-0787), Al_3Ti (PDF 37-1449), and NaCl (PDF 05-0628), with corundum (PDF 46-1212) added as internal standard[31]. X-ray wavelength $\lambda = 1.5406$ Å.

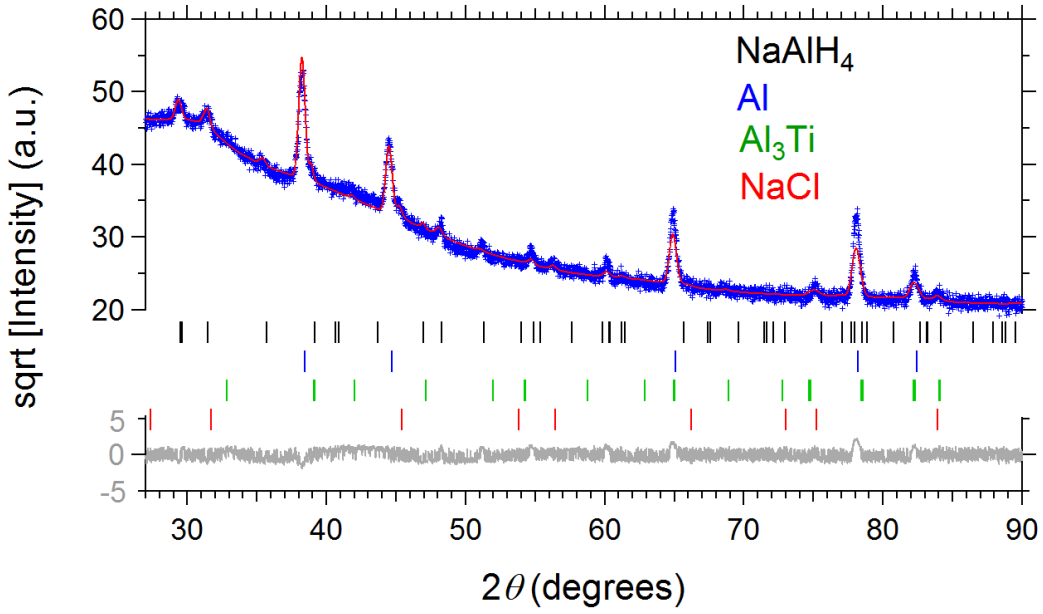

Figure 3.9: Rietveld refinement of the diffraction pattern for crushed 13-$NaAlH_4$. The blue plus symbols and the red line denote the observed and calculated intensities, respectively. The black line denotes the background. Short vertical lines indicate the position of the Bragg reflections of the following compounds from top to bottom: $NaAlH_4$ (COD ID 1533929), Al (PDF 04-0787), Al_3Ti (PDF 37-1449) and NaCl (PDF 05-0628)[31]. X-ray wavelength $\lambda = 1.5406$ Å.

Table 3.4: Quantitative phase analysis of the $NaAlH_4$/Al systems. Values give are weight percentages, and uncertainties correspond to one standard deviation as derived from Rietveld refinement[31].

Phase	7-$NaAlH_4$	13-$NaAlH_4$	20-$NaAlH_4$	30-$NaAlH_4$
$NaAlH_4$	7.3(2)	13(1)	19.6(8)	30(2)
Al	70.1(5)	67(2)	65.4(9)	54(2)
$TiAl_3$	5.3(2)	5(1)	4.8(7)	4(1)
NaCl	9.1(2)	9(1)	8.6(5)	6(1)
Amorphous	8.2(7)	6(2)	1.6(7)	6(2)

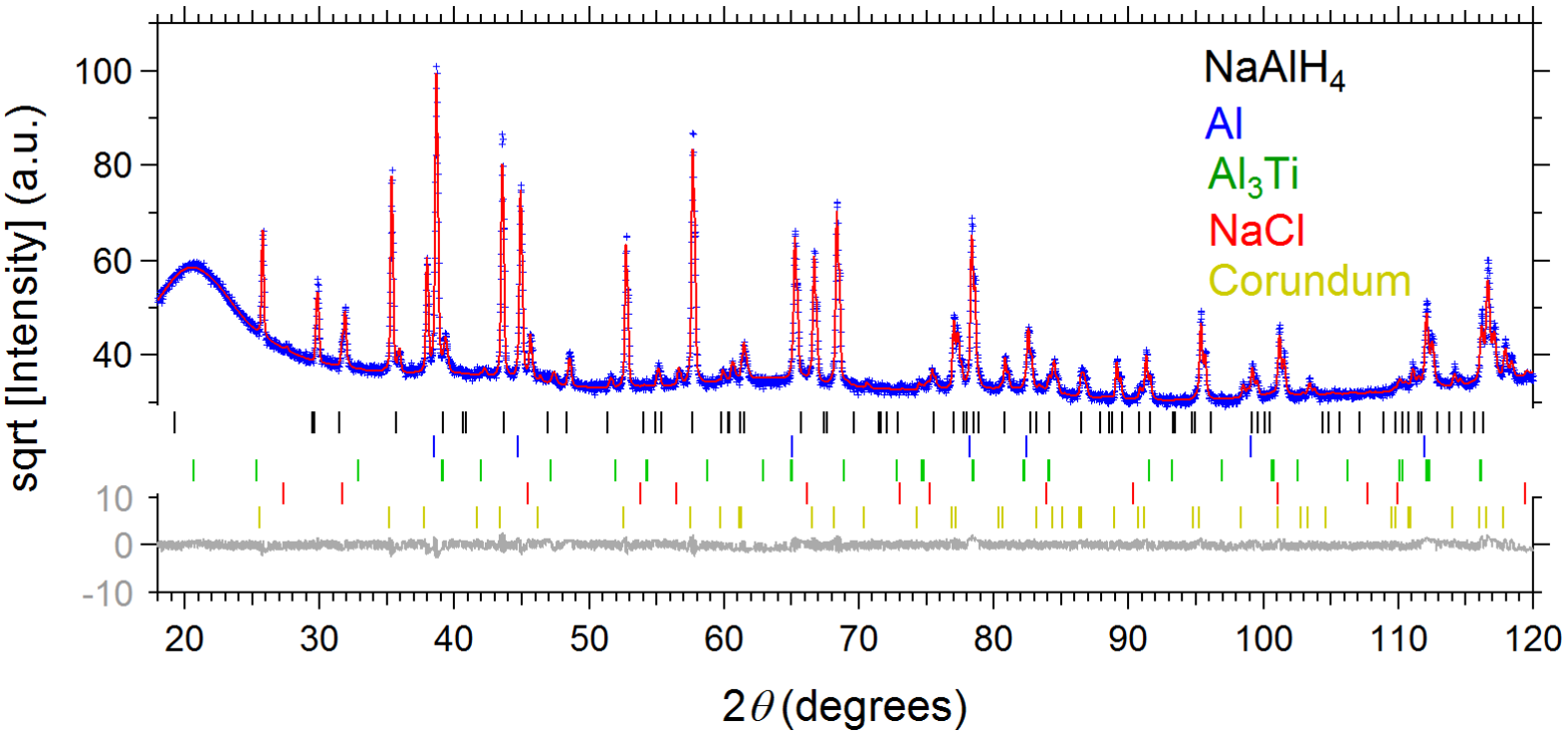

Figure 3.10: Rietveld refinement of the diffraction pattern for crushed 20-$NaAlH_4$. The blue plus symbols and the red line denote the observed and calculated intensities, respectively. Short vertical lines indicate the position of the Bragg reflections of the following compounds from top to bottom: $NaAlH_4$ (COD ID 1533929), Al (PDF 04-0787), Al_3Ti (PDF 37-1449), NaCl (PDF 05-0628), with corundum (PDF 46-1212) added as internal standard[31]. X-ray wavelength $\lambda = 1.5406$ Å.

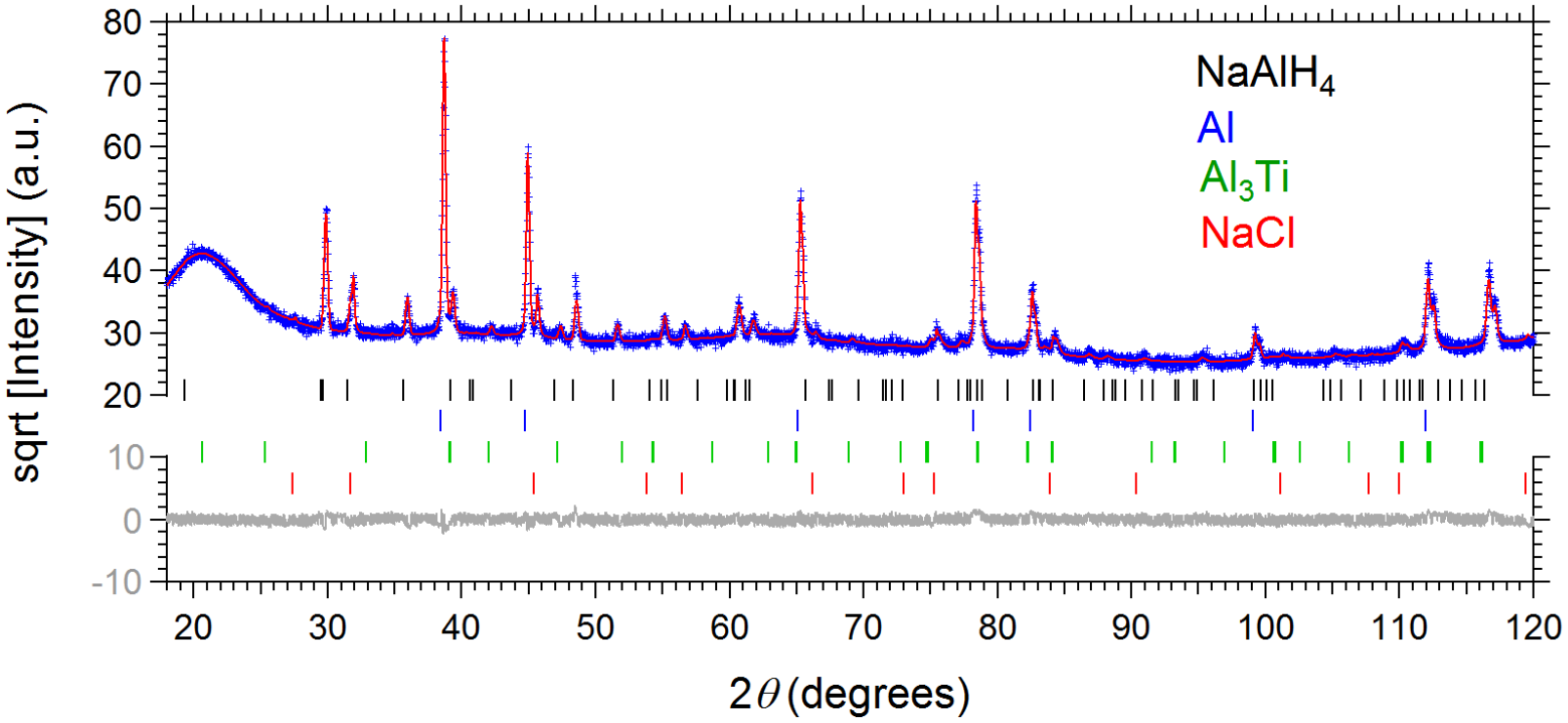

Figure 3.11: Rietveld refinement of the diffraction pattern for crushed 30-$NaAlH_4$. The blue plus symbols and the red line denote the observed and calculated intensities, respectively. Short vertical lines indicate the position of the Bragg reflections of the following compounds from top to bottom: $NaAlH_4$ (COD ID 1533929), Al (PDF 04-0787), Al_3Ti (PDF 37-1449) and NaCl (PDF 05-0628)[31]. X-ray wavelength $\lambda = 1.5406$ Å.

Chapter 4

Mg Scaffold Morphological and Structural Properties

Chapter 4 presents the experimental results on the study of the morphological and structural properties of porous Mg scaffolds as prepared in §3.1.
In order to improve the kinetic performance (§1.5) of metal hydrides infiltrated into a scaffold and eventually thermodynamically destabilize them, the scaffold has to be formed mainly by mesopores and micropores, respectively. In order to have a reduced impact on the weight of the entire system, the total porosity of the scaffold has to be maximised while maintaining the structural integrity of the scaffold.
Thus, the principal questions that Chapter 4 (Mg scaffold) and Chapter 5 (Ti-enriched Al scaffold) seek to answer are:

- Are the pores mainly in the micro and meso size range?
- Is the scaffold mainly porous?
- What are the dynamics of formation and growth of pores?

A similar Mg scaffold system, sintered for 3 instead of 6 hours, is also presented in the work published by Sofianos *et al.*[33]. As shown in[33], Mg scaffolds are intended to be used as a test bench to investigate the H_2 desorption kinetic changes of the $LiBH_4$ melt-infiltrated within it.

4.1 SEM

SEM images of the Mg scaffold in Fig. 4.1(a) show the presence of voids (1 – 2 μm), likely a remnant of the voids from the $NaMgH_3$ pellet created during the compaction of the $NaMgH_3$ powder into a pellet. The majority of pores are macro pores (Fig. 4.1(b)) with some mesopores also present (Fig. 4.1(c)). It can be seen that the pores present in the scaffold are polydisperse, do not present an ordered spatial arrangement, and form an open porous network structure, made by thin walls, similar to a sponge. The macro pores and mesopores, which are present in the scaffold were possibly created during the sintering process of the pellets applied under dynamic vacuum (see §4.3.2). Justification of this assessment is that the H_2 and the Na were removed from the pellet while the sample was heated to 450 °C for 6 hours under dynamic vacuum.

4.2 N_2 sorption

The N_2 adsorption/desorption isotherm of the porous Mg scaffold is presented in Fig. 4.2.

Despite the poor quality of the measurements compared with the N_2 adsorption/desorption isotherm of a similar Mg scaffold system, sintered for 3 instead of 6 hours, presented in the work published by Sofianos *et al.*[33], the following information can be obtained. The isotherm is of a type II, with an associated H3-type hysteresis loop at high relative pressures ($P/P_0 = 0.4(1) - 0.99(1)$)[167,184–186], where the data markers of the absorbed and desorbed branches are significantly not overlapping each other. The presence of this type of hysteresis is associated with capillary condensation taking place mainly in the mesopores and macro pores of the porous Mg scaffold. The lack of a knee in the isotherm at low relative pressures indicates the weak adsorbate-adsorbent interactions, which are due to the absence of micropores in the sample. These observations, such as the lack of micropores, the small number of mesopores, as well as the large number of

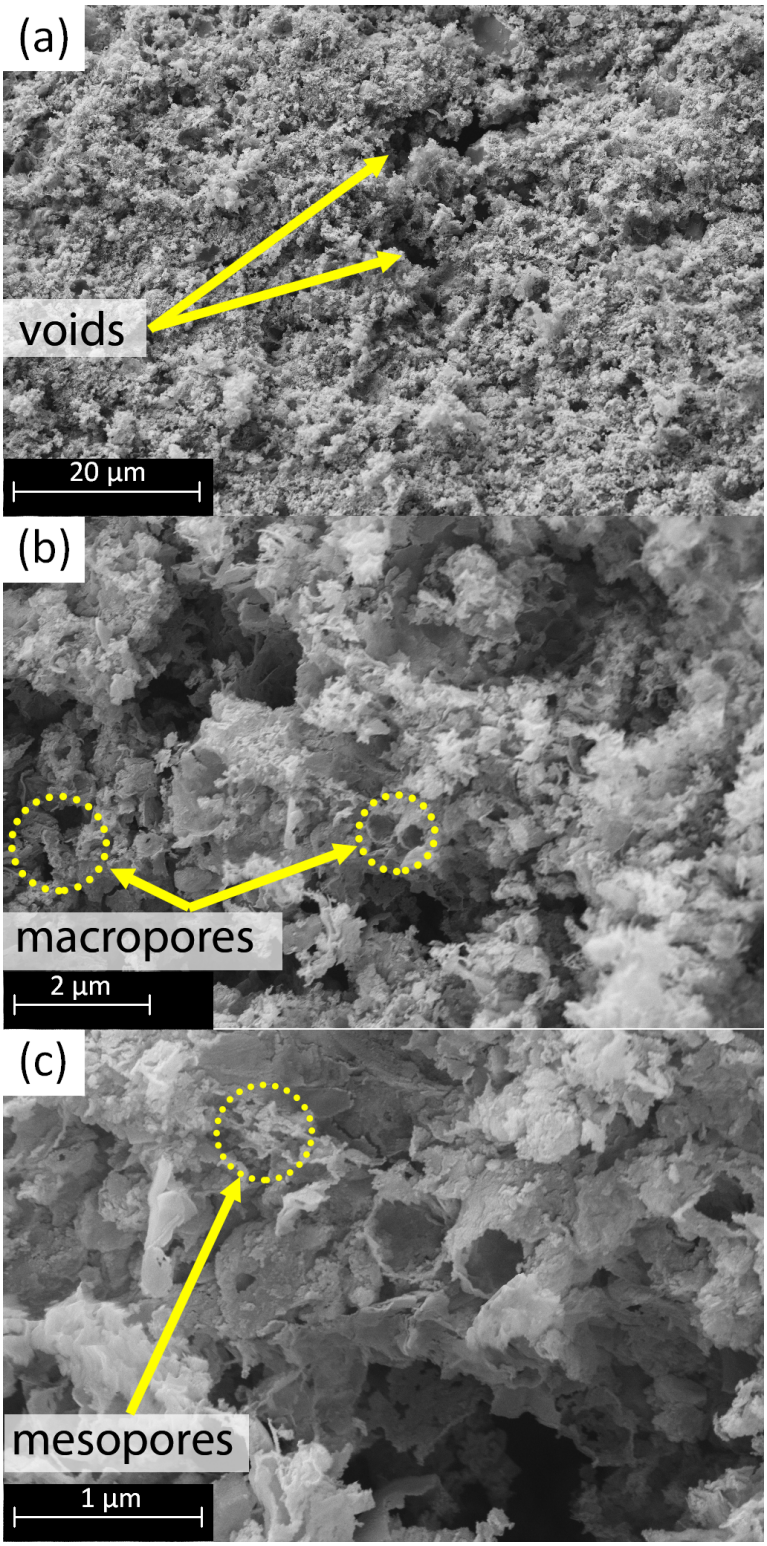

Figure 4.1: SEM micrographs of the porous Mg scaffold after the sintering process.

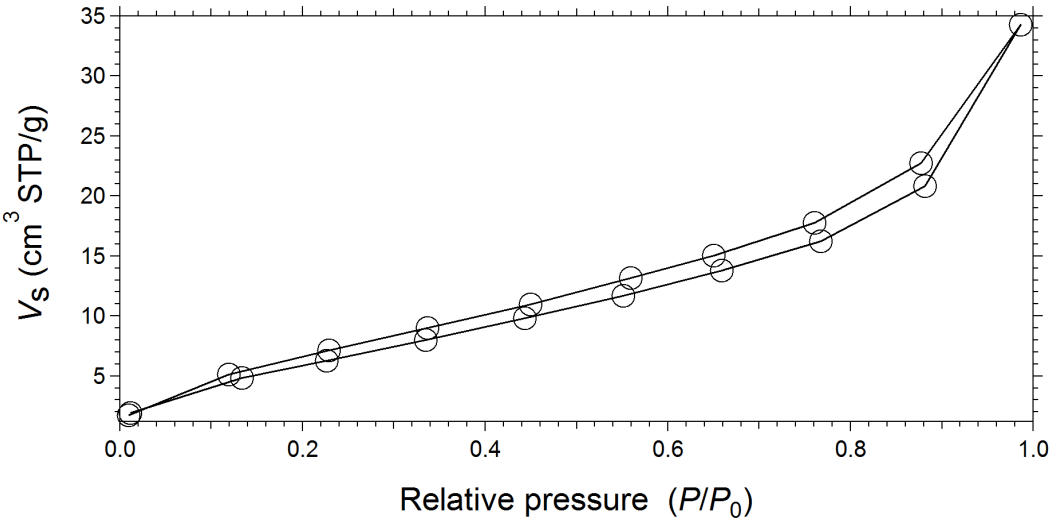

Figure 4.2: N_2 adsorption/desorption isotherm of the porous Mg scaffold.

macro pores and voids in the sample, are in agreement with the SEM micrographs (Fig. 4.1).

4.2.1 BJH

The mesopore specific pore volume distribution, shown in Fig. 4.3, of the porous Mg scaffold was calculated using the BJH method, introduced in §2.6.2, from the desorption branch of the isotherm reflecting the equilibrium phase transition (Fig. 4.2).

The specific pore volume distribution shows an increasing trend (Fig. 4.3). The specific volume due to the mesopores and small macro pores with diameter within the range of 1.9 – 138 nm (Fig. 4.3) is equal to 0.034 cm^3/g. In the work of Sofianos *et al.*[33] on a similar porous Mg scaffold (sintered for 3 hours instead of 6), just considering the pores in the range of 1.7 – 48 nm, the specific volume was found to be higher (0.06 cm^3/g) presumably because the pores had less time to grow (see §4.3.2).

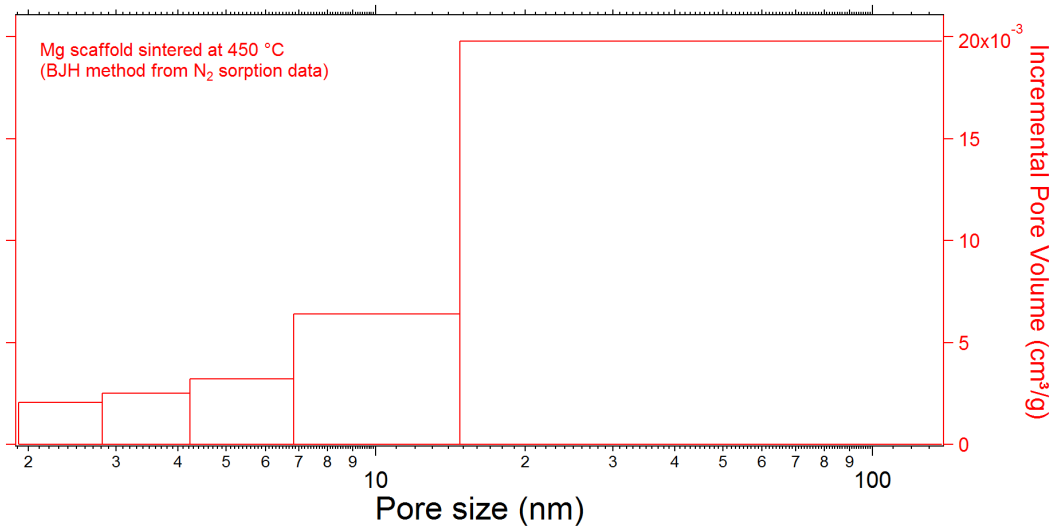

Figure 4.3: Mesopore specific pore volume distribution of the porous Mg scaffold obtained from BJH method (N_2 sorption technique).

4.2.2 BET

The specific surface area of the Mg scaffold was calculated from its N_2 sorption isotherm (see Fig. 4.2), between relative pressures of 0.1 and 0.4 with the BET multi-point method, introduced in §2.6.3. The specific surface area obtained is 26 ± 2 m^2/g, which takes into consideration the contribution of pores from 0.4 nm up to the 1 μm scale. The same specific surface area was also obtained by Sofianos *et al.* [33] for a similar porous Mg scaffold. Such a value for the specific surface area is at least one order of magnitude smaller compared with most of the carbon-based scaffolds listed in §1.5.2. This is due to the higher crystalline density and larger pore sizes of the Mg scaffold compared with carbon-based scaffolds. The higher crystalline density of the Mg scaffold results in reduced gravimetric hydrogen densities in a system formed by the Mg scaffold and metal hydrides infiltrated within it. The larger pore sizes of the Mg scaffold would result in reduced nanoconfinement effects on the metal hydrides infiltrated within it.

4.3 *In situ* SAXS/WAXS

In order to understand the dynamics of the mesopore formation during the sintering process leading to the production of Mg scaffolds, *in situ* SAXS/WAXS measurements during the decomposition of two $NaMgH_3$ pellets were carried out and the data analysed. The apparatus and experimental setup adopted is discussed in detail in §2.2.1. The two $NaMgH_3$ pellets were heated up to 450 °C and 400 °C from room temperature using the same heating rate, 5 °C/min, and similar dynamic vacuum pressure, 1.5×10^{-2} mbar, as that used to produce the Mg scaffolds (§3.1). The $NaMgH_3$ pellets used in these two experiments will be referred to as $NaMgH_3$-450 and $NaMgH_3$-400, respectively.

4.3.1 *In situ* WAXS

The *in situ* WAXS patterns, of $NaMgH_3$—450 and $NaMgH_3$—400 decompositions, are shown in Figures 4.4 and H.1(b), respectively.

In Fig. 4.4, the diffraction peaks associated with $NaMgH_3$ are observed to gradually decrease and disappear between 91 °C and 174 °C. Following the first step of $NaMgH_3$ decomposition (eq. 1.1), the intensities of the diffraction peaks associated with NaH and Mg were expected to increase. However, due to the presence of oxygen in the system, the intensities of the diffraction peaks associated with NaOH (PDF 35-1009) and MgO are, instead, increased and formed, respectively. The MgO diffraction peaks are constantly increasing in intensity, up to 304 °C, and initially were broader consistent with reduced grain sizes. After the disappearance of the diffraction peaks associated with $NaMgH_3$ (174 °C), the diffraction peaks associated with NaOH increase in intensity up to 284 °C, proving that part of the unobserved $NaMgH_3$ decomposition product, NaH, is in an amorphous/liquid form in agreement with the thermodynamic prediction, as shown in the work of Abdessameud *et al.*[47]. Between 284 °C and 312 °C, the diffraction peaks associated with NaOH are observed to suddenly decrease with the consequent disappearance

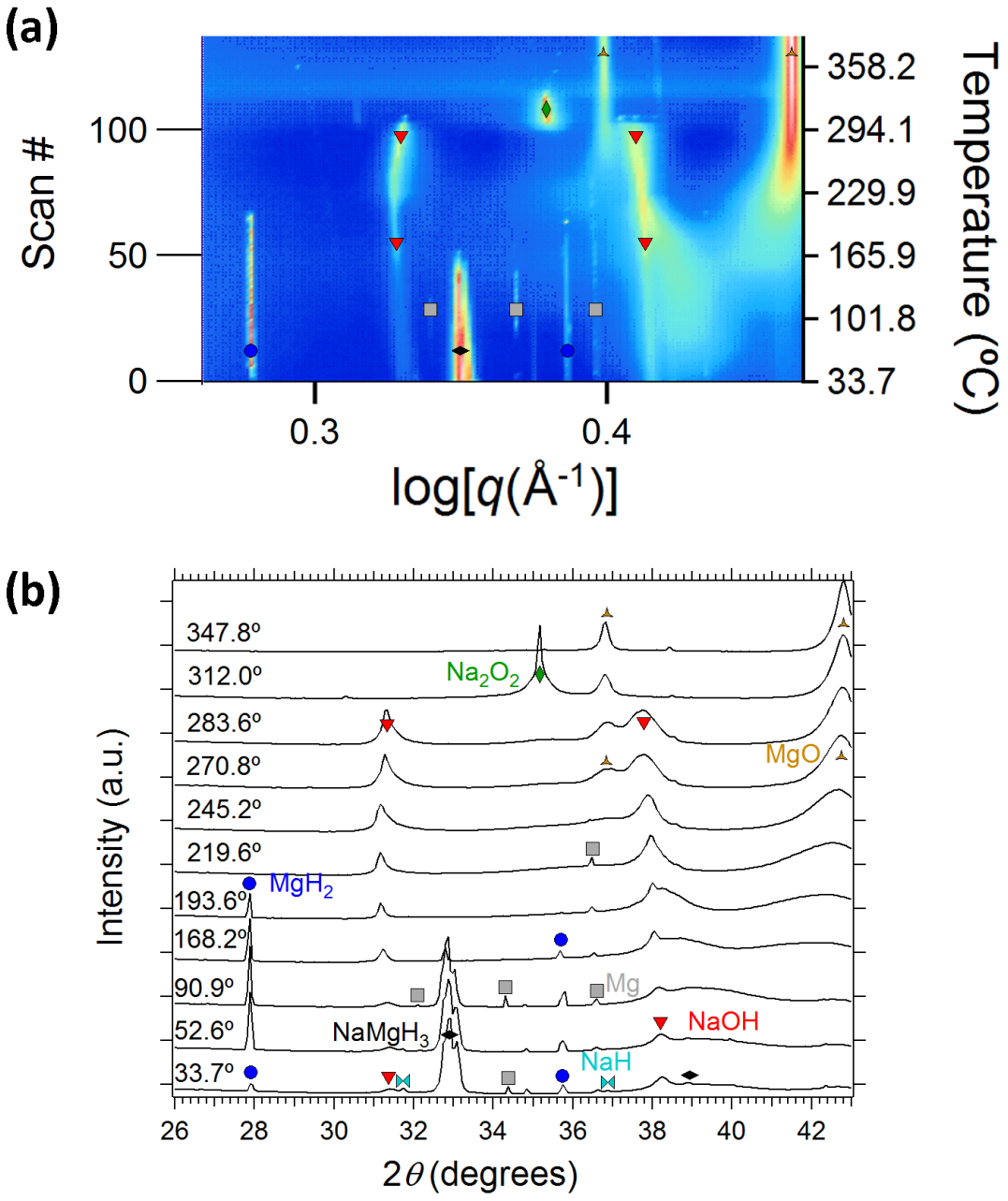

Figure 4.4: *In situ* WAXS patterns of $NaMgH_3$-450 decomposition. (a) Collated patterns viewed down the intensity axis with colours representing intensity, and (b) stack plot of individual patterns showing the peak profiles. The 2θ (degrees) has been converted for λ = 1.5406 Å.

while the diffraction peaks associated with Na_2O_2 (COD ID 4124685) appear and increase reaching their maximum, consistent with a phase transition involving

hydrogen desorption. Successively, the diffraction peaks associated with Na_2O_2 are observed to gradually decrease and disappear between 312 °C and 348 °C. The diffraction peaks associated with MgH_2 are observed to rapidly increase from 34 °C to 53 °C, reaching their maximum at 91 °C, then successively decreasing until completely disappearing at 209 °C.

The temperatures of the observed $NaMgH_3$ decomposition and of the MgH_2 formation and decomposition are higher than the temperatures predicted from the calculation[†] (Fig. 3.2), which is due to kinetic limitations.

The presence of the oxygen in the system is in part due to the presence of impurities from the starting material[33,181] and mostly due to fracturing of the borosilicate glass capillary (Fig. 5.12(b)).

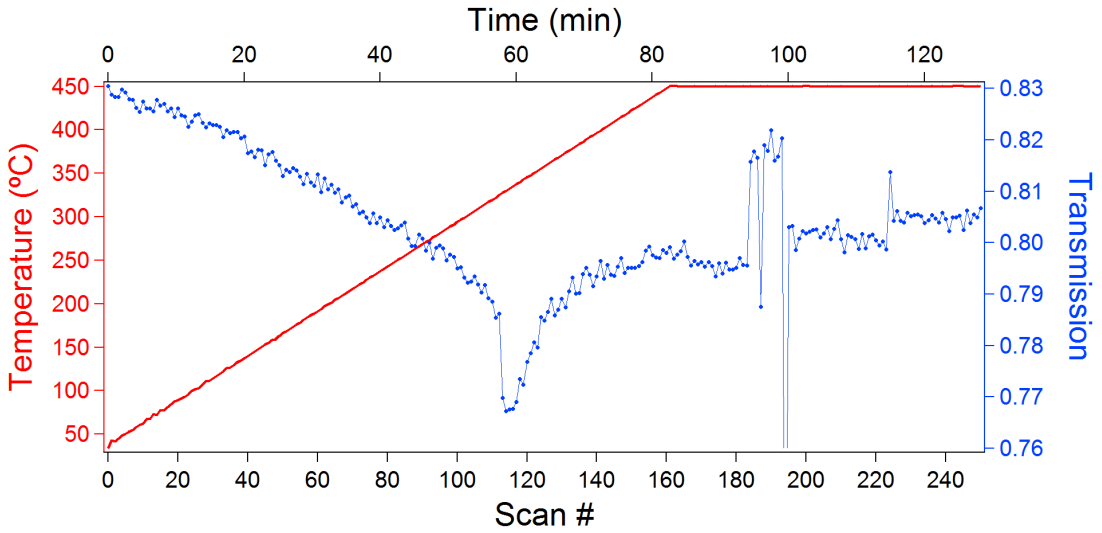

Figure 4.5: *In situ* SAXS/WAXS measured transmission, τ_s, and temperature trends for the decomposition of $NaMgH_3$-450.

For a non-oxidizing sample, the transmission (Fig. 4.5) was expected to be constant until the start of $NaMgH_3$ decomposition, during which it was expected to increase with the increase of temperature due to a reduction in scattering associated with the desorption of hydrogen. However, the transmission trend (Fig. 4.5) constantly decreases until 330 – 335 °C as a consequence of the increase in the sample mass

[†]at local thermodynamic equilibrium, considering the dynamic vacuum condition $P = 1.5 \times 10^{-2}$ mbar.

due to the oxidation. From 335 °C the transmission trend gradually increases and it stabilizes at 0.795(5) from 435 °C (Fig. 4.5). Presumably, the decrease in intensities of diffraction peaks associated with Na_2O_2 from 312 °C is due to a gradual desorption of Na_2O_2. Thus, the decrease in the sample mass due to the sodium and oxygen removal may have caused the increase in transmission. Additionally, the release of gasses from the sample could also induce it to move. When the X-ray beam spot is centred, it overlaps completely with the sample cross section. If the sample moves along the capillary, the transmission may increase due to only part of the X-ray beam hitting the sample. Thus, the sudden increase in transmission at scan #184 (Fig. 4.5) may be attributed to a decentering of the sample. Indeed, at scan #194 the sample was manually recentred and as a consequence the transmission was reduced to the previous stable value of 0.795(5). The d-spacing associated with each set of diffraction peaks ($d = 2\pi/q$ in Fig. 4.4(a)) present the same relative increase, consistent with a homogeneous thermal expansion of the associated crystal structures. Such consistencies in peak positions were found useful in identifying diffraction peaks belonging to the same phase.
For the *in situ* SAXS/WAXS experiment of $NaMgH_3$-400 decomposition, as shown in Figures H.1, the decomposition temperatures were considerably higher than those seen with $NaMgH_3$-450 as shown in Fig. 4.4. It is conjectured that this difference is, in minor part, due to different specimen size and initial phase composition. However, every reaction appears to be uniformly shifted, by 80 – 90 °C, towards higher temperatures. Sample oxidation from the early stage of the *in situ* measurements is also observed.

4.3.2 *In situ* SAXS

The *in situ* SAXS patterns, in arbitrary units ($I_{\text{a.u., scan \#}} \propto I_{\text{measured, scan \#}}/I_{\text{beam stop, scan \#}} - BG/I_{\text{beam stop, BG}}$), of $NaMgH_3$-450 and $NaMgH_3$-400 decompositions, were modelled, using McSAS analysis (§2.2.5.4). The *in situ* pore size related distributions — $\varphi_{i,\text{ scan \#}} \times const_{\text{scan \#}}$ — in Figures 4.6(a),

H.2(a) and H.1(a) were obtained by setting the same scattering length density of all scans to the same value. For each scan, the unknown $const_{\text{scan \#}}$ ($\propto [d_{\text{ss, scan \#}} \times (\Delta\rho_{\text{SLD, scan \#}})^2 \times (1 - \varphi_{\text{total, scan \#}})]/[I_{\text{beamstop, scan \#}} \times (\varphi_{\text{total, scan \#}})^2]$) is a function of transmission, $\tau_{\text{ss, scan \#}}$ ($= I_{\text{beamstop, scan \#}}/I_{0,\text{ scan \#}}$), solid thickness, $d_{\text{ss, scan \#}}$, scattering length density, $\Delta\rho_{\text{SLD, scan \#}}$, and total porosity $\varphi_{\text{total, scan \#}}$. In Figures H.2(a) and H.1(a), $\varphi_{i,\text{ scan \#}}$ is the contribution to the total porosity, $\varphi_{\text{total, scan \#}}$, of those modelled spherical pores having a size of $2R_i$, see §2.2.5.4. While in Fig. 4.6(a), $\varphi_{i,\text{ scan \#}}$ is the contribution to the total porosity, $\varphi_{\text{total, scan \#}}$, of those modelled spheroidal pores having a transverse size, with respect to the axis passing through the two origins of the spheroid, of $2a_i$ and $2b_i$. The aspect radius of semi-axes c_i to a_i and b_i was restricted to be between 0.5 and 5.0. Due to the unknown normalization coefficient, $const_{\text{scan \#}}$, the intensities in the *in situ* distributions of the partial porosity contribution, $\varphi_{i,\text{ scan \#}}$, across different SAXS patterns (that is, different scan #) can be qualitatively compared assuming that the effect of changes in the partial porosity contribution, $\varphi_{i,\text{ scan \#}}$, are dominant over the effect of changes in the $const_{\text{scan \#}}$. However, the change in the distribution shape (profile) due to the change in the relative intensities of partial porosity contribution, $\varphi_{i,\text{ scan \#}}$, in each SAXS pattern can be compared across different SAXS patterns.

During the formation of NaOH between 174 °C and 284 °C and of Na_2O_2 between 284 °C and 312.0 °C, see also Fig. 4.4, mesopores of size between 10 and 20 nm and between 30 and 45 nm, respectively, are observed gradually forming and growing. It is also observed the formation of mesopores between 40 and 50 nm in correspondence with the formation of MgO between 174 °C and 304 °C. From 312 °C, as a result of the lack of further phase formation and constant growth of the mesopores, no significant intensities of the partial porosity contribution, $\varphi_{i,\text{ scan \#}}$, are observed. In Figure 4.6, a peak in the size distribution centred at 2.0 ± 0.5 nm reaches its maximum intensity at 174 °C, consistent with the complete decomposition of $NaMgH_3$. This micro-size peak reduces in intensity and grows in

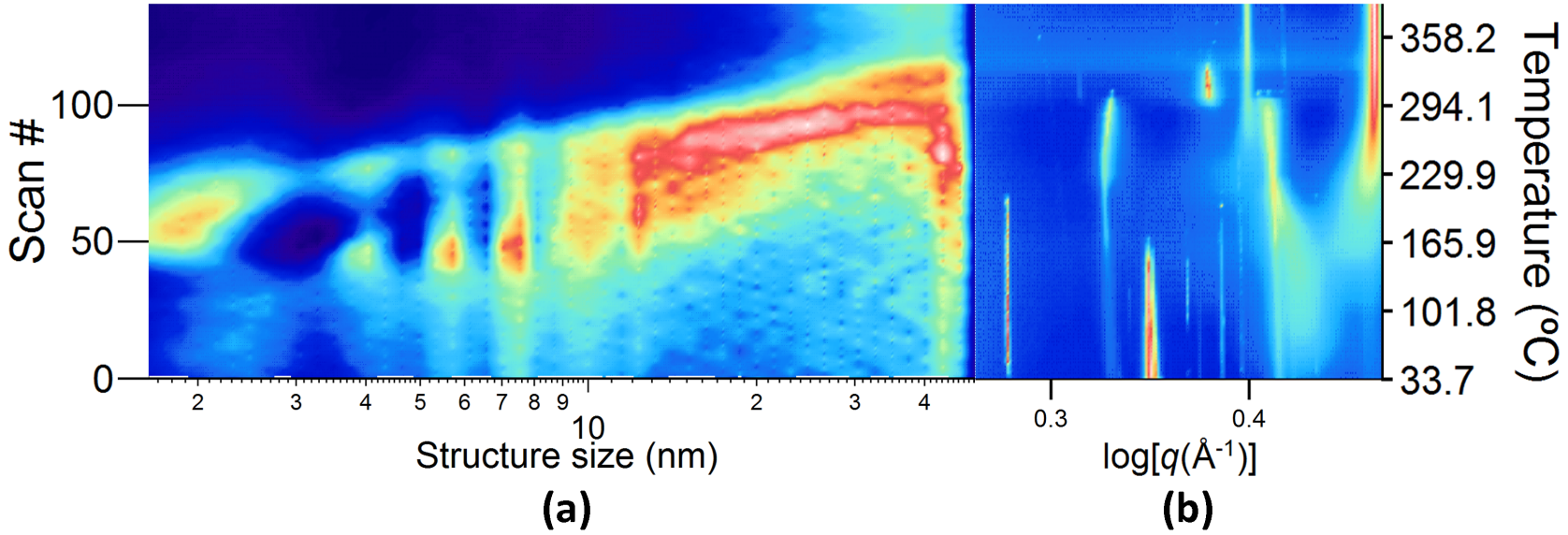

Figure 4.6: (a) *In situ* pore size related distributions, $\varphi_{i,\,\text{scan \#}} \times const_{\text{scan \#}}$, obtained applying McSAS (spheroidal pore shape, aspect radius of semi-axes c to a and b: 0.5 – 5.0) analysis to SAXS patterns of $NaMgH_3$-450 decomposition and (b) the corresponding WAXS patterns.

size consistently with NaOH formation up to 284 °C.

In Figures H.2(a) and H.1(a), mesoporosity distributions are shown obtained by applying McSAS analysis using a spherical pore shape model to the SAXS patterns of $NaMgH_3$-450 and $NaMgH_3$-400 decompositions, respectively. These distributions show a regular modulation, however it is believed that this is an artefact of the analysis and, thus, less realistic compared with the distribution in Fig. 4.6(a) obtained applying a spheroidal pore shape model instead. Despite the poor quality of the measurements due to a stronger oxidation, the mesoporosity distributions for $NaMgH_3$-400, Fig. H.1, present a trend of formation and growth, in correspondence with the phase changes, similar to the mesoporosity distributions for $NaMgH_3$-450, seen in Figures 4.6 and H.2.

4.4 Summary

SEM micrographs and N_2 adsorption/desorption, in §4.1 and 4.2.1 respectively, revealed that the pores of the Mg scaffold were polydisperse, having an open network made by thin walls. The majority of pores were macro pores, with some mesopores also present. *In situ* SAXS/WAXS analysis, in §4.3.2, revealed that mesopores are formed in conjunction with crystalline structure changes during $NaMgH_3$ decomposition. The crystalline structure change due to the first step of $NaMgH_3$ decomposition produced mesopores smaller than the mesopores produced by the oxidation of Na and NaH. Large changes in the intensity of the crystalline phases corresponds to the formation of more mesoporosity. The formed mesopores were observed to grow at a constant rate during the sintering process.

Chapter 5

Al Scaffold Morphological and Structural Properties

Chapter 5 presents the experimental results on the study of the morphological and structural properties of porous Al scaffolds as prepared in §3.2.
The principal questions that Chapter 5 seek to answer are outlined at the beginning of Chapter 4.
§5.1, §5.2 and §5.3 are mainly based on the work published by Ianni *et al.*[91]. A similar Al scaffold system, sintered for 6 instead of 12 hours, is also presented in the work published by Sofianos *et al.*[92].

5.1 SEM

A void volume fraction of 20 ± 2% was created during the compaction of the starting materials into a $NaAlH_4$ pellet. It was calculated from eq. 2.47, using the measured physical density of the pellet (Fig. 3.4(a)) and the calculated crystalline densities of the phases from the starting materials (Fig. 3.5).
The SEM images of the Al scaffold in Fig. 5.1(a) show the presence of voids, likely a remnant of the voids from the $NaAlH_4$ pellet. The majority of pores are macropores (Fig. 5.1(b)), with some mesopores present (Fig. 5.1(c)). The pores

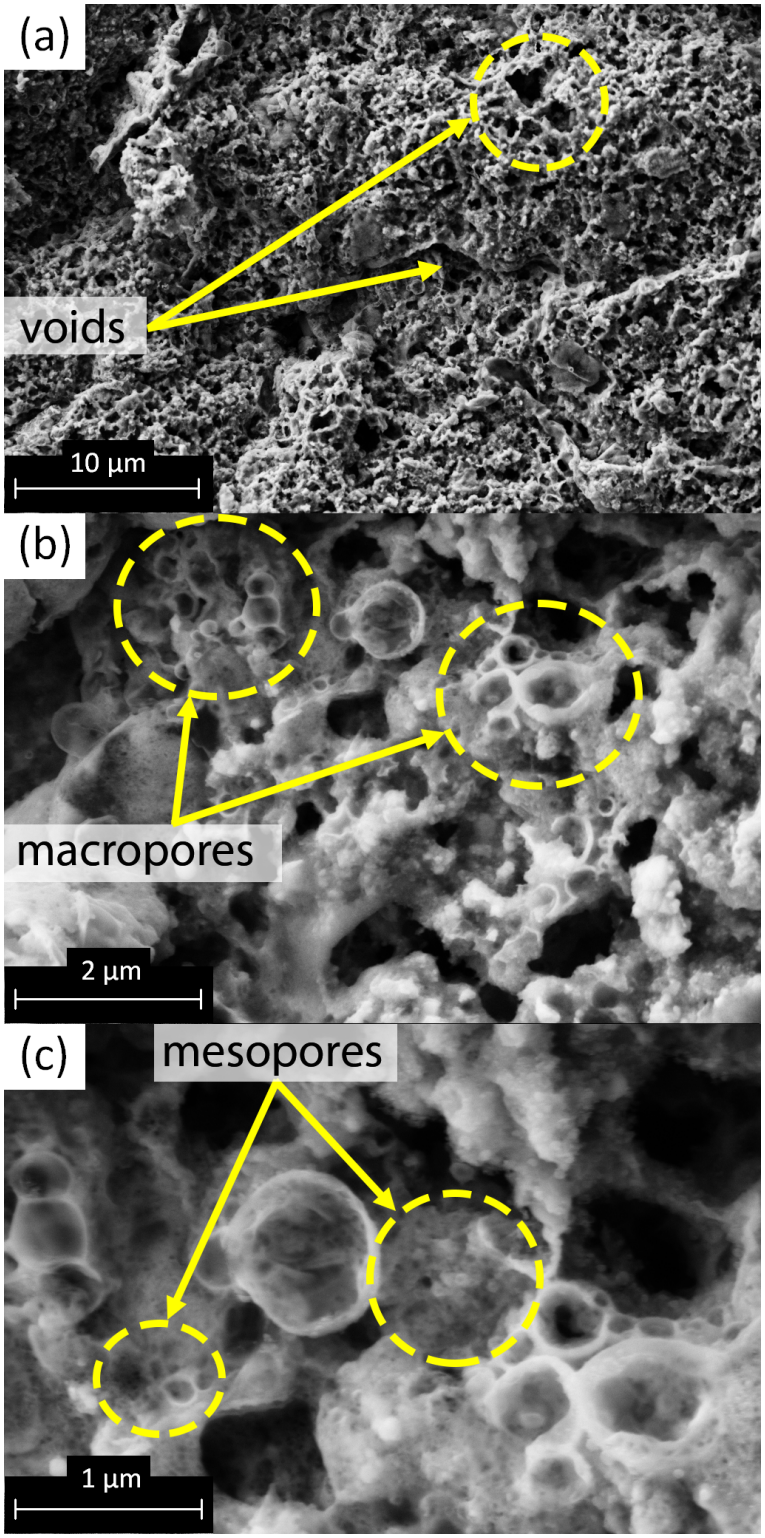

Figure 5.1: SEM micrographs of the porous Al scaffold after the sintering process[91].

are not spatially ordered, present a wide size distribution and spherical shape, and are reminiscent of a fractal distribution. The macro and mesopores present in the scaffold were most probably created during pellet sintering under a dynamic vacuum. Justification of this assessment is that the H_2 and the Na were removed from the pellet while the sample was heated to 450 °C for 12 h under dynamic vacuum. It can be observed that some pores present in the scaffold have a spherical type bubble structure that may have formed during the thermal decomposition of NaH, as these kinds of pores have previously been reported and are deemed to be created while the H_2 is extracted from the sample during its sintering process[182].

5.2 N_2 sorption

The N_2 adsorption/desorption isotherm of the porous Al scaffold, see Fig. 5.2, is of a type II, with an associated H3-type hysteresis loop at high relative pressures (P/P_0 = 0.60(5) – 0.99(1))[167,184–186]. The presence of this type of hysteresis is

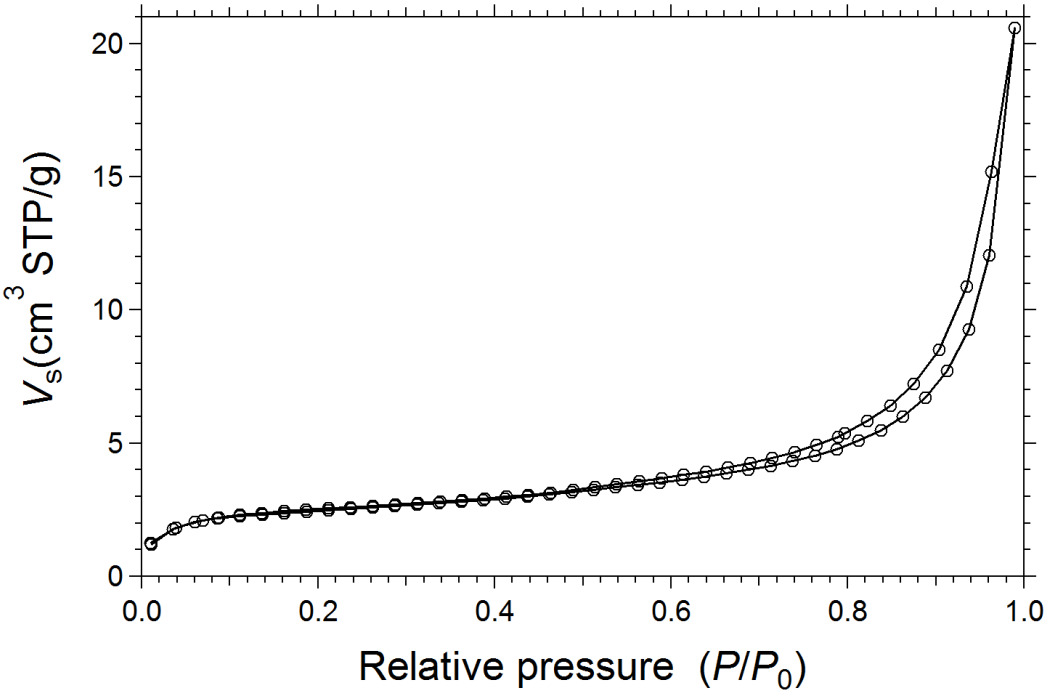

Figure 5.2: N_2 adsorption/desorption isotherm of the porous Al scaffold[91].

associated with capillary condensation taking place mainly in the macropores. The lack of a knee in the isotherm at low relative pressures indicates the weak adsorbate-adsorbent interactions, which is due to the absence of micropores in the sample. These observations, such as the lack of micropores, the small number of mesopores, as well as the large number of macropores and voids in the sample, are in agreement with the SEM micrographs (Fig. 5.1) and the SAXS measurements (Fig. 5.7).

5.2.1 BJH

The mesopore specific pore volume distribution, shown in Fig. 5.3, and the cumulative specific pore volume as a function of pore size (see Fig. 5.7) of the porous Al scaffold were calculated from the desorption branch of the isotherm, reflecting the equilibrium phase transition using the BJH method introduced in §2.6.2. The specific pore volume distribution shows an increasing trend from pore sizes of $\simeq$ 3 nm.

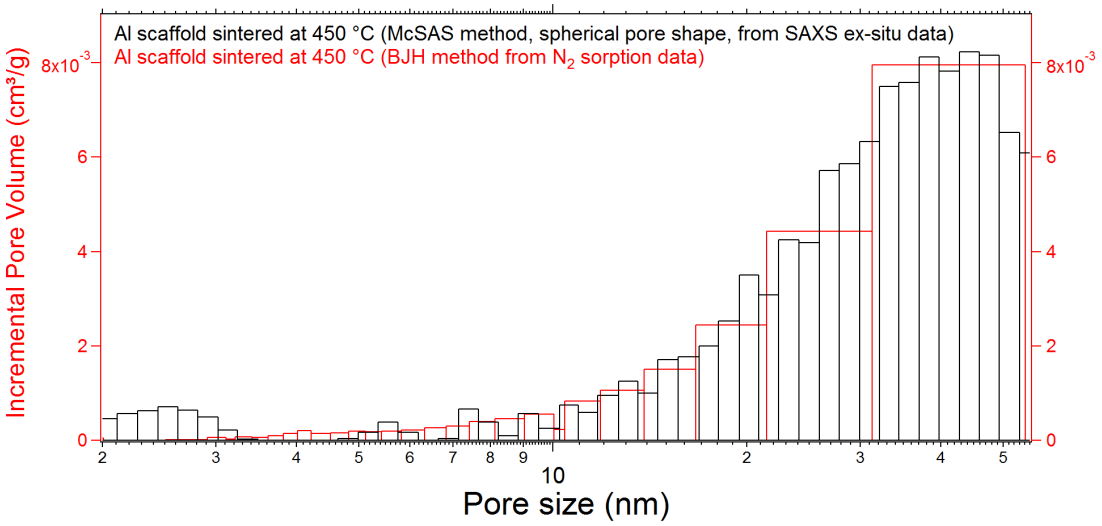

Figure 5.3: Spherical pore model and BJH mesopore specific pore volume distribution of the porous Al scaffold. This includes, in black, data obtained from McSAS (spherical pore shape) method (*in situ* SAXS technique) and, in red, data obtained from BJH method (N_2 sorption technique).

5.2.2 BET

The specific surface area of the Al scaffold was calculated from its N_2 sorption isotherm (see Fig. 5.2) between relative pressures of 0.05 and 0.30 with the BET multi-point method, introduced in §2.6.3. The specific surface area is 7.9 ± 0.1 m^2/g, taking into consideration the contribution of pores from 0.4 nm to 1 μm. The uncertainty is derived from the fitted data only, without considering the uncertainty derived from the estimated size (0.4 nm) of the N_2 molecule at −195.79 °C. Such a value for the specific surface area is at least one order of magnitude smaller compared with most of the carbon-based scaffolds listed in §1.5.2. This is due to the higher crystalline density and larger pore sizes of the Al scaffold compared with carbon-based scaffolds. The higher crystalline density of the Al scaffold results in reduced gravimetric hydrogen densities in a system formed by the Al scaffold and metal hydrides infiltrated within it. The larger pore sizes of the Al scaffold result in reduced nanoconfinement effects on the metal hydrides infiltrated within it.

5.3 *Ex situ* SAXS/WAXS

The SAXS and WAXS patterns of the porous Al scaffold are presented in Fig. 5.4(a) and (b) respectively. The WAXS pattern is consistent with the XRD pattern of the Al scaffold in Fig. 3.7. For the SAXS pattern, the absolute intensity conversion was performed following the procedure presented in §2.2.3. Rearranging the terms in eq. 2.17, the solid sample thickness is given by the following equation:

$$d_{ss} = -\frac{\ln \tau_s}{\mu} \tag{5.1}$$

The transmission of the specimen, τ_s, was obtained by taking the ratio between the beam stop counts, $I_{beamstop}$, and the upstream counts, I_0, while the linear absorption coefficient, μ, was calculated using eq. A.14, based on the phase composition of the sample listed in Table 3.3, and on phase crystal densities obtained by the Rietveld

refinement method (see Fig. 3.7). The phase composition of the amorphous phases (3.7(3) wt% in total, see Table 3.3) was estimated taking into consideration the phase composition of the starting materials (see Table 3.2), and the sintering mass loss measurements (see Table 3.3), in order to estimate the eventual Na left in the sample after the sintering process. Their densities were approximated as theoretical crystalline densities. The value obtained for the solid sample thickness was 281 μm, which considering the typical total porosity of porous Al scaffolds (introduced in §5.3.1.2) corresponds to an average sample size of 550 ± 50 μm. The estimated average sample size is compatible with the expected size of a sample contained inside a 1 mm outer diameter capillary. It is worth noting that such an average sample size is larger than the beam size (250 μm horizontally FWHM and 150 μm vertically FWHM), thus, for an X-ray centred sample, the beam would be entirely within the sample, making eq. 5.1 self-consistent[†].

From the WAXS pattern (Fig. 5.4(b)), it can be seen that the sample consisted of Al, as well as NaCl and Al_3Ti, which are reaction products when $TiCl_3$ is added to $NaAlH_4$. This pattern is in agreement with the XRD pattern of the porous Al scaffold obtained after the sintering process (Fig. 3.7) and confirms that the sample was adequately sealed in the borosilicate glass capillary, as no oxidation of the sample was seen. The lack of fringes in the SAXS pattern (Fig. 5.4(a)) reflects the polydisperse nature of the system. As suggested by SEM images (Fig. 5.1(c)), the mesopores do not present any visible spatial order, which is also confirmed by the absence of diffraction peaks in the SAXS pattern (Fig. 5.4(a))[91]. However, the detection of a hypothetical highly spatially ordered mesopore structure would be difficult due to the limitation imposed by the longitudinal coherence length of the X-rays used for SAXS measurements, despite a sufficient pore statistic, as discussed in detail in Appendix I[188,189].

[†]A partial overlapping between sample cross section and X-ray beam spot would not affect the final absolute intensities values obtained but only the estimation of the solid sample thickness.

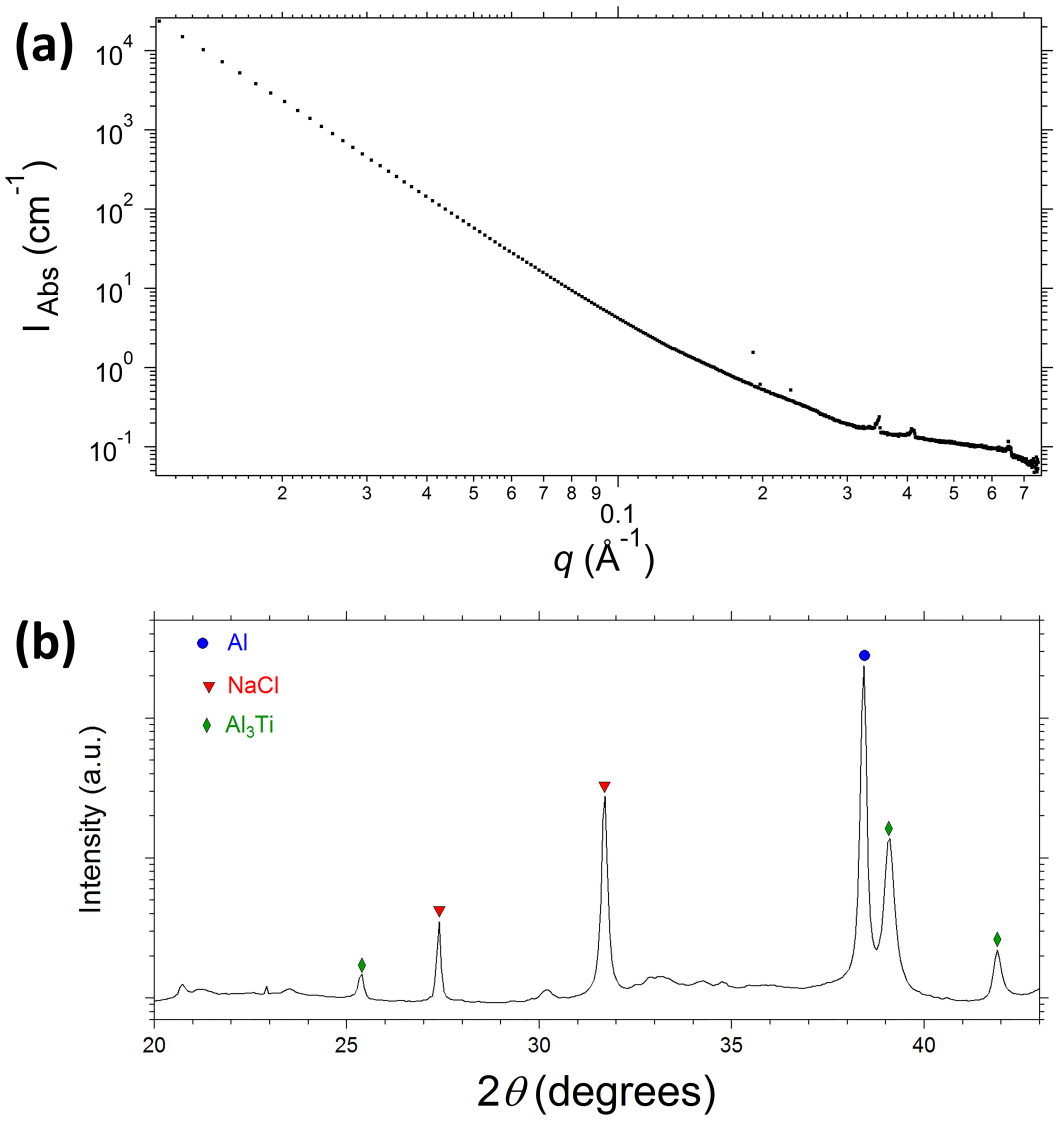

Figure 5.4: *Ex situ* (a) SAXS and (b) WAXS patterns for the porous Al scaffold at room temperature[91]. The 2θ (degrees) have been converted for $\lambda = 1.5406$ Å. In (a) the three peaks at high q are due to scattering from the beam stop, see §2.2.4.

5.3.1 Mesopore size distribution

5.3.1.1 Unified model

The scattering pattern of the Al porous scaffold was modelled with the a multi-level unified model[145] in Irena[149] (see Fig. 5.5 and §2.2.5.2). Region 1, fitted using two levels of the model, is attributed to the pore structure of the scaffold and has one

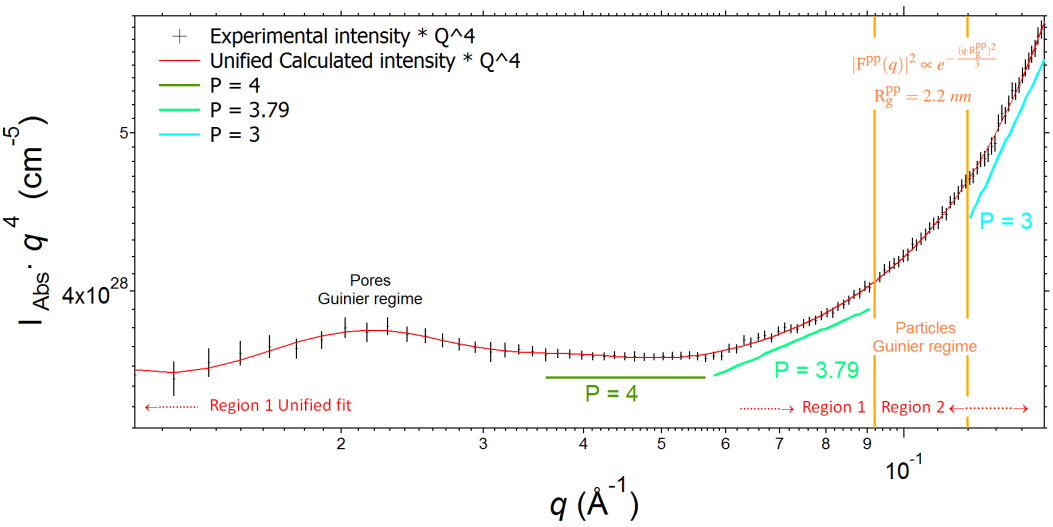

Figure 5.5: SAXS plot (black marks) and unified fit (red line) of Al scaffold plotted as $I_{\text{Abs}}q^4(\text{cm}^{-1})$ versus $q(\text{Å}^{-1})$ plotted on a log scale[91].

Guinier regime and two distinct Porod regimes, $P = 4$ and $P = 3.79 \pm 0.01$. In the q-range 0.036 – 0.057 Å^{-1}, where $P = 4$, the pore surface appears to be smooth, while in the q-range 0.06 – 0.09 Å^{-1}, where $P = 3.79$, the pore surface exhibits a roughness with a fractal dimension of $D_s = 6 - P = 2.21$ (see §2.2.5.1). For the $P = 4$ region, using the TNNLS method, a lognormal-size distribution of pores is obtained, which is shown in Fig. 5.6. It was possible to obtain the dominant, in terms of porosity, centred (19(1) nm) log-size distribution of mesopores (Fig. 5.6) for the Al scaffold by applying the TNNLS method to the SAXS pattern in the Guinier regime in Region 1 of the unified model (Fig. 5.5), since the Porod regime in Region 1 is associated with a smooth surface, $P = 4$ (spherical form factor intensity approximation).

The other Guinier regime in Region 1, associated to the level having the Porod regime, $P = 3.79$, has not been considered because of its reduced q extension (Fig. 5.5). Indeed, this extra fitting level, which is composed mainly by the Porod regime, $P = 3.79$, has been used exclusively as a fitting tool to overcome the limitation of the model by taking into consideration the change in power-law scattering variable, P, in the Porod regime. The self-similar trend of the mesopore structure expressed

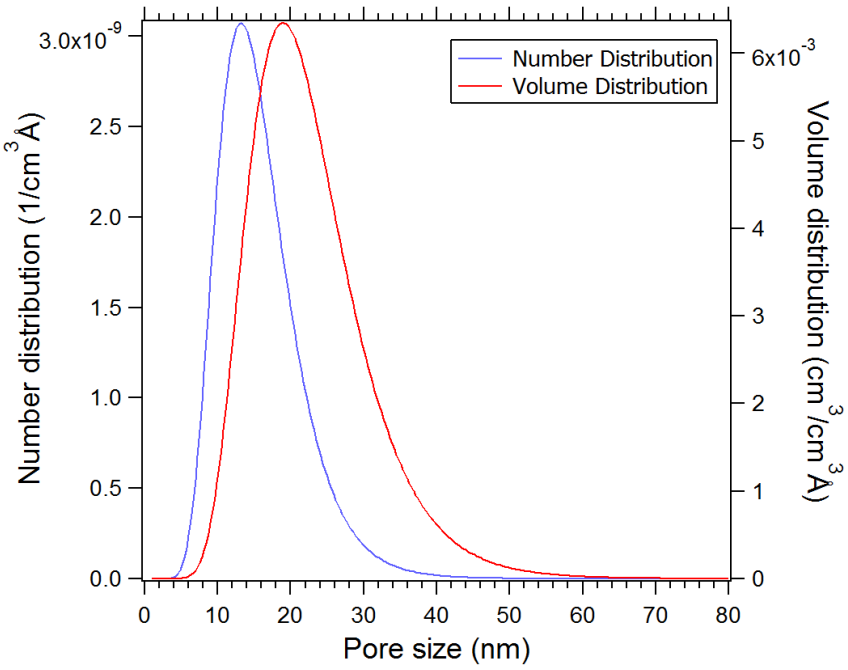

Figure 5.6: Mesopore number and volume Gaussian log-size distributions of the Al porous scaffold calculated by applying the Maximum Entropy and Total Non-negative least square (TNNLS) method from the Irena 2.62 SAS tool package, to the SAXS pattern in the Guinier regime in Region 1 of the unified model (Fig. 5.5)[148].

by the Porod regime of Region 1 is interrupted by another structure (Region 2). Such a structure presents a Guinier regime with a 2.2 nm radius of gyration, and a Porod regime possessing a power-law scattering variable, $P = 3$. Such a power-law scattering variable can be attributed either to a surface fractal or a mass fractal, as such a slope is on the transition between the two types of scattering[190].

5.3.1.2 Method of the invariant

The total porosity, φ_{total} (44.6(7)%), of the Al scaffold used for the BET/BJH measurements, was calculated using eq. 2.47, taking into account its measured physical specific volume (V_{total}, Fig. 3.4(b)), and its 100% dense crystal specific volume determined from the phase quantification (V_{solid}, Table 3.3) of the scaffold. The total specific pore volume (including the pores and voids) was calculated by subtracting the solid specific volume of the Al scaffold from the total specific volume

of the scaffold, $V_{\text{total pore}} = V_{\text{total}} - V_{\text{solid}}$ and was determined to be 0.38 cm^3/g. The specific pore volume corresponding to the formation of mesopores as calculated from the BJH method (§2.6.2) is equal to 0.027 cm^3/g (Fig. 5.7). The remaining specific pore volume, 0.353 cm^3/g, is due to the presence of macropores and voids. These observations are in agreement with the SEM micrographs (Fig. 5.1). The invariant method (see eq. 2.37) , and the local relation $2R = 2\pi/q$, was applied to the SAXS measurements of the Al scaffold in order to calculate the cumulative mesoporosity, $\varphi_{\text{partial}}(2R)$, as a function of pore size (Fig. 5.7). In order to relate the cumulative pore volume derived from the BJH method with the cumulative mesoporosity calculated using the invariant method (Fig. 5.7), eq. 5.2 was used.

$$\frac{\varphi_{\text{partial}}}{V_{\text{partial pore}}} = \frac{\varphi_{\text{total}}}{V_{\text{total pore}}} = \frac{44.6(\%)}{0.38(\text{cm}^3/\text{g})} \tag{5.2}$$

Fig. 5.7 shows that the cumulative pore volume that is associated with mesopores

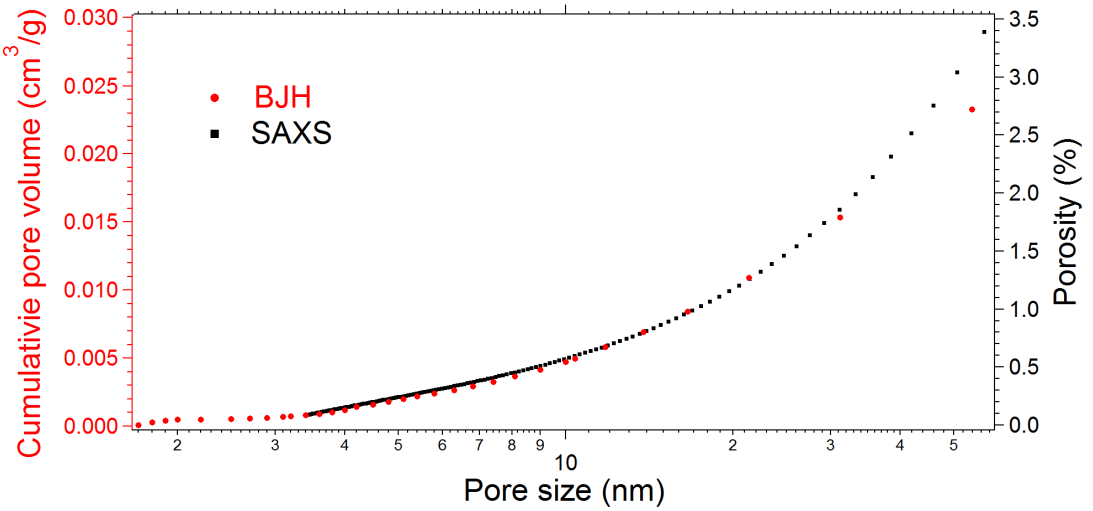

Figure 5.7: Cumulative specific pore volume as a function of pore size of the porous Al scaffold. This includes, in red, data obtained using the BJH method (N_2 sorption technique) and in black data obtained using the method of the invariant (SAXS technique)[91].

contributes a partial porosity of only $\simeq$ 2.7%, whereas the remaining 41.9% of the scaffold's porosity is due to the presence of macropores and voids. The cumulative mesoporosity as a function of pore size has been measured independently using

two different techniques, N_2 sorption (BJH method) and SAXS (method of the invariant). The two patterns (Fig. 5.7) are in agreement up to $\simeq$ 31 nm while the differences tend to be appreciable for bigger pore size ($\simeq$ 54 nm) mainly because the differences in composition and mass loss between the two Al scaffolds used in each technique (see Table 3.3). In fact, the porous Al scaffold used for the SAXS measurements has an estimated higher total porosity, $\varphi_{\text{total}} = 47.8(8)\%$. Moreover, the sample used for the N_2 sorption technique has been exposed to air for approximately one second, which could have partially oxidised the sample resulting in a reduction in porosity. Another reason is that bigger ($2R \simeq 54$ nm) pore size structures tend to be comparable with the longitudinal X-ray coherence length ($\xi_1 = 258$ nm, Appendix A.3) reducing the effect of constructive interferences which the invariant method relies on ($2R << \xi_1$). For pore sizes smaller than 3.4 nm ($q > 0.1844$ Å^{-1}), the cumulative mesoporosity as a function of pore size calculated using the invariant method (not shown in Fig. 5.7) suddenly diverges from the trend of the cumulative mesoporosity calculated using the BJH method. Such disagreement between the two techniques corresponds to the q range covering Region 2 in Fig. 5.5, determined from the unified modelled for the scattering pattern of the Al porous scaffold. This represent evidence that the dominant structure in Region 2 is a particle structure.

5.3.1.3 Calculation of porosity distribution using McSAS analysis

The mesopore specific pore volume distribution (Fig. 5.3) was also calculated using McSAS (spherical pore shape) analysis method (§2.2.5.4) applied on the SAXS measurement of the Al scaffold (Fig. 5.4(a)) and plotted in Fig. 5.3. It has been rescaled in order to match the mesopore specific pore volume distribution calculated using BJH method and, thus, it is dependent on the BJH pattern. The features of the two patterns are in agreement for pore sizes larger than 3.4 nm, similar to the two independent cumulative specific pore volume pattern trends shown in Fig. 5.7.

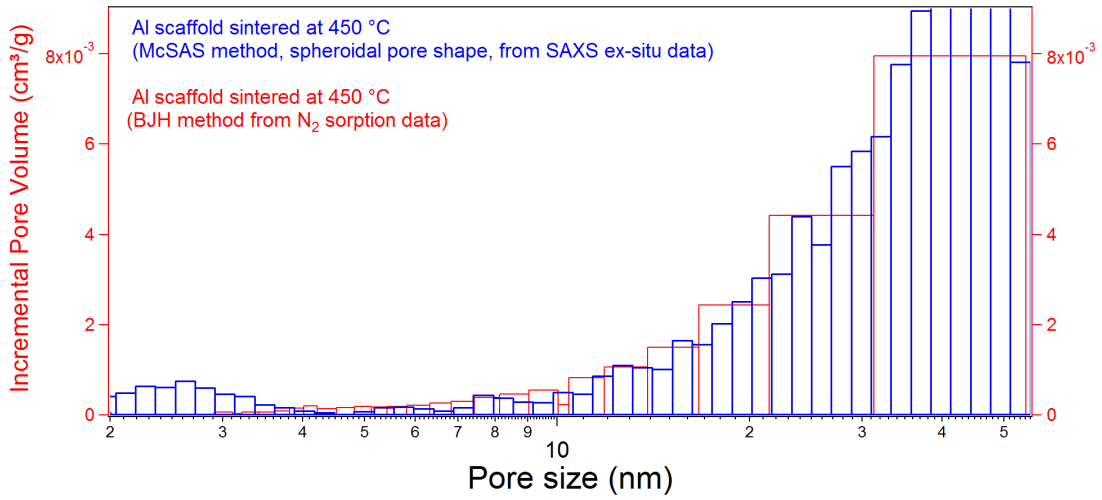

Figure 5.8: Spheroidal pore model and BJH mesopore specific pore volume distribution of the porous Al scaffold. This includes, in blue, data obtained from McSAS (spheroidal pore shape, aspect radius of semi-axes c to a and b: 0.1 – 10.0) method (*in situ* SAXS technique) and, in red, data obtained using BJH method (N_2 sorption technique).

The blue mesopore specific pore volume distribution (Fig. 5.8) was calculated using a form factor intensity for a spheroidal pore shape (aspect radius of semi-axes c to a and b: 0.1 – 10.0 — see §2.2.5.4). The distribution obtained using this spheroidal pore shape model (Fig. 5.8) is a worse match to the BJH distribution than the spherical pore shape model (Fig. 5.3). For pore sizes smaller than 3.4 nm, the two mesopore specific pore volume distributions in Fig. 5.3 are in disagreement, probably because of porosity differences due to differences in phase composition and masses loss of the different Al scaffolds used (see Table 3.3), or because the structure dominant in the Region 2 of the unified model (Fig. 5.5) is a homogeneous mass agglomerates of single phase (particles) characterised by appreciable electron density changes.

In order to check if it would be consistent to have a structure of homogeneous mass agglomerates of a single phase (particles) dominating the scattering pattern for resolutions ($r = d/2$) < 1.7 nm ($d = 3.4$ nm), a comparison between absolute intensity contributions due to the pore surface interfaces of the scaffold and due to the agglomerate-scaffold interfaces is considered below.

From the differences in amorphous phase content and mass loss (caused by the sintering process) between the Al scaffold with the highest mass loss (1.8(4) wt% amorphous content, see Table 3.3) and the Al scaffold used for *in situ* SAXS measurements (3.7(3) wt% amorphous content, see Table 3.3), the estimated amorphous Na content obtained for the former scaffold is 1.9(4) wt%. The remainder of the amorphous content is most likely metal traces from the starting materials (see Table 3.1): 1.0(2) wt%, mainly lead, and 'Ti' 0.8(2) wt%.

Relying on the scaffold phase composition (Table 3.3) and their crystalline densities obtained using Rietveld refinement analysis, the crystal density of the Al scaffold, was calculated to be $\rho_{\text{Scaffold}} = 2.71$ g/cm^3. The density of the amorphous phases were approximated as theoretical crystalline densities, for instance, $\rho_{\text{Na}} = 0.968$ g/cm^3 and $\rho_{\text{Metal traces}} = 7.15$ g/cm^3. The Al scaffold scattering length density, $\Delta\rho_{\text{SLD, Scaffold-Pores}} = \rho_{\text{SLD, Scaffold}} = 2.24 \times 10^{11}$ cm^{-2}, was calculated using eq. 2.25, and using the phase composition in Table 3.3, crystal density of the Al scaffold ($\rho_{\text{Scaffold}} = 2.71$ g/cm^3), and the real scattering factors (f_1(12 keV) in Table A.1).

Among the several phases present in the Al scaffold (Table 3.3), the Na and metal traces present the most appreciable differences in scattering length density compared with the Al scaffold, $\Delta\rho_{\text{SLD, Scaffold-Na}} = (2.24 - 0.79)\ 10^{11}$ cm^{-2} and $\Delta\rho_{\text{SLD, Scaffold-Metal traces}} = (2.24 - 6.58)\ 10^{11}$ cm^{-2} respectively. For the sake of simplicity, the system was modelled as consisting only of spherical pores of a specific radius (R) corresponding to the average pores radius of 500 nm (Fig. 5.1) and total porosity (φ_{total}) of 47.8%. For agglomerates of Na, combining equations 2.29 – 2.31, the following relation for the ratio ($I_{\text{Abs, Scaffold-Pores}}/I_{\text{Abs, Scaffold-Na}}$) between the absolute intensity contributions due to the pore surface interfaces and due to

the agglomerate-scaffold interfaces of the scaffold is obtained:

$$\begin{aligned}\frac{I_{\text{Abs, Scaffold-Pores}}}{I_{\text{Abs, Scaffold-Na}}} &= \frac{V_{\text{particle}}(r)(\Delta\rho_{\text{SLD, Scaffold-Pores}})^2 S^{\text{particle}}_{\text{Scaffold-Pores}}(r)}{V_{\text{particle}}(r)(\Delta\rho_{\text{SLD, Scaffold-Na}})^2 S^{\text{particle}}_{\text{Scaffold-Na}}(r)} \simeq \\ &\simeq \frac{(\Delta\rho_{\text{SLD, Scaffold-Pores}})^2 \frac{V_b(r)}{V_{ss}}}{(\Delta\rho_{\text{SLD, Scaffold-Na}})^2 \frac{V_{\text{Na}}}{V_{ss}}} = \\ &= \frac{(\Delta\rho_{\text{SLD, Scaffold-Pores}})^2 \frac{4\pi R^2 r}{\frac{4\pi}{3}R^3 \frac{1-\varphi_{\text{total}}}{\varphi_{\text{total}}}}}{(\Delta\rho_{\text{SLD, Scaffold-Na}})^2 \frac{\rho_{\text{Scaffold}}}{\rho_{\text{Na}}} \frac{\text{wt\% of Na}}{100}} = \\ &= \left(\frac{\Delta\rho_{\text{SLD, Scaffold-Pores}}}{\Delta\rho_{\text{SLD, Scaffold-Na}}}\right)^2 \frac{3r}{R} \frac{\varphi_{\text{total}}}{1-\varphi_{\text{total}}} \frac{\rho_{\text{Na}}}{\rho_{\text{Scaffold}}} \frac{100}{\text{wt\% of Na}}\end{aligned} \tag{5.3}$$

where the structure factor of the Na agglomerates, $S_{\text{Scaffold-Na}}$, was approximated to be the ratio between the volume of the scaffold occupied by Na agglomerates and the total solid volume of the scaffold ($\simeq V_{\text{Na}}/V_{ss}$) neglecting the interference due to the relative position between Na agglomerates ($\sin(qr_{jk})/qr_{jk} \simeq 1$ in eq. 2.22 – 2.23) justified by the reduced Na content (1.9(4) wt% of Na << 100 wt% of all phases).

The intensity ratio calculated from eq. 5.3 using the variables provided above is 0.4(2), which means that the scaffold-Na interface scattering effects are at least comparable with the scattering effects due to the pore surface interface of the scaffold. Similarly, considering agglomerates of the metal traces, the intensities ratio is 0.6(3).

It is worth noting that the intensity from the pore-surface interfaces ($I_{\text{Abs, Scaffold-Pores}}$) tends to be dominant over the intensity from the agglomerate-scaffold interfaces ($I_{\text{Abs, Scaffold-Na}}$) at larger resolutions r, which is equivalent to smaller momentum transfer $q = \pi/r$. Indeed, the relationship $I_{\text{Abs, Scaffold-Pores}}/I_{\text{Abs, Scaffold-Na}}$, in eq. 5.3, is linear in terms of r.

The results obtained using the simple model in eq. 5.3 can be considered only qualitative as it is based on an estimation of a single pore radius (R), overestimated amorphous densities (ρ_{Na} and $\rho_{\text{Metal traces}}$), and overestimated homogeneous contents (wt%) of Na and Metal traces (which should be considered only those

aggregates of size $> 2r$).

In conclusion, it is possible that the structure associated with Region 2 of the unified fit of the Al scaffold SAXS pattern in Fig. 5.5 could be due to homogeneous mass agglomerates of single phase (particles).

5.3.2 Specific surface area

The specific surface area, using eq. 2.33, was calculated as 6 ± 0.5 m^2/g and agrees well with the surface area (7.9 ± 0.1 m^2/g) measured by the N_2 adsorption/desorption method (BET) in §5.2.2.

The terms $P = 3.79$ and $I_{Abs} \times q^{3.79} = 1.387 \times 10^{27}$ $cm^{-4.79}$ were determined by fitting the SAXS measurements of the Al scaffold in the q-range 0.06 – 0.09 $Å^{-1}$ (the Porod regime of the pore structure — see Fig. 5.5). The trend of the Porod limit of the mesopore structure, associated to a fractal surface of degree of roughness $D_s = 6 - P = 2.21$, was expected to extend down to a resolution of the order of molecular size (for instance, Al, Al_3Ti and NaCl), where the hypothesis of homogeneous (uniform averaged) electron density breaks down ($q \simeq \pi / r_{mh}$, see §2.2.5.1)[139,146]. However, the trend of the Porod limit of the pore structure (Region 1 in Fig. 5.5) is interrupted at $q = 0.09$ $Å^{-1}$ ($r = 3.5$ nm) by a presumably homogeneous mass agglomerate of single phase particles (Region 2 in Fig. 5.5), characterised by appreciable electron density changes (§5.3.1.3). Assuming that the structure associated with Region 2 in Fig. 5.5 is not porous, the specific surface of the Al scaffold can be calculated using the resolution equivalent to the N_2 molecule size ($r = 0.4$ nm), which is the pore size resolution of the specific surface area obtained using the BET method (§5.2.2). The other terms in eq. 2.33 used to calculate the specific surface area are: $\rho_{Scaffold} = 2.71 g/cm^3$ and $\Delta\rho_{SLD,\ Scaffold\text{-}Pores} = 2.24 \times 10^{11}$ cm^{-2}, introduced in §5.3.1.3. $F(2.21) = 1.991$ and $r = 0.4$ nm in order to compare the result obtained from the SAXS measurement with the result obtained using the BET method.

The specific surface area derived from SAXS and BET is relatively small when compared to the specific surface area of mesoporous materials. This is mainly due

to the large number of macropores and voids present in the sample in comparison with the number of mesopores (Fig. 5.1).

5.4 *In situ* SAXS/WAXS

In order to understand the dynamic of the mesopore formation during the sintering process leading to the production of Ti-enriched Al scaffolds, *in situ* SAXS/WAXS experiments during the decomposition of two $NaAlH_4$ pellets were carried out and the data analysed. The apparatus and setting adopted is discussed in detail in §2.2.1. The two $NaAlH_4$ pellets were heated up to 400 °C and 450 °C from room temperature using the same heating rate , 5 °C/min, and similar dynamic vacuum pressure, 1.5×10^{-2} mbar, as that used to produce the Al scaffolds (§3.2). The $NaAlH_4$ pellets used in these two experiments will be referred to as $NaAlH_4$-400 and $NaAlH_4$-450, respectively.

5.4.1 *In situ* WAXS

The *in situ* WAXS patterns, of $NaAlH_4$-400 and $NaAlH_4$-450 decompositions, are shown in Figures 5.9 and 5.10, respectively.

In Fig. 5.9, the diffraction peaks associated with NaAlH4 suddenly decrease and disappear between 210 and 225 °C. Following the first step of $NaAlH_4$ decomposition (eq. 1.3), the intensities of the diffraction peaks associated with Na_3AlH_6 and Al increase. The second step of decomposition (eq. 1.4), where Na_3AlH_6 desorbs further hydrogen and produces NaH and further Al is observed over a wide temperature range; NaH diffraction peaks are observed from 225 °C and Na_3AlH_6 diffraction peaks are visible up to 353 °C.

For the *in situ* SAXS/WAXS experiment of $NaAlH_4$-450, as shown in Fig. 5.10, the decomposition temperatures were considerably higher than those seen with $NaAlH_4$-400 as shown in Fig. 5.9. It is conjectured that this difference is, in minor part, due to different specimen size and initial phase composition.

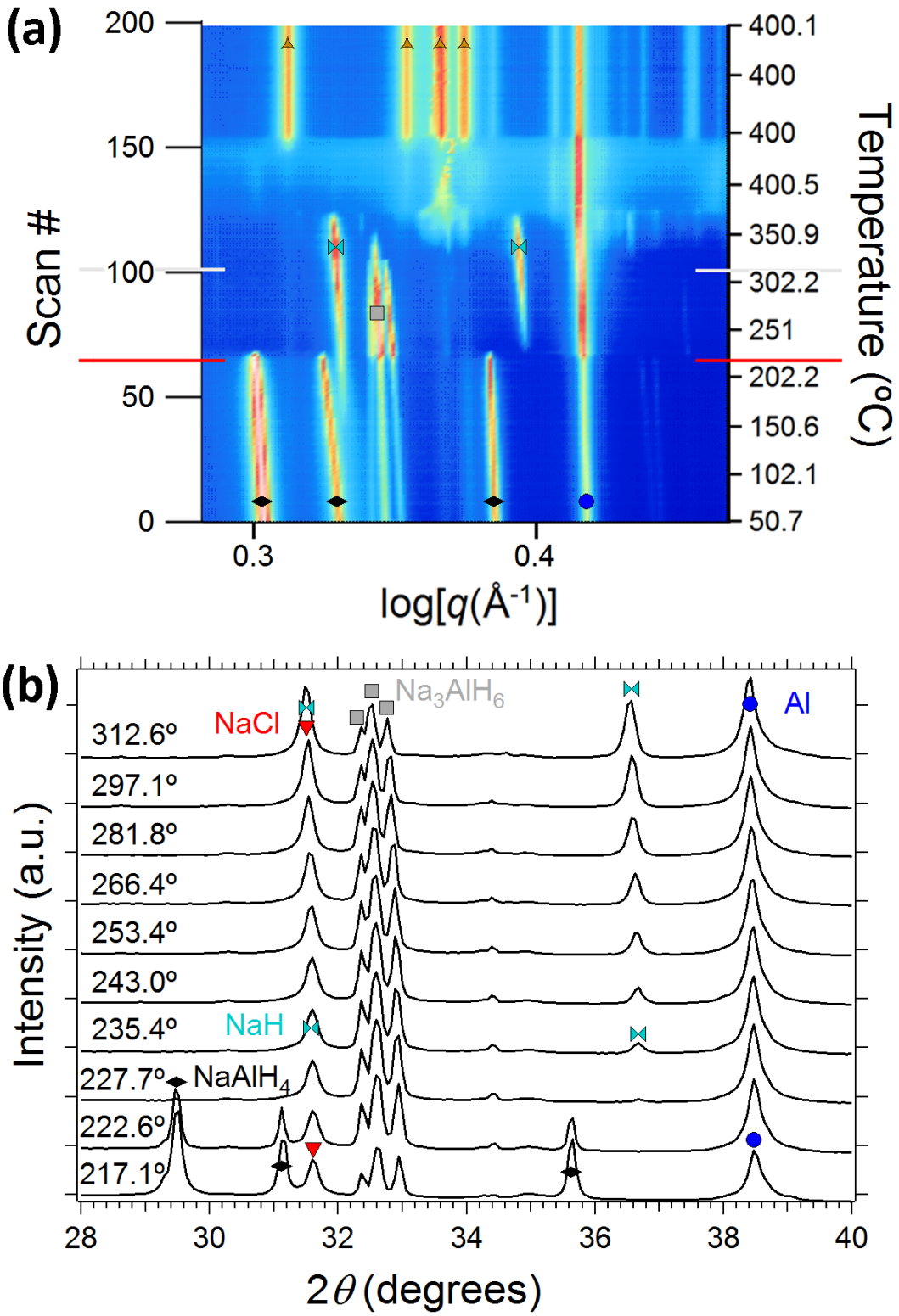

Figure 5.9: *In situ* WAXS patterns of $NaAlH_4$-400 decomposition. (a) Collated patterns viewed down the intensity axis with colours representing intensity, and (b) stack plot of individual patterns, from 217.1 °C (red line) to 312.6 °C (light grey line), showing the peak profiles. The 2θ (degrees) has been converted for $\lambda = 1.5406$ Å.

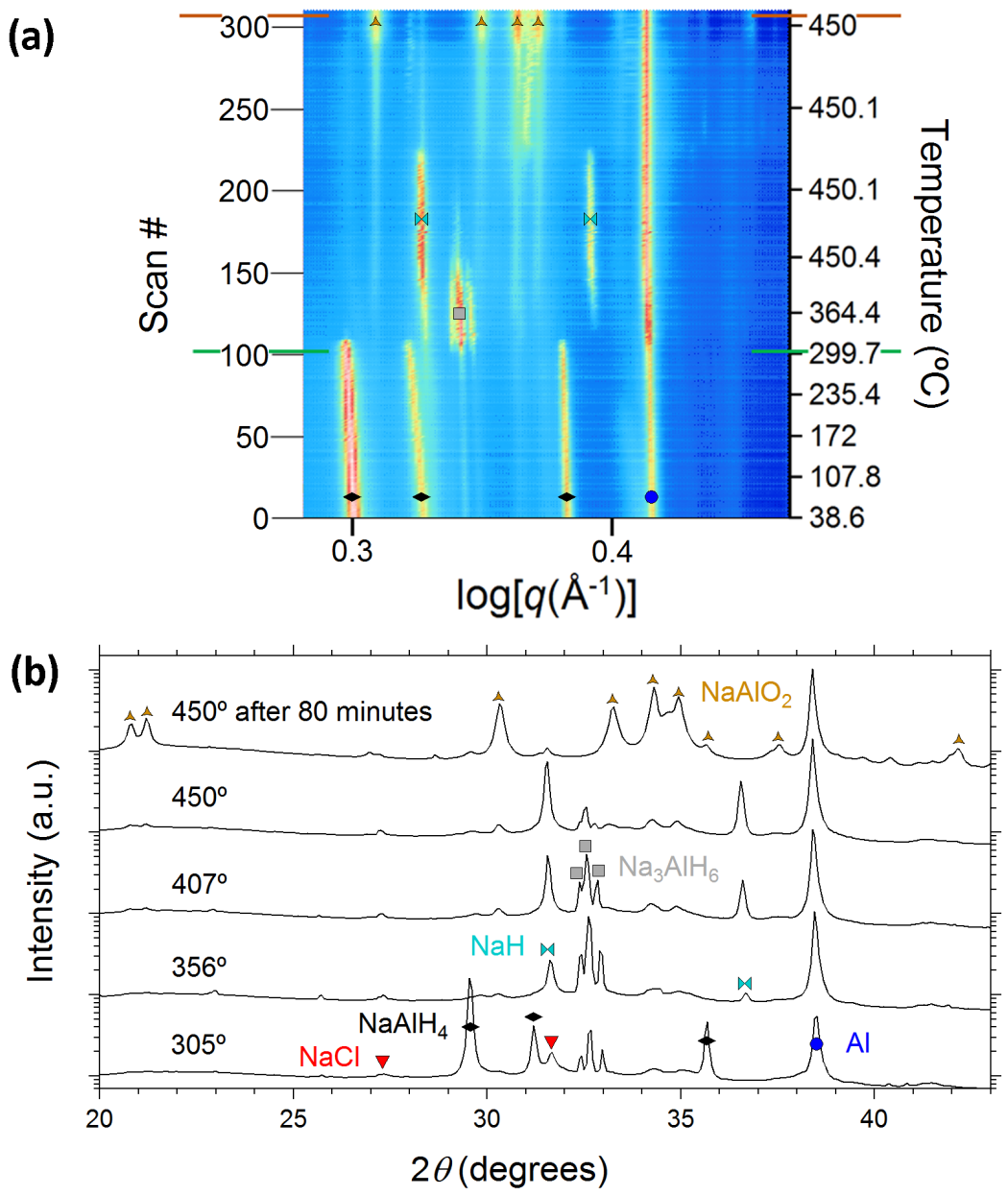

Figure 5.10: *In situ* WAXS patterns of $NaAlH_4$-450 decomposition. (a) Collated patterns viewed down the intensity axis with colours representing intensity, and (b) stack plot of individual patterns, from 305 °C (green line) to 450 °C (brown line), showing the peak profiles. The 2θ (degrees) has been converted for $\lambda = 1.5406$ Å.

However, the temperature ranges of the first two steps of decomposition between the two experiments were consistent, $\Delta T_{\text{1st step}} \simeq 15°C$ and $\Delta T_{\text{2nd step}} \simeq 125°C$ respectively.

Unfortunately, for temperatures higher than 320 °C, evidence of sample oxidation was observed in the presence of $NaAlO_2$ diffraction peaks (PDF 00-033-1200, Figures 5.9 and 5.11). This is most likely due to fracturing of the borosilicate glass capillary (Fig. 5.12(b)). At approximately 370 °C, NaH diffraction peaks suddenly disappear but no crystalline Na is observed. Neither diffraction peaks of oxidised Na and NaH were observed. The diffraction peaks of the oxidation phase $NaAlO_2$ steadily increase their intensities until approximately 400 °C after 10 minutes of isothermal sintering (scan #155), where the $NaAlO_2$ diffraction peaks reach their highest intensities and distinct defined shapes. This effect is even more evident for the experiment of $NaAlH_4$-450 decomposition (see the Fig. 5.10). It is thus presumed, that the non-crystallized Na and/or NaH have not been gasified but they are still in the system in an amorphous and/or liquid form in agreement with thermodynamic prediction, obtained using thermodynamic parameters from Table 2.2 for Na(l), and as shown in the work of Abdessameud *et al.*[47] for NaH(l). The temperatures of the first two observed $NaAlH_4$ decomposition steps are higher than the temperatures predicted from the calculation of $NaAlH_4$ decomposition[‡] (Fig. 1.5), which is due to kinetic limitations. The Al_3Ti appears only for temperatures higher than 300 °C in agreement with XRD measurements reported by Haiduc *et al.*[69]. For lower temperatures, although Ti is present in the system, no diffraction peaks of 'Ti' species have been observed.

The d-spacing associated with each set of diffraction peaks ($d = 2\pi/q$ in Figures 5.9(a) and 5.10(a)) present the same relative increase, consistent with a homogeneous thermal expansion of the associated crystal structures. Such consistencies in peak positions were found useful in identifying diffraction peaks belonging to the same phase.

The *in situ* sample phase quantification and crystalline densities were calculated at each scan # relying on information from:

- Phase quantification ratio between main phases and phase crystalline

[‡]at local thermodynamic equilibrium, considering the dynamic vacuum condition $P = 1.5 \times 10^{-2}$ mbar.

densities obtained from the Rietveld refinement on *in situ* WAXS data. The starting values for the relative phase quantification and phase crystalline densities were obtained from the previous scan's Rietveld refinement.

- Thermodynamic pathway (equations 1.3 – 1.5 and Fig. 1.5).
- Phase quantification of $NaAlH_4$ + 2 mol% $TiCl_3$ ball-milled (Table 3.2).

For the identification and quantification of the crystalline phases present in the WAXS patterns, the specimen displacements were taken in consideration, as discussed in §2.2.4.

The *in situ* phase quantification is shown in Fig. 5.11.

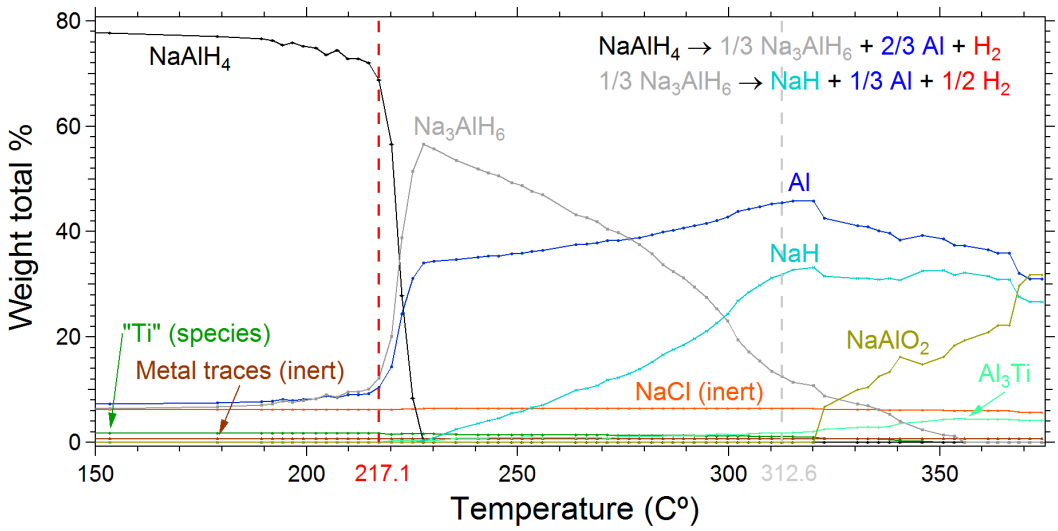

Figure 5.11: *In situ* phase quantification of the decomposition of the $NaAlH_4$ pellet heated up to 400 °C.

As shown in Fig. 5.9(b), between 225 °C and 228 °C, $NaAlH_4$ disappears while NaH appears. Up to 225 °C, one piece of information used to calculate the *in situ* phase quantification is the weight ratio between $NaAlH_4$ and Na_3AlH_6. From 228 °C up to 253 °C, after which Na_3AlH_6 disappears, the information used is the refined weight ratio between Na_3AlH_6 and NaH. From 323 °C, corresponding to the appearance of $NaAlO_2$, the refined weight ratio between Al and $NaAlO_2$ is used to keep track of the Na and/or NaH amorphous/liquid and oxygen contents. Al_3Ti first appears at

220 °C, one of the information used to quantify the Ti present in the 'Ti' species is the refined phase quantification ratio between Al and Al_3Ti.

The *in situ* transmission, defined in Appendix A.5, values, shown in Fig. 5.12(a), are normalized taking in consideration the transmission of the empty capillary ($\tau_{cap} = I_{BS}(counts/s)/I_0(counts/s) = 51787/58095$). The high precision of the

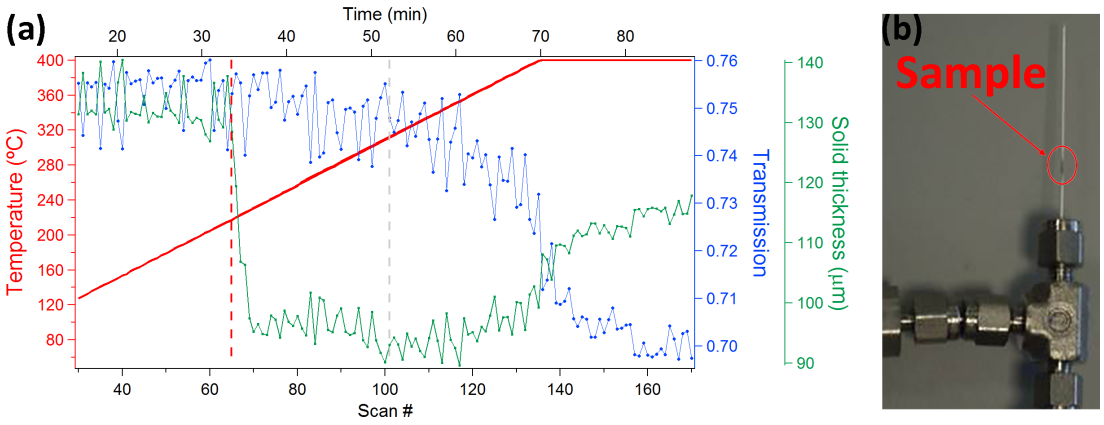

Figure 5.12: (a) *In situ* SAXS/WAXS measured transmission, τ_s, calculated solid thickness, d_{ss}, and temperature trends for the decomposition of a (b) $NaAlH_4$-400 contained into a borosilicate glass capillary connected to a dynamic vacuum pump system.

instrument used to measure the transmission (see §2.2.1), does not justify the oscillations in the transmission pattern. Such oscillations are presumably due to the movement of the sample inside the capillary (see Fig. 5.12(b)) caused by the dynamic vacuum applied and the release of hydrogen from the specimen.

In Figures 5.9(a), 5.11, 5.12(a) and 5.17(b), the vertical dotted lines correspond to two temperatures of particular interest. The red vertical dotted line at 217.1 °C corresponds to the temperature at which $NaAlH_4$ starts decomposing, see Fig. 5.9(b). The light grey vertical dotted line at 313 °C corresponds to the temperature where Na_3AlH_6 is almost completely consumed and before the sample starts oxidising (see Fig. 5.9(b)).

The averaged transmission trend (Fig. 5.12) was expected to increase slightly with the increase of temperature from 217 °C (red vertical dotted line) due to a reduction in scattering associated with the desorption of hydrogen. However, the averaged

transmission trend remains constant until 323 °C (just past the light grey vertical dotted line), with the appearance of $NaAlO_2$. The transmission continues to fall with the increase in $NaAlO_2$. From scan #155 the averaged transmission, τ_s, trend is stabilized at $\simeq 0.70$.

The solid thickness pattern (d_{ss} in Fig. 5.12(a)), calculated using eq. 5.1, suddenly drops, in correspondence with the first step of $NaAlH_4$ decomposition at 217 °C (red vertical dotted line) caused by the differences between the linear absorption coefficients of $NaAlH_4$ and the two products, Al and Na_3AlH_6. Successively, for the same reason, the solid thickness pattern slowly decreases across the second step of $NaAlH_4$ decomposition until the sample starts oxidising at 323 °C (just passed the light grey vertical dotted line). From 323 °C, as a consequence of the increase in the sample mass due to the oxidation, the solid thickness of the sample increases.

5.4.2 *In situ* SAXS

In order to convert measured SAXS intensities to absolute intensities ($I_{\text{Abs, scan \#}}$, §2.2.3) and then model the converted SAXS patterns, the solid thickness ($d_{\text{ss, scan \#}}$) and the scattering length density ($\Delta\rho_{\text{SLD, scan \#}}$) of the sample, must be calculated. The solid thickness and the scattering length density of $NaAlH_4$-400 were calculated for each scan relying on the quantitative phase analysis (Fig. 5.11) and crystalline densities reported in the previous section (§5.4.1). The converted *in situ* SAXS patterns of $NaAlH_4$-400 decomposition (Fig. 2.12), were modelled with McSAS (§2.2.5.4) in two ways:

1. The *in situ* pore size relative distributions — $(\Delta\rho_{\text{SLD, scan \#}})^2(1-\varphi_{\text{total, scan \#}})(\varphi_{i\text{, scan \#}})/(\Delta\rho_{\text{SLD, Al-Scaffold}})^2(\varphi_{\text{total, scan \#}})^2$ — in Figures 5.13(a) and 2.13, were obtained by setting the scattering length density of all scans to the same value, that of the Al scaffold (2.24×10^{11} cm^{-2}, see §5.3.1.3). This was done due to software limitations.

2. The *in situ* pore size relative distributions — $(1-$

$\varphi_{\text{total, scan \#}})(\varphi_{i\text{, scan \#}})/(\varphi_{\text{total, scan \#}})^2$ — in Figures 5.14(a) and Fig. 5.17(a), were calculated using scattering length densities calculated individually for each scan from the quantitative phase analysis.

In these equations, $\varphi_{i\text{, scan \#}}$ is the contribution to the total porosity, $\varphi_{\text{total, scan \#}}$, of those modelled spherical pores having a size of $2R_i$, see §2.2.5.4. Considering the total porosity, for the initial $NaAlH_4$ pellet (0.20 ± 0.02, see §5.1) and for the 12 hour sintered porous Al scaffolds (0.46 ± 0.02, see §5.3.1.2), the term $(1 - \varphi_{\text{total, }T})/(\varphi_{\text{total, }T})^2$ is expected to monotonically decrease with increasing temperature. If $(1 - \varphi_{\text{total, }T})(\varphi_{i\text{, }T})/(\varphi_{\text{total, }T})^2$ monotonically increases with increasing temperature, this would show that the partial porosity, $\varphi_{i\text{, }T}$, is growing faster than the decrease in $(1-\varphi_{\text{total, }T})/(\varphi_{\text{total, }T})^2$.

Associated with the first step of $NaAlH_4$ decomposition, from 217 °C to 228 °C, the intensities of the mesoporosity distributions, $\varphi_{i\text{, }T}$, increase remarkably (Figures 5.13(a) and 5.14(a)). From 228 °C, during the second step of decomposition, the intensities of the mesoporosity distributions gradually increase until reaching their maximum at 313 °C (Figures 5.13(a) and 5.14(a)). In Figures 5.11 and 5.12(a), this temperature, 313 °C, is indicated with a light grey dotted line and in Figures 5.9(a) and 5.17(b) with a solid light grey line.

There is a clear correlation between mesopore formation and crystalline structure changes during $NaAlH_4$ decompositions (Figures 5.13 and 5.14). In conjunction with the formation of $NaAlO_2$ from sample oxidation (scan #105, 323 °C), the intensities of the relative distributions of the mesopores drastically and monotonically decrease until the saturation of $NaAlO_2$ (scan #155 in Fig. 5.13, 10 minutes isothermal at 400 °C). This shows that oxidation adversely affects meso and microporosity, presumably through the oxidation of the surfaces of the meso and micropores.

For $NaAlH_4$-450, there were no appreciable changes in the pore size relative distributions, $\varphi_{i\text{, scan \#}} \times const_{\text{scan \#}}$, across the first two steps of $NaAlH_4$ decomposition, as well as during sample oxidation, see Figures 5.15(a), 5.16(a)

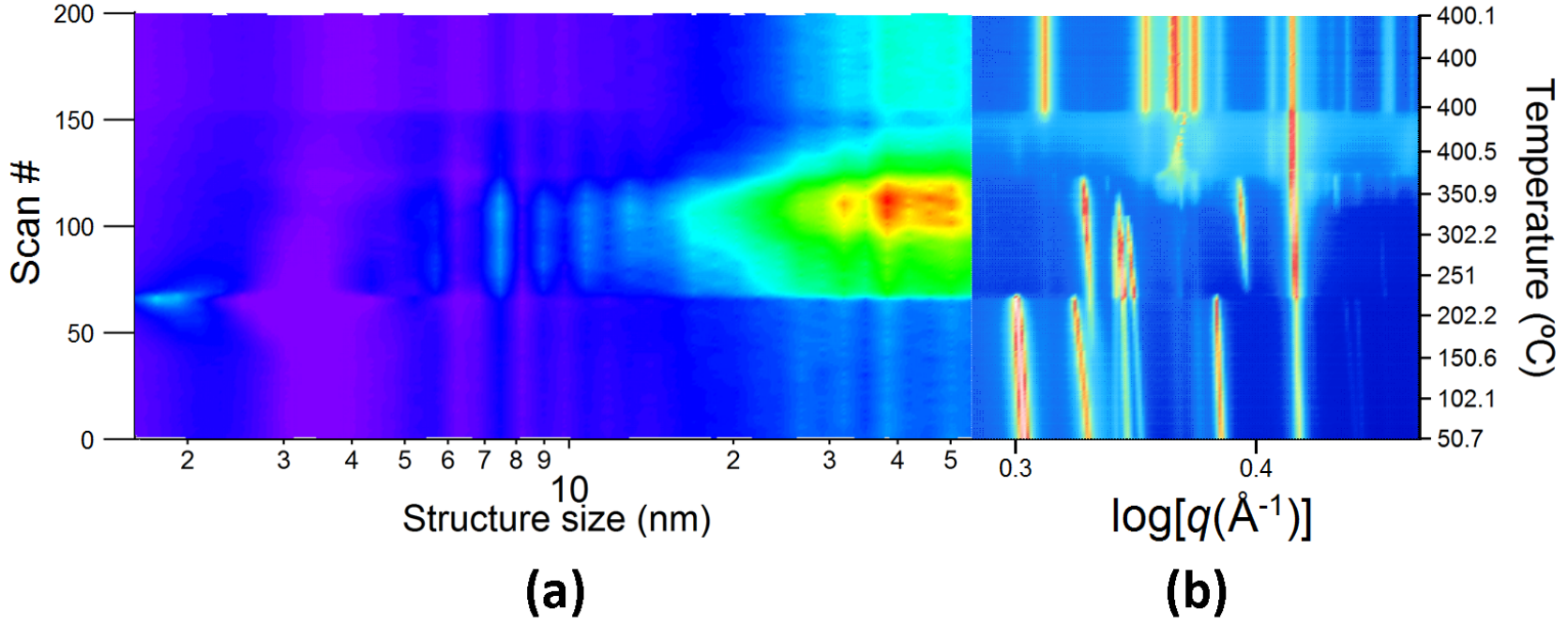

Figure 5.13: (a) *In situ* mesoporosity relative distribution, $(\Delta\rho_{\text{SLD, scan \#}})^2(1-\varphi_{\text{total, scan \#}})(\varphi_{i\text{, scan \#}})/(\Delta\rho_{\text{SLD, Al-Scaffold}})^2(\varphi_{\text{total, scan \#}})^2$, obtained applying McSAS analysis to SAXS patterns of $NaAlH_4$-400 decomposition and (b) the corresponding WAXS patterns.

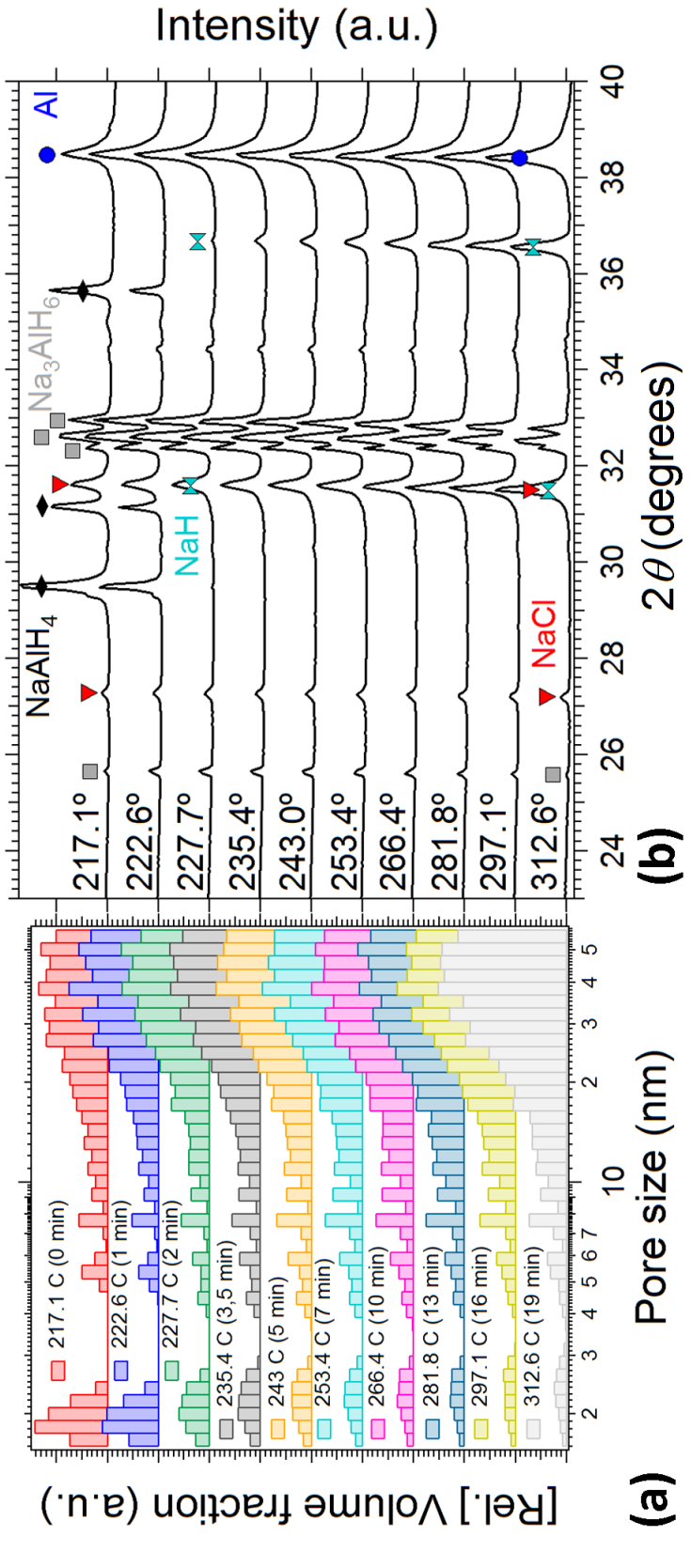

Figure 5.14: (a) *In situ* mesoporosity relative distribution, $(1-\varphi_{\text{total},T})(\varphi_{i,T})/(\varphi_{\text{total},T})^2$, obtained from McSAS analysis of SAXS patterns for $NaAlH_4$-400 decomposition and (b) corresponding WAXS patterns. The 2θ (degrees) has been converted for $\lambda = 1.5406$ Å.

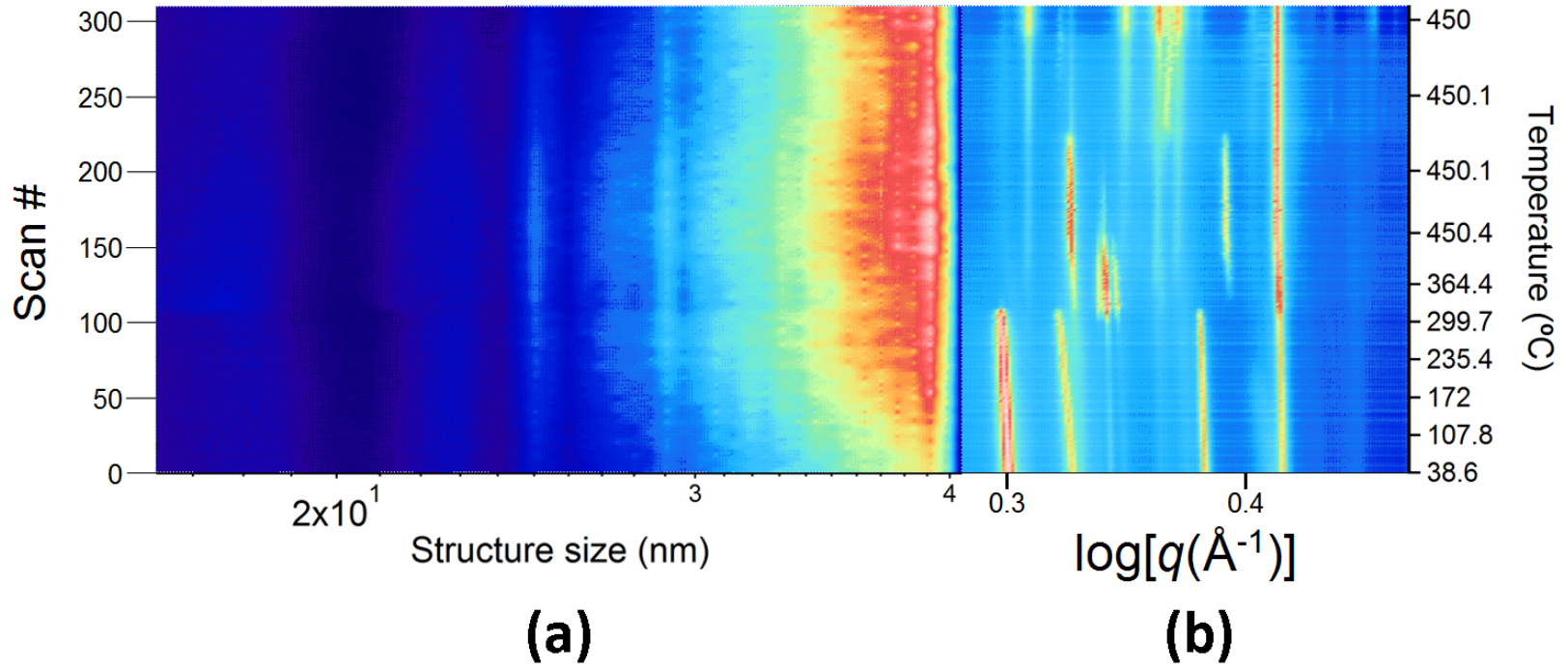

Figure 5.15: (a) *In situ* pore size relative distributions, $\varphi_{i,\,\text{scan }\#} \times const_{\text{scan }\#}$, obtained applying McSAS (spheroidal pore shape, aspect radius of semi-axes c to a and b: 0.5 – 5.0) analysis to SAXS patterns of $NaAlH_4$-450 decomposition and (b) the corresponding WAXS patterns.

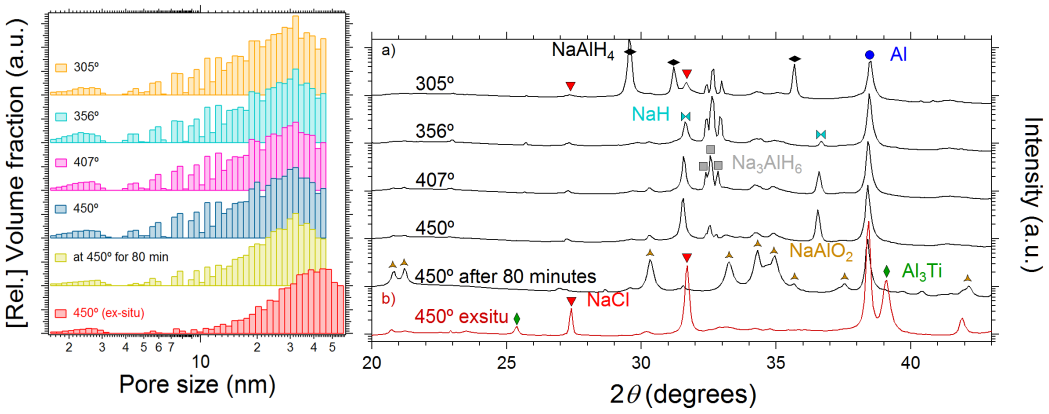

Figure 5.16: (left) Pore size relative distributions, $\varphi_{i,\,\text{scan }\#} \times const_{\text{scan }\#}$, obtained by McSAS (spherical pore shape) analysis, and (right) the corresponding WAXS patterns, where the 2θ (degrees) has been converted for $\lambda = 1.5406$ Å, for samples a) *in situ* $NaAlH_4$-450 decomposition at different temperatures and b) porous Al scaffold at room temperature previously sintered for 12 hours.

and J.1(a). It is not known why this is the case, as the WAXS data clearly show the expected decomposition steps.

5.4.3 *In situ* SAXS/WAXS analysis interpretation

Sintering is the process whereby pores in particulate materials are eliminated by atomic diffusion at high temperatures below the melting point[191–195]. In general, for metals within the first hour, the total pore volume decreases as material flows into voids which diffuse to the surface where they simply disappear. The diameter of the $NaAlH_4$ pellet was 8 mm (Fig 3.4(a)) while, after sintering, the dimeter of the produced Al scaffold was observed to be 7 mm (Fig.3.4(b)). As shown by Hu and Lu[194], mesopore evolution is characterised by coalescence and tortuosity. The final total porosity (0.46 ± 0.02, see §5.3.1.2) and mesoporosity distribution (Fig. 5.17(a)) of the 12 hour sintered Al scaffold is the result of two opposite effects: the formation of new mesopores due to $NaAlH_4$ decomposition and the growth and depletion of pores due to their diffusion to the surface. Because of the oxidation of the $NaAlH_4$ decomposed samples during the *in situ* SAXS/WAXS

experiments, only an indirect and general characterisation of the growth of pores with two isothermal sintering temperatures (400 and 450 °C) was possible. The characterisation, presented in Appendix K, shows the effects of different sintering temperatures on (*i*) the time taken for mesoporosity distributions to stop growing after the cessation of mesopore formation, and (*ii*) the mesopore sizes that present appreciable contributions to the total porosity. Appendix K shows that higher sintering temperatures are associated with longer times required for pore growth to cease, and with an increase in the size of these final mesopores having an appreciable contribution to the total porosity.

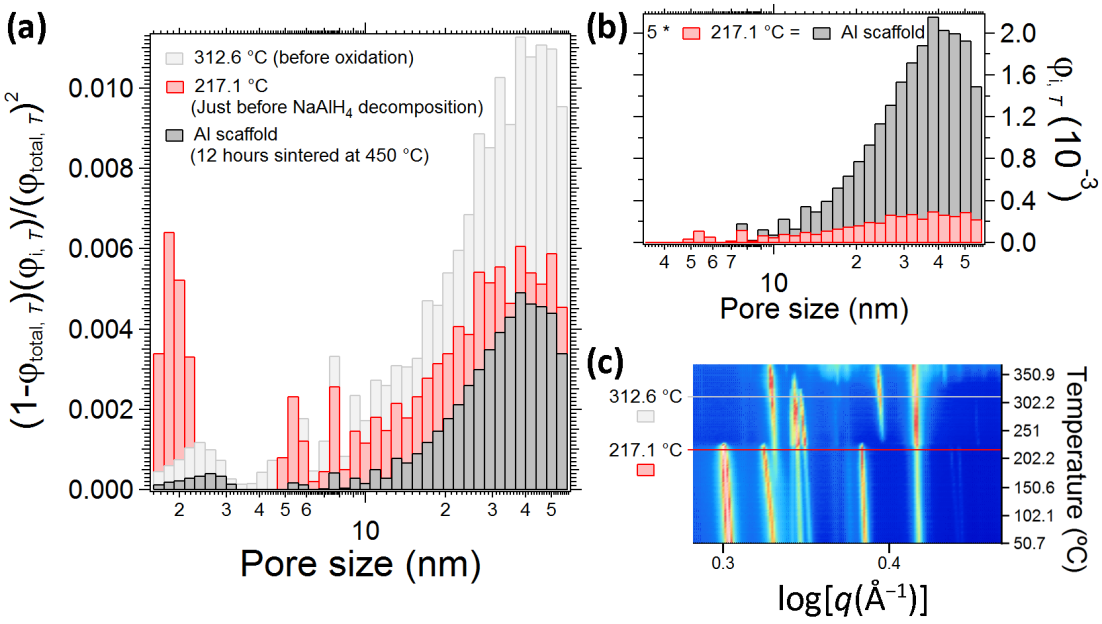

Figure 5.17: (a) Mesoporosity relative distribution, $(1-\varphi_{\text{total},\,T})(\varphi_{i,\,T})/(\varphi_{\text{total},\,T})^2$, and (b) estimated mesoporosity distribution, $\varphi_{i,T}$, calculated with assumed total porosities of 0.2 and 0.478 for red and black, respectively. Plots obtained from McSAS analysis of SAXS patterns for $NaAlH_4$-400 decomposition at two temperatures of interest (217.1 °C in red and 312.6 °C in light grey), and of the Ti-enriched porous Al scaffold at room temperature after sintering. (c) *In situ* WAXS patterns of $NaAlH_4$-400 decomposition.

In Figures 5.13(a) and 2.13, there is a peak in the size distribution centred at 2.0 ± 0.5 nm, appearing from 174 °C, and reaching its maximum intensity at 217 °C. The peak disappears in correspondence with the disappearance of the diffraction

peaks associated with $NaAlH_4$ (Figures 5.12, 5.14 and 5.17). In Figures 5.9(a), 5.11, 5.12(a) and 5.17(b), the temperature, 217 °C, is of particular interest and is indicated with a red line. This micro-size feature is reduced as quickly as the $NaAlH_4$ phase disappears from 217 °C to 228 °C (Fig. 5.14). As this micro-size feature is extended across several temperatures and sizes, it is unlikely to be due to an artefact. The distributions of pore sizes above and below 3.4 nm do not evolve one into the other; for instance, it is not observed as a shift of micro-size features toward the meso-size features compatible with micropore growth. The micro-size features could be also attributed to a non-porous structure, where the reduction in $NaAlH_4$ particle size just before any appreciable decomposition may play an important role.

In Fig. 5.17, the porosity relative distribution, $(1-\varphi_{\text{total},\,T})(\varphi_{i,\,T})/(\varphi_{\text{total},\,T})^2$, at 217 (red) and 313 (light grey) °C are shown. These correspond to the sample prior to appreciable $NaAlH_4$ decomposition, and where Na_3AlH_6 is almost completely consumed and before the sample starts oxidising, respectively. Fig 5.17(a) shows that for pore sizes greater than 3.4 nm there is a $\simeq 1.7\times$ increase in the relative total mesoporosity, $\sum_i(1-\varphi_{\text{total},\,T})(\varphi_{i,\,T})/(\varphi_{\text{total},\,T})^2$, between the two temperatures. Fig 5.17(b) shows the mesoporosity distribution assuming a total porosity of 0.2 (see §5.1) and 0.478 (see §5.3.1.2) for the sample just prior to decomposition onset, and for the final Al scaffold. These data show an increase in mesoporosity of 5×. The total porosity of the sample at 313 °C is unknown, but is expected to be between 0.2 and 0.478. Using these assumed values, the corresponding increase in total mesoporosity from 212 °C to 313 °C most likely lies in the range 1.7 – 15×. This large difference between 5 and 15× results from mesoporosity growth during extended sintering.

5.5 Summary

In Chapter 5, SEM micrographs, N_2 adsorption/desorption, and SAXS measurements, in §5.1 respectively, revealed that the pores of the Al scaffold were polydisperse with the majority of the pores being in the macroporous range, having an open network. The calculated total porosity of the Al scaffold was 46(2)% (§5.3.1.2), and the calculated specific surface areas were 7.9(1) and 6.0(5) m^2/g by BET (§5.2.2) and SAXS (§5.3.2), respectively. *In situ* SAXS/WAXS analysis, in §5.4.3, revealed that mesopores are formed in conjunction with crystalline structure changes during $NaAlH_4$ decomposition, while the pores grow and deplete from the samples with longer sintering times and higher temperatures.

Chapter 6

H_2 Desorption Kinetics and Thermodynamic Properties of $NaAlH_4$/Al System

Chapter 6 presents the experimental results on the study of H_2 desorption kinetics and thermodynamic properties of $NaAlH_4$ melt-infiltrated into a Ti-enriched porous Al scaffold as prepared in §3.3. The goal of this Chapter is to determine the catalyst (§1.5.1) and nanoconfinement (§1.5.2) effects of the Ti-enriched porous Al scaffolds on the H_2 desorption kinetics and thermodynamic properties of the melt-infiltrated $NaAlH_4$.

In order to do so, the principal questions that the Chapter seeks to answer are:

- Was $NaAlH_4$ successfully melt-infiltrated into the Al scaffolds?
- Was $NaAlH_4$ homogeneously distributed on the walls of the porous Al scaffolds and which pores are filled up first?
- Were the thermodynamic of decomposition and/or the H_2 desorption kinetics for the infiltrated $NaAlH_4$ affected by the Ti-enriched porous scaffold?

This Chapter is mainly based on the work published by Ianni *et al.* [31].

The samples analysed in this Chapter are listed in Table 6.1 which lists the samples

Table 6.1: Composition and methods of analysis employed for the samples reported in this study. The abbreviations used in the text, and symbols used in plots are also given.

Abbreviation	Symbol	Composition	Method of analysis
$NaAlH_4$-Ti	–▷–	$NaAlH_4$ + 2 mol% $TiCl_3$, ball-milled	TPD, TPD-MS
7-$NaAlH_4$	–△–	7.3 (5) wt% $NaAlH_4$ in melt-infiltrated Ti-enriched porous Al scaffold	XRD, TPD-MS
13-$NaAlH_4$	–●–	13 (1) wt% $NaAlH_4$ in melt-infiltrated Ti-enriched porous Al scaffold	XRD, TPD-MS
20-$NaAlH_4$	–⋆–	19.6 (8) wt% $NaAlH_4$ in melt-infiltrated Ti-enriched porous Al scaffold	XRD, TPD-MS
30-$NaAlH_4$	–◇–	30 (2) wt% $NaAlH_4$ in melt-infiltrated Ti-enriched porous Al scaffold	XRD, TPD-MS
$NaAlH_4$-bulk	–◁–	$NaAlH_4$ as received	TPD, TPD-MS
Al scaffold	——	Ti-enriched porous Al scaffold (see Table 3.3)	XRD, SEM, SAXS/WAXS
10-$NaAlH_4$	–+–	10.4 (9) wt% $NaAlH_4$ in melt-infiltrated Ti-enriched porous Al scaffold	SEM, SAXS/WAXS
34-$NaAlH_4$	–◇–	34 (4) wt% $NaAlH_4$ in melt-infiltrated Ti-enriched porous Al scaffold	SEM, SAXS/WAXS
24-$NaAlH_4$	–⋆–	24 (3) wt% $NaAlH_4$ in melt-infiltrated Ti-enriched porous Al scaffold	TPD
37-$NaAlH_4$	–◇–	37 (4) wt% $NaAlH_4$ in melt-infiltrated Ti-enriched porous Al scaffold	TPD

composition ($NaAlH_4$ loading into Ti-enriched porous Al scaffolds and $NaAlH_4$ standards) and method of analysis employed.

6.1 XRD

XRD patterns were recorded for the external surface and crushed internal portion of the melt-infiltrated samples (see Fig. 6.1(a) and (b), respectively). On the powder X-ray diffractometer used in this study, the infinite-thickness, calculated using eq. 2.6 and relying on the Al scaffold phase composition (Table 3.3), is $\simeq$ 160 μm. As such, for the measurements carried out on the surface of the pellet (Fig. 6.1(a)), $NaAlH_4$ was not identified in samples 7-$NaAlH_4$, 13-$NaAlH_4$ and 20-$NaAlH_4$, therefore showing that $NaAlH_4$ was successfully infiltrated into the pellet. $NaAlH_4$ was observed on the surface of 30-$NaAlH_4$, as this is near the physical limit of infiltration ($\simeq$ 30 wt%) imposed by the total porosity (Table 3.3). The only phases determined to be present were Al, NaCl and Al_3Ti from the scaffold, as expected from the total decomposition of $NaAlH_4$ with 2 mol% $TiCl_3$, and the subsequent evaporation of Na from the mixture[18,19,91,92]. $NaAlO_2$ (PDF 33-1200) is also observed in 30-$NaAlH_4$, which is due to oxidation of the sample during the XRD measurement.

In Fig. 6.1(b), the diffraction patterns of the crushed samples show the presence of $NaAlH_4$ from the infiltration procedure, as well as Al, NaCl, and Al_3Ti from the scaffold, confirming that $NaAlH_4$ is indeed infiltrated into the bulk of the scaffold.

6.2 SEM

The SEM images of the Al scaffold in Fig. 6.2(a) and (b) show a wide size distribution of spherical pores, reminiscent of a fractal distribution (see also §5.1). The infiltrated $NaAlH_4$ in 10-$NaAlH_4$ (Fig. 6.2(c) and (d)) appears to homogeneously coat the walls of the Al scaffold with the smallest pores filled.

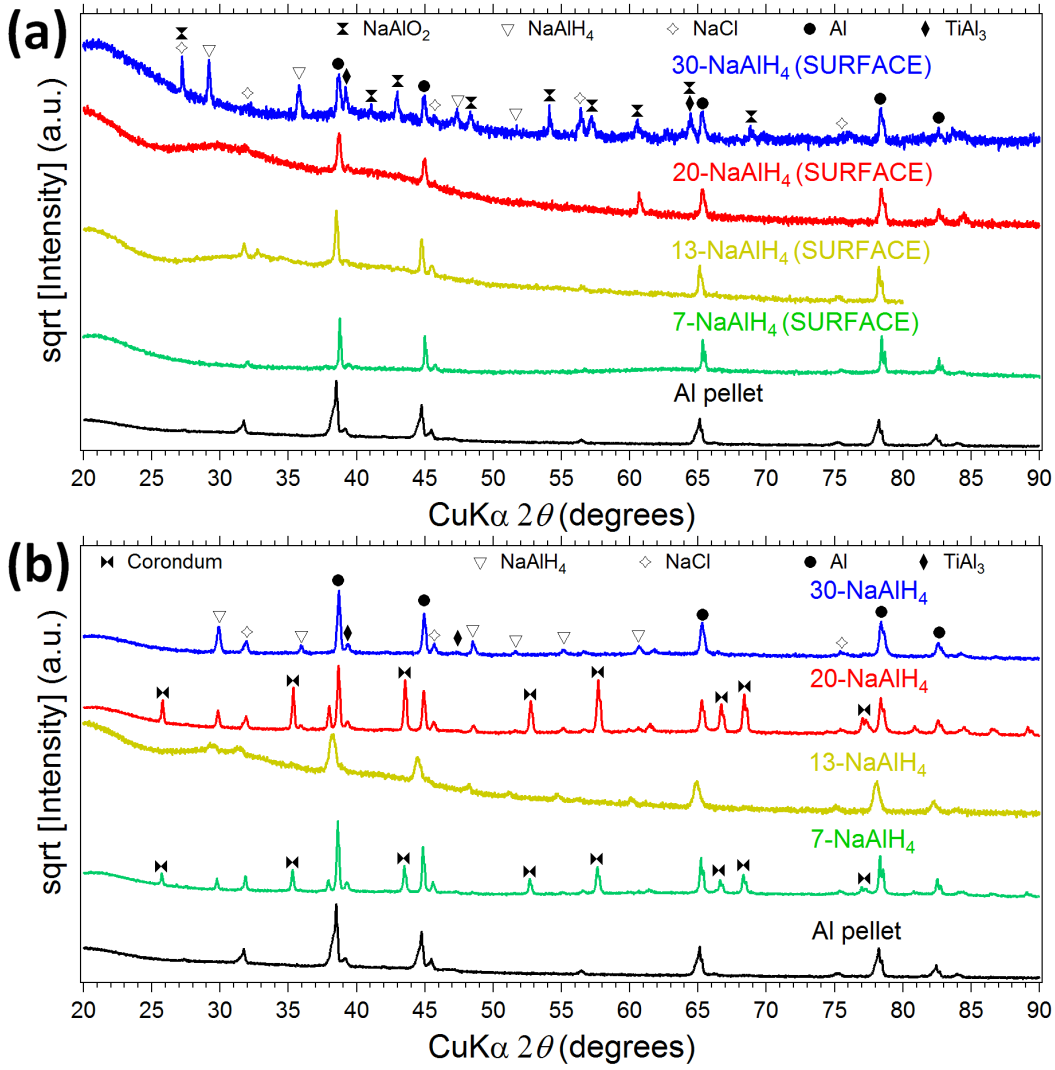

Figure 6.1: XRD patterns of (a) external surface and (b) crushed samples for different amounts of infiltrated $NaAlH_4$. $\lambda = 1.5406$ Å. The broad peak at $\simeq 32°2\theta$ is due to the sample holder.

The overloaded scaffold, 34-$NaAlH_4$ in Fig. 6.2(e) and (f), shows the presence of some incompletely filled macro pores/voids of spherical shapes, which could have been created during the fracture process due to the detachment of $NaAlH_4$. As the amount of infiltrated $NaAlH_4$ increases, the thickness of the $NaAlH_4$ layer covering the pore walls increases, filling up the smallest pores first. As the amount of $NaAlH_4$ in 34-$NaAlH_4$ exceeds the physical limit imposed by the scaffold's total porosity, and there are incomplete-filled pores in the bulk, it is inferred that the

remainder of the $NaAlH_4$ must be present on the specimen surface, as shown by the XRD surface analysis (Fig. 6.1(a)).

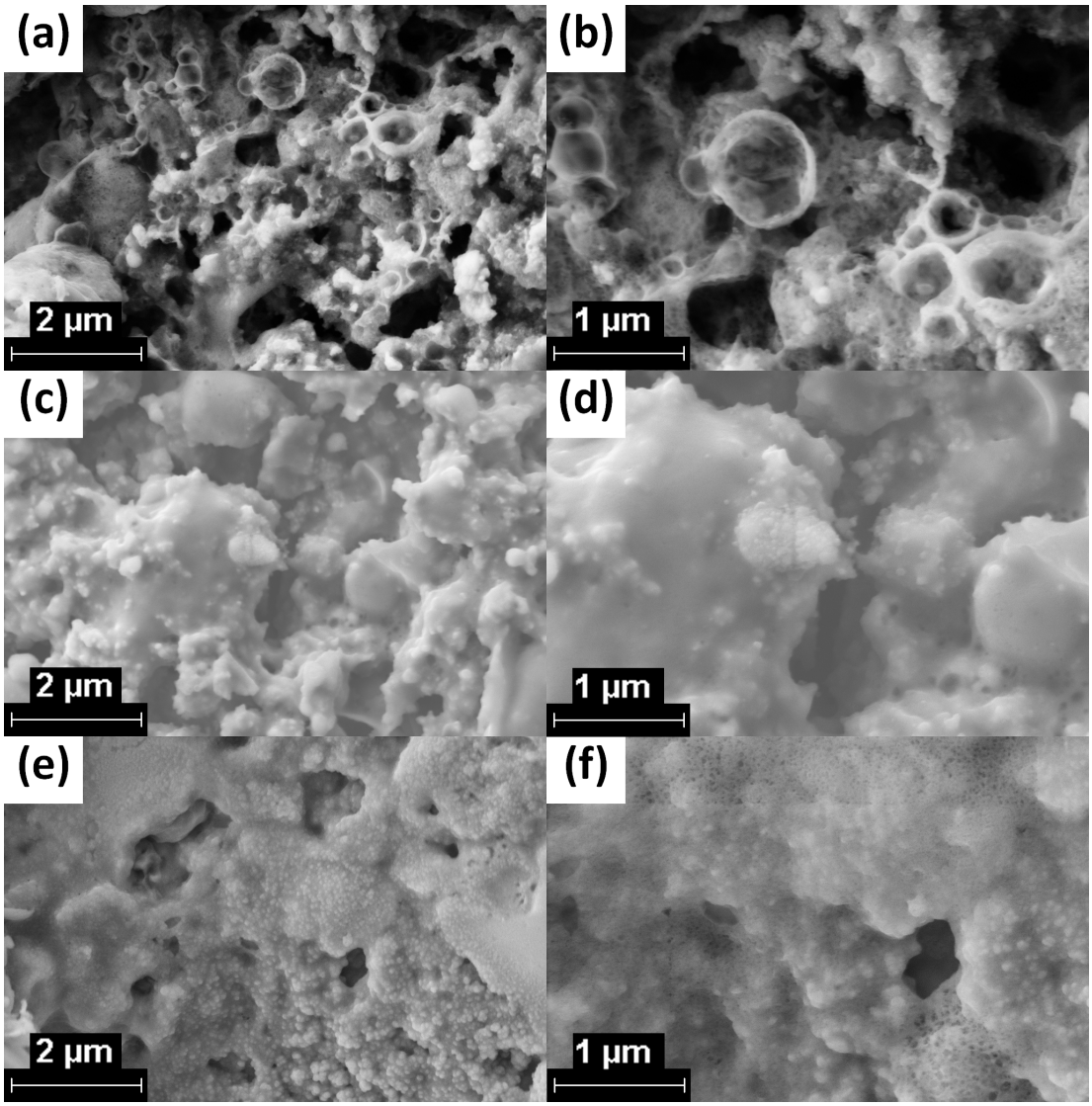

Figure 6.2: SEM micrographs of a fracture surface of the (a, b) porous Al scaffold, (c, d) 10-$NaAlH_4$ and (e, f) overloaded 34-$NaAlH_4$.

6.3 *Ex situ* SAXS/WAXS

Fig. 6.3 shows SAXS (I) and WAXS (II) data for two sets of an Al scaffold, a $NaAlH_4$ infiltrated scaffold, and a $NaAlH_4$ infiltrated scaffold after H_2 desorption (after

TPD-MS). As previously reported in Figures 5.5 and 5.7[†], the initial Al scaffold SAXS patterns (a, d), in Fig. 6.3(I), show appreciable pore sizes in the mesopore range, which is evident due to the presence of a transition in the SAXS patterns at $q \simeq 0.08(1)$ Å^{-1} (see Fig. L.1(b)), which corresponds to a pore size of $\simeq 8(1)$ nm[136]. The difference in low q-range of the two Al scaffolds may be related to the different amounts of amorphous content measured in the scaffolds, 8.9 and 1.8 wt%, respectively (Table 3.3). The WAXS patterns (Fig. 6.3(II)) of the scaffolds show the expected Al, NaCl, and Al_3Ti phases.

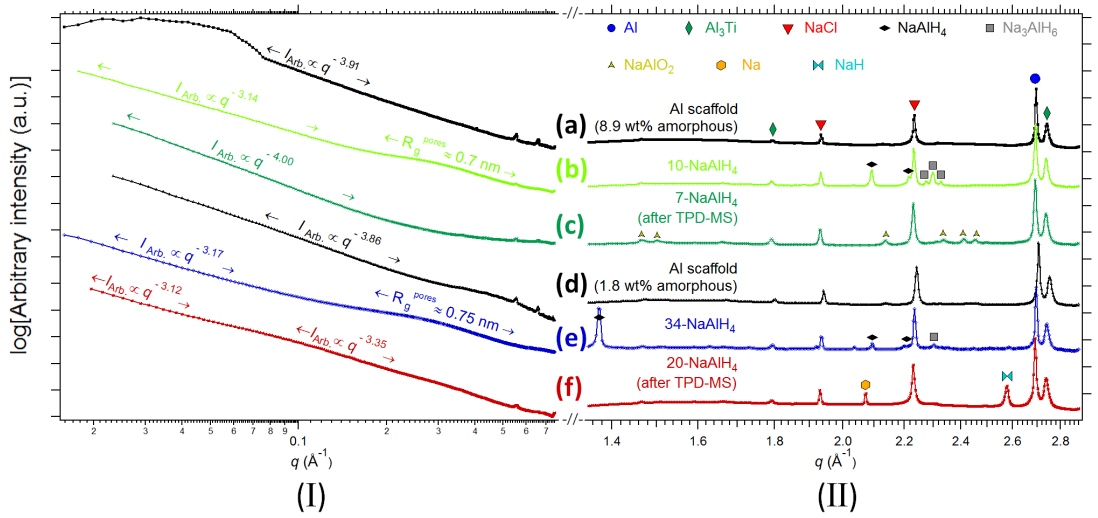

Figure 6.3: (I) SAXS and (II) WAXS patterns for two examples each of a raw Al scaffold, an infiltrated scaffold, and an infiltrated scaffold after TPD-MS. The specific specimens are (a, d) raw Al scaffolds, infiltrated scaffolds (b) 10-$NaAlH_4$ and (e) 34-$NaAlH_4$, and two infiltrated scaffolds after TPD-MS (c) 7-$NaAlH_4$ and (f) 20-$NaAlH_4$. The arrows with the Porod slope in (I) indicate the extent of the Porod regime. The two small peaks in the SAXS patterns at high q are from beam stop scattering.

The SAXS patterns of 10-$NaAlH_4$ and 34-$NaAlH_4$ are similar. Their respective Porod regimes, $I_{\text{Abs}} \propto q^{-P}$, shift toward lower q and to a more surface-fractal slope upon going from (a) to (b), and from (d) to (e). This is evidence of a reduction in the contribution of mesopores to the total porosity, which can be interpreted as

[†]It is shown in Fig. 5.7, that mesopores larger than 8(1) nm have appreciable contribution to the total porosity. This is evident by the transition in the cumulative specific pore volume pattern, as a function of pore size on the log scale, from linear to quadratic.

mesopores being filled. The bump in the SAXS patterns for (b) and (e) at $q \simeq 0.3$ $Å^{-1}$ can be attributed to micropores formed from either an incomplete filling of larger pores or from small pores that were not filled upon infiltration[88]. From a Unified Fit analysis[145,146,148], assuming spherical pores, these pores have diameters of 18(1) Å and 19(2) Å, respectively (Fig. L.1(a)).

The SAXS patterns of desorbed 7-$NaAlH_4$ and 20-$NaAlH_4$ (c, f) show that the 18(1) Å and 19(2) Å pores, respectively, have disappeared. The two samples were treated differently at the completion of their desorption; 7-$NaAlH_4$, at the completion of the TPD-MS experiment, was kept at 300 °C under dynamic vacuum (7×10^{-4} mbar H_2) for several hours, to fully decompose NaH and to remove all traces of Na. 20-$NaAlH_4$ was allowed to cool to room temperature after reaching 300 °C. 7-$NaAlH_4$ shows a featureless pattern with a slope of −4, which is indicative of smooth surfaces. Thus, the mesopores in the scaffold are no longer present, probably having been filled by Al from the decomposition of the infiltrated $NaAlH_4$. SAXS pattern (f) for 20-$NaAlH_4$ has two different slope regimes of −3.1 and −3.3, which may be characteristic of fractally rough surfaces.

The WAXS patterns of the initial Al scaffold (a, d) show only the presence of Al and Al_3Ti and NaCl resulting from the addition of $TiCl_3$. After the melt-infiltration of $NaAlH_4$, the WAXS patterns of 10-$NaAlH_4$ and 34-$NaAlH_4$ (b, e) show the presence of $NaAlH_4$ and some Na_3AlH_6 from the first desorption step of $NaAlH_4$, as well as the presence of the scaffold phases. The desorbed WAXS pattern of 7-$NaAlH_4$ (c) shows the presence of only scaffold material, and a slight oxygen contaminant, $NaAlO_2$. No NaH is observed due to the long desorption time outlined above. The WAXS pattern of 20-$NaAlH_4$ (f) shows the presence of the decomposition products Na and NaH in addition to the scaffold.

6.4 Sievert's apparatus experiments

6.4.1 TPD

Fig. 6.4 shows TPD measurements of cumulative wt% of H_2 desorbed as a function of temperature (§2.7.1), using a 2 °C/min constant heating rate condition, and normalized to the maximum wt% achieved for each sample.

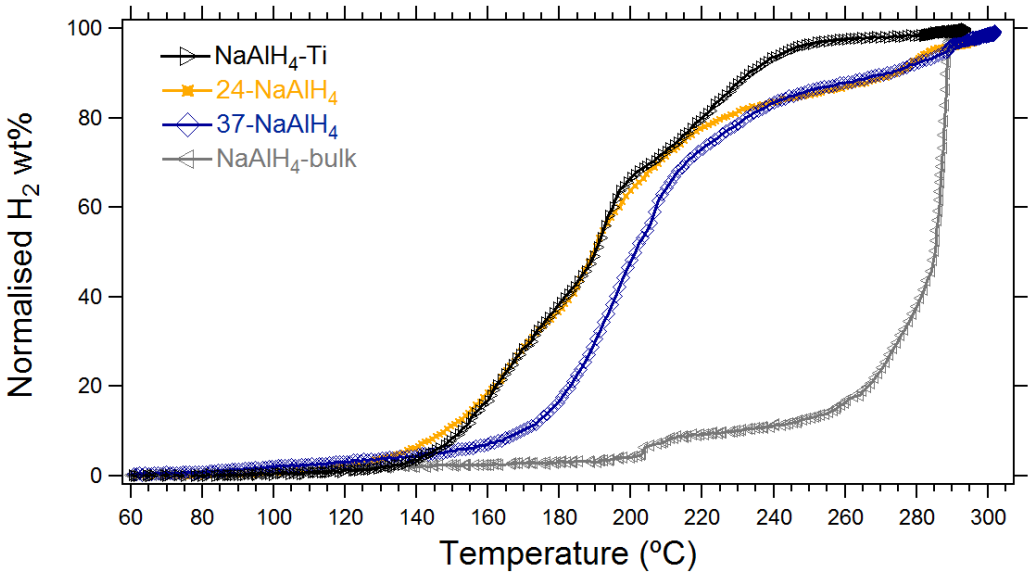

Figure 6.4: TPD data acquired by applying a constant heating rate of 2 °C/min for different infiltrated Ti-enriched Al porous scaffolds (x-$NaAlH_4$), $NaAlH_4$-Ti and bulk $NaAlH_4$. Cumulative H_2 released normalised to total H_2 released.

The catalytic effect due to the presence of Ti is shown by the shift of the cumulative wt% of H_2 desorbed of $NaAlH_4$-Ti toward lower temperatures compared with $NaAlH_4$-bulk.

The cumulative wt% of H_2 desorbed curve of the overloaded 37-$NaAlH_4$ lies between the curves of the two standards ($NaAlH_4$-Ti and $NaAlH_4$-bulk). This shows the result of two combined effects: (*i*) nanoconfinement effects due to filled up micro and mesopores (§1.5.2) and/or the catalytic effect due to the presence of Ti on the surface of the scaffold (§1.5.1), resulting in a shift of the pattern towards lower temperatures, and (*ii*) the effect of bulk $NaAlH_4$ contained inside macro pores and residing on the external surface of the scaffold, resulting in a shift of the pattern

towards higher temperatures (toward the $NaAlH_4$-bulk standard pattern).

The cumulative wt% of H_2 desorbed for 24-$NaAlH_4$ matches $NaAlH_4$-Ti between 160 and 215 °C, and transitions to match the overloaded sample 37-$NaAlH_4$ from 235 °C. This transition cannot be attributed to any thermodynamic limitation because $NaAlH_4$-Ti ($P_{\text{final}}^{H_2} = 4.5$ bar) experienced an absolute higher hydrogen back pressure compared with 24-$NaAlH_4$ ($P_{\text{final}}^{H_2} = 1.3$ bar). The transition of 24-$NaAlH_4$ from $NaAlH_4$-Ti-type behaviour to 34-$NaAlH_4$-type behaviour at 215 °C could be attributed to a transition in the dominant mechanisms that limit the hydrogen desorption rate. Considering that Ti is present only on the walls of the Al scaffolds, then the dominant mechanism at a late stage of $NaAlH_4$ decomposition could be associated with this geometrical inhomogeneity.

24-$NaAlH_4$ presents a relatively higher cumulative wt% of H_2 desorbed for temperature $<$ 160 °C compared with $NaAlH_4$-Ti. The normalization adopted in TPD measurements do not take into consideration the thermodynamic effects due to the hydrogen back pressure, see §2.7.1.1. In order to investigate if the improvement in temperature effective desorption of 24-$NaAlH_4$ can be attributed to nanoconfinement effects or thermodynamic effects due to the different hydrogen back pressure between $NaAlH_4$-Ti ($P_{\text{final}}^{H_2} = 4.5$ bar) and 24-$NaAlH_4$ ($P_{\text{final}}^{H_2} = 1.3$ bar), TPD-MS experiments were conducted.

6.4.2 TPD-MS

In order to have a direct comparison of how the $NaAlH_4$ loading affects H_2 release, the TPD-MS patterns in Fig. 6.5(a) are normalised by the total H_2 released across the first two decomposition steps in the $NaAlH_4$ decomposition process (equations 1.3 and 1.4), since the absolute mass of hydrogen release is affected by both the sample mass and $NaAlH_4$ loading. The temperature gap between the second and third desorption step is $\simeq$ 100 °C (see Fig. 3.6), which is high enough to disregard the influence of the third step on the first two steps, as shown by Nielsen *et al.*[79].

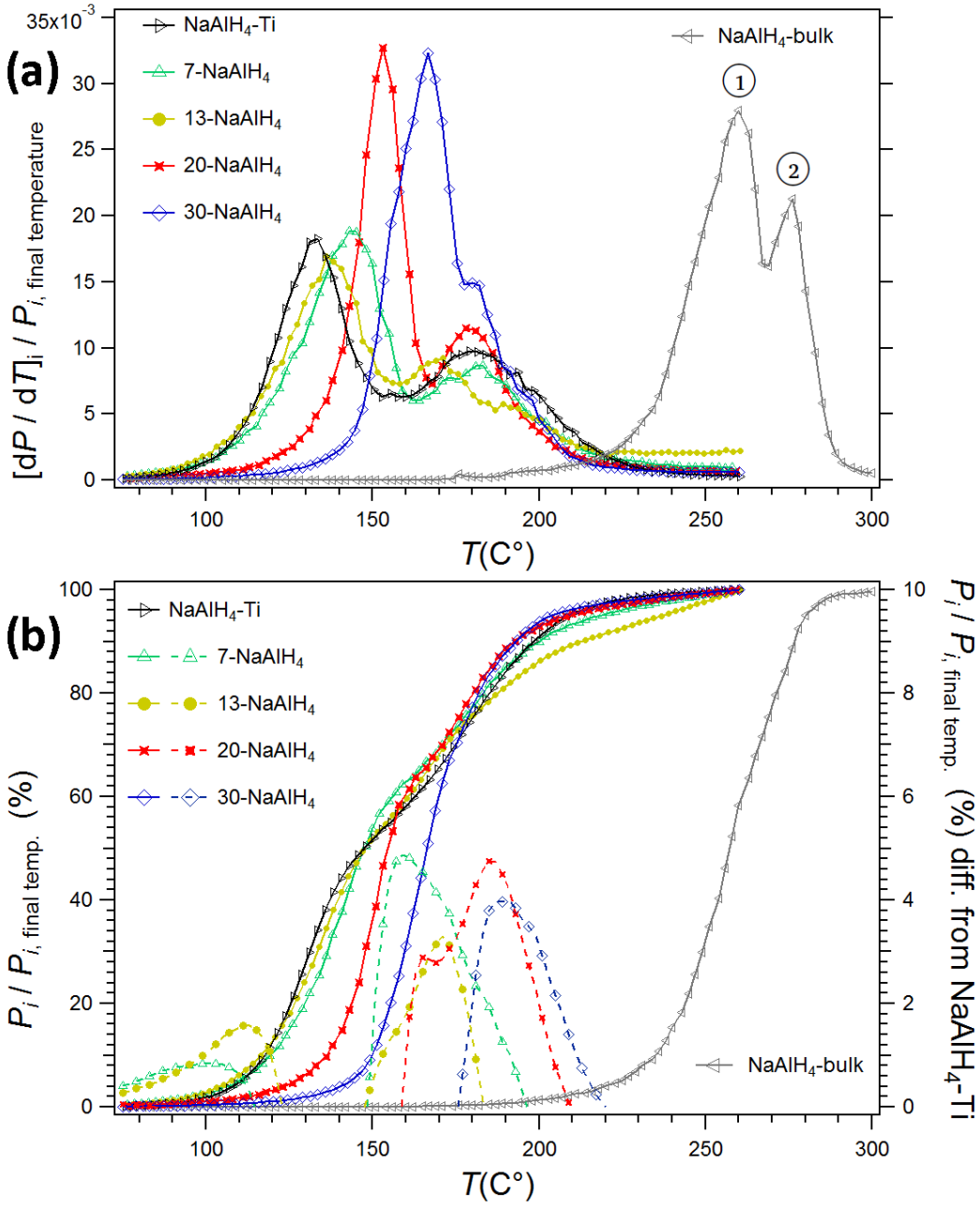

Figure 6.5: TPD-MS data, acquired by applying a constant heating rate of 2 °C/min for different infiltrated Ti-enriched Al porous scaffolds (x-$NaAlH_4$), $NaAlH_4$-Ti and bulk $NaAlH_4$. (a) rate of H_2 release with temperature normalised to unit area. (b) Cumulative H_2 released normalised to total H_2 released. The dashed lines refer to the difference in H_2 release with respect to $NaAlH_4$-Ti; only positive difference are shown to highlight the temperatures for which the infiltrated scaffolds released more H_2 than $NaAlH_4$-Ti. The final temperature is the highest temperature shown for each sample. The circled numerals in (a) refer to equations 1.3 and 1.4.

For the infiltrated Al porous scaffolds and $NaAlH_4$-Ti, the final temperature (see Fig. 6.5(a, b)) is 260 °C, and for the $NaAlH_4$-bulk standard sample, the final temperature is 310 °C.

No oxygen contamination was detected for all TPD-MS measurements presented in this thesis as showed in Fig. M.1 for a representative measurement.

The H_2 release peaks corresponding to the first two decomposition steps of $NaAlH_4$ can be clearly seen in all samples, except 30-$NaAlH_4$, where the second peak manifests as a shoulder on the first[178]. The two peaks in each pattern of H_2 release rate with temperature in Fig. 6.5(a), were fitted using two pseudo-Voigt profiles[196] implemented in Topas 5[125] (see Fig. N.1 for two representative calculations). The ratio between the areas under the first and second calculated profiles, corresponding to the total hydrogen released by each of the two steps of desorption, was constrained to be equal to 2 (3.7 wt%/1.85 wt%) in agreement with the theoretical desorption steps in equations 1.3 and 1.4. The temperatures corresponding to the desorption rate maximum and the corresponding Full Width at Half Maximum (FWHM) are reported in Table 6.2. As reported in Table 6.2 and plotted in Fig. 6.6(a), the temperatures corresponding to the first peak (T_{max}^{first}), progressively shift to increasing temperatures from that of $NaAlH_4$-Ti toward that of pure $NaAlH_4$ with increasing scaffold loading. The temperatures corresponding to the second peak of desorption for the infiltrated scaffolds remain approximately constant and approximately equal to that of the second peak of the $NaAlH_4$-Ti standard sample (184 ± 9 °C). It is proposed that this indicates a transition from H_2 release dominated by nanoconfinement and catalysis, as opposed to release dominated by bulk $NaAlH_4$. As reported in Table 6.2 and plotted in Fig. 6.6(b), the width of the second peak of desorption is roughly narrower for the highly-loaded scaffolds, tending to that of bulk $NaAlH_4$, whereas the lower-loaded scaffolds have a peak width approximately equal to that of $NaAlH_4$-Ti. This is likely caused by the reduced rate of the hydrogen source (Na_3AlH_6) provided for the second step of hydrogen desorption. Indeed, Na_3AlH_6, which is the product of the first step

of hydrogen desorption, is produced at a decreasing rate with increasing scaffold loading as shown by the trend of desorption rate of the first peaks (Figures 6.5(a) and 6.6(a)). Thus, the behaviour of the second desorption step is dependent on the first step.

Table 6.2: TPD-MS analysis results obtained for two different standard samples and four different wt% of $NaAlH_4$ melt-infiltrated into the Ti-enriched Al scaffold. First and second temperatures corresponding to the hydrogen desorption rate maximum and the corresponding Full Width at Half Maximum (FWHM) were obtained by fitting the peaks in the hydrogen desorption rate patterns using pseudo-Voigt profiles.

Sample	Heating rate (°C/min)	T_{max}^{first} (°C)[a]	ΔT_{FWHM}^{first} (°C)	T_{max}^{second} (°C)[b]	ΔT_{FWHM}^{second} (°C)	R_{wp}
$NaAlH_4$-Ti	1.9	132	26	184	40	5.5
7-$NaAlH_4$	1.9	141	28	184	32	8.1
13-$NaAlH_4$	1.8	136	27	175	38	7.9
20-$NaAlH_4$	2.2	153	15	181	21	6.0
30-$NaAlH_4$	2.0	165	21	186	26	6.5
$NaAlH_4$-bulk	2.0	256	25	276	12	12

[a] T_{max}^{first}(°C): Temperature corresponding to the first desorption rate maximum.
[b] T_{max}^{second}(°C): Temperature corresponding to the second desorption rate maximum.

Fig. 6.5(b) shows the percentage cumulative H_2 release and the difference in release between $NaAlH_4$-Ti and the infiltrated scaffolds. Only the positive differences are shown to highlight the temperature ranges for which the infiltrated scaffolds released more hydrogen than $NaAlH_4$-Ti. This range is between 148 and 220 °C, with 7-$NaAlH_4$ and 13-$NaAlH_4$ both starting at 148 °C. Outside of this temperature range, the infiltrated specimens released relatively less hydrogen than $NaAlH_4$-Ti. Fig. 6.5(b) also shows that the shape of the cumulative H_2 release curve tends from that of $NaAlH_4$-Ti to bulk $NaAlH_4$, further highlighting that the higher infiltration loadings act as bulk $NaAlH_4$.

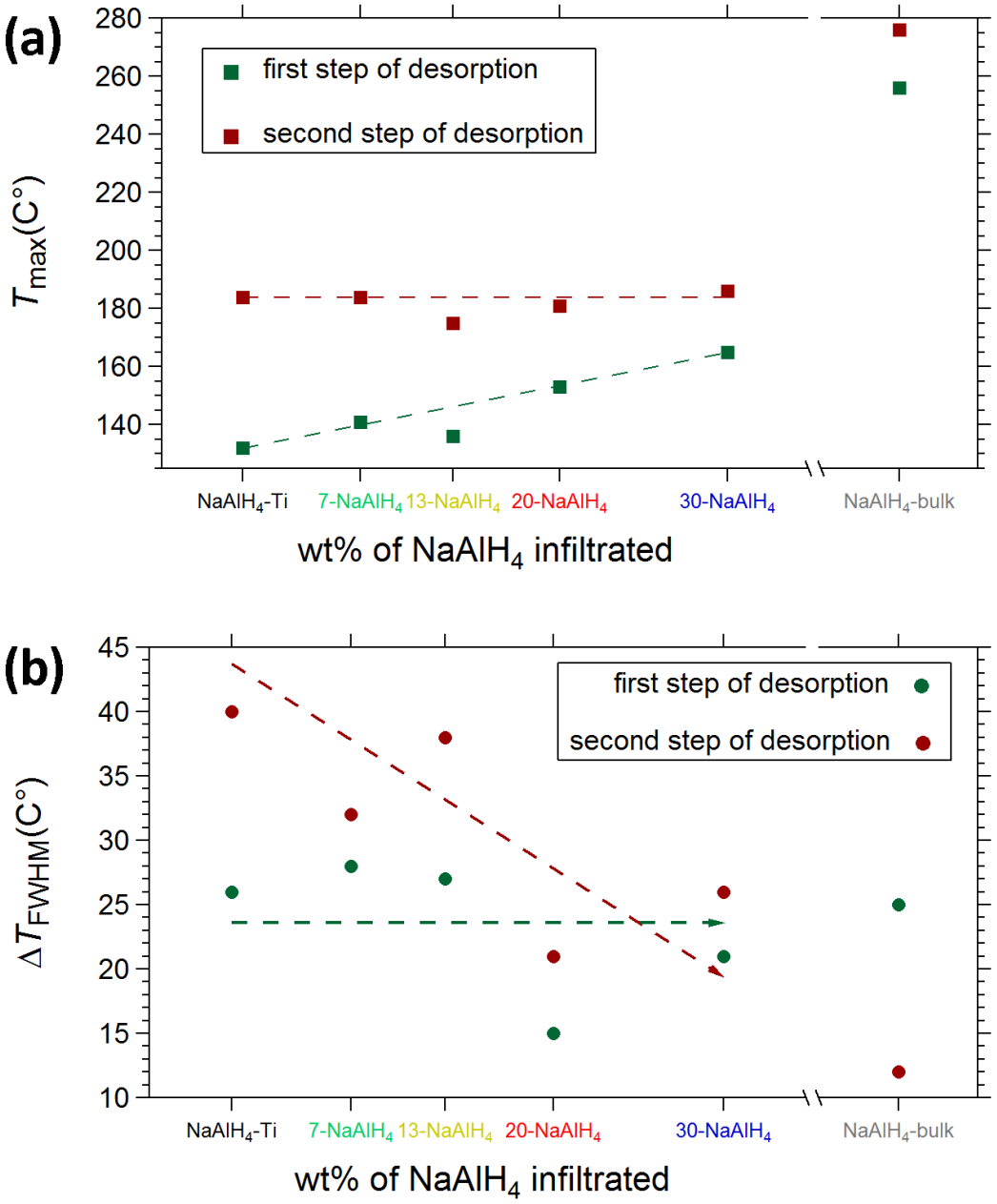

Figure 6.6: TPD-MS analysis results obtained for two different standard samples and four different wt% of $NaAlH_4$ melt-infiltrated into the Ti-enriched Al scaffold, plotted as a function of the wt% of $NaAlH_4$ infiltrated. (a) Temperatures corresponding to the maximum hydrogen desorption rate for the first and second steps and (b) corresponding Full Width at Half Maximum (FWHM) obtained by fitting the peaks in the hydrogen desorption patterns using pseudo-Voigt profiles.

The shift in the desorption temperature of the infiltrated $NaAlH_4$ shows that the

material is in intimate contact with the Ti catalyst in the Al scaffold. Assuming a consistent porosity across all non-infiltrated scaffolds, increasing the loading of infiltrated $NaAlH_4$ will decrease the specific surface area of contact between $NaAlH_4$ and Al scaffold, leading to a change in behaviour towards bulk $NaAlH_4$.

It is hypothesised that because of the low concentration of mesopores compared to macro pores (§5.3.1.2), the majority of this kinetic improvement can be attributed to the Ti catalyst in the scaffold successfully destabilising the infiltrated $NaAlH_4$, with improvements due to nanoconfinement effects from infiltrated mesopores contributing to a much lesser extent. Since Ti is present only on the walls of the Al scaffolds the overall dehydrogenation kinetic performance of the $NaAlH_4$-Ti remains superior.

An on-set temperature of desorption could not be identified. A logarithmic plot of the data presented in Fig. 6.5(a) is shown in Fig. 6.7, and there is no appreciable changes in $\log(dP/dT)$ for $T << T_{max}^{first}$[21]. The logarithmic scale normally allows for the identification of the precise on-set temperature for each pattern, but this data show a steady increase in H_2 release with temperature.

In the early stages of $NaAlH_4$ decomposition (leading edge, $T << T_{max}^{first}$), the curves of $\ln[dN_{H_2}(T)/dt]$ — see Fig. 6.7(b) — have a straight-line trend when plotted as a function of $1/T$, showing that the reaction kinetics are appropriate for Habenschaden-Küppers analysis (HKA) (§2.7.2.3). The activation energies so calculated (Table 6.3) for all samples are lower compared with the corresponding activation energies derived from isothermal experiments[40], except for $NaAlH_4$-Ti. The fact that $NaAlH_4$-Ti has a higher activation energy than all other samples (including $NaAlH_4$-bulk) is in contradiction with previous statements in §1.5.1. Indeed, according to the literature[76–78], titanium may improve the kinetics of hydride decomposition at the hydride/metal interface[27], which is the rate-limiting step in the early stages of $NaAlH_4$ decomposition[197,198]. HKA is based on the assumption that the hydrogen desorbed is exclusively from a single independent source (§2.7.1.1). Figures 6.5 and 6.6 show that as the behaviour of the first and

second desorption steps of $NaAlH_4$ do not respond the same way to the presence of the catalyst and nanoconfinement, they must be considered as dependent sources of hydrogen. The activation energy calculated by HKA is therefore biased due to interference between the first and second steps, resulting in activation energy values which cannot be applied in further analysis.

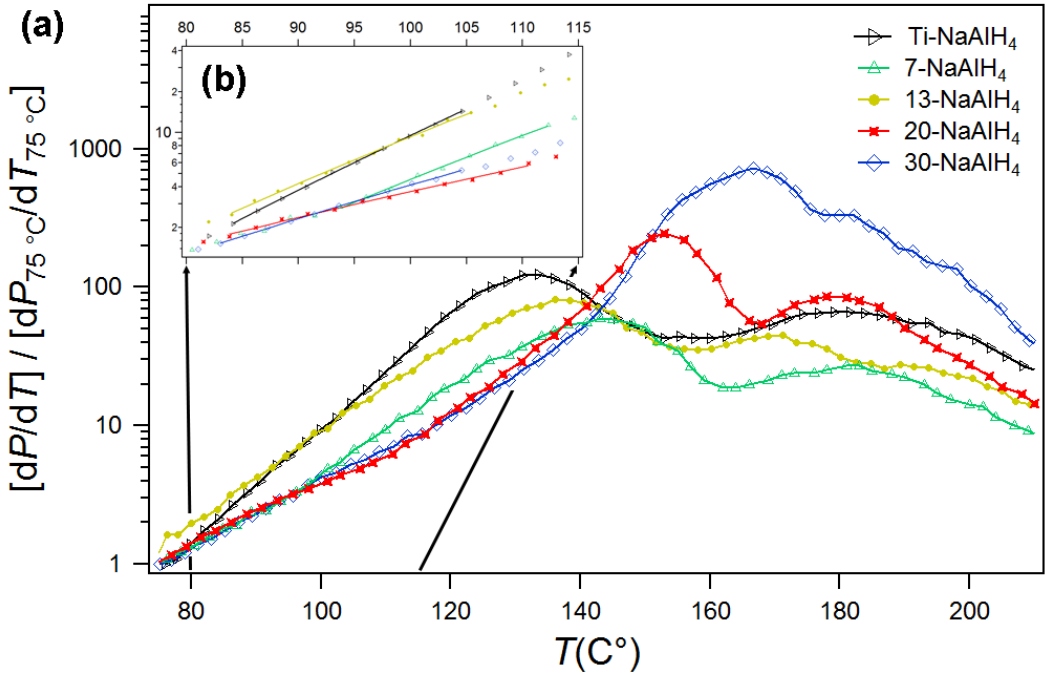

Figure 6.7: TPD-MS plots for 4 different wt% of $NaAlH_4$ infiltrated into Al porous scaffolds and $NaAlH_4$ ball-milled with 2 mol% $TiCl_3$, used as standard. The format reported on the y-axis is $[dP/dT]/[dP_{75\,°C}/dT_{75\,°C}]$. In the temperature range corresponding to the leading edge (b) the symbols and the lines denote the TPD-MS data and the calculated data using the Habenschaden-Küppers analysis, respectively.

Table 6.3: Activation energies fitted using the Habenschaden-Küppers analysis method on the leading edge temperature of the TPD-MS measurements and derived from isothermal experiments[40]. The uncertainties for the activation energies fitted correspond to 95% confidence intervals.

Leading edge analysis		
Sample	T (°C) range	E_a (kJ/mol of H_2)
$NaAlH_4$-bulk	52 – 65	85(4)
$NaAlH_4$-bulk	102 – 169	48(1)
30-$NaAlH_4$	83 – 104	64(2)
20-$NaAlH_4$	84 – 111	49(3)
13-$NaAlH_4$	84 – 105	90(4)
7-$NaAlH_4$	94 – 112	88(4)
$NaAlH_4$-Ti	84 – 104	104(2)
Derived from isothermal experiments[40]		
$NaAlH_4$-bulk	first decomposition step	118.1(1)
$NaAlH_4$-bulk	second decomposition step	120.7(1)
$NaAlH_4$-Ti	first decomposition step	79.5(1)
$NaAlH_4$-Ti	second decomposition step	97.1(1)

6.5 Summary

XRD analysis (§6.1), shows the presence of the expected phases and that the $NaAlH_4$ infiltrates the bulk of the pellet first, and only at high loadings does it come to the surface. SEM (§6.2) and SAXS (§6.3) analysis of low $NaAlH_4$ loading in the porous Al scaffold reveal that mesopores and small macro pores are filled first, leaving the larger macro pores/voids empty. Additionally, SAXS (§6.3) patterns show, after infiltration, the presence of micropores formed from either an incomplete filling of larger pores or from small pores that were not filled upon infiltration. From the TPD-MS analysis (§6.4.2) in the temperature range 148 – 220 °C, melt-infiltrated

$NaAlH_4$ Ti-enriched porous Al scaffolds show a higher relative H_2 release, compared to $NaAlH_4$ + $TiCl_3$, with both the temperature of maximum H_2 desorption, and the shape of the normalised H_2 release curve, trending from that of bulk $NaAlH_4$ + $TiCl_3$ to bulk $NaAlH_4$ with increasing scaffold loading. As the majority of pores are macro pores, kinetic improvements due to nanoconfinement effects are slightly evident. For the highly loaded samples, the largest voids and macro pores are partially filled, and the decrease in the active specific surface area of contact between $NaAlH_4$ and Al scaffold results in a decrease of the hydrogen desorption rate.

Chapter 7

Conclusions and Future Work

This final chapter is an overall summary of the goals, results, and conclusions presented in each of the previous Chapters. Included here is also a section to be considered to further the work on hydrogen storage systems using metal hydrides infiltrated into porous metal scaffolds for vehicle applications.

7.1 Conclusions

The need for a sustainable and renewable energy economy led the scientific community into alternative energy research including the hydrogen economy. Considering the hydrogen cycle, the hydrogen is, initially, produced from solar/wind power, and is then stored and converted back into clean energy using fuel cells as needed. The goal of this thesis was to provide a hydrogen storage system that would meet the technology requirement for vehicle applications.

In Chapter 1 it was shown that some systems based on solid complex metal hydrides have superior volumetric and effective gravimetric energy densities compared with high-pressure hydrogen tank systems, which are currently the most advanced/developed technology. However, metal hydride systems suffer from a low hydrogen sorption kinetic and are not currently suitable for vehicle applications.

As described in Chapter 3, Mg and Ti-enriched porous Al scaffolds were successfully

produced in order to improve the hydrogen sorption kinetics of melt-infiltrated metal hydrides by catalytic and nanoconfinement effects. The scaffolds maintained their structural integrity.

The morphological and structural properties of Mg and Al porous scaffolds were studied in Chapters 4 and 5, respectively. It was shown that Mg and Al scaffolds have an open porous network structure where the majority of pores are macro pores. The specific pore volume corresponding to the formation of mesopores of a Mg and a Ti-enriched Al scaffold are 0.034 and 0.027 cm^3/g, respectively. For this Al scaffold, the mesopores contributes a partial porosity of only 2.7%, whereas the remaining 41.9% of the scaffold's porosity is due to the presence of macropores and voids. For these Mg and Ti-enriched Al scaffolds the specific surface areas are 7.9(1) and 26(2) cm^2/g, respectively. Mg and Al scaffolds have bigger pores and smaller cumulative specific pore volume in comparison to carbon-based scaffolds, but they are expected to have higher thermal conductivities which would allow for better heat management during hydrogen absorption and desorption.

As discussed in Chapter 6, the infiltrated $NaAlH_4$ homogeneously coats the walls of the Al scaffold with the smallest pores filled first. For the lower $NaAlH_4$ loadings, the kinetic effects due to the presence of catalytic Ti on the surface of the Al scaffold were dominant. As the majority of pores are macro pores, thermodynamic destabilization and/or kinetics improvements due to nanoconfinement effects were only slightly evident; the infiltrated scaffolds at lower loadings release relatively more hydrogen than bulk Ti-catalysed $NaAlH_4$ in the temperature range of 148 – 220 °C, with the temperatures tending toward bulk $NaAlH_4$ with increased loadings. Unfortunately, the effective gravimetric energy densities of the systems were considerably reduced because of the weight of the scaffolds.

7.2 Future work

Several recommendations are listed below for designing future systems based on what was learned from the outcomes of this thesis.

- Further complex metal hydrides candidates need to be produced and screened for those having higher effective gravimetric energy densities according to technology requirements imposed by the fuel cells.

- Computational approaches, such as Density Functional Theory (DFT)[199], should be employed to investigate if nanoconfinement effects would eventually stabilize or destabilize the thermodynamic properties of each of these metal hydride candidates.

- Metal hydrides used to produce porous metal scaffolds could be melted and gradually cooled down before being sintered in order to remove the initial voids present in the pellets. This extra step can be applied only if there are thermodynamic conditions that would allow the metal hydride to be melted.

- In order to maximise the total porosity of metal scaffolds produced from metal hydrides, the elemental composition and density of the metal hydride should be such that the non-scaffold decomposition products are gaseous to allow them to easily leave the scaffold, and that the bulk density of the remaining scaffold material is minimised, whilst maintaining structural integrity.

- According to the outcomes from the pore formation and growth dynamic during the sintering processes obtained in Chapters 4 and 5, a metal scaffold that would have the majority of pores in the mesopore size range could be successfully produced. The ideal metal hydride candidate should decompose quickly in a single desorption step under reduced sintering temperatures and time to allow for fast pore formation.

Below are further techniques and methods useful to be employed for future work.

- Support Scanning Electron Microscope (SEM) with Transmission Electron Microscopy (TEM)[107] in order to observe internal morphology and crystallization of samples at magnifications corresponding to a field of view in the range of 400 to 1000 nm.

- Support X-Ray Diffraction (XRD) with X-ray Photoelectron Spectroscopy (XPS)[71] in order to identify and quantify the elemental composition of the amorphous phases.

- Use the 3D object reconstruction technique, introduced in Chapter 2, to measure the external volume of a pellet without physical contact.

- The specific surface area of an open porous network calculated using the Brunauer-Emmett-Teller (BET) method from N_2 sorption data tends to be overestimated[173], as reported in Chapter 5. Additionally, it has an uncertainty of $> 20\%$ because it relies on an estimation of the cross section of spherical N_2 adsorbed molecule that does not depend on the materials of the scaffold walls[172]. Samples investigated using the N_2 technique are exposed to air for approximately one second, which can appreciably alter the sample properties. Thus, it is convenient to calculate the specific surface area, counting also closed pores, using the SAXS technique when possible.

- Model N_2 Sorption data using a Non local Density Functional Theory (NLDFT)[104] instead of Barrett-Joyner-Halenda (BJH) method in order to determine more accurately the pore-size distributions[173,200].

- In order to detect features caused by macro-size structures using Small-Angle X-ray Scattering (SAXS), the camera length has to be increased, extending the q-range toward lower q-values and the X-ray source has to be more coherent, as explained in Chapter 2, compared with the SAXS settings used in this thesis. This will allow the invariant method to be employed to calculate the extended specific pore volume distribution and the specific total pore

volume. It is recommended that the apparatus setup used for Ultra SAXS measurements[201] ($d_{max} = 2\pi/q_{min} \simeq 6$ μm) use a Si(511) Channel-Cut Monochromator (CCM)[202] or C*(111)[203] monochromators, which, for an X-ray energy of 8 keV, will give longitudinal coherence lengths (ξ_l) of $\simeq 17$ and 3 μm, respectively.

- In order to investigate eventual improvements in the hydrogen sorption reversibility due to the presence of a metal scaffold that avoids the segregation of decomposition products, hydrogenation cycling experiments are required. In order to compare these results for a $NaAlH_4$ nanoconfined system, it would be convenient to use techniques such as hydrogenation cycle TPD[89,97] or TPD-MS[75,79] reproducing the same procedures and conditions reported in the literature.

Appendices

Appendix A

Properties of X-rays Radiation

While electrons are used to study surfaces and films, X-ray and neutrons are used to investigate bulk features of materials due to their penetration depth. For X-rays passing through a material, the dominant interaction is between the X-ray electric field and the charge distribution in the material.

A.1 Generation of X-rays

Conventionally, X-rays are obtained by an electron bombardment of a water-cooled metal anode. Electrons are initially generated at the cathode, usually a tungsten filament, heated up applying a moderate voltage (Fig. A.1(a)). The higher voltage applied across the electrodes, usually -40 kV for X-ray Diffraction (XRD) techniques, accelerate the electrons towards the anode ($E_{\text{max, e}} = 40$ keV) where one of the products of the interaction with the anode is an emission of a broad-wavelength band of radiation called continuum, also referred to as white radiation or Bremsstrahlung (Fig. A.1(b)). Bremsstrahlung electromagnetic radiation is produced by the deceleration of the free pre-accelerated electrons when deflected due to the electrostatic field generated typically in the proximity of atomic electrons present in the anode. Such white spectrum of intensity presents a cut-off at energy comparable to $E_{\text{max, e}}$ and the intensities are higher on the plane

transverse (perpendicular) to the direction of the charge deceleration, see Fig. A.3. In addition to electron interactions leading to the production of white radiation, there are also electron interactions which produce characteristic radiation. If a high-energy free electron strikes a bound atomic electron, and the energy of the free electron is greater than the binding energy of the atomic electron, it is possible that the atomic electron will be ejected from its atomic position, departing from the atom with a kinetic energy ($E_e - \Phi$) equivalent to the difference between the energy E_e of the initial free electron and the binding energy Φ of the atomic electron. As long as the vacancy in the shell exists, the atom is in an unstable state and can regain stability by transference of an electron from one of the outer orbitals to fill the vacancy. The energy difference between the initial and final states of the transferred electron may be given off in the form of an X-ray photon. As all emitted X-ray photons have energies proportional to the differences in the energy states of atomic electrons, the lines from a given element will be characteristic of that element (Fig. A.1(c))[204]. For XRD purpose, often the anode consists of a copper target that results in CuK_α ($\lambda = 0.1542$ nm, 8.05 keV) radiation (Fig. A.1(b)). In addition, an alternative transition gives CuK_β ($\lambda = 0.1392$ nm) radiation that is often removed by applying a Ni foil that absorbs K_β more strongly than K_α. At high resolution, a fine structure is found ($CuK_{\alpha1}$ and $CuK_{\alpha2}$) which arise from a splitting of both the K- and M-level into a doublet due to electron spin. Monochromators are generally adopted to reduce $CuK_{\alpha2}$ radiation. Some alternative target materials in use are Cr ($\lambda = 0.2291$ nm, 5.4 keV), Fe ($\lambda = 0.1938$ nm, 6.4 keV), Co ($\lambda = 0.1791$ nm, 6.9 keV), Mo ($\lambda = 0.0711$ nm, 17.4 keV) and W ($\lambda = 0.021$ nm, 59 keV). The least binding energy of an atomic electron for a specific element at which a vacancy can be created in the particular shell is referred to as the 'edge' or 'critical excitation' energy. X-rays passing through materials containing elements having edge energy lower than the X-rays energy may be heavily absorbed due to the ionization of the materials component atoms. For instance, CuK_α radiation ($E = 8.05$ keV) are absorbed by Ti ($E_{\text{K-absorption edge}} = 5.0$ keV), Cr ($E_{\text{K-absorption edge}}$

= 6.0 keV), Mn ($E_{\text{K-absorption edge}}$ = 6.5 keV), Fe ($E_{\text{K-absorption edge}}$ = 7.1 keV) and Co ($E_{\text{K-absorption edge}}$ = 7.7 keV). This property is used in X-ray fluorescence techniques for elemental analysis where the material of the tube target is selected depending on the edge energy of the sample component elements[†].

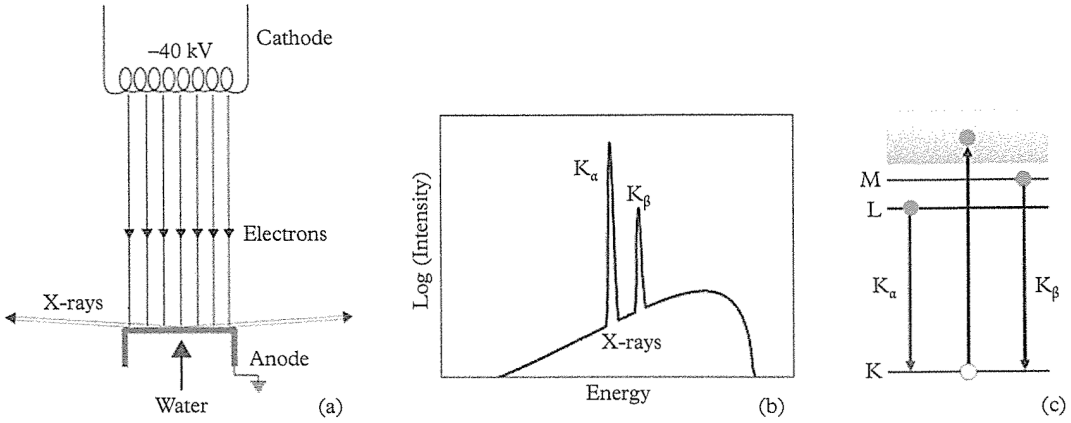

Figure A.1: (a) Standard X-ray tube. (b) The spectrum from the tube has discrete fluorescent lines superimposed on the continuous background. (c) Schematic atomic level diagram indicating transition between an L and K shell (K_α line) and between M and K (K_β line) [138].

Synchrotron radiation consists essentially of Bremsstrahlung radiation generated by electrons or positrons circulating in a cyclotron (Fig. A.2(b)). A dramatic effect of relativity is that the radiation pattern is strongly concentrated. When deflected from their straight path upon passing through a bending magnet, the electrons emit a rather narrow spray of X-rays tangentially to the plane of the electron beam (Fig. A.2(a)). It has been found that, because the primary source of radiation is so intense, it is possible to use a high degree of monochromatization between source and specimen, giving a source that is wavelength (and, therefore, energy) tunable, as well as being highly monochromatic. At the Australian Synchrotron (SAXS/WAXS) the X-ray energy range is between 5.5 keV and 21 keV which

[†]The variation of the X-ray tunable energy, produced by a synchrotron source, in the vicinity of an absorption edge of one of constituent element of the sample, lead to a unique 'anomalous' X-ray diffraction profile.

correspond to wavelengths between 0.59 Å and 2.25 Å[127]. The characteristics of synchrotron radiation are[138]:

- Collimated emission[108,110] ($\propto 1/\gamma$).
- Higher intensity compared with an X-ray obtained by electrons bombardment.
- Linear polarization when viewed in the horizontal plane of acceleration.
- Continuous spectrum (5.5 keV – 21 keV).
- Beam size: $<$ 1 μm to 1 nm.

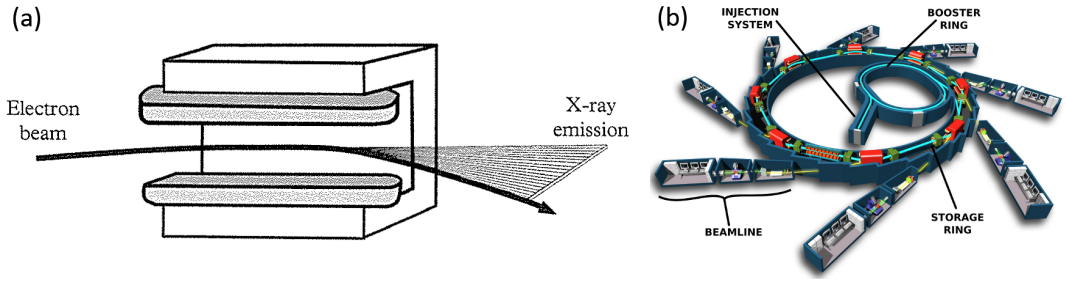

Figure A.2: (a) Scheme of a bending magnet. As a result of the centripetal acceleration electromagnetic radiation is emitted[138]. (b) Schematic diagram of Australian Synchrotron storage ring (cyclotron) as used to generate X-rays (synchrotron)[127].

A.2 X-ray interaction with matter

X-rays, having conventional magnetic field intensities ($\omega << e|\boldsymbol{B}|/m_e = \omega_{cyclotron}$), interact with matter through the electrons contained in atoms. During these interactions, the electrons are accelerated to velocities much less than the speed of light. Thus, from now on, we consider only dielectric materials (relative permeability $\mu_r = 1$). When the electromagnetic radiation (the X-rays) interacts with an electron (a charged particle) it becomes a secondary source of electromagnetic radiation that scatters the incident radiation. In a non-relativistic

scenario ($v_e << c$), an electron can be treated as a point irradiator source because the intensity ($\propto |\langle \boldsymbol{E} \rangle|^2$) detected at the distance r from the current source position is not affected by the distance travelled since the electromagnetic wave was emitted ($r_0 << r$). The electric vector component of the electromagnetic field so irradiated, derived by solving the electromagnetic wave equation, is[110]:

$$e\boldsymbol{E}(\boldsymbol{r}, t) = m_e \frac{r_e}{r} \boldsymbol{a}_T (t - r/c) \tag{A.1}$$

$\boldsymbol{a}_T$ is the transverse acceleration of the electron compared with the wave vector (k_0, see Fig. A.3(a)) at the time of emission of the electromagnetic wave ($t - r/c$), in order to consider phase changes. r is the vector between the position of the electron and the position of the electric field generated and r_e is the Thompson scattering length or classical electron radius ($r_e = e^2/4\pi\epsilon_0 m_e c^2 = 2.82 \times 10^{-5}$ Å).

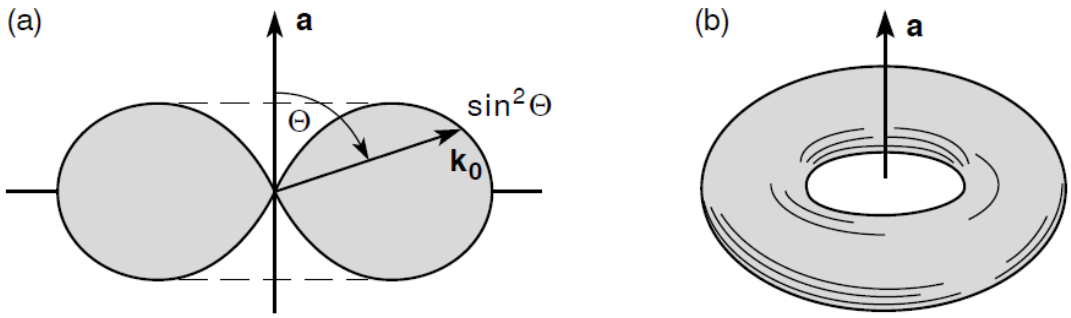

Figure A.3: (a) Radiation intensity pattern observed at great distance ($r >> r_0$) of a point source accelerated charge, and (b) its three-dimensional toroidal appearance[110].

For the sake of understanding, a simplistic classic model of interaction is adopted where a linear polarized ($\hat{\mathbf{z}}$) and monochromatic ($E_z(t, x) = \mathrm{Re}[E_{z,0} e^{-i\omega t + ikx}]$), incident X-ray exerts a force on an electron, causing it to accelerate, oscillate, and hence emit the scattered X-ray. The differential force balance equation, considering only an electromagnetic wave having a wavelength that allow to neglect the longitudinal movement of the electron ($\lambda >> 2\pi x_e$, across a period), can be

express as:

$$m_e\left(\frac{d^2 z_e}{dt^2}+\frac{1}{\tau}\frac{dz_e}{dt}+\omega_s z_e\right)=-e[E_z(t)+\underbrace{v_e\times B_y(t)}_{\simeq 0}] \tag{A.2}$$

Considering the time-averaged relation between the electric and magnetic field ($|\langle \boldsymbol{E}\rangle|/c = |\langle \boldsymbol{B}\rangle|$), for electron velocity no relativistic, the magnetic source term can be neglected. The first term is the acceleration (d^2z_e/dt^2), the second term is a dissipative force term that accounts for intensity loss[‡] and the third term is due to the restoring force for an oscillator of resonant frequency ω_s that take into consideration the bonding force between electron and nucleus. A particular solution of the electron equation of motion (eq. A.2) is $z_e(t) = \mathrm{Re}[z_{e,0}e^{-i\omega t}]$, where:

$$z_{e,0} = -\frac{eE_{z,0}}{m_e}\frac{1}{(\omega_s^2-\omega^2-i\omega/\tau)} \tag{A.3}$$

which corresponds to an acceleration of $d^2z_e/dt^2 = \mathrm{Re}[-\omega^2 z_{e,0}e^{-i\omega t}]$. Replacing the function of acceleration so found into eq. A.1, it is so possible to make in relation the incident and the emitted electric field:

$$\boldsymbol{E}(\boldsymbol{r},t) = E_{z,0}\frac{r_e}{r}\sin\Theta\cdot\mathrm{Re}\left[\frac{\omega^2}{(\omega_s^2-\omega^2-i\omega/\tau)}e^{-i\omega(t-r/c)}\right] \tag{A.4}$$

From eq. A.4, it is worth noticing how the intensity of the emitted electric field is inversely proportional to the mass of the scatterer, contained in the Thompson length (r_e), justifying the assumption of neglecting nucleons emissions.

Considering the spatial dispersion effect due to the relative position of the electrons ($\Delta\boldsymbol{r}_s$) compared with the surrounding nucleus ($\boldsymbol{r}$), see Fig A.4, for an observer, far away from the scattering atom ($r >> |\Delta\boldsymbol{r}_s| \implies r_s = r - \boldsymbol{k}_0\cdot\Delta\boldsymbol{r}_s$) and ignoring for each electron the effect of incident waves scattered by neighboring electrons[§], the

[‡]Electron achieve thermal equilibrium through collision with the surrounding lattice where τ is the photoelectric mean free life of the electron. We assume $\omega\tau << 1$ ($v_{\mathrm{Fermi}}\tau << 1/q$), in order to consider only temporal (no spatial) dispersion effects ($\implies$ Fourier transform of refractive index $n(\omega,q) = n(\omega)$).

[§]Born approximation.

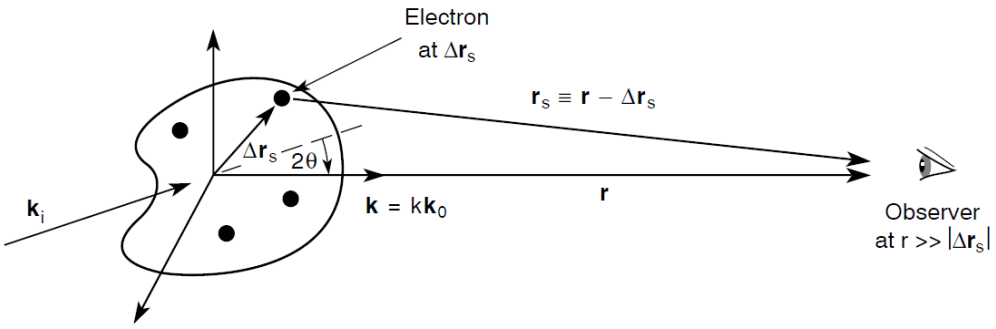

Figure A.4: Scattering diagram for radiation incident on a many-electron atom, semi-classically described as a collection of quantized point electrons surrounding a nucleus of charge $+Ze$ at $\boldsymbol{r} = 0$ [110].

emitted electric field appear to be:

$$\begin{aligned}
\boldsymbol{E}(\boldsymbol{r},t) &= \frac{m_\mathrm{e} r_\mathrm{e}}{e}\sum_{s=1}^{Z}\frac{\boldsymbol{a}_{\mathrm{T},s}(t-r_s/c)}{r_s} = \\
&= E_{\mathrm{z},0}\frac{r_\mathrm{e}}{r}\sin\Theta\cdot\mathrm{Re}\Bigg[\sum_{s=1}^{Z}\underbrace{\int n_{\mathrm{e},s}(\Delta\boldsymbol{r}_s)\mathrm{e}^{-\mathrm{i}\overbrace{(\boldsymbol{k}-\boldsymbol{k}_\mathrm{i})}^{\Delta\boldsymbol{k}=\boldsymbol{q}}\cdot\Delta\boldsymbol{r}_s}\mathrm{d}^3\Delta\boldsymbol{r}_s}_{f_{0,s}(\boldsymbol{q})}\underbrace{\frac{\omega^2}{(\omega_s^2-\omega^2-\mathrm{i}\omega/\tau)}}_{f_{1,s}(\omega)+\mathrm{i}f_{2,s}(\omega)}\mathrm{e}^{-\mathrm{i}\omega(t-r/c)}\Bigg] = \\
&= E_{\mathrm{z},0}\frac{r_\mathrm{e}}{r}\sin\Theta\cdot\mathrm{Re}\Bigg[\sum_{s=1}^{Z}\underbrace{4\pi\int\frac{n_{\mathrm{e},s}(\Delta r_s)\sin(q\Delta r_s)\Delta r_s^2}{q\Delta r_s}\mathrm{d}\Delta r_s}_{f_{0,s}(q)}\underbrace{\frac{\omega^2}{(\omega_s^2-\omega^2-\mathrm{i}\omega/\tau)}}_{f_{1,s}(\omega)+\mathrm{i}f_{2,s}(\omega)}\mathrm{e}^{-\mathrm{i}\omega(t-r/c)}\Bigg]
\end{aligned} \tag{A.5}$$

Eq. A.5 is the generalization of eq. A.4, where $\Delta\boldsymbol{k}$ (usually referred to $\boldsymbol{q}$) is defined as transferred momentum of the scattered electromagnetic wave, see Fig. 2.2. $F^{\mathrm{atom}}(q,\omega) = \sum_{s=1}^{Z} f_{0,s}(q)(f_{1,s}(\omega) + \mathrm{i}f_{2,s}(\omega))$ is the complex atomic scattering factor. The last step of eq. A.5 come from the assumption of spherical symmetry distribution for every electron, expressed through the electron density $n_{\mathrm{e},s}$. $\sum_{s=1}^{Z} f_{0,s}(q) = F_0^{\mathrm{atom}}(q)$ is commonly referred to atomic form factor. Form factor spherical symmetry can be either intrinsic or the result of spherical averaging (like in powder diffraction). In principle, $n_{\mathrm{e},s}$ introduced in eq. A.5 can be calculated by an atom of each element, which is obviously a quantum-mechanical problem. In Fig A.5 are presented the atomic form factor calculated for several elements.

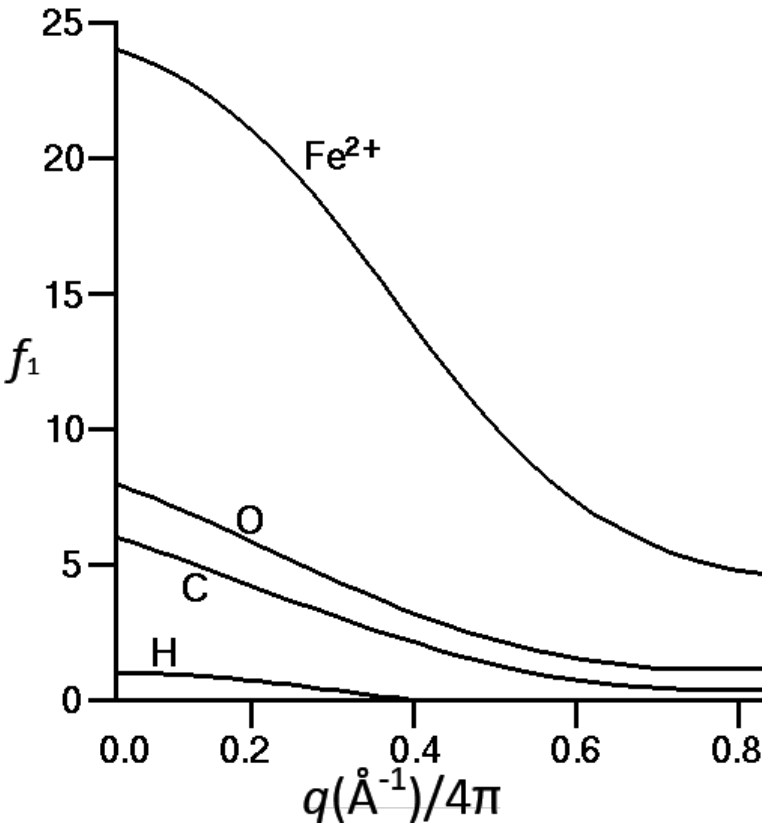

Figure A.5: Real part of atomic scattering factor as a function of X-ray momentum transferred for several elements[205].

For $|\boldsymbol{q}\cdot\Delta\boldsymbol{r}_s| << \pi$, $F(\boldsymbol{q},\omega)$ can be approximated as independent of the momentum transferred $\boldsymbol{q}$, which means that it is not affected by the relative position of the atomic electrons. Among the lightest elements ($Z < 40$), hydrogen has the smallest radius (Bohr radius, $a_0 = 0.53$ Å) which lead to $|\boldsymbol{q}| << \pi/a_0 \simeq 6$ Å^{-1}. Instead, considering sodium, which is one of the biggest atoms ($a = 1.86$ Å), $|\boldsymbol{q}| << \pi/a \simeq 1.7$ Å^{-1}. Under these conditions, $f_{0,s}(q) = 1$ and $F^{\text{atom}}(q,\omega) = F^{\text{atom}}(\omega) = \sum_{s=1}^{Z} f_{1,s}(\omega) + \mathrm{i}\sum_{s=1}^{Z} f_{2,s}(\omega) = f_1(\omega) + \mathrm{i}f_2(\omega)$. It worth noting that in such condition and for ω tending to infinity, $f_{1,s}(\omega)$ tends to one and $f_1(\omega)$ tends to the atomic number Z, see $f_1(\omega)$ and $f_2(\omega)$ plotted in Fig A.6.

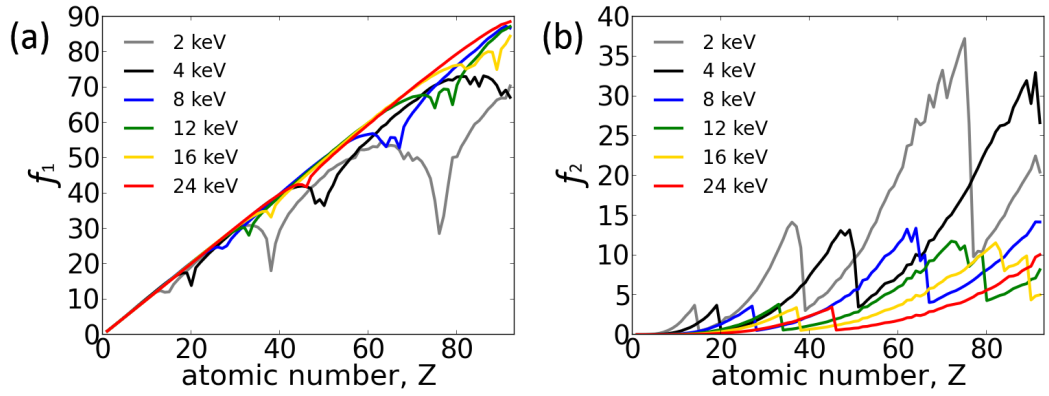

Figure A.6: (a) Calculated real, f_1, and (b) experimental imaginary, f_2, atomic scattering factor for no deflected ($q = 0$) X-rays at different energies[206].

A.3 Coherence properties of X-rays

Visible light passing through a gas has a frequency with respect to the molecules of the gas, $\omega << \omega_s$, leading to a typical Rayleigh emission where, form eq. A.5, the intensity ($\propto |\langle \boldsymbol{E} \rangle|^2$) is $\propto \omega^4$. The imaginary term, $-\mathrm{i}/\tau$, in eq. A.5 represents instead the intensity loss of the electromagnetic wave and it tends to be predominant for frequencies getting close to resonance frequencies, responsible for fluorescent emissions ($\omega \simeq \omega_s$). For X-ray energies above 24 keV passing through light elements (atomic number $Z < 40$), the X-ray spectrum lies to the high-frequency side of various resonances, $\omega >> \omega_s$, associated with the binding of electrons, see Fig. A.6(b)[108]. The electrons scattering the X-rays behave like free particles (Drude model, $\omega_s = 0$) moving in a periodic potential, where the mass of the electron (m_e) is replaced by an effective electron mass (m_e^*) that is used to simplify bands structure (spherical Fermi surface)[207]. For a transverse electromagnetic wave ($\boldsymbol{E} \perp \boldsymbol{k}_0$), the electromagnetic emission source is composed only by the transverse electron flux, $\boldsymbol{J}_\mathrm{T}$, in the direction of propagation ($\boldsymbol{k}_0$). Eq. A.5 is a particular (harmonic) solution of the electromagnetic wave equation below:

$$\left(\frac{\partial^2}{\partial t^2} - c^2 \nabla^2 \right) \boldsymbol{E}(\boldsymbol{r}, t) = -\frac{1}{\epsilon_0} \frac{\partial \boldsymbol{J}_\mathrm{T}(\boldsymbol{r}, t)}{\partial t} \tag{A.6}$$

Rearranging the terms in eq. A.6 and combining it with eq. A.5, for a non spatially dispersive source, the temporal part of wave equation can be expressed introducing the refractive index $n(\omega)$, which expresses the ratio between the speed of light in vacuum and the phase velocity of the particular harmonic solution ($= c/v = ck(\omega)/\omega$):

$$\left(\frac{\partial^2}{\partial t^2} - \frac{\omega^2}{n^2(\omega)}\right)\boldsymbol{E}(t) = 0 \tag{A.7}$$

where $n(\omega)$ is the real part of the of the complex refractive index $N(\omega) = n(\omega) - \mathrm{i}\beta(\omega)$. For X-rays ($\omega >> \omega_s$) the complex refractive index can be approximated as follows:

$$\begin{aligned}\lim_{\omega_s/\omega\to 0} N(\omega) &= \lim_{\omega_s/\omega\to 0}\left[1 - \sum_{s=1}^{Z}\frac{\omega_{\mathrm{p}}^2}{(\omega_s^2 - \omega^2 - \mathrm{i}\omega/\tau)}\right]^{\frac{1}{2}} = \\ &= 1 - \frac{1}{2}\sum_{s=1}^{Z}\frac{\omega_{\mathrm{p},s}^{*\,2}}{(-\omega^2 - \mathrm{i}\omega/\tau)} = 1 - \frac{1}{2}\sum_{s=1}^{Z}\frac{\omega_{\mathrm{p},s}^{*\,2}}{\omega^2}\left(f_1^*(\omega) + \mathrm{i}f_2^*(\omega)\right) = \\ &= 1 - \delta(\omega) - \mathrm{i}\beta(\omega)\end{aligned} \tag{A.8}$$

where the effective plasma frequency ${\omega_{\mathrm{p},s}^*}^2 = n_{\mathrm{e}}e^2/m_{\mathrm{e}}^*\epsilon_0$ takes in consideration the approximated uniform distribution of electrons in the atom (n_{e}). The X-ray spectrum generally lies to the high-frequency side of various electron plasma frequencies considering the typical values of electron density in the materials[¶]. The complex refractive index has the form of $N(\omega) = 1 - \delta(\omega) - \mathrm{i}\beta(\omega)$[‖] where, for $\omega >> \omega_{\mathrm{p}}$, δ and β both are positive and tend to zero according to $1/\omega^2$ ($\propto \lambda^2$) ($0 < \lambda << 1$ and $0 < \beta << 1$). Concerning visible light, the real part of the refractive index n can deviate strongly from unity (n of glass in visible light ranges from 1.5 to 1.8) while the deviation from unity for X-rays in different media is generally of the order of 10^{-5} (10^{-8} air). Most important for X-rays, the refractive index changes ($\mathrm{d}n(\omega)/\mathrm{d}\omega = \mathrm{d}\delta/\mathrm{d}\omega$) in media, responsible for temporal dispersion

[¶]The plasma frequency for aluminium is 1.57×10^{15} rad/s while X-rays frequency are at least 10^4 times higher.

[‖]The choice of $-\mathrm{i}\beta$ is consistent with a wave description $E_{\mathrm{z}}(t,x) = \mathrm{Re}[E_{\mathrm{z},0}\mathrm{e}^{-\mathrm{i}\omega t + \mathrm{i}kx}]$. A choice of $\mathrm{i}\beta$ is consistent with $E_{\mathrm{z}}(t,x) = \mathrm{Re}[E_{\mathrm{z},0}\mathrm{e}^{+\mathrm{i}\omega t - \mathrm{i}kx}]$.

because it doesn't have a strong frequency dependence, can be neglected. For any harmonic wave contribution of an X-ray passing through a medium, the phase velocity (crest velocity of the wave) is larger than the velocity of light ($v_{\mathrm{ph}} = c/n(\lambda) > c$). It does not contradict the law of relativity, which required that only the signals carrying information (group velocity, $\partial\omega/\partial k$) do not travel faster than c.

In reality, an X-ray beam is not perfectly monochromatic but composed by a narrow ($\Delta\lambda/\lambda << 1$) packet of harmonic waves which lead to a temporal dispersion along the direction of propagation. Considering X-ray emissions at $x = 0$ and at a generic x, in order to generate interferences consisting in intensities modulated in time (not temporaly averaged intensities), the relative phases among the harmonic waves of a packet waves at the first emission (0) has to remain the same at the second emission (x) location. Introducing the longitudinal coherence length (ξ_l) that refers to the distance over which the phase information is fully lost (change of a factor π), in order generate modulated intensities, the following approximation has to occur: $x << \xi_l$. Such a longitudinal coherence length, would limit the size (x) of the structure that can be investigated using X-ray as a probe. For instance, if investigating the crystal structure it would limit the crystallite size, if investigating the pores/particles distribution or their surface roughness, it would limit the size of the pores/particles and in case of highly ordered space arrangement of pores/particles it would limit the total size of the structure [(# of diffractive pore/particle layers) × (d-spacing)]. Considering an X-ray beam, composed by a packet of waves ($\Delta\lambda$) centred around λ and passing through a medium of uniform electron density (n_e), in order to avoid loose of phase information, the relative phase shift ($\Delta\Phi$), from eq. A.15, is required to be:

$$\Delta\phi = \frac{(1-\delta(\lambda))2\pi x}{\lambda} - \frac{(1-\delta(\lambda+\Delta\lambda))2\pi x}{\lambda+\Delta\lambda} << \pi \tag{A.9}$$

$$\lim_{\Delta\lambda/\lambda\to 0} \delta(\lambda+\Delta\lambda) = \delta(\lambda) + \underbrace{\frac{\mathrm{d}\delta(\lambda)}{\mathrm{d}\lambda}}_{>0}\Delta\lambda \tag{A.10}$$

Combining eq. A.9 and eq. A.10:

$$x << \underbrace{\frac{1}{2}\frac{\lambda^2}{\Delta\lambda}}_{\xi_l}\left[\frac{1}{\underbrace{1-\delta+\lambda\frac{d\delta(\lambda)}{d\lambda}}_{+\delta}}\right] \simeq \xi_l\left[\frac{1}{1+\delta}\right] \tag{A.11}$$

For X-rays, from eq. A.8, $\delta(\lambda) \propto \lambda^2$ leading to the approximation $-\delta+\lambda(d\delta/d\lambda) \simeq +\delta$ in eq. A.11. Although the longitudinal coherence length in the medium decreases, see eq. A.11, the change can be neglected ($\delta << 1$). Currently, at Australian Synchrotron, the X-ray energy has an energy resolution ($\Delta\lambda/\lambda$) of 2 $\times 10^{-4}$, optimized at 12 keV ($\lambda = 1.0332$ Å), which corresponds to a (temporal) longitudinal coherence length (ξ_l) of 258 nm. The longitudinal coherence length is schematically defined in Figure A.7.

A propagating X-ray presents mainly particle-like behaviour and follows an optical path due to its not considerably spatial diffusion. It is considered as a ray indeed. Spatial transverse coherence length (ξ_t) refer to the transverse distance across a beam over which the rays of the beam remain parallel to the direction of propagation of the beam. Scattering events (emissions), along the direction of propagation of the beam, transversally separated much less compared with the transverse coherence length ($\Delta y, \Delta z << \xi_t$) will not be affected by the X-rays spatial dispersion. In a similar way, compared with the (temporal) longitudinal coherence length, the (spatial) transverse coherence length of an X-ray passing through a medium is not appreciably affected by the presence of the medium itself. Relying on the schematic calculation provided in Fig. A.7(b), $2\xi_t\Delta\theta = \lambda$ where $\Delta\theta = D/R$, the transverse coherence length under vacuum is defined as $\xi_t = \lambda/(2D/R)$, where D is the size of the X-ray source and R is the distance between the source and the sample position. Due to reduced diffusion of X-rays, the source size is comparable with the beam size at the sample position. At the Australian Synchrotron (SAXS/WAXS), the beam sizes at sample position (focus) are 250 μm horizontal × 25 μm vertical (FWHM). For a distance from the source of, say, $R =$

40 m, the transverse coherence length (ξ_t), in the horizontal and vertical plane of acceleration, are respectively $\xi_{t,h} = 8$ μm and $\xi_{t,v} = 80$ μm.

The coherence lengths put an upper limit on the separation of two emitting electrons if they are to give rise to interference where the relative phase need to be taken into account before squaring the electro and magnetic fields in order to obtain the total scattered intensities. If they are further separated, they scatter independently, squaring the two amplitudes separately and subsequently add them to get the total scattered intensity. This is not different from classical optics.

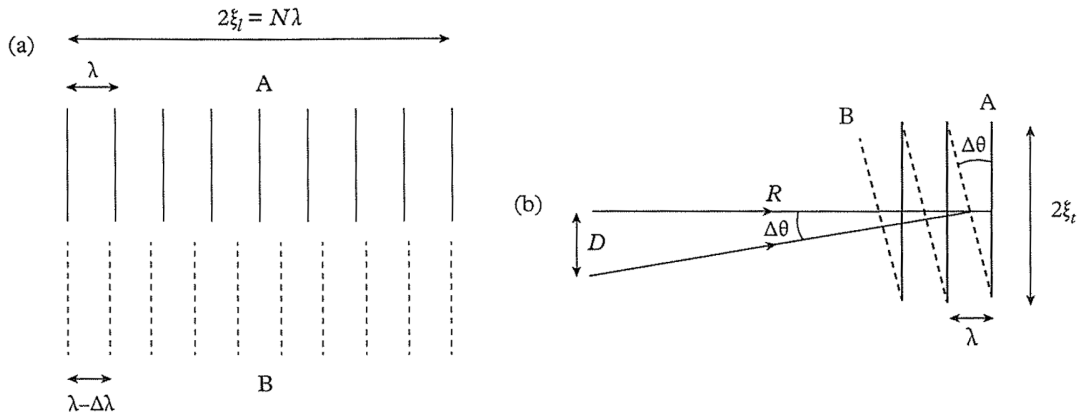

Figure A.7: Schematic (a) longitudinal and (b) transverse coherence length[108,138].

An X-ray passing through a medium, doesn't drastically change its original (under vacuum) coherence lengths, which is the main reason why X-ray are widely adopted to investigate the electron distribution in media. On the other hand, the transverse and longitudinal coherence lengths are much smaller compared with the conventional lasers, mainly because the differences in wavelengths (commercial lasers wavelengths (λ) are over 2000 Å). X-ray Free Electron Lasers (XFEL) technique, recently available only in Stanford (USA) and Hamburg (Germany) combine X-ray and high-coherent laser properties. The XFEL new frontier of research consists in 'performing time-resolved coherent scattering experiments in the hard X-ray regime from which fundamental dynamics in condensed matter ordered and disordered systems can be explored'[203].

A.4 Photoelectric (PE) scattering

Having determined X-ray $\boldsymbol{E}(\boldsymbol{r},t)$ scattered by a semi-classical multi-electron atom, we can now calculate the differential and total atomic scattering cross sections:

$$\begin{aligned}
&\frac{\mathrm{d}\sigma_{\mathrm{PE}}(\omega)}{\mathrm{d}\Omega} = \frac{\mathrm{d}\overline{P}(\Theta,\phi)}{|\overline{\boldsymbol{S}}_{\mathrm{inc.}}|\mathrm{d}\Omega} = r_{\mathrm{e}}^2 |F^{\mathrm{atom}}(q,\omega)|^2 \sin^2\Theta \\
&\sigma_{\mathrm{PE}}(\omega) = \frac{\overline{P}_{\mathrm{Scatt.}}}{|\overline{\boldsymbol{S}}_{\mathrm{inc.}}|} = \frac{8\pi}{3} r_{\mathrm{e}}^2 |F^{\mathrm{atom}}(q,\omega)|^2 \\
&\text{where} \qquad \overline{\boldsymbol{S}}_{\mathrm{inc.}} = \frac{1}{2}\sqrt{\frac{\epsilon_0}{\mu_0}} E_{\mathrm{z},0}^2 \, \boldsymbol{k}_0 \\
&\text{and} \qquad F^{\mathrm{atom}}(q,\omega) = \sum_{s=1}^{Z} f_{0,s}(q)(f_{1,s}(\omega) + \mathrm{i} f_{2,s}(\omega))
\end{aligned} \tag{A.12}$$

where the electromagnetic time-averaged P and $\boldsymbol{S}$ (Poynting vector) are the scattered power and incident energy flux[††], respectively, see Fig. 2.6, and $F^{\mathrm{atom}}(q,\omega)$ is the complex atomic scattering factor, see Appendix A.2. The cross section is the effective area for redirecting incident radiation and the differential cross section contains information about the shape, size and interactions of the scattering bodies. This is achieved by detecting the energy flux ($\boldsymbol{S}$) as a function of scattering angle to obtain a scattering pattern.

A.5 X-ray absorption by a medium

Absorption means an attenuation of the transmitted beam, losing its intensity through all types of interactions, photoelectric (PE), Compton scattering (C), pair production (PP), and Thomson or Rayleigh scattering (R). Considering a radiation passing through a medium, the intensity decrease following an exponential model dependent on the distance crossed and on a coefficient of the material (the linear absorption coefficient, μ)[108]. The transmission, defined as the ratio between the

[††]The energy densities, P and $\boldsymbol{S}$, are not univocally defined, they depend upon the relation adopted among the four electromagnetic potentials. The cross section (σ), instead, is univocally defined (invariant).

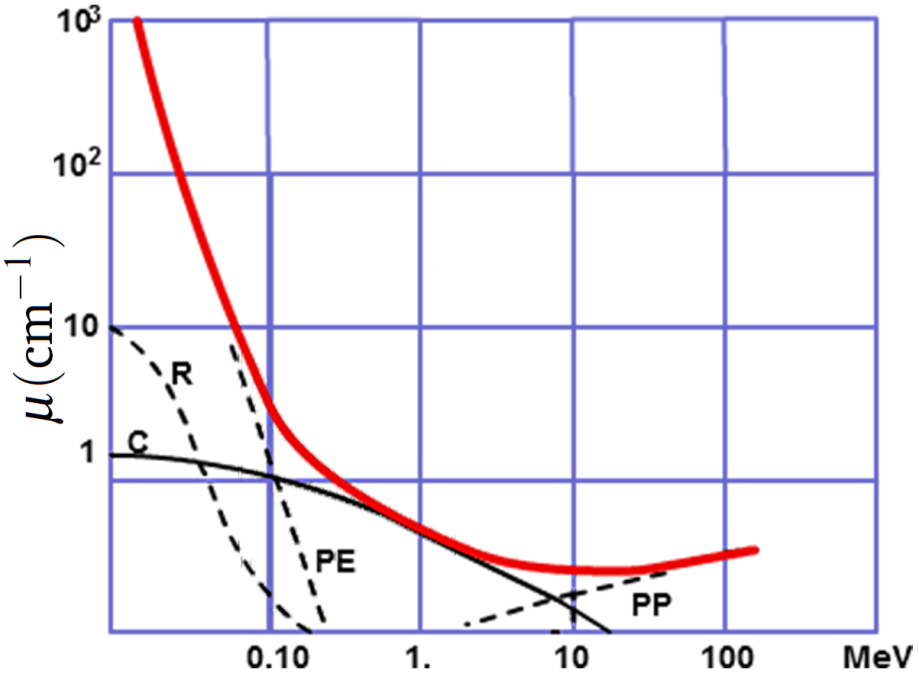

Figure A.8: Approximated total linear absorption coefficient (μ), in red, for iron plotted as a function of radiation energy. The four radiation-matter interactions that contribute to the total absorption are shown in black. The four types of interactions are: photoelectric (PE), Compton scattering (C), pair production (PP), and Thomson or Rayleigh scattering (R) [135].

intensity, $I(x)$, of a beam passed through an x length of a medium and the intensity, $I(0) = I_0$, of the beam at the edge of the medium, is given by:

$$\frac{I}{I_0} = \mathrm{e}^{-\mu_{\mathrm{total}} x} \qquad \text{where} \qquad \mu_{\mathrm{total}} = \mu_{\mathrm{PE}} + \mu_{\mathrm{C}} + \mu_{\mathrm{PP}} + \mu_{\mathrm{R}} \tag{A.13}$$

The linear absorption coefficients are a function of the radiation energy and in the X-ray range, left side (0.012 MeV) of the plot in Fig. A.8, the dominant interaction is the photoelectric. From a practical point of view, the most useful way to quantify photoelectric absorption is in terms of the mass absorption coefficient, $\mu(\omega)/\rho_{\mathrm{m}}$, because for a given element, $(\mu(\omega)/\rho_{\mathrm{m}})_j$ is independent of the form of matter being considered. The mass absorption patterns as a function of energy in the X-ray range for every element can be found in the National Institute of Standards and Technology (NIST) database [208], see values in Table A.1 processed in Appendix

A.6 for a 12 keV X-ray. Thus, the mass absorption coefficient of a mixture can be readily evaluated, knowing the weight fraction % of each element (w_j), using the following relation:

$$\left(\frac{\mu}{\rho_{\mathrm{m}}}\right)_{\mathrm{mixture}} = \sum_{j}^{\#\text{ of elements}} w_j \left(\frac{\mu}{\rho_{\mathrm{m}}}\right)_j \tag{A.14}$$

A transverse electric field propagating at a radial distance, r, from the emitting electron source, from eq. A.7 and A.8, is given by:

$$E(r,t) = \mathrm{Re}\Big[\underbrace{E_{\mathrm{z},0}\,\mathrm{e}^{-\mathrm{i}\omega(t-r/c)}}_{\text{vacuum propagation}}\underbrace{\mathrm{e}^{-\mathrm{i}(2\pi\delta/\lambda)r}}_{\phi\text{- shift}}\underbrace{\mathrm{e}^{-(2\pi\beta/\lambda)r}}_{\phi\text{- decay}}\Big] \tag{A.15}$$

where the first exponential factor represents the phase advance had the wave been propagating in vacuum, the second factor (containing $2\pi\delta r/\lambda$) represents the modified phase shift due to the medium, and the factor containing $2\pi\beta r/\lambda$ represents the decay of the wave amplitude[110]. Considering an X-ray propagating along the direction $\hat{\mathbf{x}}$, combining eq. A.15 and A.14, the following relation is obtained: $I(x)/I_0 = \mathrm{e}^{-2(2\pi\beta/\lambda)x}$ where, from eq. A.8, $\mu(\omega) = 2(2\pi\beta/\lambda) = \omega_{\mathrm{p}}^2 f_2(\omega)/c\omega$. It is worth noticing that, for X-ray radiation, $\mu(\omega)$ is proportional to ω^{-1}. f_1 and f_2 are linked by Kramers-Kroning relations[110]. Thus, obtaining $f_2(\omega)$ through absorption measurements, across a sufficient broad range of frequencies, that the Kramers-Kroning integrals converges, one can determinate $f_1(\omega)$. Finally, as also reported in Table A.1, the refractive index can be calculated using its definition provided in eq. A.8. The energy absorbed by the scattered electron is eventually dissipated, mostly as heat by collisional interaction with the surrounding lattice (τ[‡‡] is first introduced in eq. A.2), and so the electron come to rest.

[‡‡] $1/\tau = 1/\tau_{\mathrm{ei}} + 1/\tau_{\mathrm{ee}} \simeq 1/\tau_{\mathrm{ee}}$, $\tau_{\mathrm{ee}}(m_{\mathrm{i}}/m_{\mathrm{e}})^{1/2} = \tau_{\mathrm{ei}}(m_{\mathrm{e}}/m_{\mathrm{i}})^{1/2}$, $\tau_{\mathrm{ee}} < \tau_{\mathrm{ei}}$

Table A.1: Linear mass attenuation coefficient, imaginary and real scattering factors and variation of refractive index (compared with the vacuum, $n = 1$) for several elements passed through by a 12 keV X-ray.

Element	Z	μ / ρ_m $\Longrightarrow$	f_2 $\Longrightarrow$	f_1 $\Longrightarrow$	δ
		(cm^2/g)	(e/atom)	(e/atom)[a]	
H	1	0.38133	0.1096×10^{-3}	1	2.574×10^{-10}
O	8	3.50736	0.01600	8.027	2.069×10^{-9}
Na	11	9.08	0.05953	11.08	1.346×10^{-6}
Al	13	15.34	0.1180	13.13	3.792×10^{-6}
Cl	17	33.89	0.3426	17.26	4.516×10^{-9}
Ti	22	66.69	0.9110	22.4	6.082×10^{-6}
Pb	82	82.53	4.8764	75	1.186×10^{-5}

[a] Notice the variation compared to the atomic number ($f_1 - Z$) due to electrons binding energy.

A.6 Mass absorption patterns for elements as a function of energy

Cl https://physics.nist.gov/PhysRefData/XrayMassCoef/tab3.html

Energy (MeV)	mu/rho (cm^2/g)	log(E)	log(mu/rho)
3.00E-03	1.47E+03	-2.52288	3.168203
4.00E-03	7.04E+02	-2.39794	2.847388
5.00E-03	3.90E+02	-2.30103	2.591176
6.00E-03	2.38E+02	-2.22185	2.377306
8.00E-03	1.08E+02	-2.09691	2.031408
1.00E-02	5.73E+01	-2	1.757775
1.50E-02	1.78E+01	-1.82391	1.251395
2.00E-02	7.74E+00	-1.69897	0.888685
3.00E-02	2.43E+00	-1.52288	0.384712

E(MeV)	log(E)	log(mu/rh	mu/rho (cm^2/g)
0.012	-1.92082	1.530076	33.89036

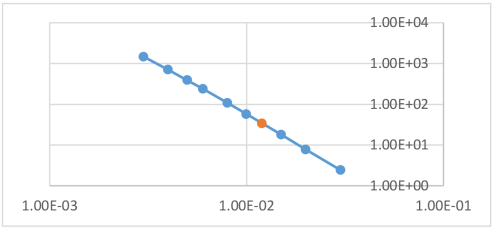

Al

Energy (MeV)	mu/rho (cm^2/g)	log(E)	log(mu/rho)
3.00E-03	7.88E+02	-2.52288	2.896526
4.00E-03	3.61E+02	-2.39794	2.556905
5.00E-03	1.93E+02	-2.30103	2.286456
6.00E-03	1.15E+02	-2.22185	2.061829
8.00E-03	5.03E+01	-2.09691	1.701827
1.00E-02	2.62E+01	-2	1.418798
1.50E-02	7.96E+00	-1.82391	0.90064
2.00E-02	3.44E+00	-1.69897	0.536685

E(MeV)	log(E)	log(mu/rh	mu/rho (cm^2/g)
0.012	-1.92082	1.185803	15.33922

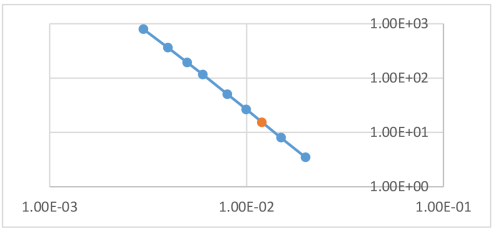

Ti

Energy (MeV)	mu/rho (cm^2/g)	log(E)	log(mu/rho)
3.00E-03	3.32E+02	-2.52288	2.52153
4.00E-03	1.52E+02	-2.39794	2.180986
4.97E-03	8.38E+01	-2.30396	1.923244
4.97E-03	6.88E+02	-2.30396	2.837462
5.00E-03	6.84E+02	-2.30103	2.834929
6.00E-03	4.32E+02	-2.22185	2.635785
8.00E-03	2.02E+02	-2.09691	2.305996
1.00E-02	1.11E+02	-2	2.044148
1.50E-02	3.59E+01	-1.82391	1.554731
2.00E-02	1.59E+01	-1.69897	1.200029

E(MeV)	log(E)	log(mu/rh	mu/rho (cm^2/g)
0.012	-1.92082	1.824077	66.69243

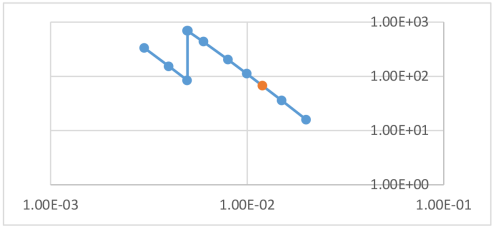

Rare Metal (Lead)

Energy (MeV)	mu/rho (cm^2/g)	log(E)	log(mu/rho)
3.00E-03	1.97E+03	-2.52288	3.293363
3.07E-03	1.86E+03	-2.51337	3.268812
3.07E-03	2.15E+03	-2.51337	3.33163
3.30E-03	1.80E+03	-2.48132	3.254306
3.55E-03	1.50E+03	-2.44926	3.174932
3.55E-03	1.59E+03	-2.44926	3.200029
3.70E-03	1.44E+03	-2.43186	3.158965
3.85E-03	1.31E+03	-2.41446	3.117603
3.85E-03	1.37E+03	-2.41446	3.136086
4.00E-03	1.25E+03	-2.39794	3.097257
5.00E-03	7.30E+02	-2.30103	2.863561
6.00E-03	4.67E+02	-2.22185	2.669503
8.00E-03	2.29E+02	-2.09691	2.359266
1.00E-02	1.31E+02	-2	2.115943
1.30E-02	6.70E+01	-1.88488	1.82614
1.30E-02	1.62E+02	-1.88488	2.209783
1.50E-02	1.12E+02	-1.82391	2.047664
1.52E-02	1.08E+02	-1.81816	2.032619
1.52E-02	1.49E+02	-1.81816	2.171726
1.55E-02	1.42E+02	-1.80892	2.151063
1.59E-02	1.34E+02	-1.79967	2.128399
1.59E-02	1.55E+02	-1.79967	2.189771
2.00E-02	8.64E+01	-1.69897	1.936313

E(MeV)	log(E)	log(mu/rh	mu/rho (cm^2/g)
0.012	-1.92082	1.916608	82.52927

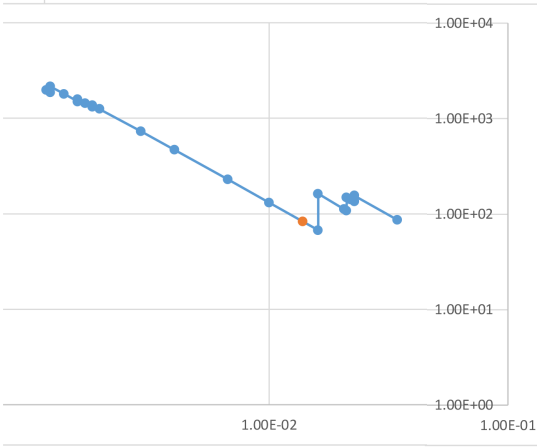

Na

Energy (MeV)	mu/rho (cm^2/g)		log(E)	log(mu/rho)
3.00E-03	5.07E+02	5.02E+02	-2.52288	2.705008
4.00E-03	2.26E+02	2.24E+02	-2.39794	2.354301
5.00E-03	1.19E+02	1.18E+02	-2.30103	2.077004
6.00E-03	7.03E+01	6.92E+01	-2.22185	1.846955
8.00E-03	3.02E+01	2.94E+01	-2.09691	1.479719
1.00E-02	1.56E+01	1.50E+01	-2	1.192289
1.50E-02	4.69E+00	4.31E+00	-1.82391	0.671543
2.00E-02	2.06E+00	1.76E+00	-1.69897	0.313234

E(MeV)	log(E)	log(mu/rh	mu/rho (cm^2/g)
0.012	-1.92082	0.95813	9.080924

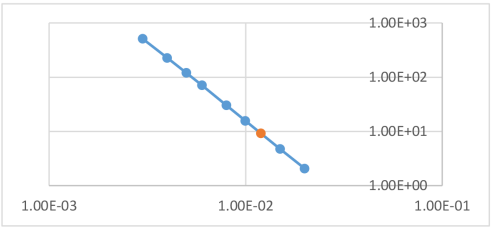

H https://physics.nist.gov/PhysRefData/XrayMassCoef/tab3.html

Energy (MeV)	mu/rho (cm^2/g)	log(E)	log(mu/rho)
3.00E-03	5.61E-01	-2.52288	-0.25088
4.00E-03	4.55E-01	-2.39794	-0.34237
5.00E-03	4.19E-01	-2.30103	-0.37748
6.00E-03	4.04E-01	-2.22185	-0.3934
8.00E-03	3.91E-01	-2.09691	-0.40738
1.00E-02	3.85E-01	-2	-0.41409
1.50E-02	3.76E-01	-1.82391	-0.42435
2.00E-02	3.70E-01	-1.69897	-0.43239

E(MeV)	log(E)	log(mu/rh	mu/rho (cm^2/g)
0.012	-1.92082	-0.4187	0.381327

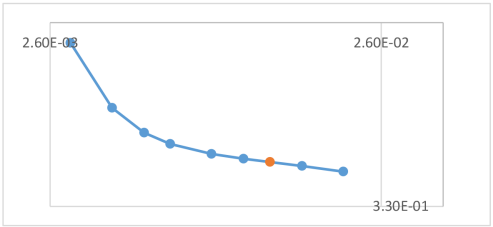

O https://physics.nist.gov/PhysRefData/XrayMassCoef/tab3.html

Energy (MeV)	mu/rho (cm^2/g)	log(E)	log(mu/rho)
3.00E-03	2.17E+02	-2.52288	2.33666
4.00E-03	9.32E+01	-2.39794	1.969183
5.00E-03	4.79E+01	-2.30103	1.680336
6.00E-03	2.77E+01	-2.22185	1.44248
8.00E-03	1.16E+01	-2.09691	1.06558
1.00E-02	5.95E+00	-2	0.774663
1.50E-02	1.84E+00	-1.82391	0.263873
2.00E-02	8.65E-01	-1.69897	-0.06293

E(MeV)	log(E)	log(mu/rh	mu/rho (cm^2/g)
0.012	-1.92082	0.544981	3.507364

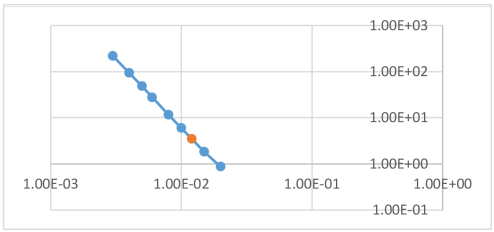

Appendix B

Lorentz-Polarization and Temperature Aberration

In Appendix A.4, we obtained the differential cross section (see eq. A.12) of an incident electromagnetic wave having the transverse component of the incident electric field (polarization) laying only in the plane of diffraction, the plane where both $\boldsymbol{k}_i$ and $\boldsymbol{k}$ (see Fig. 2.2) lays. Recognizing the relation, $\pi/2 = 2\theta + \Theta$, between 2θ, from Fig. 2.2, and Θ from Fig. A.3, in eq. A.12, $\sin^2(\Theta)$ can be replaced by $\cos^2(2\theta)$. For an unpolarized incident beam, such as that coming from an X-ray tube, the component of the incident electric field perpendicular to the plane of diffraction is θ independent[113]. $\cos^2(2\theta)$ is thus replaced by $(\cos^2(2\theta)+1)/2$ in eq. A.12 that is commonly referred to the Thompson scattering differential cross section. The Lorenz correction gathers three different trigonometrical correction factors for the differential cross section[113]:

- Finite diffraction peak width.
- Number density of crystals oriented at the Bragg condition.
- Integrated intensity per unit length of diffraction line.

Combining the three factors of the Lorenzian correction, the polarization factor and a further factor that take into consideration the correction due to the presence of an

incident or diffracted beam monochromator, $\cos^2(2\theta_m)$, the result is the LP factor in eq. B.1, also plotted in Fig. B.1.

$$P = \frac{1+\cos^2 2\theta_m \cos^2 2\theta}{1+\cos^2 2\theta_m} \quad ; \quad L = \frac{1}{\sin 2\theta}\cos\theta\frac{1}{\sin 2\theta} = \frac{\cos\theta}{\sin^2 2\theta} = \frac{1}{4\sin^2\theta\cos\theta}$$
$$LP = \frac{1+\cos^2 2\theta\cos^2 2\theta_m}{8(1+\cos^2 2\theta_m)\sin^2\theta\cos\theta} \tag{B.1}$$

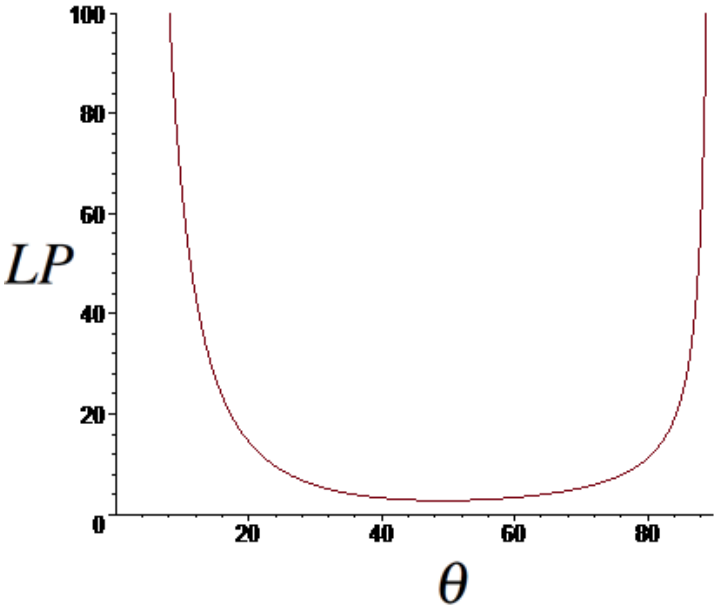

Figure B.1: Lorenz-polarization (only) correction factor for differential cross section of an unpolarized incident electromagnetic wave passing through a medium[113].

The temperature factor takes into consideration the atomic thermal vibration in a crystal that increases as the temperature increases. An increase in temperature has three main effects:

- Expansion of unit cells, shifting lines towards lower θ position.
- Decrease in diffraction line intensity $(F_0^{\text{atom}}(\theta_{h,k,l}) \times \exp\left[-B^{\text{atom}}(\sin(\theta_{h,k,l})/\lambda)^2\right])$.
- Increase in the background between peaks.

Appendix C

TOPAS

C.1 Launch mode refinement output

```
'macro taken from http://topas.dur.ac.uk/topaswiki/doku.php?id=variable_divergence_lpsd
'macro for doing variable divergence (fixed illumination length) with the inbuilt lpsd
convolution '
' Inputs required:  illumination length (mm), and detector size (degrees) '
' Corrects for both peak shape and intensity.  '
'use this macro if you just want to give the values:  '
macro Variable_Divergence_lpsd(lenv, detv) { Variable_Divergence_lpsd(, lenv, , detv) }
'use this macro if you want to refine something:  '
macro Variable_Divergence_lpsd(lenc, lenv, detc, detv) {
  #m_argu lenc 'illuminated length in mm '
  #m_argu detc 'size of detector in degrees '
  If_Prm_Eqn_Rpt(lenc, lenv, min 0.0001 max 60)
  If_Prm_Eqn_Rpt(detc, detv, min 0.0001 max 179.9999)
  lpsd_th2_angular_range_degrees =CeV(detc, detv);
  lpsd_equitorial_divergence_degrees =(-2 ArcTan((Rp-Sqrt(Rp^2+CeV(lenc,lenv)^2 Cos(Th)^2))
Sin(Th) / (CeV(lenc,lenv) Cos(Th)^2))) Rad;
  lpsd_equitorial_sample_length_mm =Sin(Th);
  lpsd_beam_spill_correct_intensity 1
}
r_exp 2.84483116 r_exp_dash 5.71243363 r_wp 4.12322628 r_wp_dash 8.27945671 r_p 3.16723813
r_p_dash 7.12150887 weighted_Durbin_Watson 1.12099149 gof 1.44937469
iters 100000
do_errors
xdd "7-NaAlH4.raw"
  r_exp 2.84483116 r_exp_dash 5.71243363 r_wp 4.12322628 r_wp_dash 8.27945671 r_p 3.16723813
r_p_dash 7.12150887 weighted_Durbin_Watson 1.12099149 gof 1.44937469
```

```
  'range 1
  bkg @ 687.155059'_5.13284383 3.42177282'_6.95771977 14.6107121'_5.31312761
26.9075076'_3.46956457 10.0729983'_2.72833743 11.7690817'_1.60701287 -9.97890734'_1.14015301
  start_X 18
  finish_X 120
  LP_Factor( 0)
  Rp 250
  Rs 250
  'Variable_Divergence_Intensity
  'Variable_Divergence_Shape( 6)
  Variable_Divergence_lpsd(6, 2.944)
  axial_conv
    filament_length 12
    sample_length 25
    receiving_slit_length 17
    primary_soller_angle 2.5
    secondary_soller_angle 2.5
    axial_n_beta 30
  lam
    ymin_on_ymax 0.0001
    la 0.0159 lo 1.534753 lh 3.6854
    la 0.5691 lo 1.540596 lh 0.437
    la 0.0762 lo 1.541058 lh 0.6
    la 0.2517 lo 1.54441 lh 0.52
    la 0.0871 lo 1.544721 lh 0.62
    la !Kbeta_area 0.001623490071_LIMIT_MIN_1e-005 lo 1.392216 lh 0.5502872
    la =Kbeta_area*0.51134; :  0.00083 lo 1.3925949 lh 0.5505868
    la =Kbeta_area*0.226804; :  0.00037 lo 1.3917581 lh 0.5546122
    la =Kbeta_area*0.206186; :  0.00033 lo 1.3934905 lh 1.2654733
    la =Kbeta_area*0.113402; :  0.00018 lo 1.3913004 lh 0.8290293
    prm wpa = Get(weight_percent_amorphous); :  4.77923'_0.44401
    prm wpa_orig =100 wpa / (100-cor_cwp); : 8.11414‘_0.75383
    prm wp_sc = 100 / (100-cor_cwp); :  1.69779'_0.00000
  elemental_composition
  {
  Rietveld Corrected Original
  AL 70.554'_0.104 67.182'_0.353 77.131'_0.599
  CL 3.417'_0.060 3.254'_0.063 5.524'_0.106
  H 0.339'_0.010 0.323'_0.010 0.548'_0.018
  NA 4.148'_0.067 3.949'_0.074 6.705'_0.126
  O 20.319'_0.095 19.348'_0.000 0.000'_0.000
  TI 1.224'_0.051 1.165'_0.051 1.978'_0.086
  Other 0.000'_0.000 4.779'_0.444 8.114'_0.754
  }
```

```
    'without:  70.188/2.052 = 34.2
    'with:  69.497/2.694 = 25.8
    prm !ratio = 78.83/2.79; :  28.25448
  element_weight_percent Al al_atom 70.55417660'_0.10384442
str
  LVol_FWHM_CS_G_L( 1, 57.63608'_1.71682, 0.89, 73.14305'_2.32193,@, 165.42054'_9.91233,@,
111.05428'_3.77472)
  r_bragg 1.93282142
  phase_MAC 31.5902045
  phase_name "Corundum, syn"
  MVW( 611.768, 255.025'_0.009, 43.163'_0.201)
  prm cor_cwp =Get(corrected_weight_percent); :  41.10000'_0.00000
  spiked_phase_measured_weight_percent 41.1
  space_group 167
  scale @ 0.0140578292'_9.368e-005
  Phase_LAC_1_on_cm( 125.83621'_0.00467)
  Phase_Density_g_on_cm3( 3.98339'_0.00015)
  Trigonal(@ 4.760285'_0.000067,@ 12.995296'_0.000317)
  site Al_1 num_posns 12 x 0 y 0 z 0.35228 occ Al !occ_Al_1_000461212 1 beq !beq_Al_1_000461212
0.45
  site O_1 num_posns 18 x 0.3062 y 0 z 0.25 occ O !occ_O_1_000461212 1 beq !beq_O_1_000461212
0.45
'============================================================================================


str
  LVol_FWHM_CS_G_L( 1, 57.03458'_2.44625, 0.89, 54.03317'_2.31752,@, 60.71143'_2.60395,@,
147470694051.32352'_1.44937_LIMIT_MIN_50 min =50;)
  r_bragg 4.77650629
  phase_MAC 37.3608182
  phase_name "NaAlH4"
  MVW( 216.012, 287.331'_0.112, 4.538'_0.138)
  prm NaAlH4_cwp =Get(corrected_weight_percent); :  4.32107'_0.13949
  prm =NaAlH4_cwp wp_sc; : 7.33628‘_0.23683
  space_group I41/a:2
  scale @ 0.00371515257'_0.0001174
  Phase_LAC_1_on_cm( 46.64042'_0.01810)
  Phase_Density_g_on_cm3( 1.24838'_0.00048)
  Tetragonal(@ 5.028998'_0.000702,@ 11.361060'_0.003066)
  site Na1 num_posns 4 x 0 y 0.25 z 0.125 occ Na+1 1 beq 5.124369592
  site Al1 num_posns 4 x 0 y 0.25 z 0.625 occ Al+3 1 beq 2.805717426
  site H1 num_posns 16 x 0.2626 y 0.5967 z 0.04 occ H-1 1 beq 1
  Preferred_Orientation(@, 1.03016'_0.06287„ 0 2 0)
str
  LVol_FWHM_CS_G_L( 1, 51.27495'_2.21444, 0.89, 71.68283'_3.09581„,@, 80.54251'_3.47844)
```

```
  r_bragg 2.52759149
  phase_MAC 75.7992574
  phase_name "NaCl"
  MVW( 233.771, 179.684'_0.017, 5.633'_0.098)
  prm NaCl_cwp =Get(corrected_weight_percent); :  5.36353'_0.10327
  prm =NaCl_cwp wp_sc; : 9.10616‘_0.17534
  space_group 225
  scale @ 0.00681389251'_0.0001231
  Phase_LAC_1_on_cm( 163.75510'_0.01528)
  Phase_Density_g_on_cm3( 2.16038'_0.00020)
  Cubic(@ 5.642914'_0.000176)
  site Na_1 num_posns 4 x 0 y 0 z 0 occ Na !occ_Na_1_000050628 1 beq 1
  site Cl_1 num_posns 4 x 0.5 y 0.5 z 0.5 occ Cl !occ_Cl_1_000050628 1 beq 1
  /*
    Primary Reference:  Swanson, Fuyat.  Natl.  Bur.  Stand.  (U. S. ), Circ.  539 II, 41 (1953).
    Crystal Structure:  Crystal Structure Source:  LPF.
    Optical Data:  Dana's System of Mineralogy, 7th Ed.  II, 4.
  */
str
  LVol_FWHM_CS_G_L( 1, 73.44779'_1.22714, 0.89, 86.68747'_1.44119,@, 148.19410'_3.26476,@,
178.00121'_4.44873)
  r_bragg 1.32907522
  phase_MAC 49.4798548
  phase_name "Aluminum"
  MVW( 107.926, 66.467'_0.001, 43.374'_0.181)
  prm Al_cwp =Get(corrected_weight_percent); :  41.30091'_0.31149
  prm =Al_cwp wp_sc; : 70.12038‘_0.52885
  space_group 225
  scale @ 0.307237917'_0.001097
  Phase_LAC_1_on_cm( 133.41380'_0.00242)
  Phase_Density_g_on_cm3( 2.69633'_0.00005)
  Cubic(@ 4.050742'_0.000025)
  site Al_1 num_posns 4 x 0 y 0 z 0 occ Al !occ_Al_1_000040787 1 beq 1
str
  LVol_FWHM_CS_G_L( 1, 32.98630'_5.28713, 0.89, 39.48583'_6.20936,@,
70.53416'_14.84764_LIMIT_MIN_0.3,@, 75.89924'_17.89541_LIMIT_MIN_0.3)
  r_bragg 2.07493796
  phase_MAC 105.2727
  phase_name "Al3Ti"
  MVW( 257.623, 127.590'_0.043, 3.293'_0.137)
  prm Al3Ti_cwp =Get(corrected_weight_percent); :  3.13527'_0.13609
  prm =Al3Ti_cwp wp_sc; : 5.32303‘_0.23106
  space_group 139
  scale @ 0.00509000834'_0.0002183
```

```
  Phase_LAC_1_on_cm( 352.96670'_0.11944)
  Phase_Density_g_on_cm3( 3.35288'_0.00113)
  Tetragonal(@ 3.851814'_0.000474,@ 8.599750'_0.001998)
  site Ti_1 num_posns 2 x 0 y 0 z 0 occ Ti !occ_Ti_1_000371449 1 beq !beq_Ti_1_000371449 0.39478
  site Al_1 num_posns 2 x 0 y 0 z 0.5 occ Al !occ_Al_1_000371449 1 beq !beq_Al_1_000371449 0.7264
  site Al_2 num_posns 4 x 0 y 0.5 z 0.25 occ Al !occ_Al_2_000371449 1 beq !beq_Al_2_000371449
0.51085
    for strs { Specimen_Displacement(sd, -0.33370‘_0.00106) }
    hkl_Is
      hkl_m_d_th2 0 0 5 2 8.000000 11.05083 I 411.7491084
      hkl_m_d_th2 0 0 6 2 6.666667 13.27009 I 0.003472735948_LIMIT_MIN_1e-015
      hkl_m_d_th2 0 0 7 2 5.714286 15.49436 I 137.3670193
      hkl_m_d_th2 0 0 8 2 5.000000 17.72452 I 1.085760776_LIMIT_MIN_1e-015
      hkl_m_d_th2 0 0 9 2 4.444444 19.96147 I 1377.051586
      hkl_m_d_th2 0 0 10 2 4.000000 22.20614 I 853.5769088
      hkl_m_d_th2 0 0 11 2 3.636364 24.45946 I 23.94590306_LIMIT_MIN_1e-015
      hkl_m_d_th2 0 0 12 2 3.333333 26.72244 I 202.4577816
      hkl_m_d_th2 0 0 13 2 3.076923 28.99608 I 68.23573074_LIMIT_MIN_1e-015
      hkl_m_d_th2 0 0 14 2 2.857143 31.28144 I 161.2054571
      hkl_m_d_th2 0 0 15 2 2.666667 33.57965 I 93.4026827
      hkl_m_d_th2 0 0 16 2 2.500000 35.89184 I 133.0944368
      hkl_m_d_th2 0 0 17 2 2.352941 38.21925 I 172.0925393
      hkl_m_d_th2 0 0 18 2 2.222222 40.56316 I 216.4906247
      hkl_m_d_th2 0 0 19 2 2.105263 42.92492 I 200.8578948
      hkl_m_d_th2 0 0 20 2 2.000000 45.30598 I 157.7246755
      hkl_m_d_th2 0 0 21 2 1.904762 47.70788 I 143.1819188
      hkl_m_d_th2 0 0 22 2 1.818182 50.13224 I 42.93491439_LIMIT_MIN_1e-015
      hkl_m_d_th2 0 0 23 2 1.739130 52.58085 I 115.9975474_LIMIT_MIN_1e-015
      hkl_m_d_th2 0 0 24 2 1.666667 55.05558 I 179.8943003
      hkl_m_d_th2 0 0 25 2 1.600000 57.55850 I 38.38785666_LIMIT_MIN_1e-015
      hkl_m_d_th2 0 0 26 2 1.538462 60.09181 I 361.7681562
      hkl_m_d_th2 0 0 27 2 1.481481 62.65795 I 576.8933662
      hkl_m_d_th2 0 0 28 2 1.428571 65.25956 I 362.0835463
      hkl_m_d_th2 0 0 29 2 1.379310 67.89956 I 151.0330596_LIMIT_MIN_1e-015
      hkl_m_d_th2 0 0 30 2 1.333333 70.58117 I 259.6110878
      hkl_m_d_th2 0 0 31 2 1.290323 73.30796 I 79.56637824_LIMIT_MIN_1e-015
      hkl_m_d_th2 0 0 32 2 1.250000 76.08392 I 275.3614576
      hkl_m_d_th2 0 0 33 2 1.212121 78.91354 I 165.118814_LIMIT_MIN_1e-015
      hkl_m_d_th2 0 0 34 2 1.176471 81.80189 I 670.3398257
      hkl_m_d_th2 0 0 35 2 1.142857 84.75476 I 2.491914408e-013_LIMIT_MIN_1e-015
      hkl_m_d_th2 0 0 36 2 1.111111 87.77875 I 64.71874785_LIMIT_MIN_1e-015
      hkl_m_d_th2 0 0 37 2 1.081081 90.88156 I 1.000013553e-015_LIMIT_MIN_1e-015
      hkl_m_d_th2 0 0 38 2 1.052632 94.07217 I 1.983498084_LIMIT_MIN_1e-015
      hkl_m_d_th2 0 0 39 2 1.025641 97.36119 I 6.883491379e-014_LIMIT_MIN_1e-015
```

```
      hkl_m_d_th2 0 0 40 2 1.000000 100.76131 I 378.1670661
      hkl_m_d_th2 0 0 41 2 0.975610 104.28797 I 135.620841_LIMIT_MIN_1e-015
      hkl_m_d_th2 0 0 42 2 0.952381 107.96022 I 183.5956928_LIMIT_MIN_1e-015
      hkl_m_d_th2 0 0 43 2 0.930233 111.80205 I 166.8376477_LIMIT_MIN_1e-015
      hkl_m_d_th2 0 0 44 2 0.909091 115.84441 I 63.11577266_LIMIT_MIN_1e-015
      hkl_m_d_th2 0 0 45 2 0.888889 120.12843 I 1127.62786
      LVol_FWHM_CS_G_L( 0.89, 0.85325, 0.89, 1.34028„„ 1.50593351)
      phase_name "bkg"
      scale @ 5.94774776'_0.05264
      space_group "P4"
      Tetragonal( 0.5, 40)
C_matrix_normalized
{
1 2 3 4 5 6 7 8 9 10 11 12 13 14 15 16 17 18 19 20 21 22 23 24 25 26 27 28 29 30 31 32
bkg14bf5f0 1:  100 -96 97 -89 88 -69 25 -4 5 -6 0 -1 6 0 -4 1 -10 0 -1 5 -7 -0 4 -5 5 -0 6 -8 9 1
-0 -98
bkg14bf690 2:  -96 100 -95 95 -86 75 -22 -1 1 -2 -0 1 -5 0 4 -1 8 0 0 -2 2 -1 -6 8 -9 1 -9 13 -15
-1 1 96
bkg14bf730 3:  97 -95 100 -90 92 -71 32 2 -3 4 0 -1 3 0 -4 1 -5 -0 -0 1 -2 -0 5 -6 6 -0 10 -14 17
0 0 -95
bkg14bf7d0 4:  -89 95 -90 100 -84 81 -24 -4 6 -7 -0 1 -2 0 4 -1 3 1 -0 2 -3 -1 -7 9 -10 1 -12 17
-20 -0 1 89
bkg14bf870 5:  88 -86 92 -84 100 -70 45 0 -0 0 0 -1 1 0 -4 1 -2 -0 -0 -1 0 -1 5 -7 6 -0 10 -13 16
-0 -0 -85
bkg14bf910 6:  -69 75 -71 81 -70 100 -28 -1 1 -3 0 1 -0 0 4 -1 1 1 -0 3 -5 -1 -6 8 -8 1 -9 12 -15
-1 1 69
bkg14bf9b0 7:  25 -22 32 -24 45 -28 100 -0 1 -0 1 -0 -3 0 -1 -0 4 -1 0 -3 3 -1 1 -2 4 0 2 -2 3 -1
1 -19
m59f00391_0 8:  -4 -1 2 -4 0 -1 -0 100 -86 53 -3 0 -2 0 2 3 3 -2 2 -2 3 -1 -2 3 -2 -2 3 -5 7 -2 1
-0
m59f00391_1 9:  5 1 -3 6 -0 1 1 -86 100 -72 0 -1 3 0 -3 -1 -5 2 -2 3 -4 -0 3 -4 2 1 -5 7 -10 2 -1
1
scaleeff0c0_ 10:  -6 -2 4 -7 0 -3 -0 53 -72 100 -0 0 -3 0 1 1 6 -2 1 -4 6 1 -3 3 -2 -1 6 -9 12 -1
1 -1
a13eb2a8_ 11:  0 -0 0 -0 0 0 1 -3 0 -0 100 -37 0 0 0 -37 -1 4 1 -0 -1 9 -2 0 1 29 0 0 -1 3 2 -0
c13eb3a8_ 12:  -1 1 -1 1 -1 1 -0 0 -1 0 -37 100 -1 0 2 -25 2 2 0 3 -2 2 -2 -1 0 16 -2 2 -2 1 2 1
m59f00391_2 13:  6 -5 3 -2 1 -0 -3 -2 3 -3 0 -1 100 0 -1 1 -49 -5 -0 3 -1 1 -1 0 -0 -1 -2 2 -3 0
-0 -5
m59f00391_3 14:  0 0 0 0 0 0 0 0 0 0 0 0 0 100 0 0 0 0 0 0 0 0 0 0 0 0 0 0 -0 0 0 0
m59f00391_9 15:  -4 4 -4 4 -4 4 -1 2 -3 1 0 2 -1 0 100 -3 25 4 -6 23 -24 -11 -1 1 -1 3 0 -0 1 1
-1 4
sd 16:  1 -1 1 -1 1 -1 -0 3 -1 1 -37 -25 1 0 -3 100 -1 -10 -2 -1 2 -21 7 -2 0 -78 2 -4 4 -6 -5 -1
scaleeff318_ 17:  -10 8 -5 3 -2 1 4 3 -5 6 -1 2 -49 0 25 -1 100 2 -2 7 -7 -5 1 -1 0 2 3 -4 6 0 -0
7
```

```
a13eb728_ 18:  0 0 -0 1 -0 1 -1 -2 2 -2 4 2 -5 0 4 -10 2 100 -61 3 -7 -2 -0 -0 -0 8 -1 1 -1 0 -0
0
c13eb828_ 19:  -1 0 -0 -0 -0 -0 0 2 -2 1 1 0 -0 0 -6 -2 -2 -61 100 -4 10 8 -0 -0 -0 1 -0 0 -1 0 1
1
m59f00391_4 20:  5 -2 1 2 -1 3 -3 -2 3 -4 -0 3 3 0 23 -1 7 3 -4 100 -69 -7 2 -2 1 0 1 1 -1 -0 -2
-2
scaleeff570_ 21:  -7 2 -2 -3 0 -5 3 3 -4 6 -1 -2 -1 0 -24 2 -7 -7 10 -69 100 5 -1 1 1 -1 0 -1 1
-2 3 3
a13ebc28_ 22:  -0 -1 -0 -1 -1 -1 -1 -1 -0 1 9 2 1 0 -11 -21 -5 -2 8 -7 5 100 -2 1 -1 16 -1 2 -2
-2 7 -0
m59f00391_5 23:  4 -6 5 -7 5 -6 1 -2 3 -3 -2 -2 -1 0 -1 7 1 -0 -0 2 -1 -2 100 -86 45 -7 -12 16
-19 -6 -2 -5
m59f00391_6 24:  -5 8 -6 9 -7 8 -2 3 -4 3 0 -1 0 0 1 -2 -1 -0 -0 -2 1 1 -86 100 -60 1 19 -24 27 5
3 7
scaleeff7c8_ 25:  5 -9 6 -10 6 -8 4 -2 2 -2 1 0 -0 0 -1 0 0 -0 -0 1 1 -1 45 -60 100 -1 -16 21 -27
-1 -3 -7
a13ec0a8_ 26:  -0 1 -0 1 -0 1 0 -2 1 -1 29 16 -1 0 3 -78 2 8 1 0 -1 16 -7 1 -1 100 2 -1 -1 5 4 0
m59f00391_7 27:  6 -9 10 -12 10 -9 2 3 -5 6 0 -2 -2 0 0 2 3 -1 -0 1 0 -1 -12 19 -16 2 100 -91 63
1 0 -9
m59f00391_8 28:  -8 13 -14 17 -13 12 -2 -5 7 -9 0 2 2 0 -0 -4 -4 1 0 1 -1 2 16 -24 21 -1 -91 100
-82 -1 -1 12
scaleeffa20_ 29:  9 -15 17 -20 16 -15 3 7 -10 12 -1 -2 -3 -0 1 4 6 -1 -1 -1 1 -2 -19 27 -27 -1 63
-82 100 0 1 -14
a13ec4a8_ 30:  1 -1 0 -0 -0 -1 -1 -2 2 -1 3 1 0 0 1 -6 0 0 0 -0 -2 -2 -6 5 -1 5 1 -1 0 100 -56 -1
c13ec5a8_ 31:  -0 1 0 1 -0 1 1 1 -1 1 2 2 -0 0 -1 -5 -0 -0 1 -2 3 7 -2 3 -3 4 0 -1 1 -56 100 1
scaleeffa98_ 32:  -98 96 -95 89 -85 69 -19 -0 1 -1 -0 1 -5 0 4 -1 7 0 1 -2 3 -0 -5 7 -7 0 -9 12
-14 -1 1 100
}
```

C.2 Specimen displacement macro

```
'macro taken from http://topas.dur.ac.uk/topaswiki/doku.php?id=debye-scherrer_specimen_
displacement
macro Debye_Scherrer_Specimen_Displacement { DSSD }
macro DSSD(u, u_v) { DSSD(u, u_v„90) } ''standard displacement perpendicular to the beam
macro DSSD(u, u_v, s, s_v)
{
  #m_argu u ''offset of the sample from the centre of the gonio
  #m_argu s ''angle subtended from the "sample" position to the actual centre of the gonio (in
deg)
  If_Prm_Eqn_Rpt(u, u_v, min =-Rs/10; max =Rs/10;) ''max offset of a tenth of a radius
```

```
  If_Prm_Eqn_Rpt(s, s_v, min =-180; max =180;) ''full rotation is provided by a negative u
length.
  '' You need "Rad" at the beginning, as th2_offset takes a value in degrees, and this formula is
in radians
  ''This is the small angle implementation, the full one should have Arcsin() around everything
after the Rad
  th2_offset = Rad (CeV(u, u_v) / Rs) Sin(2 Th - CeV(s, s_v) Deg);
}
```

Appendix D

Photoelectric Differential Cross Section as a Function of Wavelength

The following equation expresses the relation between the atomic absorption total cross section and the imaginary part of the atomic scattering factor (f_2) as a function of angular frequency[108] (ω):

$$\sigma_{\text{atom}} = \left(\frac{\mu}{n}\right)_{\text{atom}} = \frac{1}{n_{\text{atom}}} \frac{\omega_{\text{p}}^2 f_2(\omega)}{c\omega} \tag{D.1}$$

where n_{atom} is the atomic number density. This equation is obtained from the last step of eq. A.8, while f_2 was introduced in eq. A.5. The differential cross section (of sample or per unit of volume) as a function of wavelength is given explicitly for two different particular cases as follow:

$$\begin{aligned} \frac{\partial \Sigma_{\text{PE}}}{\partial \Omega}(q,\lambda) &\overset{\text{X-ray only}}{\simeq} \frac{\lambda^3}{\lambda_0^3} \frac{\mathrm{d}\Sigma_{\text{PE}}}{\mathrm{d}\Omega}(q,\lambda_0) \qquad \text{for} \qquad \lambda \simeq \lambda_s \\ \frac{\partial \Sigma_{\text{PE}}}{\partial \Omega}(q,\lambda) &\overset{\text{X-ray only}}{\simeq} \frac{\lambda}{\lambda_0} \frac{\mathrm{d}\Sigma_{\text{PE}}}{\mathrm{d}\Omega}(q,\lambda_0) \qquad \text{for} \qquad \lambda << \lambda_s \qquad \forall s \end{aligned} \tag{D.2}$$

λ_s is the wavelength of the binding energy associated to an electron (s).

Appendix E

MATLAB Code

```
function [] = ReadDatFile()
clear all
cd('J:\SAE\PHYSICS\HSRG\Data\SizeDist-McSAS\ABS-INT-400-NaAlH4-In-situ-McSas-MatLab')
%21v-shot1_3254.dat is the BG.
fid = fopen('21v-shot1_3254_SAXS.dat','r');
datacell2 = textscan(fid, '%f%f%f', 'HeaderLines', 1,'HeaderLines',2);
fclose(fid);
vshot13254=[datacell2{1},datacell2{2},datacell2{3}];
%ds.dat are the solid thicknesses.
fid2 = fopen('ds.dat','r');
datacell3 = textscan(fid2, '%f');
fclose(fid2);
ds=[datacell3{1}];
%It is countes the # of patterns (NF).
files=dir('1*.dat');
NF = length(files);
for nf=1:NF
nf
files = ['1 (' num2str(nf) ').dat'];
fid = fopen(files,'r');
datacell = textscan(fid, '%f%f%f', 'HeaderLines', 1,'HeaderLines',2);
fclose(fid);
% a1 is a SAXS data.
a1=[datacell{1},datacell{2},datacell{3}];
a1=[a1(:,1),a1(:,2) - vshot13254(:,2),a1(:,3) + vshot13254(:,3)];
% Below, it si removed the artefacts due to second order scattering
% (scattering of scattered X-rays).
a1=a1(1:298,:);
a1( 254:263 , :  )  = [];
```

```
a1( 207 , :  )  = [];
a1( 168 , :  )  = [];
a1( 144 , :  )  = [];
a1( 139 , :  )  = [];
% Changes in the units of measure, from Å^-1 to nm^-1 and from cm^-1 to m^-1, and normalization
% dividing by solid thickness.  The intensity is multiplied by 100 because in McSAS it is express
% in m^-1.  0.1055 cm is the thickness of the carbon film used to calibrate the SAXS apparatus.
a1 = [10*a1(:,1),10.55*a1(:,2)/ds(nf,1),10.55*a1(:,3)/ds(nf,1)];
filename = files(1:end-4);
save(['saxs_',filename,'.dat'], 'a1','-ascii');
end
end
```

Appendix F

$NaAlH_4$ Certificate of Analysis

Certificate of Analysis

SIGMA-ALDRICH

Product Name	Sodium aluminum hydride, hydrogen-storage grade
Product Number	685984
Product Brand	ALDRICH
CAS Number	13770-96-2
Molecular Formula	$NaAlH_4$
Molecular Weight	54.00

TEST	SPECIFICATION	LOT 04631JHV RESULTS
APPEARANCE	LIGHT TO DARK GREY POWDER	FAINT GREY POWDER
X-RAY DIFFRACTION PATTERN	CONFORMS TO STANDARD PATTERN.	CONFORMS TO STANDARD PATTERN.
HYDROGEN EVOLUTION	92% (MINIMUM)	97.9%
TRACE ANALYSIS, ICP	REPORT RESULTS	TRACE METALS (PPM) K 950 AS 23 LI 1.7 B 1.4 MG 6.9 BA 6.6 MN 3.1 CA 15 NI 5.6 CR 2.7 PB 1500 CU 2.4 SN 150 FE 9.1 TI 2.1
TRACE ANALYSIS, ICP	CONFIRMS SODIUM AND ALUMINUM COMPONENTS	CONFIRMS SODIUM AND ALUMINUM COMPONENTS
PURITY		>99.3%
QUALITY CONTROL		SEPTEMBER 2007
ACCEPTANCE DATE		

Barbara Rajzer, Supervisor
Quality Control
Milwaukee, Wisconsin USA

Appendix G

A Rietveld Refinement Limitation

A minor limitation for the quantification of Ti-containing phases using the Rietveld refinement method is caused by the higher (compared to the other atoms present in the sample) binding energy of Ti ($Z = 22$, $E_{\text{K-absorption edge}} = 5.0$ keV) core electrons, which are comparable ($\omega \simeq \omega_s$, see Appendix A.3) with the X-ray energies used (*ex situ*, $E_{\text{X-ray}} = 8$ keV and *in situ*, $E_{\text{X-ray}} = 12$ keV), see Fig. A.6(b). In fact, in TOPAS, the atomic scattering factor, $F^{\text{atomic}}(q, \omega)$, (see Appendix A.2) is implemented by correcting the zero order ($\omega >> \omega_s$) atomic form factor intensity, $F^{\text{atomic}}(q, \omega \rightarrow \infty) = F_0^{\text{atomic}}(q)$, adding to it a first order in energy (ω_s/ω) compensation function. Such complex compensation function used for energies ranging from 10 to 30000 eV tend to be less accurate for atoms having electron binding energies comparable with the X-ray energies used[209].

Appendix H

$NaMgH_3$-400 and -450 McSAS Spherical Pore Shape Analysis

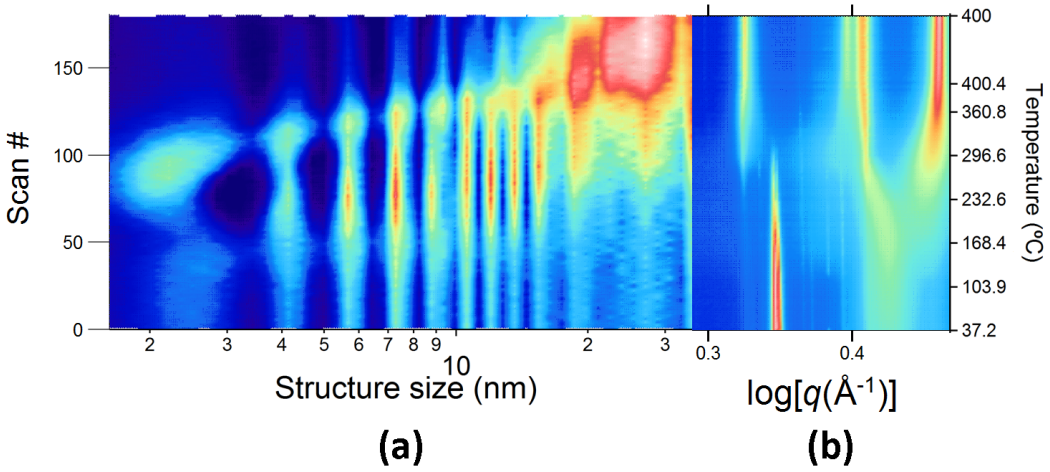

Figure H.1: (a) *In situ* pore size related distributions, $\varphi_{i,\,\text{scan \#}} \times const_{\text{scan \#}}$, obtained applying McSAS (spherical pore shape) analysis to SAXS patterns of $NaMgH_3$-400 decomposition and (b) the corresponding WAXS patterns.

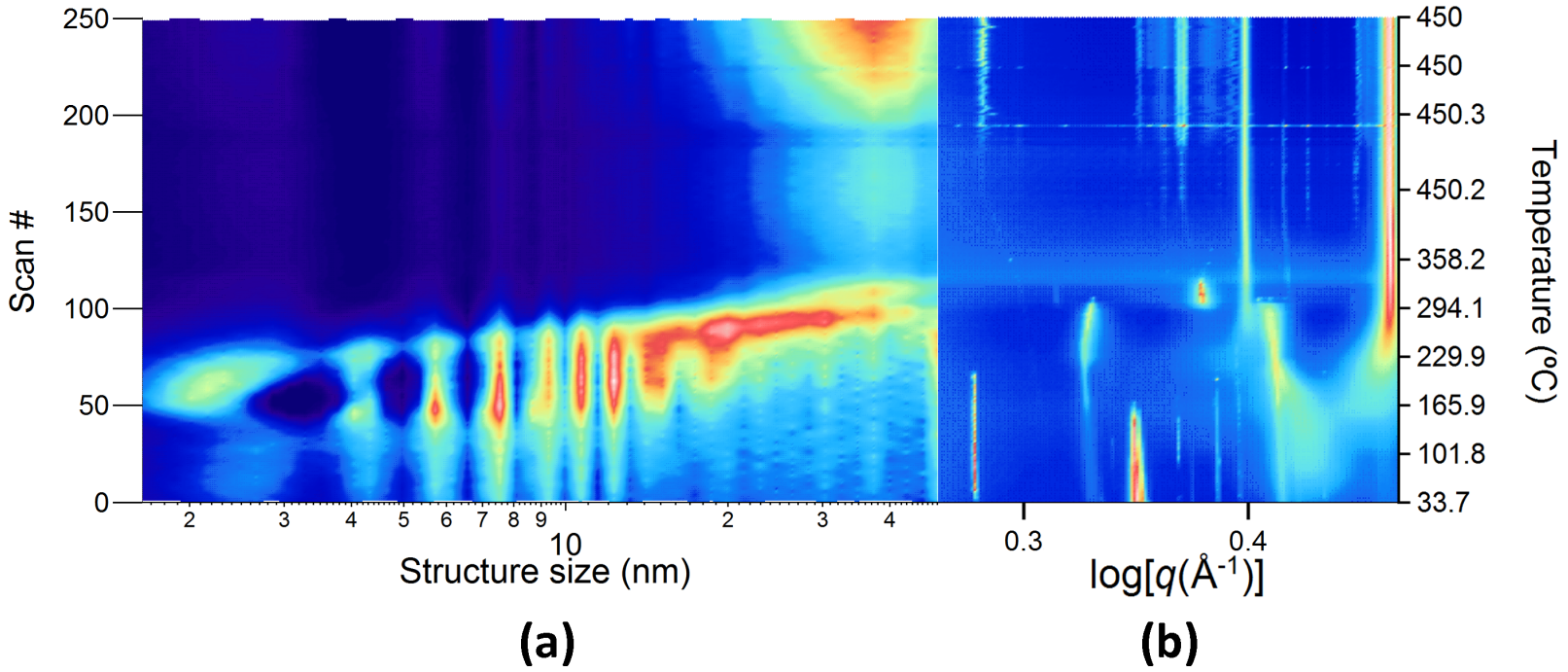

Figure H.2: (a) *In situ* pore size related distributions, $\varphi_{i,\ \text{scan}\ \#} \times const_{\text{scan}\ \#}$, obtained applying McSAS (spherical pore shape) analysis to SAXS patterns of $NaMgH_3$-450 decomposition and (b) the corresponding WAXS patterns.

Appendix I

Pore Statistic

The longitudinal coherence length (ξ_l) of the X-rays adopted, as discussed in Appendix A.3, is 258 nm, which would limit the number of diffractive pore layers that would produce a positive interference along the direction of the X-rays propagation. For instance, for a spatially ordered mesopore body centered cubic (BCC) structure having a d_{110}-space of the order of 10 nm, the number of diffractive pore layers would be limited to much less than (<< 258 nm/10 nm =) 25.8. Similarly, overall less effective, due to transverse horizontally and vertically coherence lengths ($\xi_{t,h} = 8$ μm and $\xi_{t,v} = 80$ μm) with respect to the plan of electron acceleration, the number of diffractive layers, along the transverse directions with respect to the X-rays propagation, would be limited to be << 800 and 8000 respectively. Such limitation on the portion of an eventual spatially ordered pore aggregation, that would produce constructive interferences, would result in a broadening of the diffraction peaks. In fact, considering the portion of an eventual spatially ordered pore aggregation composed by 5 (<< 25.8) diffractive pore layers, according to the Scherrer equation 2.13 (using a k = 0.9)[113,210], the diffraction peak in the SAXS pattern, that would appear in correspondence with the d_{110}-space relative momentum transfer $q = 0.0628$ Å^{-1}, would extend across a q-range of $\Delta q = q^+ - q^- = 0.112 - 0.035 = 0.077$ Å^{-1}. If mesopores are arranged in a spatially-ordered structure, the relative diffraction peaks would be difficult to

detect due to the effect of peak broadening caused by the limitation imposed by the longitudinal coherence length of the X-rays used.

For the hypothetical spatially ordered pore aggregation introduced above (BCC, d_{110}-space $\simeq$ 10 nm), the relative uncertainty on the peak intensities would be expected to be less than 1%. Let's consider, for example, the spatially ordered mesopore BCC structure, introduced above, having a d_{110}-space of the order of 10 nm and mmultiplicity = 12, for which a diffraction peak in the SAXS pattern would appear at $q = 0.0628$ Å^{-1}. Because diffraction peak intensities are proportional to the amount of ordered pore aggregation, if a 1% relative uncertainty on diffraction peak intensities is required, a 1% relative uncertainty on the number of ordered pore aggregation is required. The number of ordered pore aggregates, having N_{layers} (number of layers), that would contribute to the d_{110}-space relative diffraction peak ($q_{110} = 0.0628$ Å^{-1}) would be equivalent to the ratio (n) between the statistical volume ($V_{\text{illuminated}}$) and the volume occupied by the suitable orientated ($O_{\text{orientation}} = \sin(\theta_{110}) \times \Delta\theta_{110}/2$) aggregations ($V_{\text{aggregation}} = [N_{\text{layers}} \times d_{110}\text{-space}]^3 = [k \times \lambda]^3/[\Delta\theta_{110} \times \cos(\theta_{110})]^3$). The statistical volume ($V_{\text{illuminated}}$) of diffraction to be considered is limited by the physical illuminated volume of the sample, consisting of an area of the beam (250 μm horizontally FWHM × 150 μm vertically FWHM) multiplied by the thickness of the sample (550 ± 50 μm). Only the (100 × φ_{meso} =) 3 ± 1%, corresponding to mesopore contribution as discussed in §5.3.1, of such volume ($V_{\text{illuminated}}$) has to be considered. Following the Poisson statistics[117], a 1% relative uncertainty in the number of ordered pore aggregates ($0.01 = \sqrt{n}/n$) corresponds to number of ordered pore aggregates, n ($= V_{\text{illuminated}} \times \varphi_{\text{meso porosirty}} \times m_{\text{multiplicity}} \times O_{\text{orientation}}/V_{\text{aggregation}}$), of 10^4. The minimum q-range ($\Delta q_{110} = 4\pi \times \Delta \sin(\theta)/\lambda$) extension for this specific diffraction peak required in order to have at least a 1% relative uncertainty on the diffraction peak intensities is calculated using $\Delta\theta_{110}$ ($\theta = \theta_{110} \pm \Delta\theta_{110}/2$) obtained by combining the equations above. $\Delta\theta_{110}$, in radians, is given in the following

equation:

$$\Delta\theta_{110} = \left(\frac{2n}{V_{\text{illuminated}}\varphi_{\text{meso}}m_{\text{multiplicity}}\sin\theta_{110}}\right)^{\frac{1}{4}}\left(\frac{k\lambda}{\cos\theta_{110}}\right)^{\frac{3}{4}} \tag{I.1}$$

The minimum q-range, Δq_{110}, so obtained is 0.005 Å^{-1}[†] at q_{110} value of 0.0628 Å^{-1} which is relative small compared with the q-axis range of the measured SAXS pattern (Fig. 5.4(a)). If pores are arranged in a spatially ordered structure and investigated using adequately coherent X-rays, relative small broadened diffraction pecks ($\Delta q_{hkl} > q_{hkl} \pm 4\%$) would present statistically significant intensities.

[†]This specific q-range would correspond to a mesopore ordered aggregation of (N_{layers} =) 21 layers.

Appendix J

$NaAlH_4$-450 McSAS Spherical Pore Shape Analysis

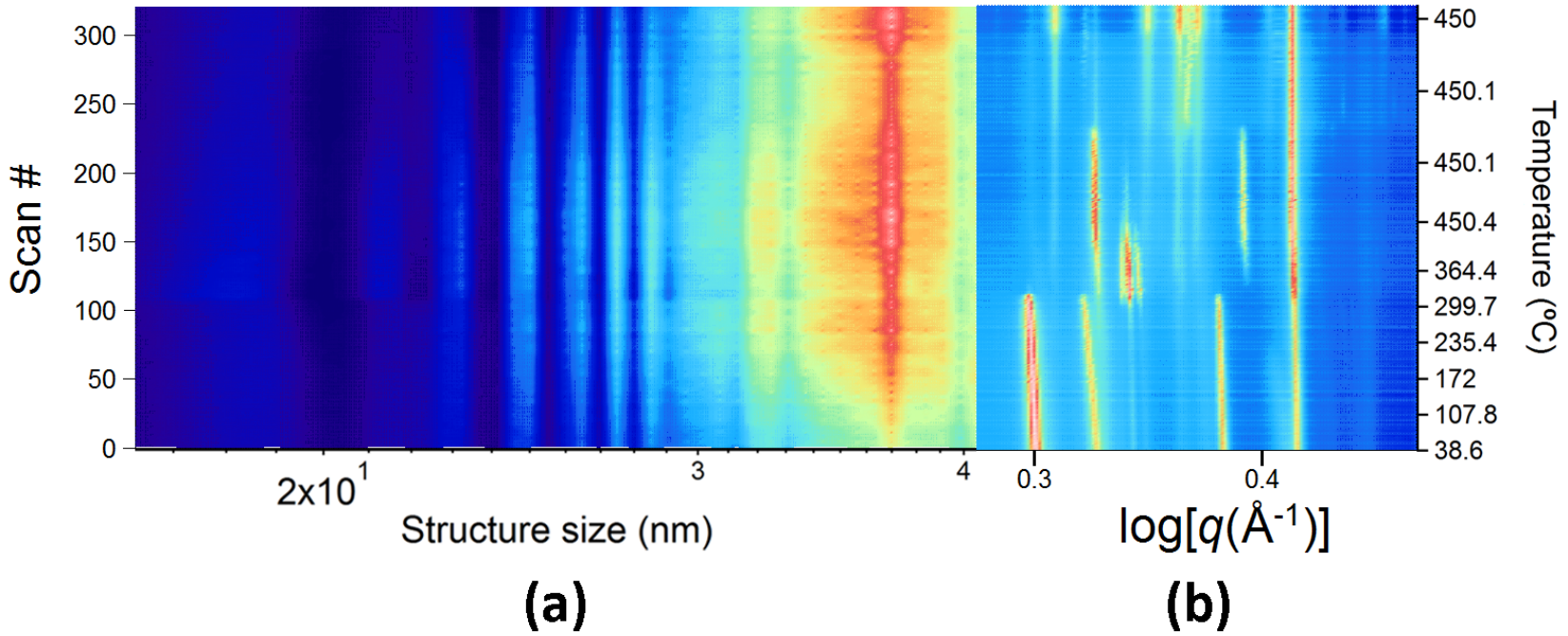

Figure J.1: (a) *In situ* pore size relative distributions, $\varphi_{i,\,\text{scan \#}} \times const_{\text{scan \#}}$, obtained applying McSAS (spherical pore shape) analysis to SAXS patterns of $NaAlH_4$-450 decomposition and (b) the corresponding WAXS patterns.

Appendix K

Sintering Temperature and Time Effects on the Growth of Pores

In Fig. K.1, normalized$I_{\mathrm{Abs}}q^4$ SAXS data are plotted in the vicinity of the high-q Porod limit range of the porous structure for two sets of *in situ* measurements (400 and 450 °C isothermal sintering condition). The time is given as minutes from the saturation of $NaAlO_2$. Once the $NaAlO_2$ phase formation saturates, mesopores are no longer formed by crystalline structure changes.

The q value at which each data set in Fig K.1 first intersects 1 on the vertical axis increases with decreasing time. These points represent the transition of $I_{\mathrm{Abs}}q^4$ between the q-range affected by mesopore sizes that have appreciable contribution to the total porosity (lower q, before constant trend of $I_{\mathrm{Abs}}q^4$), see eq. 2.36, and the Porod regime (constant trend of $I_{\mathrm{Abs}}q^4$). The decrease in this q value with time shows that the pores are growing. For the 400 °C set of patterns, the pores stopped growing after at most 2 minutes, whereas for the 450 °C set it took at most 60 min. For the 400 °C set of patterns, the 2 min patterns has a higher mesoporosity contribution to the total porosity compared with the 60 min pattern for the 450 °C set because the transition to the Porod regime occurs at a lower q value.

Fig. K.1, also shows that the high q scattering does not change over time. This shows that the behaviour at small length scales is time-independent, and most likely

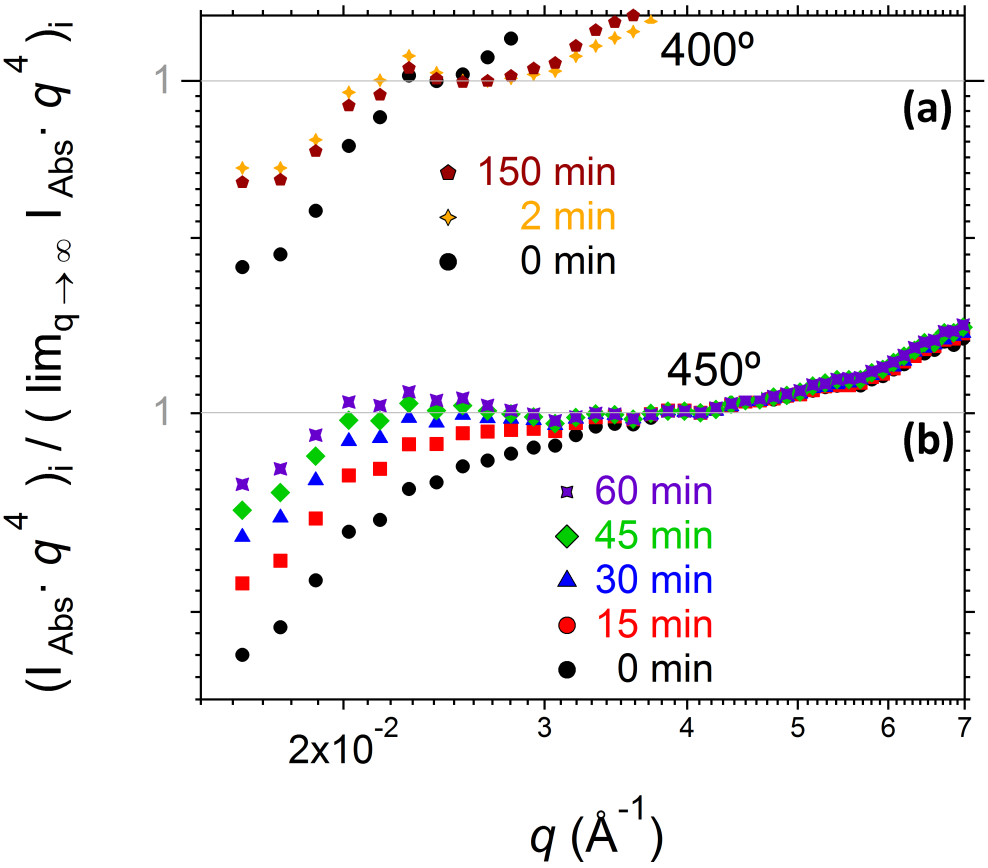

Figure K.1: SAXS data of oxidized (a) $NaAlH_4$-400 and (b) $NaAlH_4$-450 decomposed samples given as $I_{Abs}q^4$ normalised at q = (a) 0.0241 Å^{-1} and (b) 0.0411 Å^{-1}. The time is given as minutes from the saturation of $NaAlO_2$.

due to surface effects in all types of porosity related to the movement of Al at the elevated temperature.

Appendix L

Unified Fit

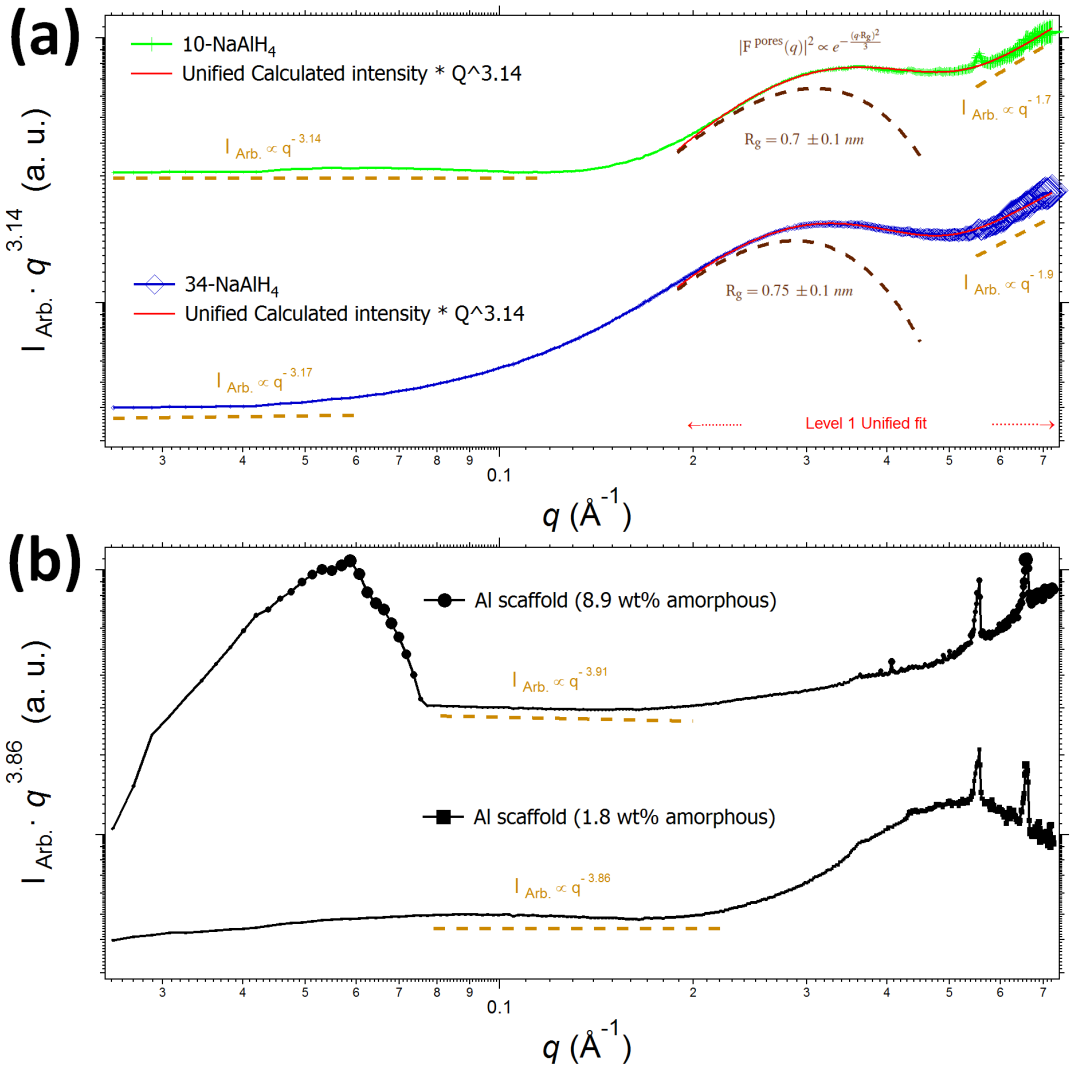

Figure L.1: (a) SAXS data for the 10-$NaAlH_4$ and 34-$NaAlH_4$ samples, plotted as $I_{\mathrm{Abs}} \times q^{3.14}$ (a. u.) *vs.* q ($\mathrm{Å}^{-1}$) on a log *vs.* log scale. The red line, the dark brown and light brown dashed lines denote the unified calculated intensity, Guinier regime and Porod regime contributions to the calculated intensity, respectively. (b) SAXS data for the Ti-enriched Al scaffold (8.9 wt% amorphous) and Al scaffold (1.8 wt% amorphous), plotted as $I_{\mathrm{Abs}} \times q^{3.86}$ (a. u.) *vs.* q ($\mathrm{Å}^{-1}$) on a log *vs.* log scale. The light brown dashed lines denote the Porod regime.

Appendix M

TPD-MS Measurements for Oxygen Contamination

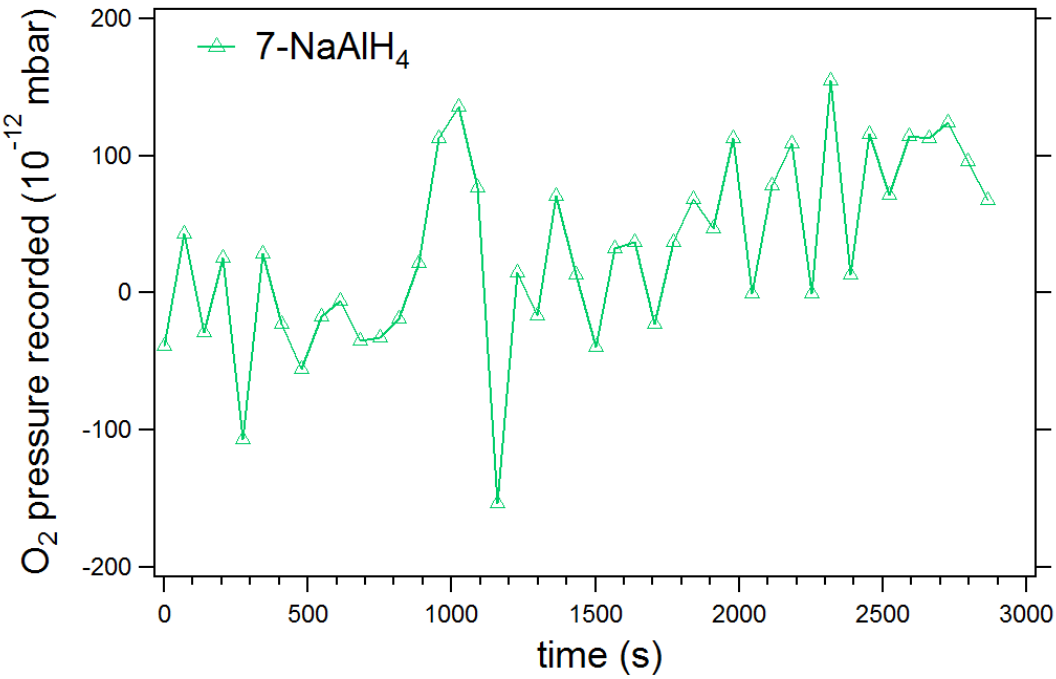

Figure M.1: TPD-MS plot of O_2 pressure (mbar) *vs.* time (s) as recorded by the mass-spectrometer for the 7-$NaAlH_4$ sample. The pattern is fluctuating around 0 mbar, typical of device noise. The hydrogen pressure recorded for the same sample at $t = 0$ seconds is 7.3×10^{-10} mbar, which monotonically increases up to 7.6×10^{-5} mbar.

Appendix N

TPD-MS Data Fit

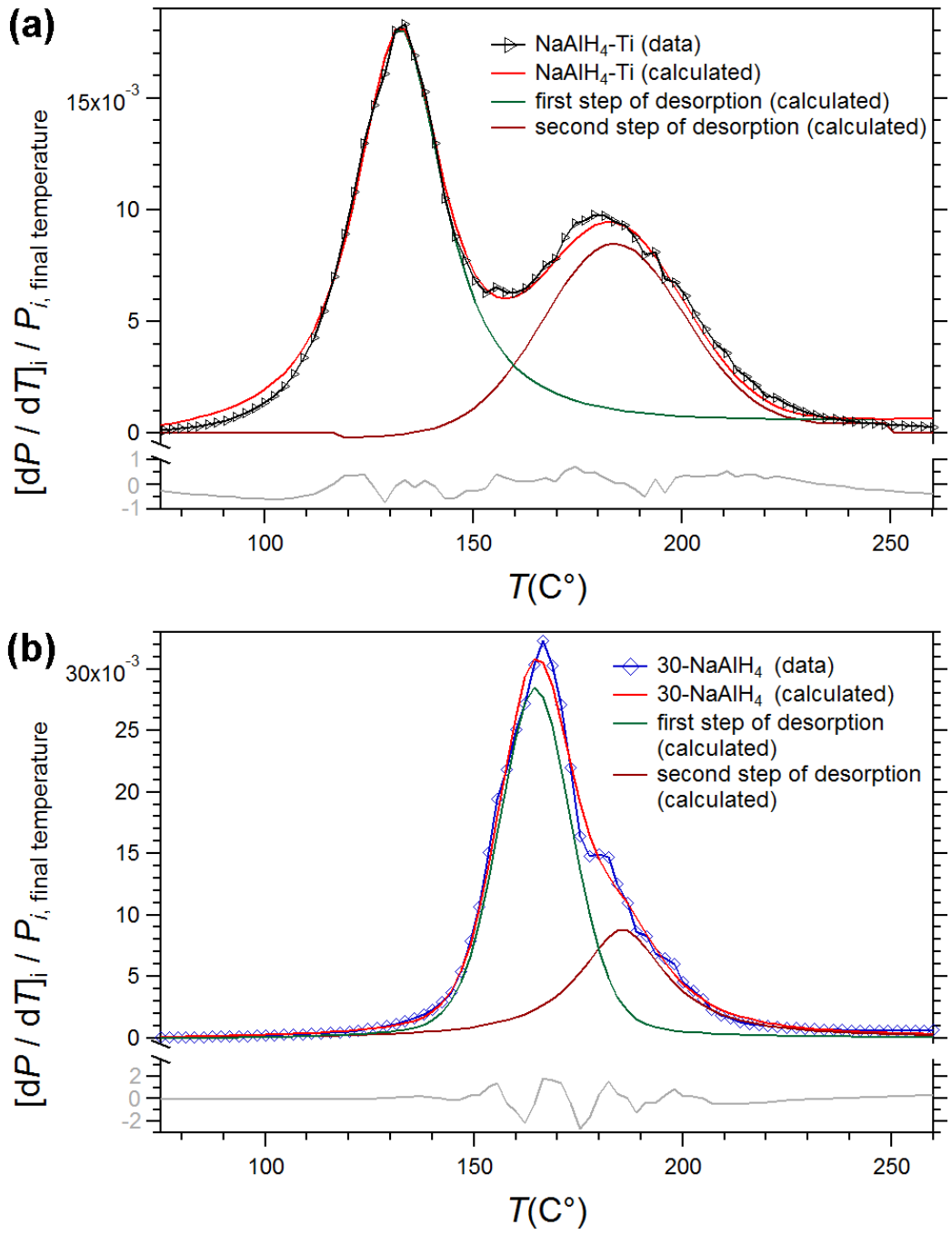

Figure N.1: Rate of H_2 release with temperature normalised per unit area acquired by applying a constant heating rate of 2 °C/min, for (a) $NaAlH_4$-Ti and (b) 30-$NaAlH_4$. (a) blue and (b) black symbols connected with lines denote the observed TPD-MS data. The green, cranberry and red lines denote the calculated TPD-MS data, fitted using two pseudo-Voigt profiles, for the first and second step of desorption, and the sum of the two, respectively.

Appendix O

Statement From the Co-Authors

To Whom It May Concern I, Enrico Ianni, contributed significantly to all components of the paper/publication entitled 'Synthesis and characterisation of a porous Al scaffold sintered from $NaAlH_4$' (*Journal of Materials Science*, 2018, 53, 1076 – 1087).

(Enrico Ianni, Candidate)

I, as a Co-Author, endorse that this level of contribution by the candidate indicated above is appropriate.

(M. V. Sofianos) (D. A. Sheppard) (M. R. Rowles)

(T. D. Humphries) (S. Liu) (C. E. Buckley)

To Whom It May Concern I, Enrico Ianni, contributed significantly to all aspects of all components of the paper/publication entitled 'Synthesis of $NaAlH_4$/Al composites and their applications in hydrogen storage' (*International Journal of Hydrogen Energy*, 2018, 43, 17309 – 17317).

(Enrico Ianni, Candidate)

I, as a Co-Author, endorse that this level of contribution by the candidate indicated above is appropriate.

(M. V. Sofianos) (M. R. Rowles) (D. A. Sheppard)

(T. D. Humphries) (C. E. Buckley)

References

1. D. Abbott, *Proceedings of the IEEE*, 2010, **98**, 42–66.

2. C. Cuevas-Cubria, A. Schultz, R. Petchey, F. Beaini and R. New, *Commonwealth of Australia*, 2011, **42**, 1–105.

3. J. Skea, *Building Research & Information*, 2012, **40**, 432–445.

4. B. Mendoza, *Advances in Space Research*, 2005, **35**, 882–890.

5. W. A. Hermann, *Energy*, 2006, **31**, 1685–1702.

6. C. L. Archer and M. Z. Jacobson, *Journal of Geophysical Research: Atmospheres*, 2005, **110**, 1–20.

7. H. N. Pollack, S. J. Hurter and J. R. Johnson, *Reviews of Geophysics*, 1993, **31**, 267–280.

8. J. Milliman and K. Farnsworth, *Gloucester Point, VA: School of Marine Science, College of William and Mary*, 1999.

9. N. N. Panicker, *Ocean Engineering*, 1976, **3**, 429–439.

10. R. D. Ray, R. Eanes and B. F. Chao, *Nature*, 1996, **381**, 595.

11. R. G. Quayle and M. J. Changery, OCEANS 81, pp. 903–907.

12. L. Schlapbach and A. Züttel, *Nature*, 2001, **414**, 353–358.

13. A. Züttel, A. Borgschulte and L. Schlapbach, *Hydrogen as a future energy carrier*, John Wiley & Sons, 2011.

14. CHFCA, *What is hydrogen?*, http://www.chfca.ca/education-centre/what-is-hydrogen/, (accessed 15/12/2018).

15. J. M. Ogden, *Annual Review of Energy and the Environment*, 1999, **24**, 227–279.

16. B. Decourt, B. Lajoie, R. Debarre and O. Soupa, *Hydrogen-Based Energy Conversion*, SBC Energy Instiute, 2014.

17. C. H. Park, S. Y. Lee, D. S. Hwang, D. W. Shin, D. H. Cho, K. H. Lee, T.-W. Kim, T.-W. Kim, M. Lee and D.-S. Kim, *Nature*, 2016, **532**, 480.

18. T. D. Humphries, D. Birkmire, B. C. Hauback, G. S. McGrady and C. M. Jensen, *Physical Chemistry Chemical Physics*, 2013, **15**, 6179–6181.

19. T. D. Humphries, J. W. Makepeace, S. Hino, W. I. David and B. C. Hauback, *Journal of Materials Chemistry A*, 2014, **2**, 16594–16600.

20. K.-S. Lee, J. S. Spendelow, Y.-K. Choe, C. Fujimoto and Y. S. Kim, *Nature Energy*, 2016, **1**, 16120.

21. D. Sun, S. S. Srinivasan, G. Chen and C. M. Jensen, *Journal of Alloys and Compounds*, 2004, **373**, 265–269.

22. D. Sperling and J. S. Cannon, *The hydrogen energy transition: cutting carbon from transportation*, Academic Press, 2004.

23. V. Quaschning and F. Trieb, Hypothesis IV Symposium, 2001, pp. 199–202.

24. D. Sheppard, M. Paskevicius, T. Humphries, M. Felderhoff, G. Capurso, J. B. von Colbe, M. Dornheim, T. Klassen, P. Ward, J. Teprovich Jr, C. Corgnale, R. Zidan, D. Grant and C. Buckley, *Applied Physics A*, 2016, **122**, 1–15.

25. US Department of Energy, *Target Explanation Document: Onboard Hydrogen Storage for Light-Duty Fuel Cell Vehicles*, 2015, https://www.energy.gov/sites/prod/files/2015/05/f22/fcto_targets_onboard_hydro_storage_explanation.pdf, (accessed 13/07/2016).

26. R. von Helmolt and U. Eberle, *Journal of Power Sources*, 2007, **165**, 833–843.

27. D. P. Broom, *Hydrogen storage materials: the characterisation of their storage properties*, Springer Science & Business Media, 2011.

28. Toyota, *2016 Mirai Product Information*, https://pressroom.toyota.com/releases/2016+toyota+mirai+fuel+cell+product.download, (accessed 15/12/2018).

29. A. Léon, in *Hydrogen storage*, Springer, 2008, pp. 81–128.

30. A. Züttel, *Naturwissenschaften*, 2004, **91**, 157–172.

31. E. Ianni, M. V. Sofianos, M. R. Rowles, D. A. Sheppard, T. D. Humphries and C. E. Buckley, *International Journal of Hydrogen Energy*, 2018, **43**, 17309–17317.

32. X. Liu, D. Peaslee, C. Z. Jost, T. F. Baumann and E. H. Majzoub, *Chemistry of Materials*, 2011, **23**, 1331–1336.

33. M. V. Sofianos, D. A. Sheppard, M. R. Rowles, T. D. Humphries, S. Liu and C. E. Buckley, *RSC Advances*, 2017, **7**, 36340–36350.

34. V. Stavila, R. K. Bhakta, T. M. Alam, E. H. Majzoub and M. D. Allendorf, *ACS nano*, 2012, **6**, 9807–9817.

35. S. Abdessameud, *Thesis*, 2016.

36. B.-M. Lee, J.-W. Jang, J.-H. Shim, Y. W. Cho and B.-J. Lee, *Journal of Alloys and Compounds*, 2006, **424**, 370–375.

37. T. D. Humphries, D. A. Sheppard and C. E. Buckley, *Coordination Chemistry Reviews*, 2017, **342**, 19–33.

38. J. Bloch and M. H. Mintz, *Journal of Alloys and Compounds*, 1997, **253**, 529–541.

39. E. Fromm, *Kinetics of Metal-Gas Interactions at low temperatures: hydriding, oxidation, poisoning*, Springer Science & Business Media, 2012, vol. 36.

40. G. Sandrock, K. Gross and G. Thomas, *Journal of Alloys and Compounds*, 2002, **339**, 299–308.

41. C. C. Wang, Y. Cheng, E. Ianni, S. P. Jiang and B. Lin, *Electrochimica Acta*, 2017, **246**, 997–1003.

42. K. Ikeda, S. Kato, Y. Shinzato, N. Okuda, Y. Nakamori, A. Kitano, H. Yukawa, M. Morinaga and S. Orimo, *Journal of Alloys and Compounds*, 2007, **446**, 162–165.

43. D. A. Sheppard, M. Paskevicius and C. E. Buckley, *Chemistry of Materials*, 2011, **23**, 4298–4300.

44. K. Momma and F. Izumi, *Journal of applied crystallography*, 2011, **44**, 1272–1276.

45. D. T. Shane, R. L. Corey, R. C. Bowman, Jr, R. Zidan, A. C. Stowe, S.-J. Hwang, C. Kim and M. S. Conradi, *The Journal of Physical Chemistry C*, 2009, **113**, 18414–18419.

46. S. Z. Karazhanov, A. Ulyashin, P. Vajeeston and P. Ravindran, *Philosophical Magazine*, 2008, **88**, 2461–2476.

47. S. Abdessameud, M. Mezbahul-Islam and M. Medraj, *The Scientific World Journal*, 2014, **2014**, 16.

48. K. Ikeda, Y. Kogure, Y. Nakamori and S. Orimo, *Scripta Materialia*, 2005, **53**, 319–322.

49. M. M. Gugelchuk, in *Sodium Aluminum Hydride*, 2001.

50. C. Qiu, S. M. Opalka, G. B. Olson and D. L. Anton, *Zeitschrift Für Metallkunde*, 2006, **97**, 1484–1494.

51. K. Gross, G. Thomas and C. Jensen, *Journal of Alloys and Compounds*, 2002, **330**, 683–690.

52. C. Jensen and K. Gross, *Applied Physics A*, 2001, **72**, 213–219.

53. A. Zaluska, L. Zaluski and J. Ström-Olsen, *Journal of Alloys and Compounds*, 2000, **298**, 125–134.

54. B. Bogdanović, R. A. Brand, A. Marjanović, M. Schwickardi and J. Tölle, *Journal of Alloys and Compounds*, 2000, **302**, 36–58.

55. T. N. Dymova, Y. M. Dergachev, V. A. Sokolov and N. A. Crechanaya, *Dokl. Akad. Nauk SSSR*, 1975, **224**, 556.

56. T. N. Dymova, N. G. Eliseeva, S. I. Bakum and Y. M. Dergachev, *Dokl. Akad. Nauk SSSR*, 1974, **215**, 256.

57. M. Senna, *Journal of Thermal Analysis and Calorimetry*, 2007, **90**, 107–113.

58. V. Skripnyuk, E. Rabkin, Y. Estrin and R. Lapovok, *Acta Materialia*, 2004, **52**, 405–414.

59. H. Wang, H. J. Lin, W. T. Cai, L. Z. Ouyang and M. Zhu, *Journal of Alloys and Compounds*, 2016, **658**, 280–300.

60. R. A. Varin and L. Zbroniec, *Journal of Alloys and Compounds*, 2010, **506**, 928–939.

61. R. A. Varin and R. Parviz, *International Journal of Hydrogen Energy*, 2012, **37**, 9088–9102.

62. R. A. Varin, L. Zbroniec, T. Czujko and Z. S. Wronski, *International Journal of Hydrogen Energy*, 2011, **36**, 1167–1176.

63. J. Aresfernandez, F. Agueyzinsou, M. Elsaesser, X. Ma, M. Dornheim, T. Klassen and R. Bormann, *International Journal of Hydrogen Energy*, 2007, **32**, 1033–1040.

64. W. Oelerich, T. Klassen and R. Bormann, *Journal of Alloys and Compounds*, 2001, **315**, 237–242.

65. G. Liang, J. Huot, S. Boily, A. Van Neste and R. Schulz, *Journal of Alloys and Compounds*, 1999, **292**, 247–252.

66. M. Resan, M. Hampton, J. Lomness and D. Slattery, *International Journal of Hydrogen Energy*, 2005, **30**, 1417–1421.

67. C. P. Balde, H. A. Stil, A. M. van der Eerden, K. P. de Jong and J. H. Bitter, *The Journal of Physical Chemistry C*, 2007, **111**, 2797–2802.

68. B. Bogdanović, M. Felderhoff, A. Pommerin, F. Schueth and N. Spielkamp, *Advanced Materials*, 2006, **18**, 1198–1201.

69. A. Haiduc, H. Stil, M. Schwarz, P. Paulus and J. Geerlings, *Journal of alloys and compounds*, 2005, **393**, 252–263.

70. C. M. Jensen, R. Zidan, N. Mariels, A. Hee and C. Hagen, *International Journal of Hydrogen Energy*, 1999, **24**, 461–465.

71. Y. Liu, X. Zhang, K. Wang, Y. Yang, M. Gao and H. Pan, *Journal of Materials Chemistry A*, 2016, **4**, 1087–1095.

72. X. Zhang, Y. Liu, K. Wang, M. Gao and H. Pan, *Nano Research*, 2015, **8**, 533–545.

73. W. Luo and K. J. Gross, *Journal of Alloys and Compounds*, 2004, **385**, 224–231.

74. T. K. Nielsen, P. Javadian, M. Polanski, F. Besenbacher, J. Bystrzycki and T. R. Jensen, *The Journal of Physical Chemistry C*, 2012, **116**, 21046–21051.

75. T. K. Nielsen, M. Polanski, D. Zasada, P. Javadian, F. Besenbacher, J. Bystrzycki, J. Skibsted and T. R. Jensen, *ACS nano*, 2011, **5**, 4056–4064.

76. A. Leon, O. Kircher, J. Rothe and M. Fichtner, *The Journal of Physical Chemistry B*, 2004, **108**, 16372–16376.

77. Q. J. Fu, A. Ramirez-Cuesta and S. C. Tsang, *The Journal of Physical Chemistry B*, 2006, **110**, 711–715.

78. S. Chaudhuri and J. T. Muckerman, *The Journal of Physical Chemistry B*, 2005, **109**, 6952–6957.

79. T. K. Nielsen, P. Javadian, M. Polanski, F. Besenbacher, J. Bystrzycki, J. Skibsted and T. R. Jensen, *Nanoscale*, 2014, **6**, 599–607.

80. M. Rueda, L. M. Sanz-Moral and Á. Martín, *The Journal of Supercritical Fluids*, 2018, **141**, 198 – 217.

81. X. Yu, Z. Tang, D. Sun, L. Ouyang and M. Zhu, *Progress in Materials Science*, 2017, **88**, 1–48.

82. L. Wang, M. Z. Quadir and K.-F. Aguey-Zinsou, *International Journal of Hydrogen Energy*, 2016, **41**, 18088–18094.

83. P. Huen, M. Paskevicius, B. Richter, D. Ravnsbæk and T. Jensen, *Inorganics*, 2017, **5**, 57.

84. S. Zhang, A. F. Gross, S. L. Van Atta, M. Lopez, P. Liu, C. C. Ahn, J. J. Vajo and C. M. Jensen, *Nanotechnology*, 2009, **20**, 204027.

85. P. Javadian, D. A. Sheppard, C. E. Buckley and T. R. Jensen, *International Journal of Hydrogen Energy*, 2015, **40**, 14916–14924.

86. M. V. Sofianos, A.-L. Chaudhary, M. Paskevicius, D. A. Sheppard, T. D. Humphries, M. Dornheim and C. E. Buckley, *Journal of Alloys and Compounds*, 2019, **775**, 474–480.

87. P. Javadian, C. Zlotea, C. M. Ghimbeu, M. Latroche and T. R. Jensen, *The Journal of Physical Chemistry C*, 2015, **119**, 5819–5826.

88. S. Chumphongphan, U. Filsø, M. Paskevicius, D. A. Sheppard, T. R. Jensen and C. E. Buckley, *International Journal of Hydrogen Energy*, 2014, **39**, 11103–11109.

89. J. Gao, P. Adelhelm, M. H. W. Verkuijlen, C. Rongeat, M. Herrich, P. J. M. van Bentum, O. Gutfleisch, A. P. M. Kentgens, K. P. de Jong and P. E. de Jongh, *The Journal of Physical Chemistry C*, 2010, **114**, 4675–4682.

90. P. Javadian, T. K. Nielsen, D. B. Ravnsbaek, L. H. Jepsen, M. Polanski, T. Plocinski, I. Kunce, F. Besenbacher, J. Bystrzycki and T. R. Jensen, *Journal of Solid State Chemistry*, 2015, **231**, 190–197.

91. E. Ianni, M. V. Sofianos, D. A. Sheppard, M. R. Rowles, T. D. Humphries, S. Liu and C. E. Buckley, *Journal of Materials Science*, 2018, **53**, 1076–1087.

92. M. V. Sofianos, D. A. Sheppard, E. Ianni, T. D. Humphries, M. R. Rowles, S. Liu and C. E. Buckley, *Journal of Alloys and Compounds*, 2017, **702**, 309–317.

93. A. Rossin, G. Tuci, L. Luconi and G. Giambastiani, *ACS Catalysis*, 2017, **7**, 5035–5045.

94. C. P. Baldé, B. P. Hereijgers, J. H. Bitter and K. P. d. Jong, *Journal of the American Chemical Society*, 2008, **130**, 6761–6765.

95. B. Chen, X. Zhao, A. Putkham, K. Hong, E. B. Lobkovsky, E. J. Hurtado, A. J. Fletcher and K. M. Thomas, *Journal of the American Chemical Society*, 2008, **130**, 6411–6423.

96. Z. Wronski, R. Varin, C. Chiu, T. Czujko and A. Calka, *Journal of alloys and compounds*, 2007, **434**, 743–746.

97. C. P. Baldé, B. P. Hereijgers, J. H. Bitter and K. P. de Jong, *Angewandte Chemie International Edition*, 2006, **45**, 3501–3503.

98. H. E. Kissinger, *Analytical chemistry*, 1957, **29**, 1702–1706.

99. M. Fichtner, *Physical Chemistry Chemical Physics*, 2011, **13**, 21186–21195.

100. V. Berube, G. Chen and M. Dresselhaus, *International Journal of Hydrogen Energy*, 2008, **33**, 4122–4131.

101. M. Fichtner, *Nanotechnology*, 2009, **20**, 204009.

102. S. Ma and H.-C. Zhou, *Chemical Communications*, 2010, **46**, 44–53.

103. S. Sartori, K. D. Knudsen, Z. Zhao-Karger, E. G. Bardaji, J. Muller, M. Fichtner and B. C. Hauback, *The Journal of Physical Chemistry C*, 2010, **114**, 18785–18789.

104. G. Kupgan, T. P. Liyana-Arachchi and C. M. Colina, *Langmuir*, 2017, **33**, 11138–11145.

105. T. T. Nguyen, D. A. Sheppard and C. E. Buckley, *Journal of Alloys and Compounds*, 2017, **716**, 291–298.

106. M. S. Tortoza, T. D. Humphries, D. A. Sheppard, M. Paskevicius, M. R. Rowles, M. V. Sofianos, K.-F. Aguey-Zinsou and C. E. Buckley, *Physical Chemistry Chemical Physics*, 2018, **20**, 2274–2283.

107. M. Felderhoff, K. Klementiev, W. Grünert, B. Spliethoff, B. Tesche, J. M. B. von Colbe, B. Bogdanović, M. Härtel, A. Pommerin and F. Schüth, *Physical Chemistry Chemical Physics*, 2004, **6**, 4369–4374.

108. J. Als-Nielsen and D. McMorrow, *Elements of modern X-ray physics*, John Wiley & Sons, 2011.

109. M. Nespolo, *Acta Crystallographica Section A: Foundations and Advances*, 2016, **72**, 168–170.

110. D. Attwood and A. Sakdinawat, *X-rays and Extreme Ultraviolet Radiation: Principles and Applications*, Cambridge university press, 2017.

111. W. David, *Nature*, 1990, **346**, 731.

112. R. W. Cheary, A. A. Coelho and J. P. Cline, *Journal of Research of the National Institute of Standards and Technology*, 2004, **109**, 1.

113. B. D. Cullity and S. R. Stock, *Elements of X-ray Diffraction*, Pearson Education, 2014.

114. R. Jenkins and R. L. Snyder, *Introduction to X-Ray Powder Diffractometry*, Wiley Online Library, 2012.

115. J. K. Cockcroft and A. N. Fitch, in *Experimental setups*, 2008, pp. 20–57.

116. Department of Earth & Planetary Sciences, The University of New Maxico, http://epswww.unm.edu/xrd/xrd-course-info.htm/, (accessed 06/06/2016).

117. J. R. Connolly, *Sample Preparation and Systematic Diffractometer Errors*, http://epswww.unm.edu/media/pdf/07-Errors-Sample-Prep.pdf, (accessed 15/12/2018).

118. The International Center for Diffraction Data, http://www.icdd.com/, (accessed 15/12/2018).

119. Crystallography Open Database, http://www.crystallography.net/cod/, (accessed 15/12/2018).

120. S. Gražulis, A. Daškevič, A. Merkys, D. Chateigner, L. Lutterotti, M. Quirós, N. R. Serebryanaya, P. Moeck, R. T. Downs and A. Le Bail, *Nucleic Acids Research*, 2012, **40**, D420–D427.

121. S. Gražulis, D. Chateigner, R. T. Downs, A. F. T. Yokochi, M. Quirós, L. Lutterotti, E. Manakova, J. Butkus, P. Moeck and A. Le Bail, *Journal of Applied Crystallography*, 2009, **42**, 726–729.

122. R. Hill and C. Howard, *Journal of Applied Crystallography*, 1987, **20**, 467–474.

123. G. Porod, *Small-angle X-ray scattering. Academic Press, London, United Kingdom*, 1982.

124. H. Rietveld, *Journal of applied Crystallography*, 1969, **2**, 65–71.

125. A. A. Coelho, *Journal of Applied Crystallography*, 2018, **51**, 210–218.

126. R. Snellings, L. Machiels, G. Mertens and J. Elsen, *Geologica belgica*, 2010, **13**, 183–196.

127. Australian Synchrotron, *SAXS/WAXS Beamline Technical Specifications*, http://archive.synchrotron.org.au/aussyncbeamlines/saxswaxs/saxs-specifications, (accessed 15/12/2018).

128. A. Brûlet, D. Lairez, A. Lapp and J.-P. Cotton, *Journal of Applied Crystallography*, 2007, **40**, 165–177.

129. R. L. Cappelletti, T. J. Udovic, H. Li and R. L. Paul, *Journal of applied crystallography*, 2018, **51**, 1323–1328.

130. Australian Synchrotron, *scatterBrain Manual*, https://archive.synchrotron.org.au/images/scatterBrainManual2.pdf, (accessed 15/12/2018).

131. C. A. Dreiss, K. S. Jack and A. P. Parker, *Journal of Applied Crystallography*, 2006, **39**, 32–38.

132. B. R. Pauw, A. Smith, T. Snow, N. Terrill and A. F. Thünemann, *Journal of applied crystallography*, 2017, **50**, 1800–1811.

133. B. R. Pauw, *Journal of Physics: Condensed Matter*, 2013, **25**, 383201.

134. N. V. Y. Scarlett, M. R. Rowles, K. S. Wallwork and I. C. Madsen, *Journal of Applied Crystallography*, 2011, **44**, 60–64.

135. NDT Resource Center, *Sources of Attenuation*, https://www.nde-ed.org/EducationResources/CommunityCollege/Radiography/Physics/attenuation.htm, (accessed 08/02/2018).

136. O. Spalla, S. Lyonnard and F. Testard, *Journal of Applied Crystallography*, 2003, **36**, 338–347.

137. M. H. Verkuijlen, J. Gao, P. Adelhelm, P. J. M. van Bentum, P. E. de Jongh and A. P. Kentgens, *The Journal of Physical Chemistry C*, 2010, **114**, 4683–4692.

138. W. H. De Jeu, *Basic X-Ray scattering for soft matter*, Oxford University Press, United Kingdom, 2016.

139. R. Besselink, T. Stawski, A. Van Driessche and L. Benning, *The Journal of Chemical Physics*, 2016, **145**, 211908.

140. SASfit, *Sphere & Spherical Shells*, https://kur.web.psi.ch/sans1/SANSSoft/versions/doc/html/group__ff__sphere.html, (accessed 15/12/2018).

141. H. D. Bale and P. W. Schmidt, *Physical Review Letters*, 1984, **53**, 596.

142. A. J. Hurd, D. W. Schaefer, D. M. Smith, S. B. Ross, A. Le Méhauté and S. Spooner, *Physical Review B*, 1989, **39**, 9742.

143. P. Pfeifer and P. W. Schmidt, *Physical review letters*, 1988, **60**, 1345.

144. P.-z. Wong and A. J. Bray, *Physical review letters*, 1988, **60**, 1344.

145. G. Beaucage, *Journal of Applied Crystallography*, 1995, **28**, 717–728.

146. G. Beaucage, *Journal of Applied Crystallography*, 1996, **29**, 134–146.

147. R. Winter, A. Gabke, C. Czeslik and P. Pfeifer, *Physical Review E*, 1999, **60**, 7354.

148. G. Beaucage, H. K. Kammler and S. E. Pratsinis, *Journal of Applied Crystallography*, 2004, **37**, 523–535.

149. J. Ilavsky and P. R. Jemian, *Journal of Applied Crystallography*, 2009, **42**, 347–353.

150. M. Paskevicius, H.-Y. Tian, D. A. Sheppard, C. J. Webb, M. P. Pitt, E. M. Gray, N. M. Kirby and C. E. Buckley, *Journal of Physical Chemistry C*, 2011, **115**, 1757–1766.

151. I. Breßler, B. R. Pauw and A. Thünemann, *Journal of applied crystallography*, 2015, **48**, 962–969.

152. B. R. Pauw, J. S. Pedersen, S. Tardif, M. Takata and B. B. Iversen, *Journal of applied crystallography*, 2013, **46**, 365–371.

153. P. Spencer, *Calphad*, 2008, **32**, 1–8.

154. V. Drebushchak, *Journal of Thermal Analysis and Calorimetry*, 2008, **95**, 313–317.

155. Scientific Group Thermodata Europe, *Thermodynamic Properties of Inorganic Materials*, Springer-Verlag, Berlin-Heidelberg, 1999, vol. 19.

156. O. Knacke, O. Kubaschewski and K. Hesselmann, *Thermochemical properties of inorganic substances*, Springer Berlin, 1991, vol. 1.

157. A. J. Bard, R. Parsons and J. Jordan, *Standard potentials in aqueous solution*, CRC press, 1985, vol. 6.

158. D. R. Lide and H. V. Kehiaian, *CRC handbook of thermophysical and thermochemical data*, Crc Press, 1994, vol. 1.

159. Wikipedia, *Scanning Electron Microscope*, https://en.wikipedia.org/wiki/Scanning_electron_microscope, (accessed 15/12/2018).

160. P. S. Mbule, *Thesis*, 2009.

161. J. I. Goldstein, D. E. Newbury, J. R. Michael, N. W. Ritchie, J. H. J. Scott and D. C. Joy, *Scanning electron microscopy and X-ray microanalysis*, Springer, 2017.

162. Instructables, *Making a 3D Print of a Real Object Using 123D Catch and Meshmixer*, http://www.instructables.com/id/Making-a-3D-print-of-a-real-object-using-123D-Catc/?ALLSTEPS, (accessed 15/12/2018).

163. Autodesk, *Autocad Architecture*, http://www.autodesk.com.au/products/autocad-architecture/overview, (accessed 15/12/2018).

164. Autodesk, *ReCap-360*, http://www.autodesk.com/products/recap-360/overview, (accessed 15/12/2018).

165. G. Halsey, *The Journal of Chemical Physics*, 1948, **16**, 931–937.

166. W. D. Harkins and G. Jura, *Journal of the American Chemical Society*, 1944, **66**, 1362–1366.

167. K. S. W. Sing, *Pure and Applied Chemistry*, 1985, **57**, 603–619.

168. V. Zhdanov, V. Fenelonov and D. Efremov, *Journal of colloid and interface science*, 1987, **120**, 218–223.

169. E. Barrett, *J. Am. Chem. Soc.*, 1951, **73**, 373.

170. J. Lord Kelvin, *Philosophical Magazine*, 1871, **42**, 5.

171. S. Brunauer, L. S. Deming, W. E. Deming and E. Teller, *Journal of the American Chemical society*, 1940, **62**, 1723–1732.

172. S.-J. Park and M.-K. Seo, in *Chapter 2 - Solid-Gas Interaction*, ed. S.-J. Park and M.-K. Seo, Elsevier, 2011, vol. 18, pp. 59–145.

173. M. Kruk, M. Jaroniec and A. Sayari, *Langmuir*, 1997, **13**, 6267–6273.

174. T. Blach and E. M. Gray, *Journal of Alloys and Compounds*, 2007, **446**, 692–697.

175. X.-L. Wang and S. Suda, *International Journal of Hydrogen Energy*, 1992, **17**, 139–147.

176. A.-L. Chaudhary, M. Paskevicius, D. A. Sheppard and C. E. Buckley, *Journal of Alloys and Compounds*, 2015, **623**, 109–116.

177. M. Paskevicius, *Thesis*, 2009.

178. D. A. King, *Surface Science*, 1975, **47**, 384–402.

179. A. De Jong and J. Niemantsverdriet, *Surface Science*, 1990, **233**, 355–365.

180. E. Habenschaden and J. Küppers, *Surface Science*, 1984, **138**, L147–L150.

181. D. A. Sheppard, M. Paskevicius and C. E. Buckley, *Chemistry of Materials*, 2011, **23**, 4298–4300.

182. J. Banhart, *Progress in materials Science*, 2001, **46**, 559–632.

183. T. D. Humphries, D. A. Sheppard, M. R. Rowles, M. V. Sofianos and C. Buckley, *Journal of Materials Chemistry A*, 2016, **4**, 12170–12178.

184. F. Su, X. Zhao, Y. Wang, J. Zeng, Z. Zhou and J. Y. Lee, *The Journal of Physical Chemistry B*, 2005, **109**, 20200–20206.

185. L. Yan, X. Bo, Y. Zhang and L. Guo, *Electrochimica Acta*, 2014, **137**, 693–699.

186. C. Zhao, W. Wang, Z. Yu, H. Zhang, A. Wang and Y. Yang, *Journal of Materials Chemistry*, 2010, **20**, 976–980.

187. H2 Technology Consulting, *Recommended Best Practices for the Characterization of Storage Properties of Hydrogen Storage Materials*, 2012, https://energy.gov/sites/prod/files/2014/03/f12/best_practices_hydrogen_storage.pdf, (accessed 15/12/2018).

188. P. Yang, D. Zhao, D. I. Margolese, B. F. Chmelka and G. D. Stucky, *Nature*, 1998, **396**, 152.

189. D. Zhao, J. Feng, Q. Huo, N. Melosh, G. H. Fredrickson, B. F. Chmelka and G. D. Stucky, *science*, 1998, **279**, 548–552.

190. D. J. Kohls and G. Beaucage, *Current Opinion in Solid State and Materials Science*, 2002, **6**, 183–194.

191. I.-W. Chen and X.-H. Wang, *Nature*, 2000, **404**, 168–171.

192. P. Chen and I. Chen, *Journal of the American Ceramic Society*, 1996, **79**, 3129–3141.

193. S. Gabelkov, R. Tarasov and A. Mironova, *Powder Metallurgy and Metal Ceramics*, 2011, **50**, 151–156.

194. Z. Hu and K. Lu, *Journal of the American Ceramic Society*, 2014, **97**, 2383–2386.

195. I. Nettleship, T. Chen and K. Ewsuk, *Journal of the American Ceramic Society*, 2007, **90**, 3793–3799.

196. A. A. Coelho, *TOPAS-Academic, Version 6*, 2015, http://www.topas-academic.net/Technical_Reference.pdf, (accessed 15/12/2018).

197. A. Borgschulte, R. Gremaud and R. Griessen, *Physical Review B*, 2008, **78**, 094106.

198. F. Schweppe, M. Martin and E. Fromm, *Journal of alloys and compounds*, 1997, **261**, 254–258.

199. T. Mueller and G. Ceder, *ACS nano*, 2010, **4**, 5647–5656.

200. M. L. Ojeda, J. M. Esparza, A. Campero, S. Cordero, I. Kornhauser and F. Rojas, *Physical Chemistry Chemical Physics*, 2003, **5**, 1859–1866.

201. T. M. Willey, L. Lauderbach, F. Gagliardi, T. van Buuren, E. A. Glascoe, J. W. Tringe, J. R. Lee, H. K. Springer and J. Ilavsky, *Journal of Applied Physics*, 2015, **118**, 055901.

202. S. Narayanan, A. Sandy, D. Shu, M. Sprung, C. Preissner and J. Sullivan, *Journal of synchrotron radiation*, 2008, **15**, 12–18.

203. R. Alonso-Mori, C. Caronna, M. Chollet, R. Curtis, D. S. Damiani, J. Defever, Y. Feng, D. L. Flath, J. M. Glownia and S. Lee, *Journal of synchrotron radiation*, 2015, **22**, 508–513.

204. R. Jenkins and R. E. Meyers, *John Wiley & Sons Ltd, Chichester*, 2000, 13269–13288.

205. School of Crystallography, Birkbeck College, University of London, *Scattering of X-rays by a Collection of Electrons as in an Atom*, http://pd.chem.ucl.ac.uk/pdnn/diff1/scaten.htm, (accessed 15/12/2018).

206. GISAXS, *Atomic Scattering Factors*, http://gisaxs.com/index.php/Atomic_scattering_factors, (accessed 15/12/2018).

207. F. Bassani, G. P. Parravicini, R. Ballinger and J. L. Birman, *Physics Today*, 1976, **29**, 58.

208. National Institute of Standards and Technology, *X-Ray form Factor, Attenuation and Scattering Tables*, https://physics.nist.gov/PhysRefData/FFast/html/form.html, (accessed 15/12/2018).

209. Topas Wiki, *7.3 Calculation of structure factors*, http://topas.dur.ac.uk/topaswiki/doku.php?id=manual_part_1, (accessed 15/12/2018).

210. H. P. Klug and L. E. Alexander, *X-ray diffraction procedures: for polycrystalline and amorphous materials*, Wiley-VCH, 1974, p. 992.